THE EFFECTS OF SUPRAMOLECULAR INTERACTIONS ON IRON(II) SPIN CROSSOVER COMPOUNDS

A Thesis Submitted in Partial Fulfilment of the Requirements for the Degree of
Doctor of Philosophy *in* ***Chemistry***

Rosanna Juliet Archer

University of Canterbury

2013

Table of Contents

Acknowledgments

First and foremost, I would like to thank my enthusiastic supervisor Prof. Paul Kruger, for his inspiration and ideas and for all of his advice and wisdom during both my Honours and PhD projects. Along with a wonderful supervisor, I also had the privilege of working with a fantastic group of people in the Kruger research group, both past and present. In particular, thank you Chris, Marky, Alan, Dave and Shane for making the office a cheerful and friendly place to be. I must also thank the members of the Hartshorn, Fitchett and Steel groups for their support and advice throughout my time here.

The entire academic and general staff of the Chemistry department also deserve my gratitude for being prepared to share their knowledge; special mentions must be made to Dr. Chris Fitchett, Dr. Matt Polson, Dr. Jan Wikaira, and Prof. Peter Steel for their assistance in my foray into the world of crystallography; Dr. Marie Squire for her invaluable knowledge of NMR and Mass Spec., along with Dr. Meike Holzenkaemfer for all of her assistance with NMR and Mass Spec. as well. I would also like to thank Wayne Mackay, Rob McGregor and the rest departmental technical staff, for the wonderful work they do to keep the department running smoothly and for keeping all of us in chemicals, glassware and working equipment.

During this project I was fortunate enough to visit the Université de Bordeaux to perform magnetic susceptibility, surface reflectivity and photomagnetic measurements with Prof. Roldophe Clérac, Mathieu Rouzieres and Prof. Corine Mathonière. All of your time, knowledge and assistance have been greatly appreciated and also I would like to thank you and your research groups for making me feel so welcome when I was a very long way from home!

I would also like to acknowledge our collaborators Prof. Keith Murray and Dr. Boujemaa Moubaraki (Monash University – magnetic susceptibility measurements), Guy Jameson (Otago University – Mössbauer) and Prof. Vickie McKee (Loughborough University – Synchotron) for performing the measurements outlined in Chapter Three of this work. Also I would like to acknowledge Prof. Bryce Williamson for elucidating the thermodynamic parameters from the solution studies in Chapters Two and Five.

I would like to express my gratitude to the Marsden Fund, for providing a PhD scholarship, the Claude McCarthy Fellowship, for funding to visit the Université de Bordeaux and to the NZIC for providing conference travel funding.

And finally, to all my friends and family, especially Tim Douglas, for their love, encouragement and support.

Abbreviations:

SCO: Spin Crossover
LS: Low-Spin
HS: High-Spin
LIESST: Light-Induced Excited Spin-State Trapping
RT: Room Temperature
NMR: Nuclear Magnetic Resonance
IR: Infrared
UV-Vis.: UV-Visible
HR-ESMS: High Resolution Electrospray Mass Spectrometry
TGA: Thermogravimetric Analysis
m.p.: Melting Point
DMSO: Dimethyl Sulphoxide
MeOH: Methanol
EtOH: Ethanol
MeCN: Acetonitrile

Atom Colouring Scheme:
Black: Carbon
White: Hydrogen
Red: Oxygen
Blue: Nitrogen
Gold: Iron (II)
Light Green: Fluorine
Dark Green: Chlorine
Pink: Boron
Maroon: Bromine

Abstract

Molecules with functional properties, especially ones that display spin crossover behaviour, are becoming increasingly well researched due to their potential applications as the active components in molecular memory, optical displays or sensors.[1,2] To this end, a series of Fe(II) coordination compounds utilising imidazolylimine and pyridylimine based ligands have been synthesised and their spin crossover behaviour analysed through a variety of techniques including variable temperature X-ray crystallography, magnetic susceptibility, surface reflectivity and UV-Visible spectroscopy. Light-Induced Excited Spin-State Trapping (LIESST) effects have also been analysed *via* photomagnetic measurements.

Particular attention was paid to the supramolecular interactions present within the solid-state and the effect that these interactions may have on spin crossover behaviour. Subtle changes to the complexes through counter-anion exchange, solvent effects and ligand design were explored and careful structural analysis completed.

This study was separated into two distinct categories. The first describes the synthesis, structural characterisation and spin crossover behaviour of Fe(II) dinuclear triple helicates. Four dinuclear triple helicates have been synthesised, three of which display spin crossover behaviour. Weak LIESST effects were observed in two of these examples. Variation in the ligand field strength between the complexes was achieved through modification of the coordinating "head group" and differences between the flexibility of the ligand backbone were also explored.

The latter part of this study describes the synthesis, structural characterisation and spin crossover behaviour of novel Fe(II) mononuclear complexes. A series of related ligands which differ in the *p*-substituent have been synthesised and their coordination chemistry with Fe(II) metal ions examined. Subtle changes to the counter-anion and crystallised solvent molecules were also explored during this study. Five mononuclear Fe(II) complexes were shown to undergo spin crossover and the structural changes associated with the spin-state conversion have been analysed *via* variable temperature X-ray crystallography and compared with magnetic susceptibility measurements. Two complexes were also analysed for LIESST behaviour and these complexes showed full photo-excitation into the high-spin state at 10 K.

Deputy Vice-Chancellor's Office
Postgraduate Office

UNIVERSITY OF CANTERBURY
Te Whare Wānanga o Waitaha
CHRISTCHURCH NEW ZEALAND

Co-Authorship Form

This form is to accompany the submission of any thesis that contains research reported in co-authored work that has been published, accepted for publication, or submitted for publication. A copy of this form should be included for each co-authored work that is included in the thesis. Completed forms should be included at the front (after the thesis abstract) of each copy of the thesis submitted for examination and library deposit.

Please indicate the chapter/section/pages of this thesis that are extracted from co-authored work and provide details of the publication or submission from the extract comes:

Chapter Three of this thesis extracted from: Archer, R. J; Hawes, C. S.; Jameson, G. N. L.; McKee, V. Moubaraki, B.; Chilton, N. F.; Murray, K. S.; Schmitt, W.; Kruger, P. E. "Partial Spin Crossover Behaviour in a Dinuclear Iron(II) Triple Helicate" *Dalton Trans.* **2011**, *40* 12368-12373

Please detail the nature and extent (%) of contribution by the candidate:

40% - Synthesis of compound, analysis, manuscript preparation

Certification by Co-authors:

If there is more than one co-author then a single co-author can sign on behalf of all

The undersigned certifys that:

- The above statement correctly reflects the nature and extent of the PhD candidate's contribution to this co-authored work
- In cases where the candidate was the lead author of the co-authored work he or she wrote the text

Name: *Prof. Paul Kruger* Signature: Paul Kruger Date: 29/11/15

Deputy Vice-Chancellor's Office
Postgraduate Office

UNIVERSITY OF CANTERBURY
Te Whare Wānanga o Waitaha
CHRISTCHURCH NEW ZEALAND

Co-Authorship Form

This form is to accompany the submission of any thesis that contains research reported in co-authored work that has been published, accepted for publication, or submitted for publication. A copy of this form should be included for each co-authored work that is included in the thesis. Completed forms should be included at the front (after the thesis abstract) of each copy of the thesis submitted for examination and library deposit.

Please indicate the chapter/section/pages of this thesis that are extracted from co-authored work and provide details of the publication or submission from the extract comes:

Pages 77-78 were extracted from: Thompson, J. R.; Archer, R. J.; Hawes, C. S.; Ferguson, A.; Wattiaux, A.; Mathonière, C. Clérac, R.; Kruger, P. E. "Spin Crossover Behaviour and Light-Induced Excited Spin State Trapping in an Fe(II) Imidazolylimine Complex: $[FeL_3](ClO_4)_2$" *Dalton Trans.* **2012** 41, 12720-12725.

Please detail the nature and extent (%) of contribution by the candidate:

10% - Assistance with synthesis, analysis and manuscript preparation.

Certification by Co-authors:

If there is more than one co-author then a single co-author can sign on behalf of all

The undersigned certifys that:

- The above statement correctly reflects the nature and extent of the PhD candidate's contribution to this co-authored work
- In cases where the candidate was the lead author of the co-authored work he or she wrote the text

Name: *Prof. Paul Kruger* Signature: Paul Kruger Date: 29/11/13

CHAPTER ONE

Introduction

1.1 Preamble and Scope

This study investigates the spin crossover behaviour of a series of Fe(II) coordination compounds with a particular focus on how supramolecular interactions affect this behaviour. The fields of both supramolecular chemistry – the study of weak intermolecular forces and their use in forming large self-assembled structures; and spin crossover – the study of bistable compounds which transition between high- and low-spin states under external perturbation such as temperature, light, or pressure, are broad in scope and as such a full overview of both fields will not be provided within this introduction. Instead, this introduction will briefly cover the pertinent aspects of supramolecular chemistry covering the history, principles and potential applications that utilise these concepts. The subject of supramolecular chemistry is generally split into two main areas, discrete and infinite assemblies. As the present study involves the synthesis of discrete coordination compounds, the study of infinite coordination assemblies will only be covered briefly. Relevant facets of spin crossover phenomena will be discussed within the second half of this introduction covering the main principles of thermal spin crossover and light-induced excited spin-state trapping and concludes with an overview of potential applications. This study describes spin crossover behaviour in Fe(II) systems exclusively and as such the behaviour of other metal ions which may display spin crossover behaviour will not be discussed. Finally, the techniques employed during this research will be explained and the aims and scope of the study will be outlined in detail.

1.2 History of Supramolecular Chemistry

Supramolecular chemistry as it is known today has its roots in the 1960s with research into the synthesis of macrocyclic compounds able to bind cationic species. These macrocycles took on many forms with the notable work by Pederson into the crown ether macrocycles[3], Lehn's study of cryptands[4,5], and research by Cram into spherand and cavitand type macrocycles,[6,7] all of which were found to bind cationic species. This research culminated in Pederson, Lehn, and Cram being awarded the Nobel Prize in 1987 for "*their development and use of molecules with structure-specific interactions of high selectivity"*.[8] Selected examples of these molecules are illustrated in **Fig 1.2.1**.

However, the work by Lehn, Cram and Pederson was not the first instance of supramolecular chemistry with the term "*supramolecular*" originally being derived from the German "*übermoleküle"* (supermolecule) coined by Wolf in 1937, describing the interaction between two acetic acid molecules in solution to form a dimer.[9] This interaction was defined as "*entities of higher organisation resulting from the association of two or more coordinatively*

saturated species." Indeed, investigations into the associations between molecules have occurred since the early 1800s, particularly through the study of enzymatic reactions.

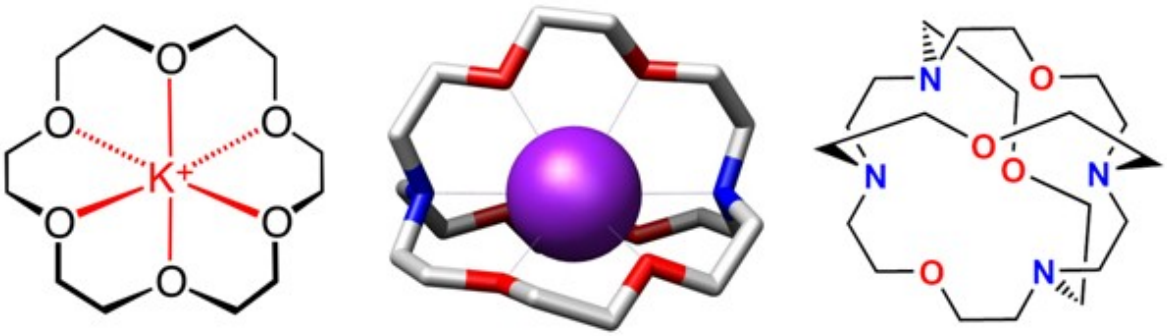

Fig 1.2.1 *Structure of 18-Crown-6 shown coordinating a potassium ion (**left**), structure of 2.2.2-Cryptand shown coordinating a potassium ion (**middle**) and structure of a spherand (**right**).*[10-12]

In 1894 Fischer introduced the "*lock and key*" concept to describe the specificity of enzymes for their given substrates,[13] a concept which relied upon weak interactions occurring between the enzyme and its respective substrate. As the understanding of chemical bonds grew, advancements in X-ray crystallographic technology also played a significant role in understanding the weaker interactions between molecules. The elucidation of the structure of DNA by Watson and Crick in 1953, in which hydrogen bonding between nucleotides was found to be critical to the structure of DNA, cemented the importance of weaker interactions within biologically relevant molecules (**Fig 1.2.2**).[14]

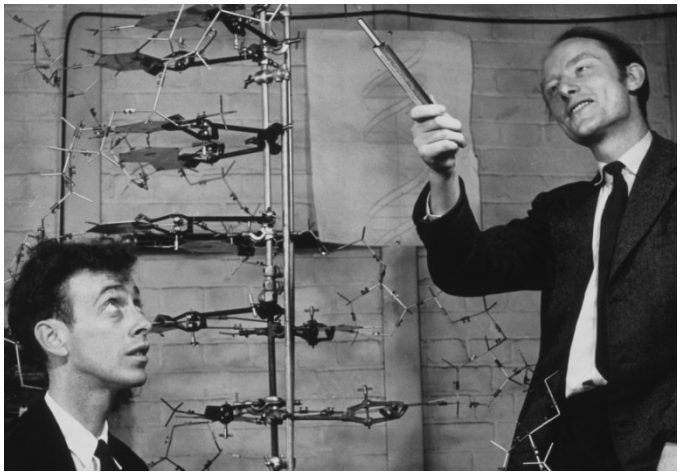

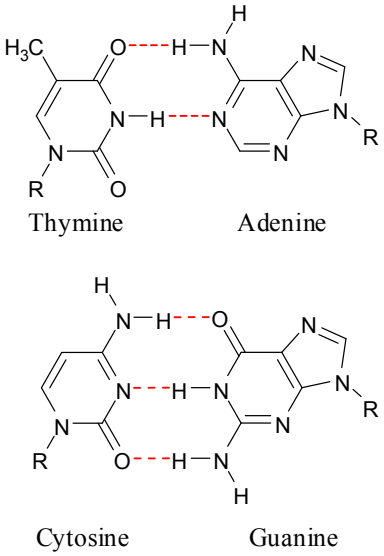

Fig 1.2.2 *Watson and Crick with a model of DNA (**left**)*[15] *and a closer inspection of the hydrogen bonding interactions between nucleotide bases (**right**).*

The subsequent explosion of interest in the field of supramolecular chemistry came in part from the multi-disciplinary nature of the research. Not only the exclusive realm of the supramolecular chemist; the field is buoyed by inputs from synthetic organic chemists (ligand synthesis), computational and theoretical chemists (prediction and design of supramolecular entities), physicists (understanding the nature of these weaker interactions), crystallographers, biochemists, biologists and many other scientific disciplines.[16] To this end supramolecular chemistry is one of the fastest growing areas of modern chemistry which now spans a host of compounds, from the organic macrocyclic species described above and the phenomenal scope of metallosupramolecular complexes, to the complexities of miniature molecular machines.[17]

The current introduction is not exhaustive and will cover selected aspects of this broad subject matter. For further information the reader is directed to the following references which give an excellent overview of supramolecular chemistry in greater detail.[17-20]

1.3 Synthons in Supramolecular Chemistry

1.3.1 Overview

It was Lehn who described supramolecular chemistry as "*the designed chemistry of the intermolecular bond"*[21] and from this definition it is important to understand the nature of the "*intermolecular bond"*. Where conventional chemistry focuses on the interactions between atoms and the formation of covalent bonds, supramolecular chemistry involves the study of the weaker interactions between molecules. These weaker interactions have an advantage in that their formation is reversible and systems involving these interactions are able to equilibrate to the most thermodynamically stable state and as such any errors in assembly are corrected. This process gives rise to the ability of these systems to "*self-assemble*" where single units are able to aggregate to form thermodynamically stable, complex structures in high yield. In order to achieve a system that self-assembles it is important to have information encoded into the smaller units to direct the aggregation of the highly ordered final structure. The supramolecular chemist has a tool-box of interactions at their disposal to design particular structural characteristics into the final compound. These interactions are known as "*synthons"* and have been defined by Corey as "*structural units within molecules which can be formed and/or assembled by known or conceivable synthetic operations."*[22,23] The varied nature of these synthons gives rise to an overwhelming abundance of and diverse nature in supramolecular complexes within the literature.

1.3.2 The Hydrogen Bond

An important supramolecular synthon is the hydrogen bond. First postulated by Pauling in 1931[24] the hydrogen bond is described by IUPAC as "*an attractive interaction between a hydrogen atom from a molecule or a molecular fragment (X-H) in which X is more electronegative than H, and an atom or group of atoms in the same or a different molecule, in which there is evidence of bond formation.*"[25] As anticipated the hydrogen bond can range in strength depending on the nature of the atoms, geometries, and bond distances involved. A conventional hydrogen bond, where both the hydrogen bond donor (D) and the acceptor (A) are largely electronegative (for example O-H···N), have bond strengths between 20 – 40 kJ mol^{-1} whereas weaker hydrogen bonds occur between less electronegative species such as C-H···O, with these interactions typically having bond strengths in the 2 – 20 kJ mol^{-1} range.[20]

The C-H···A interactions or "*non-conventional hydrogen bonds*"[26,27] are significantly weaker than their conventional counterparts but still play an important role as stabilising forces within the solid state. Where the carbon atom is in an electron-deficient environment, this leads to a greater contribution of the electrostatic forces between the components and therefore creates a stronger interaction. Along with a variation in the strength of the hydrogen bond due to electrostatic interactions, the hydrogen bond is also directional in nature with D-H···A angles closer to 180° giving the strongest interactions. Examples of typical hydrogen bonding parameters are defined in **Table 1.3.1**.

Hydrogen bonds form complementary interactions with both donor and acceptor species required to form bonds. This complementarity can be exploited by the supramolecular chemist to make highly ordered structures with surprising stability as shown in **Fig 1.3.2**.

In particular, molecules incorporating hydrogen bond donors have been shown to have a strong affinity for anionic species, making them ideal in potential anion-sensing applications.[28]

	Strong	Moderate	Weak
D-H···A	Partially Covalent	Mostly Electrostatic	Electrostatic
Energy	60-120 kJ mol^{-1}	16-60 kJ mol^{-1}	< 12 kJ mol^{-1}
Lengths (Å)	D-H ~ H···A	D-H < H···A	D-H << H···A
H···A	1.2 – 1.5	1.5 – 2.2	2.2 – 3.2
D···A	2.2 – 2.5	2.5 – 3.2	3.2 – 4.0
Example	F-H and proton sponge interactions	α-helices and β-sheet configurations of polypeptide chains	Bifurcated hydrogen bonding interactions

Table 1.3.1 *Table showing the typical properties of hydrogen bonds.* [20,29-31]

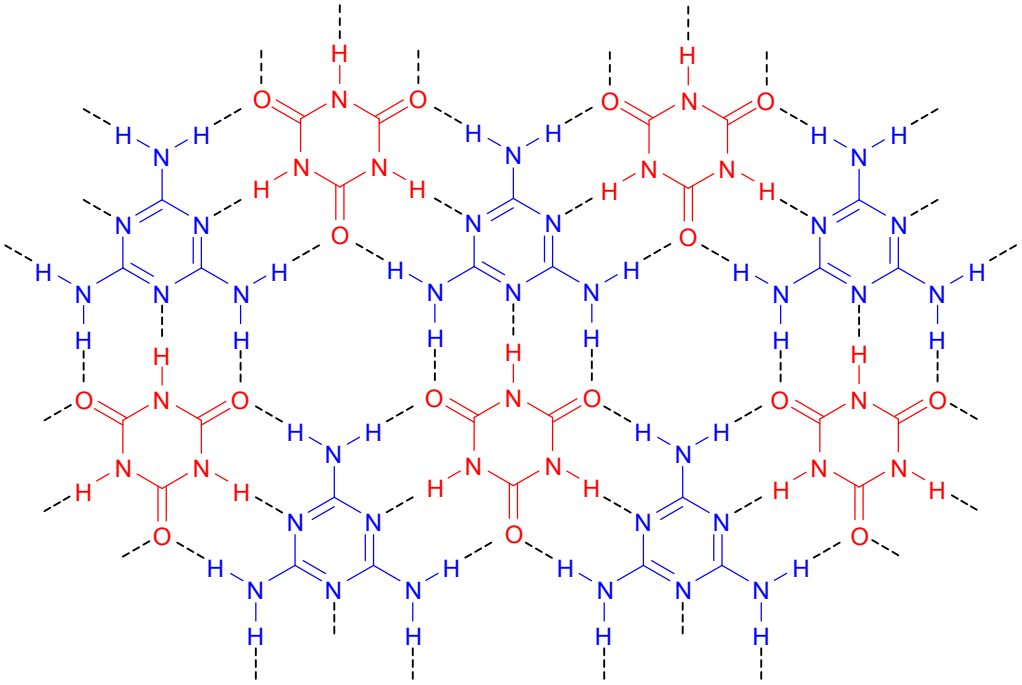

Fig 1.3.2 *2D-Hydrogen bonding network between Melamine and Cyanuric Acid reported by Whitesides[32,33] and initially described by Junichi.[34] Figure adapted from reference.[35]*

1.3.3 π-π Interactions

Strong attractive interactions between π-systems in aromatic molecules have been shown to have a stabilising effect on molecules.[36-38] Experimental observations of these interactions include the stacking of nucleotide bases in DNA[39] and the propensity for aromatic molecules to intercalate with DNA,[40] also aromatic interactions have been reported to stabilise the tertiary structures of proteins.[41,42] Computational methods have been used to show that greater stability can be acquired through the parallel alignment of aromatic systems in an offset manner (offset face-to-face π-π interaction) or through T-shaped interactions (C-H···π, or edge-to-face interactions). The offset, or slipping, of one aromatic system relative to the other is due to the optimisation of electrostatic interactions that occur with this configuration. In order to be considered a face-to-face π-π interaction the interplanar distance between the aromatic systems lies between 3.3 – 3.8 Å. The face-to-face π-π interaction has an interaction strength of approximately 2 kJ mol^{-1}. However, greater interaction strengths, up to 50 kJ mol^{-1} have been observed between highly conjugated aromatic systems, such as between porphyrin rings.[36]

The edge-to-face C-H···π interaction occurs due to an electrostatic interaction between the electron poor σ-system (hydrogen atoms outside the ring) and the electron rich π-system (above and below the ring). This leads to the "*herringbone*" pattern frequently observed in crystal

structures of aromatic molecules. This supramolecular synthon has been utilised in crystal engineering and found applicability in host-guest chemistry with aromatic systems being employed to encapsulate other aromatic species. Examples of this include the selective encapsulation of C_{60}-fullerene within an aromatic pincer (the "*Buckycatcher*"[43] see **Fig 1.3.3**) and numerous examples of planar aromatic molecules encapsulated within cages.[44-48]

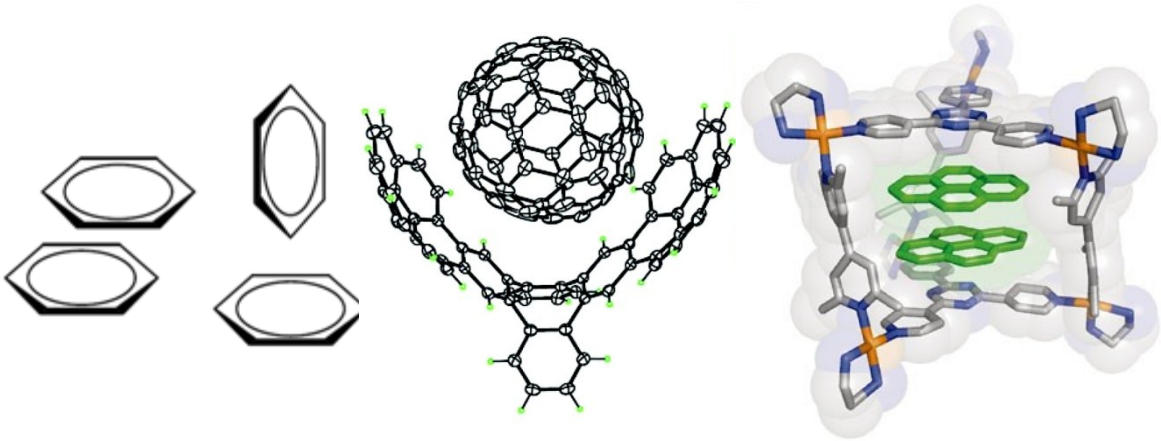

Fig 1.3.3 *Examples of π-π Interactions. Offset face-to-face π-π interaction and edge-to-face C-H···π interaction* ***(left)****,*[49] *the "buckycatcher" interaction with C_{60}-fullerene* ***(centre)***[43] *and the encapsulation of pyrene within a prism-shaped molecular cage* ***(right)***[46,47]

1.3.4 Other Supramolecular Interactions

As the field of supramolecular chemistry continues to grow, new supramolecular synthons continue to be developed and investigated. Where conventional covalent chemistry deals with interactions between open shell atoms; supramolecular interactions can occur between closed shell atoms with s^2, d^8 or d^{10} electronic configurations. Interactions between Ag-Ag (argentophilic) or Au-Au atoms (aurophilic) are well-studied and typically have bond strengths similar to those observed in hydrogen bonding systems.[50] Mainly observed in the solid state, the bond lengths for these interactions are typically between 2.8 – 3.3 Å for aurophilic interactions[51] and < 3.4 Å for argentophilic interactions.[52] These interactions have been utilised in the formation of rotaxanes,[51] regioselective photochemical dimerisation reactions,[52] and the formation of interesting crystallographic topologies.[53,54]

A halogen bond is analogous to a hydrogen bond but involves an electron deficient halogen atom interacting with an electron rich atom such as a nitrogen or oxygen atom or a Lewis base.[55,56] Halogen bonds can form with a wide range in bond strengths between approximately 5 and 180 kJ mol^{-1}.[56,57] Like hydrogen bonds these interactions are highly directional and can

overcome hydrogen bonding interactions within competitive recognition processes.[58] Halogen bonding is not only limited to interactions within the solid state but has also been observed in the gaseous phase.[59,60] Due to the robust behaviour of these interactions, halogen bonds are being investigated for their crystal engineering,[61] receptor-guest,[62] and biological properties[63] along with potential uses as magnetic conductors,[64] and in the photochemical[65] and liquid crystal fields.[66]

Cation-π interactions have been shown to play an important role in molecular recognition with interactions between the cation and electron-rich π system having bond energies in the order of 5 – 80 kJ mol^{-1}.[20] Work conducted by Dougherty observed the binding of an aliphatic ammonium guest within a cyclophane host in aqueous conditions[67,68] and they also have a stabilising effect in the tertiary structure of proteins and other biological recognition processes.[68,69] Anion-π interactions are also studied for their roles in molecular recognition, templation, and biological processes.[70-73]

The field of supramolecular chemistry is constantly evolving and new supramolecular synthons are discussed frequently, including examples of the use of reversible covalent bonds to synthesise large structures and networks.[74] A summary of these interactions is provided in **Table 1.3.5**.

1.3.5 The Coordination Bond and the Field of Metallosupramolecular Chemistry

Arguably the most important tool in the supramolecular chemist's toolbox is that of the metal-ligand coordination bond.[16,20] The majority of transition metal-ligand bonds form reversibly with a predetermined geometry, providing a structural component to the design of supramolecular assemblies. The choice of metal ion gives a particular set of coordination numbers, geometries, and sizes. The supramolecular chemist can choose the most apt metal and this provides an important architectural design element to these systems. A selection of transition metal ion geometries is provided in **Fig 1.3.4**.

Along with this predetermined geometric component, other characteristics of transition metal ions are important in supramolecular systems. Transition metals are able to have variable redox, electrochemical, catalytic, optical or magnetic properties enabling the supramolecular compound to perform a particular function. It is important to balance these other functions with the robustness of the metal-ligand bond in order to maintain the structural integrity of the supramolecular complex. Often the incorporation of further complexity into supramolecular architectures leads to deterioration in stability; however, when structure and function co-exist, an impressive variety of applications may be envisaged.[28,75-80]

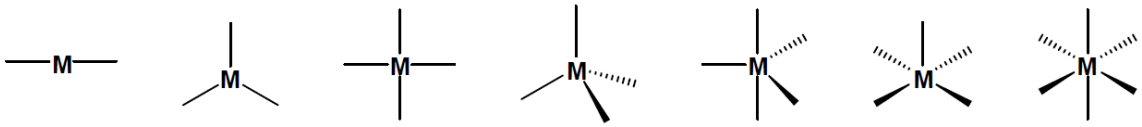

Fig 1.3.4 *Typical metal ion geometries for first-row transition metals; linear, trigonal planar, square planar, tetrahedral, trigonal bipyramidal, square pyramidal, and octahedral (**from left to right**).*

Transition metal ions have been utilised in the design of structures with various topologies. These can be separated into two distinct classes; the discrete assemblies comprising of structures such as molecular triangles and squares, cages, helicates, knots, catenanes, and rotaxanes;[81-85] and the infinite assemblies consisting of highly ordered three dimensional networks such as metal-organic frameworks and porous coordination polymers.[86-88]

Interaction Type	Directionality	Bond Energy (kJ mol^{-1})	Example
Closed-Shell Metal-Metal Bond	Nondirectional	5 – 60	Argentophilic (Ag···Ag)
Coordination Bonds	Directional	100 – 300	Metal – Pyridine
Hydrogen Bonds	Directional	4 – 120	Carboxylic Acid Dimer
Halogen Bonds	Directional	10 – 50	Sulfur – Iodine Complex
π – π Interactions	Directional	2 – 50	Benzene Dimer
Cation – π / Anion – π	Directional	5 – 80	$^{+}N(CH_3)_4$·Toluene

Table 1.3.5 *Relevant parameters for supramolecular interactions, values for typical systems shown here.*[89]

1.4 Discrete Assemblies

1.4.1 Molecular Polygons and Cages

The success of supramolecular chemistry lies in the ability for the chemist to "*design*" a structure from first principles and be able to synthesise the structure in relatively high yields through the process of self assembly.[90] In this manner, supramolecular chemistry can be likened to "*molecular lego*" a term first introduced by Stoddart[91] where access to a variety of components with different geometries that, when connected, yield an almost endless array of possible structures. This is comparable to the "*node and spacer*" concept prevalent in the analysis of infinite assemblies where a "node" and "spacer" entity of particular geometries interact to give the sought after final

structure.[92] Although the design principles in supramolecular chemistry are logical, many highly complex and interesting structures have been discovered serendipitously.[93]

Simple two dimensional shapes such as squares,[82,94-96] rectangles,[97,98] triangles,[99,100] hexagons[101] and grids[102] have been readily synthesised *via* self-assembly. By increasing the length of the interacting components, larger structures up to the nanometre range may be obtained.[103] Extension into the third dimension provides access to polyhedral structures and cages. A schematic of possible discrete assemblies is shown in **Fig 1.4.1**.

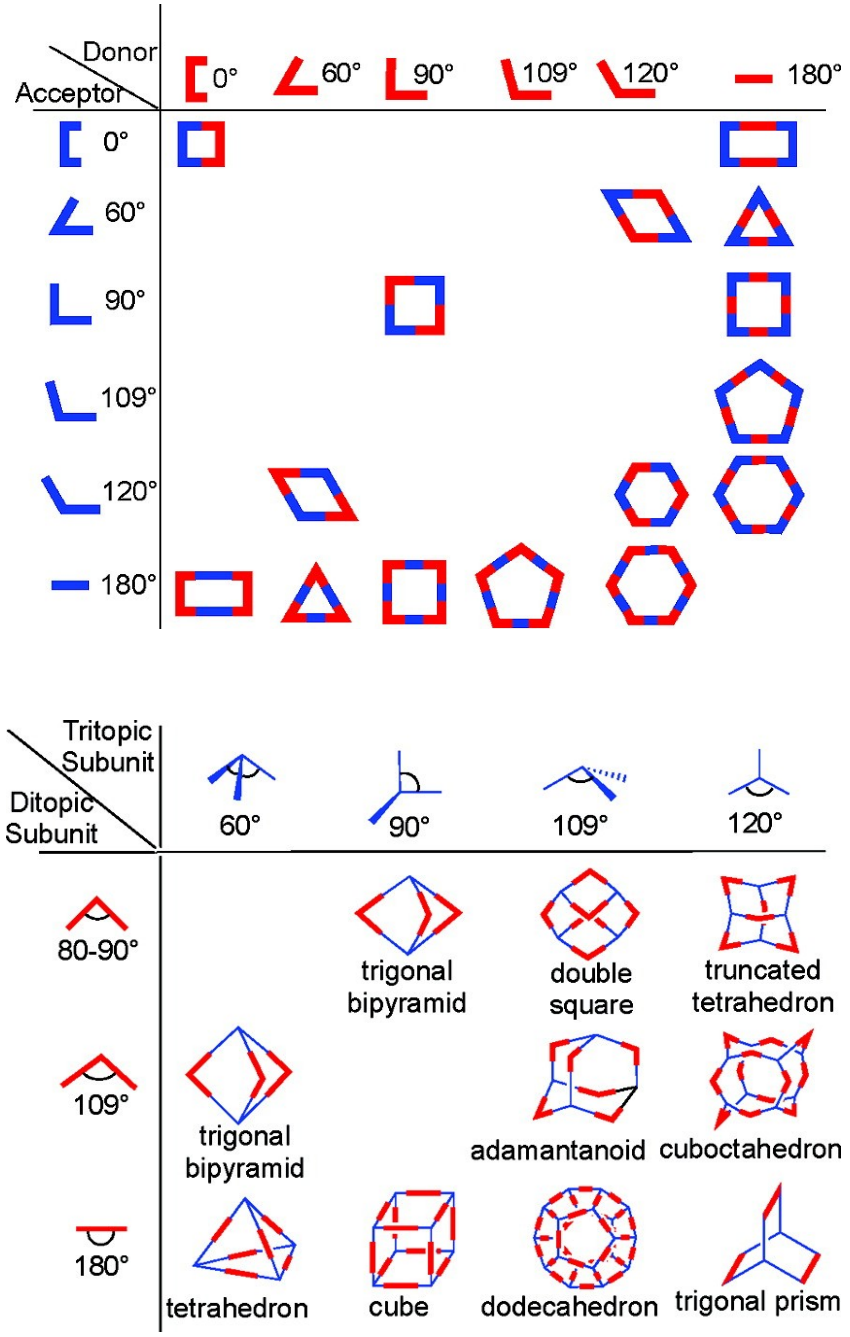

Fig 1.4.1 *Schematic for the combination of various individual components of different geometries to access a variety of two- and three-dimensional architectures. Image from reference.*[90]

1.4.2 Metallo-Helicates

The term "*metallo-helicate*" was first coined by Lehn to describe an inorganic species where ligands connect the metal centres by twisting about the central metal-metal axis.[104] This helical twisting imparts chirality on the resulting complex which can then be defined as either the Δ-isomer (also known as the P-isomer) where the twist is right-handed (clockwise) or the opposite left-handed species (the Λ or M-isomer).[105] Helicate forms and terminology are described in **Fig 1.4.2**. Along with chirality, these helicates are widely studied due to their self-assembly and self-recognition abilities. Initial studies by Lehn clearly illustrated the self-recognition of metallo-helicate complexes when a mixture of organic ligands with between two and five bipyridyl coordination sites, were reacted with Cu(I) ions. Only ligands with the same number of coordination sites formed helicates, with the reaction mixture spontaneously forming four distinct metallo-helicate species without any evidence of mixed ligand complexes.[106]

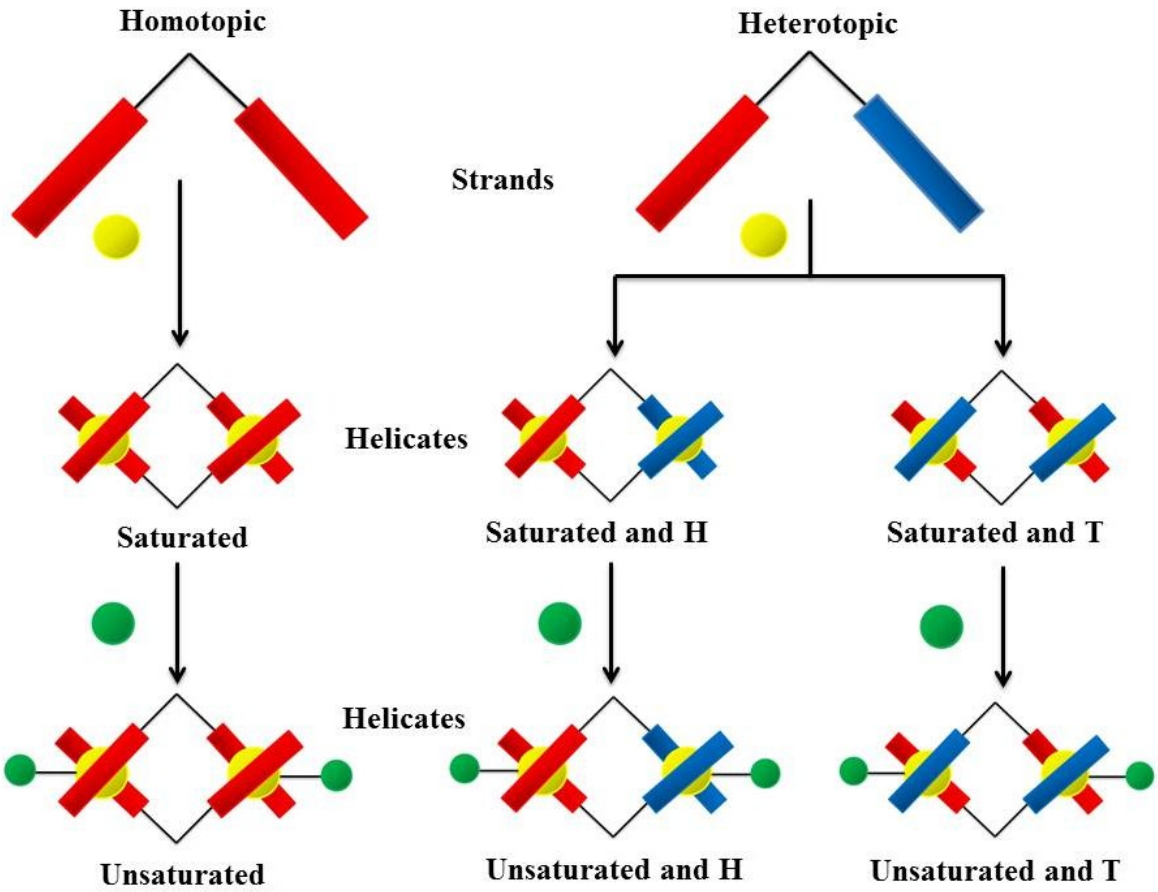

Fig 1.4.2 *Diagram showing the types of helicate complexes where H and T denotes head and tail domains respectively. Adapted from reference.*[107]

In order to form helicates certain criteria must be met in the design of the organic ligand:

(i) the ligands must possess several binding domains along the strand that are capable of co-ordinating to various metal ions.

(ii) the ligands must include spacers between the binding domains that are rigid enough to prevent two binding units of the same ligand co-ordinating to the same metal ion but at the same time must be flexible enough to wrap around the metal ions and produce a helical architecture.[108]

The final geometry and properties of the helicate is encoded by the initial choice of ligand and metal ions used. Given the limitless possibilities for ligand design using classic covalent synthesis and the plentiful interesting properties of metal cations, helicates have been shown to display a remarkable range of properties. For example work conducted by Hannon designed a ruthenium containing dinuclear triple helicate that was able to bind non-covalently in the major groove of DNA and subsequently coil the DNA molecule, leading to cytotoxicity within human breast cancer cells. The binding process was also reported by an associated photo-response.[109] Other helicate complexes have been designed to exploit the varying coordination geometries of redox-coupled metal centres, for example the Cu(I)/Cu(II) redox couple which has been shown by Fabbrizzi to switch between a dinuclear double helicate (tetrahedral Cu(I)) and two dissociated mononuclear complexes when the metal centres are oxidised to Cu(II). This process was shown to be reversible and also occurred in conjunction with a quenching of fluorescence in the monomeric species.[110,111]

Other complexes also can be described under the umbrella term of "*helicate*" although they differ from the metallo-supramolecular helicate species defined above. These may include: compounds where the helical motif is present due to hydrogen bonding, π-π interactions or other non-covalent interactions rather than the interactions between metal ions and organic ligands (often termed "*foldamers*");[112,113] compounds that contain only one metal cation – generally this involves one ligand which rotates in a helical fashion about a single metal centre;[114-116] and compounds which contain an aggregate of metal centres where the ligands do not connect the metal centres in a linear fashion but the arrangement of the ligands imparts chirality onto the final complex – for example the circular helicates.[105,107,117,118]

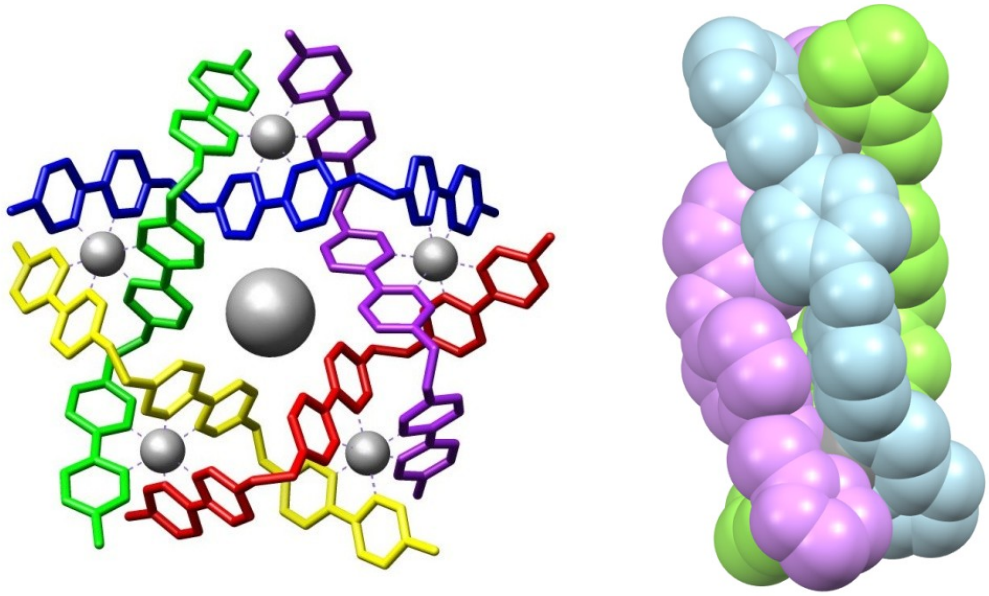

Fig 1.4.3 *Diagram showing a pentanuclear circular helicate reported by Lehn*[117,119] ***(left)*** *and a dinuclear triple helicate complex reported by Kruger (**right**). Image adapted from reference.*[120]

1.4.3 Knots, Rotaxanes and Catenanes: Beautiful Molecular Machines

More complicated supramolecular architectures continue to be designed with inspiration drawn from structures of great beauty. The synthesis of interwoven molecular motifs have utilised many of the supramolecular interactions previously discussed, particularly in templating roles during synthesis.[85,121] Molecular knots can be readily synthesised from analogous metallo-helicate species as initially investigated by Sauvage in the synthesis of the molecular trefoil knot.[122,123] In this example, a dinuclear double helicate containing two flexible ligands with two separate bidentate coordination sites and two tetrahedral Cu(I) ions was employed. The dinuclear double helicate can be thought of as the "*open-knot"* form, providing the appropriate twist for the required knot. The trefoil knot was synthesised from this open-knot precursor by linking the ends with oligoethylene glycol units. Although initially low yielding, subtle alterations to the initial ligand design and ring closing procedure led to a significant improvement in the yield (up to approximately 75%) of the final trefoil knot. Hunter was also successful in synthesising a molecular trefoil knot through metal-directed templation, although this example utilised a single ligand strand with three bidentate coordination sites which was able to thread through itself upon coordination to the Zn(II) ion. This synthetic process also follows the initial synthesis of the open-knot motif which was subsequently tied off to give the trefoil knot.[124,125] Other molecular compounds with interesting twisted and interweaved topologies continue to be synthesised and investigated including a universal 3-ravel

knot synthesised by Lindoy,[126] a pentafoil molecular knot synthesised by Leigh[127] and molecular borromean rings synthesised by Stoddart.[128] Selected examples of molecular knots are illustrated in **Fig 1.4.4**.

The concept of templation by metal ions is not only used in the synthesis of molecular knots but is also frequently used in the synthesis of catenanes – molecular interlocked ring structures.[129] Like the molecular knots, catenanes utilise templation to hold individual components in the correct orientation prior to ring closing reactions to give the final interlocked structures. Various templation methods have been used to synthesise a variety of catenated structures including, metal-templation,[130] hydrogen bonding,[131] π-π stacking,[84] and anion-directed templation.[132] Although the structures are naturally beautiful, a driving factor in the design of these compounds is the potential to form molecules which can undergo a function, potentially leading to molecular machines.[133] For example, these catenanes can undergo significant structural transformations influenced by external perturbations which involve the rotation of the rings relative to one another. Electrochemically driven movement can be achieved by exploiting the coordination geometry preference of the Cu(I)/Cu(II) redox couple as shown by Sauvage.[134] Ring systems containing both bidentate and tridentate coordination sites were shown to move to optimise tetrahedral 4-coordinate binding to a central Cu(I) ion. Oxidation of this Cu centre caused the rings to move to optimise the 6-coordinate binding through two tridentate coordination sites. Indeed, this does not have to involve metal ions exclusively with similar movements being observed through redox-active organic molecules.

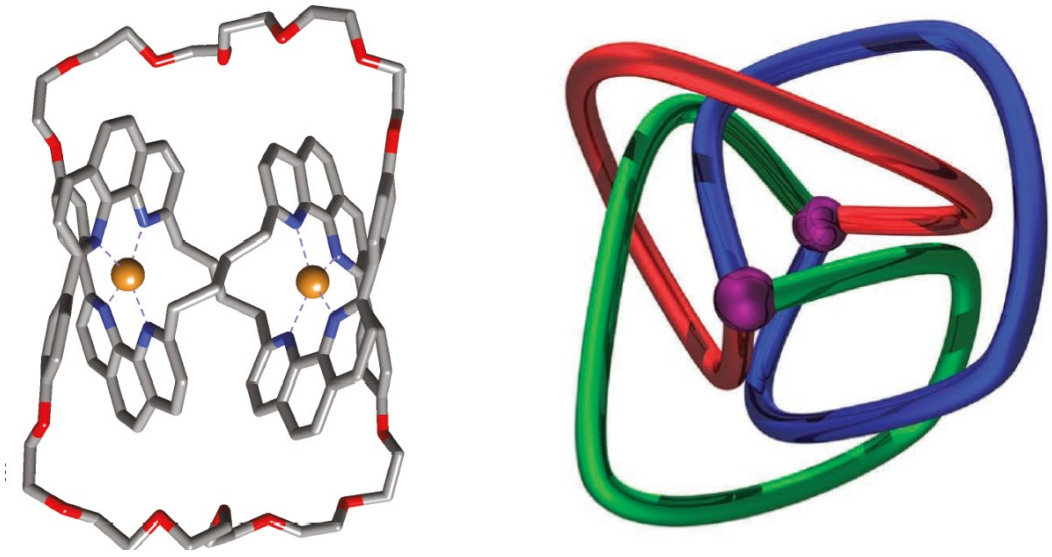

Fig 1.4.4 *Examples of molecular knots: (**left**) a trefoil knot synthesised by Sauvage [85,122,123] showing the Cu(I) ions in their templation role and (**right**) a diagram of the universal 3-ravel synthesised by Lindoy [126] Images from references.*[85,126]

This mechanical movement has been explored in great depth in rotaxane molecules – structures where a linear component is threaded through a cyclic component and both ends are capped with sterically bulky units to prevent the dissociation of the components. The movement of the ring component along the linear chain has been likened to a "*molecular shuttle*" with the movement being prompted by redox,[135] pH,[136] or photoactivation (**Fig 1.4.5**).[137] Current efforts are focused on incorporating these molecular machines into macroscopic devices.[138]

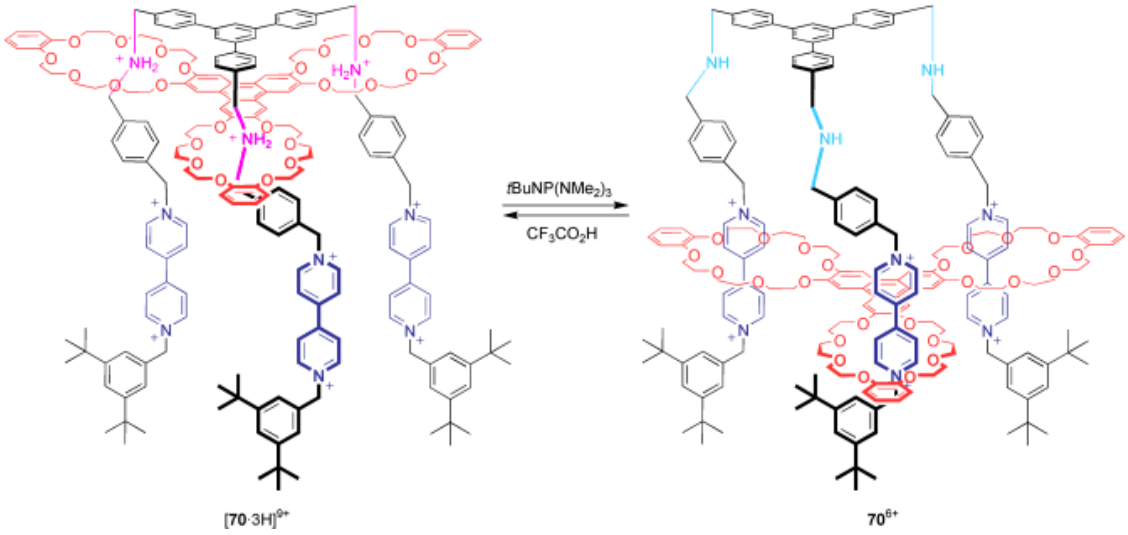

Fig 1.4.5 *Example of an acid-base activated "molecular elevator" designed by Stoddart.*[139] *Image from reference.*[140]

1.5 Potential Applications of Supramolecular Chemistry

Biological systems utilise supramolecular interactions to form large complicated chemical structures. The non-covalent interactions furnished by hydrogen bonding, electrostatic interactions, π-π stacking and metal-ligand bonds are all involved in aspects of biological systems. The structure and function of enzymes have been well studied with enzymes showing remarkable abilities to selectivity bind substrates from complicated mixtures within the cellular environment. Mirroring this selectivity using synthetic molecules is one of the primary tenets of host-guest chemistry. The sensing, separation and catalysis of guest molecules within the host environment are some of the many potential applications involving supramolecular interactions.

Molecular sensing requires the host-guest system to not only bind a particular guest with appropriate strength and selectivity, but to report the binding event. To achieve this, a system must incorporate both a binding site (usually involving supramolecular interactions to favourably bind the guest) and a reporter site. Most commonly the reporter site uses a chromophore whereby upon

guest binding the optical properties of the compound change. Where changes in absorbance of the chromophore upon guest binding occur in the visible region of the electromagnetic spectrum, "*naked-eye"* sensors arise (**Fig 1.5.1**). Changes in fluorescence may also be used to report the binding of a guest through either the activation of fluorescent processes or conversely the quenching of these processes upon guest binding.

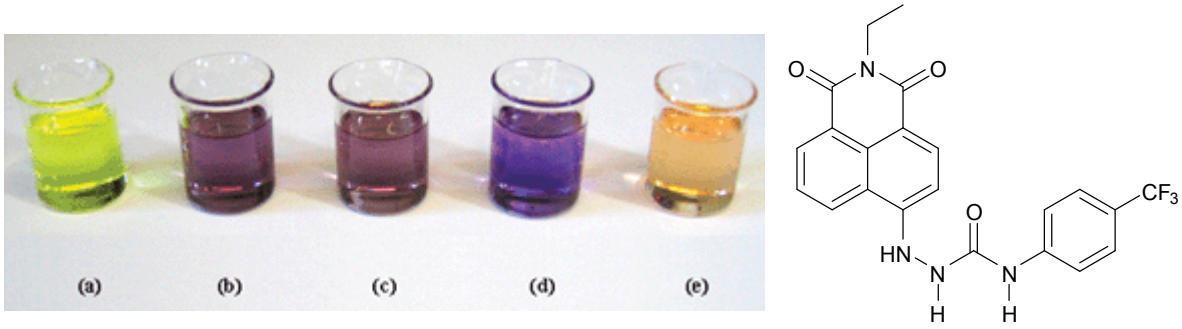

Fig 1.5.1 *Colourmetric anion sensor using an organic 1,8-naphthalimide chromophore. Chromogenic response of the free host* ***(a)*** *to 1 eq.* AcO^- ***(b)***, *1 eq.* $H_2PO_4^-$ ***(c)***, *1 eq.* F^- ***(d)*** *and excess* F^- ***(e)***.[141]

Encapsulation of guest molecules may also alter the physical properties of the guest. Work by Pederson showed that potassium cations were able to dissolve in organic solvents when encapsulated by the crown-ether host.[3] Altering the solubility of the host enables the guest molecule to be transported into other media, a process which has particular relevance in targeted drug delivery.

Along with altering the solubility of the guest, host molecules may be able to provide a separate and stable environment within the cavity compared to the bulk solution. For example, Nitschke successfully imparted air-stability on P_4 (white phosphorus – a highly pyrophoric compound) by encapsulating a molecule of P_4 within a self-assembled host.[142] This idea is incorporated within the concept of "*molecular flasks*" – host molecules that facilitate the reaction of components, which would otherwise react slowly (or not at all). This process mimics the way enzymes function with their respective substrates.[44] Reactions that occur within the cavity of a supramolecular host have a higher effective molarity, therefore increasing the rate of reaction. Another benefit of performing a chemical reaction within a molecular host is that the conformation of the reactants may be controlled, resulting in either a faster reaction rate or high product purity. Research by Rebek showed an approximate 200-fold increase in the rate of the Diels-Alder reaction between *p*-benzoquinone and cyclohexadiene within a self-assembled host compared to the reaction under normal synthetic conditions.[143] The confined space within a molecular flask may also lead to unusual stereo- and regio-selectivities for well known chemical reactions. For example,

Fujita showed that although anthracene usually forms [9,10] adducts when reacted with dieneophiles under normal Diels-Alder conditions; when the reaction occurs within a self-assembled cage only the terminal anthracene rings are available for reaction and the *syn* product forms in *ca.* 90% yield.[144] In both of these examples, reactivity increases markedly once the reactants have successfully been encapsulated within the host, however, competition for guest access to the host limits the efficacy of these systems.

Cyclo-additions, photochemical dimerisations (**Fig 1.5.2**), rearrangements and radical reactions have all been facilitated by encapsulation within supramolecular hosts.[44,145-151] Not only can the host function as a simple container in which the reaction occurs, it may also participate in the chemical reaction. Work conducted by Fujita reported that a self-assembled host undergoes a radical transfer mechanism leading to the photochemical oxidation of an adamantane guest.[152] Other catalytic reactions have been shown to occur within host molecules with enantiomeric selectivity being utilised through a chirally resolved host by Raymond[153] and traditional catalytic molecules have been incorporated within the host, such as research also shown by Raymond where an iridium based catalytic centre was encapsulated within the host molecule to facilitate a C-H bond activation process.[154]

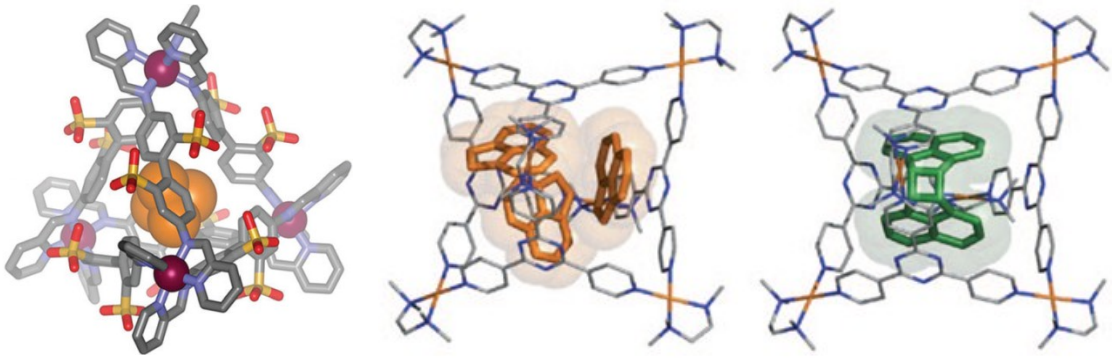

Fig 1.5.2 *Examples of host-guest compounds showing a tetrahedral cage stabilising the pyrophoric P_4 molecule (**left**)[142] and the photochemical [2+2] dimerisation process occurring within a cage (**centre/right**).*[146]

Although the examples above focus on the potential applications of discrete supramolecular assemblies, applications of infinite assemblies are arguably more important. The driving force for the development of infinite assemblies is in their gas sorption, separation and catalytic abilities.[86-88,155-157] Applications of infinite assemblies generally require the maintenance of stable pores within the solid-state, a requirement which has proved challenging with interpenetration of networks a common occurrence.[158] The vast potential for the design and synthesis of infinite networks was

expressed in the landmark paper by Yaghi describing the synthesis of a family of isoreticular "*Metal-Organic Frameworks"* (MOFs) including the famous MOF-5.[86] Further development by the groups of Yaghi, Kitagawa, Ferey and others continue to improve the physical properties of these systems for numerous applications, in particular the selective uptake of gaseous molecules.

The significant challenges of increasing atmospheric carbon dioxide and the need to find alternative energy sources are driving current investigations into the uptake of carbon dioxide, methane and hydrogen gases by porous coordination polymers. Although an exceptionally vibrant and rich field of research, the discussion goes beyond the scope of this particular study and the reader is directed to a selection of excellent reviews focusing on the development of this field.[88,159-161]

1.6 Spin Crossover

1.6.1 Overview

Spin crossover (SCO) describes the switching of a compound between the low-spin (LS) and high-spin (HS) electronic configurations with an external perturbation such a temperature, pressure or light. This phenomenon exploits the energy splitting of the d-orbitals within transition metal ions with $d^4 – d^7$ electronic configurations. In an octahedral transition metal ion, the d-orbitals are split into two distinct energy levels; the lower energy t_{2g} orbitals (containing the d_{xy}, d_{xz}, d_{yz} orbitals) and the higher energy e_g orbitals (containing the dz^2 and dx^2- y^2 orbitals). The relative energy gap between these two sets of orbitals (Δ_O) is dependent upon the ligand-field strength of the coordinating ligands. The coordination of strong-field ligands results in a larger energy difference between the t_{2g} and e_g orbitals, whereas in coordination compounds with weak-field ligands this energy gap is considerably smaller. Electrons will preferentially occupy lower energy orbitals, however, there is an associated energy cost (the interelectronic repulsion energy, *P*) when electrons are paired within the same orbital. When $\Delta_O > P$ the LS state is favoured and conversely when $\Delta_O < P$ electrons will occupy the higher energy e_g orbitals resulting in the HS state. If $\Delta_O \approx P$ then switching between the two spin states may occur, giving rise to SCO behaviour.[1,162-165]

As stated above, metals with $d^4 – d^7$ electronic configurations can give rise to SCO systems but of these the complexes of Fe(II), Fe(III), and Co(II) systems have been most widely studied.[164] In particular, SCO behaviour in octahedral Fe(II) compounds have been extensively researched, due in part to the vivid changes in colour, magnetic, and geometric properties that occur concurrently with the spin transition. Fe(II) with a d^6 electronic configuration results in a diamagnetic LS state, with all six electrons paired in the lower energy t_{2g} orbitals (S = 0). Comparatively, in the HS state there are four unpaired electrons creating a paramagnetic (S = 2)

species. LS Fe(II) complexes are considerably darker in colour than their HS counterparts, providing a visible indication of SCO. These characteristic changes in the properties of Fe(II) compounds undergoing SCO also include considerable changes in the coordination geometry of the Fe(II) centre. As the antibonding e_g orbitals are occupied in the HS state there is a considerable lengthening of the metal-ligand bonds.

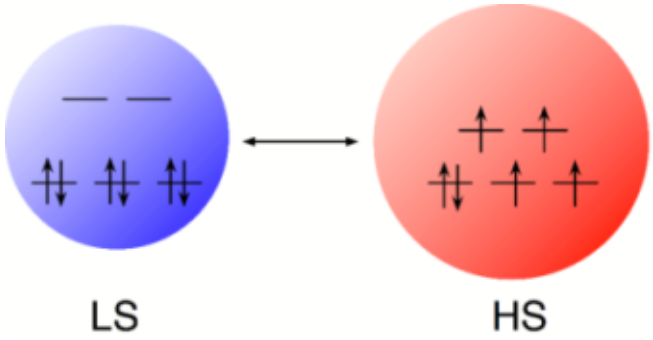

Fig 1.6.1 *Schematic diagram of the spin state transition in a d^6 octahedral metal ion* ***(left)***.[166]

SCO can occur in a variety of different forms depending on the interaction between individual SCO centres within the bulk sample (**Fig 1.6.2**). When there is little interaction between individual metal centres the process can be described as a gradual SCO. This can be thought of as a "*simple thermal equilibrium involving a Boltzmann distribution over all vibronic levels of the two spin states*."[1] This type of curve often occurs when SCO centres are distributed throughout a media, for example in solution studies; or when the SCO centres are diluted within a network.[167] Significant interactions between SCO centres through either supramolecular interactions or bonding interactions between metal centres in polymeric complexes, may result in abrupt spin transitions where all the metal centres within a sample transition over a narrow temperature range. Thermal hysteresis is often observed in these systems, with wide hysteretic loops of 70 K being observed.[168] Multi-step transitions have also been shown to occur.[169-176] This behaviour is typically observed in discrete polymeric systems where the individual SCO centres are in slightly different chemical or physical environments. This is not exclusively polymeric behaviour however and there have been examples of multi-step SCO behaviour occurring in mononuclear compounds.[177-181]

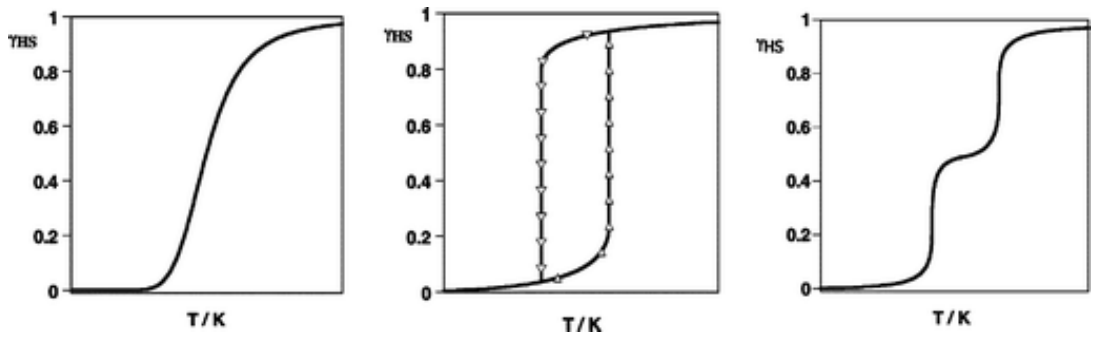

Fig 1.6.2 *General examples of SCO curves showing a gradual SCO (**left**), an abrupt SCO with thermal hysteresis (**centre**) and a two-step transition (**right**) where γ_{HS} is the proportion of HS centres within a sample. Image from reference.*[163]

1.6.2 Light-Induced Excited Spin-State Trapping (LIESST)

Curiously, it was discovered in the early 1980s by McGarvey that a selection of Fe(II) and Fe(III) complexes in solution showed efficient excitation into the HS state by pulsed laser sequences.[182,183] At very low temperatures the excited HS state can be "*trapped*" after excitation of the complex by green light (514 nm) as shown by Decurtins.[184,185] This effect is described as "*Light-Induced Excited Spin-State Trapping (LIESST).*" Irradiating the excited HS complex with red light (820 nm) was found to restore the LS state, a process known as "*reverse-LIESST*".[186] Research into this behaviour has focused primarily on improving the stability of the excited state with most examples of LIESST only occurring at temperatures below 60 K.[187] Above this temperature the thermal energy is generally sufficient for the complex to relax into the LS state. The mechanism of these processes is given below (**Fig 1.6.3**) and is typical for Fe(II) SCO systems.[1,188,189]

This light-induced switchability provides an exciting avenue for the potential use of these complexes in applications such as optical switches or as the active components in magneto-optical storage.[190] To realise this potential however, the temperature at which the meta-stable HS state can be trapped must be increased. There have been examples reported in the literature with excited states stable up to 100 K[191-195] showing that stabilisation of these metastable states can occur. A few criteria must be met in order to design a SCO system that is likely to display long-lived LIESST behaviour. These criteria were collated by Letard[190,196] and relate to the proposed formula

$$\textbf{(1)} \qquad T(\text{LIESST}) = T_0 - 0.3T_{1/2}$$

which discusses the relationship between the T(LIESST) value – the critical temperature at which light-induced HS information is erased,[190] the $T_{1/2}$ value – the temperature at which the sample has equal amounts of HS and LS species (*i.e.* when 50% of the sample has undergone the transition)

and the T_0 value – the theoretical value of T(LIESST) where $T_{1/2} = 0$ K . This relationship explains that the weaker the ligand field strength (which directly correlates to lower $T_{1/2}$) the longer the lifetime of the photoinduced state. This was postulated initially by Hauser as the "*inverse energy gap law*"[197] and fits closely with the observations in Letard's work. This is not exclusively the case however, with extremely long-lived photoinduced excited states being reported in LS Fe(II) complexes with the phenomenon being reported as "*strong-field LIESST*"[193].

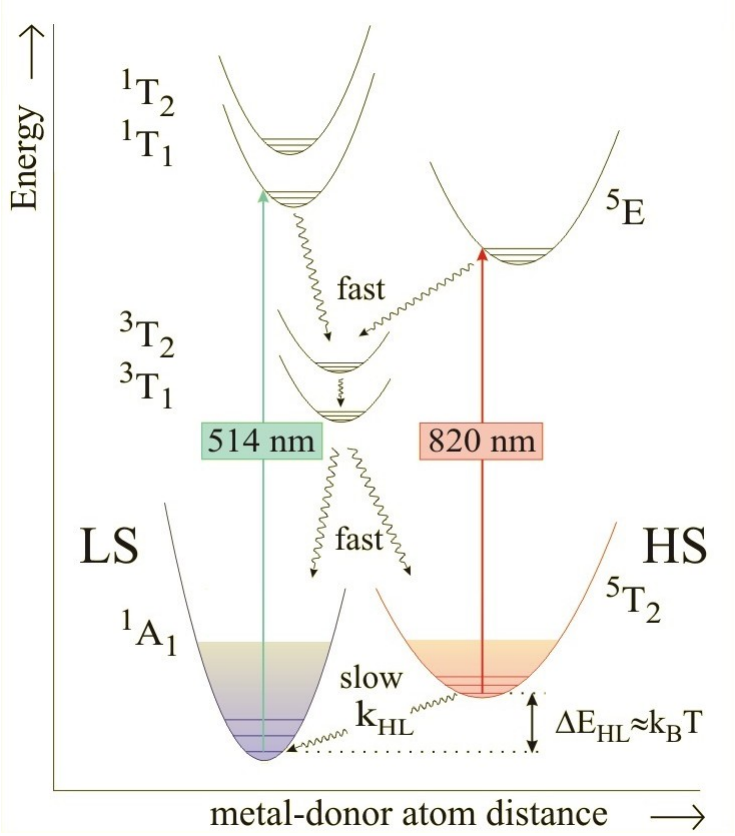

Fig 1.6.3 *Diagram of the mechanisms of LIESST and reverse-LIESST in an Fe(II) SCO complex. Image originally published in reference,*[163] *but altered from higher resolution source.*[198]

The other important component that affects the lifetime of the photoinduced HS state is that of the T_0 value. In Letard's work SCO compounds with N_6 coordination spheres were clustered together based on structural similarities between complexes. SCO compounds comprising of six monodentate ligands correlate well with the T_0 = 100 K line, *tris*-bidentate compounds with T_0 = 120 K, *bis*-tridentate with T_0 = 150 K along with a few examples of macrocyclic ligands which correlate well to a T_0 = 180 K line. Co-Fe Prussian-blue analogues synthesised by Hashimoto[199] were also included and these compounds were estimated to have a T_0 = 200 K, however, the mechanism of photoexcitation in this case is not simply that of SCO but can be better described as charge-transfer-induced spin transition and as such some care must be observed

during comparisons of the data. Finally, alterations between SCO complexes involving outer-sphere interactions, have a limited effect on the resulting *T*(LIESST) value. These outer-sphere interactions may include cooperativity effects, solvent effects, crystal packing and anion exchange effects. The above study provided some detailed insights into the relationship between complex structure and the longevity of the photo-induced HS state.

Other methods of photoactivation could also provide a viable route for long-lived photo-induced HS states; such as through utilising secondary photochemical processes such as that shown by Boillot where a stylbene-type ligand was photoisomerised in such a way as to alter the ligand field strength to induce SCO. Given that the lifetime of both the *cis* and *trans* isomers is long at room temperature this may provide a highly successful alternative approach.[189,200]

1.6.3 Factors Affecting Spin Crossover Properties

1.6.3-1 Ligand Field Considerations

It is well known that many $\{FeN_6\}^{2+}$ coordination spheres afford the appropriate ligand field strength for the formation of Fe(II) SCO compounds.[201,202] Indeed, there is an abundance of highly varied ligand systems with $\{FeN_6\}^{2+}$ coordination spheres which have been shown in the literature to form SCO complexes. The current study will focus on SCO systems with di-imine ligands and as such the coverage of other, equally important, ligand types will be limited. Comprehensive reviews of SCO compounds with various ligand systems have been recently reported by Halcrow[165,203] and by Gütlich and Goodwin in the three volumes of *Spin Crossover in Transition Metal Compounds I-III.*[204] For further topical articles the *European Journal of Inorganic Chemistry* has recently published a special issue entitled: *Spin-Crossover Complexes: Cluster Issue*.[205]

Subtle alterations to the exclusively LS complex of $[Fe(\mathbf{1})_3]^{2+}$ have been shown to form complexes which display SCO behaviour.[202] Work conducted by Scklover showed that modifications distant from the donor atoms had little effect with $[Fe(\mathbf{2})_3](PF_6)_2$ remaining in the LS state.[206] Modifications adjacent to the donor atoms significantly alter the ligand field strength with the $[Fe(\mathbf{3})_3]^{2+}$ system showing gradual and incomplete SCO behaviour.[207] Interestingly, the di-substituted analogue **4** showed no evidence of coordination to the Fe(II) centre, presumably due to steric crowding.[208] Substitution at the 3,3'- positions (**5**) also result in a weakening of the ligand field strength as steric interactions between the substituents cause the pyridine rings to twist relative to one another. This reduces both the σ- and π-interactions to the Fe(II) metal centre resulting in complexes having a thermally accessible HS state typically above 250 K.[203,209]

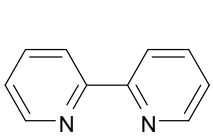

1

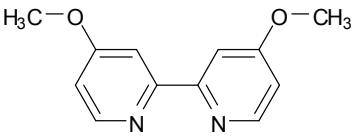

2

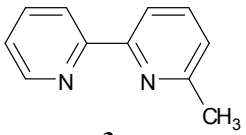

3

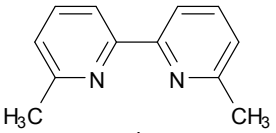

4

Conversion of the 6-membered aromatic pyridine rings to 5-membered entities has been shown to give better access to ligands with SCO potential when coordinated to Fe(II). This is particularly apparent where pyrazole, imidazole, triazole and thiazole units have replaced one of the pyridine rings in **1**. The pyridine-imidazole ligand (**6**) confers SCO behaviour upon an $[Fe(\mathbf{6})_3]^{2+}$ complex with a continuous spin transition centred above room temperature.[210] Various combinations of isomers of this form have been synthesised and give a range of *tris*-bidentate complexes which cover a range of spin states.[211] Trends are difficult to ascertain with seemingly similar ligand systems showing remarkably different SCO properties upon coordination with Fe(II). One such example is that for the $[Fe(\mathbf{7})_3]^{2+}$ system where the $[Fe(\mathbf{7})_3](BF_4)_2$ complex shows gradual SCO centred around 200 K, however, the $[Fe(\mathbf{7})_3](ClO_4)_2$ analogue shows an abrupt transition.[212] Also the degree of solvation of the sample has been shown to play an important role with the complex $[Fe(\mathbf{8})_3]X_2$ ($X = BF_4^-$, ClO_4^-, PF_6^-) showing increased transition temperatures with increasing levels of hydration.[213]

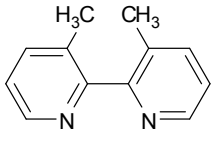

5

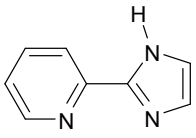

6

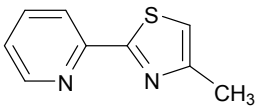

7

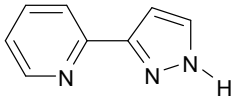

8

Replacing both pyridine rings with the 5-membered imidazole rings results in further reduction of the ligand field strength with $[Fe(\mathbf{9})_3]^{2+}$ being found exclusively in the HS state.[214] Interestingly, if the ring systems are reduced from imidazole to imidazoline the resulting $[Fe(\mathbf{10})]_3(ClO_4)_2$ not only undergoes SCO with a $T_{1/2}$ of 116 K, but the transition is also abrupt with a hysteresis of 6.5 K. This is attributed to the enhanced metal-ligand π-interaction as the electron density within the di-imine functionality remains within the chelate ring rather than being delocalised around the imidazole unit.[215]

It is apparent that subtle alteration to the original 2,2'-bipyrdine and related ligands opens up a range of spin states and SCO behaviour. Two main trends can be obtained from the substantial range of Fe(II) complexes formed with these ligand types although it is important to state that seemingly minor crystal packing effects give remarkably different properties. Broadly speaking the following insights have been made into the modification of ligand field strength.

1. Sterically bulky groups close to the donor atoms have an effect of weakening the ligand field strength. Likewise, any group which causes the binding geometry of these ligands to deviate away from planar also weakens the ligand field strength. However, if the substituent is too bulky then coordination may not occur.

2. Substituting 5-membered heterocyclic rings into the 2,2'-bipyridine framework also acts to reduce the ligand field strength and have provided an effective method for accessing the SCO region in these systems.

These design principles can be extended to the synthesis of Schiff-base di-imine ligands. The ease of accessing a range of ligands through simple imine condensation reactions between various aldehyde and amine groups is a powerful tool in synthesising interesting SCO materials. Most Schiff-base ligands have used the pyridine group with the addition of methyl substituents to weaken the ligand field through steric effects similar to those seen in the $[Fe(\mathbf{3})]^{2+}$ systems and typically are of the form $[Fe\mathbf{L}_2(NCS)_2]^{2+}$. In particular, systems with extended linear aromatic substituents were mainly reported in line with research into second order non-linear optical compounds by Letard.[216] It was noted that the incorporation of 5-membered heterocycles into these systems could be readily achieved but surprisingly has had only limited study in relation to the formation of SCO compounds.[202] In light of this, the present study will focus on the $[Fe(\mathbf{11})_3]^{2+}$ and $[Fe(\mathbf{12})_3]^{2+}$ coordination spheres as previously reported by Kruger[120,217-219] and shown to form Fe(II) SCO complexes. The isomeric ligand **12** also has been utilised by the groups of Hannon[220] and Mastumoto[221] to form SCO compound on coordination with Fe(II).

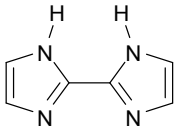

9

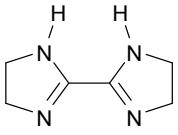

10

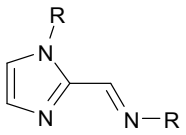

11

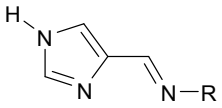

12

1.6.3-2 Supramolecular and Crystal Packing Interactions

Supramolecular interactions have been shown on numerous occasions to vary the SCO properties of closely related systems.[1,163,222-226] As anticipated these interactions have a particularly important effect on the cooperativity within a given system with complexes that interact strongly typically showing abrupt transitions and hysteretic behaviour.

One such example was shown through the analysis of three related complexes, [Fe(**btz**)$_2$(NCS)$_2$], [Fe(**phen**)$_2$(NCS)$_2$], and [Fe(**dppz**)$_2$(NCS)$_2$] where btz = 2,2'-bithiazoline, phen = 1,10-phenanthroline and dppz = dipyridol[3,2-α:2'3'-*c*]phenazine.[227-229] The three ligands have varying degrees of aromaticity with **btz** being described as mainly aliphatic, **phen** aromatic, and **dppz** as an extended aromatic system. Close investigation of the three crystal lattices show that they all have similar crystal packing arrangements[163] and that no significant inter-complex interactions occur in [Fe(**btz**)$_2$(NCS)$_2$]. However, there are significant aromatic interactions in the [Fe(**phen**)$_2$(NCS)$_2$] and [Fe(**dppz**)$_2$(NCS)$_2$] complexes and as expected the interactions are stronger in the extended aromatic complex. The result of this is that there is a significant increase in the degree of cooperativity between Fe(II) centres within the crystal lattice as the aromaticity increases and this is mirrored in the magnetic susceptibility curves which show a gradual SCO for [Fe(**btz**)$_2$(NCS)$_2$], an abrupt SCO for [Fe(**phen**)$_2$(NCS)$_2$] and an abrupt SCO with an approximately 50 K wide hysteresis loop for [Fe(**dppz**)$_2$(NCS)$_2$].

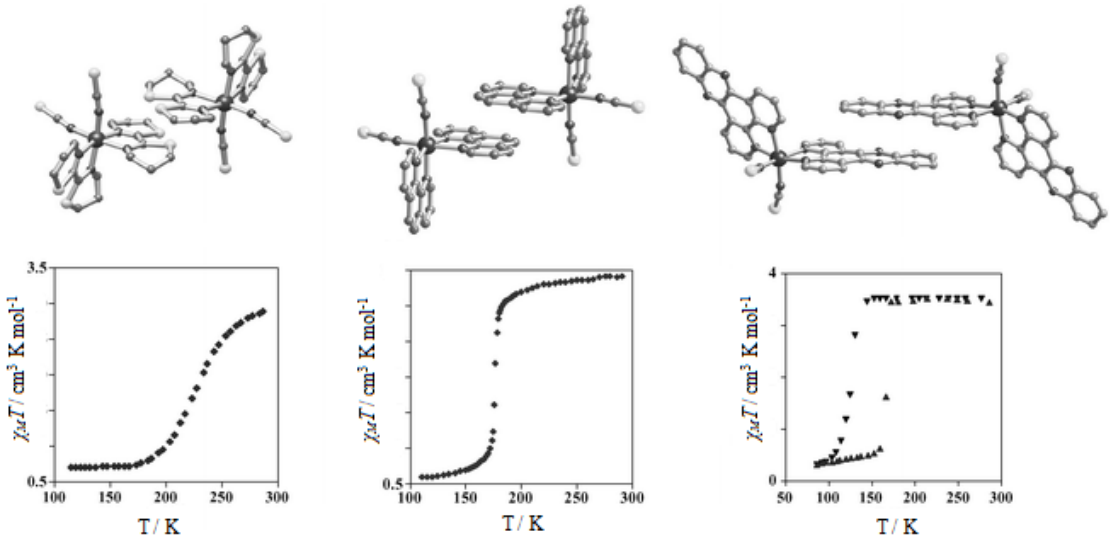

Fig 1.6.4 *Variation in SCO behaviour with improved ligand aromaticity.*[227-229] *Image from reference.*[163]

Subtle alterations to the counter anion[230-237] and solvent molecules[235,238-242] within the crystal lattice have also caused significant changes to the SCO properties of a given system.

While changes to ligands, counter-anions and solvent molecules have been shown to alter SCO behaviour, there have also been numerous examples of different crystallographic phases of the same compound having different magnetic properties and SCO behaviour. These crystallographic phases can be often thought of as crystallographic isomers (or "*polymorphs*") and have typically been discovered serendipitously through subtle alterations in synthetic technique. With the vast improvements in X-ray crystallography for accurate structure determination within the solid state, these polymorphs have been described in significant detail and the behaviour of the

respective SCO phenomenon is investigated. Further information can be accessed through the critical review by Tao.[223]

A vivid example of the effects of polymorphism on SCO was observed by Kahn between the three polymorphs of the complex *fac*-[Fe(**dppa**)$(NCS)_2$] where dppa = (3-aminopropyl)*bis*(2-pyridylmethyl)amine.[243] It was noted that the crystallisation of the solvated complex typically occurred after 2 hours to give the product as long yellow-brown prismatic crystals. If the crystallisation took longer, between 5 – 7 days, then three polymorphic phases resulted. Polymorph **A** formed as yellow-green plates, **B** formed as yellow prisms and **C** formed as pale-yellow elongated hexagonal plates. The magnetic properties of all three phases were investigated by variable temperature magnetic susceptibility and Mössbauer spectroscopy which revealed that polymorph **A** undergoes a relatively gradual SCO with a $T_{1/2}$ at approximately 176 K, **B** remains in the HS state over the measured temperature range of 4.5 – 295 K and **C** exhibits a very abrupt SCO with a hysteresis width of 8 K.

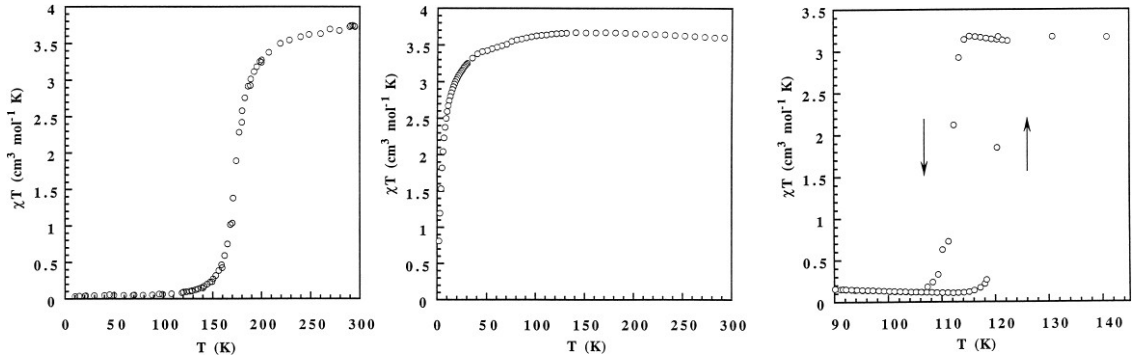

Fig 1.6.5 *χT versus T plots for the three polymorphic structures of fac-[Fe(**dppa**)$(NCS)_2$]. From left to right, polymorph **A**, **B**, **C**.*

As more is understood about how these supramolecular interactions affect the SCO phenomena, research is being conducted into exploiting these interactions for particular applications. Research by Shores has described SCO molecules which are able to convert spin states upon interaction with a particular anion with the ultimate aim of designing anion-sensing SCO molecules.[237,244-247] The formation of SCO cages are also being investigated for their potential as chemosensing entities. Examples include those from Kruger, with the formation of an anion-encapsulating SCO active tetrahedral cage;[219] and Batten with the design of a SCO, LIESST, and reverse-LIESST active "*nanoball*".[248]

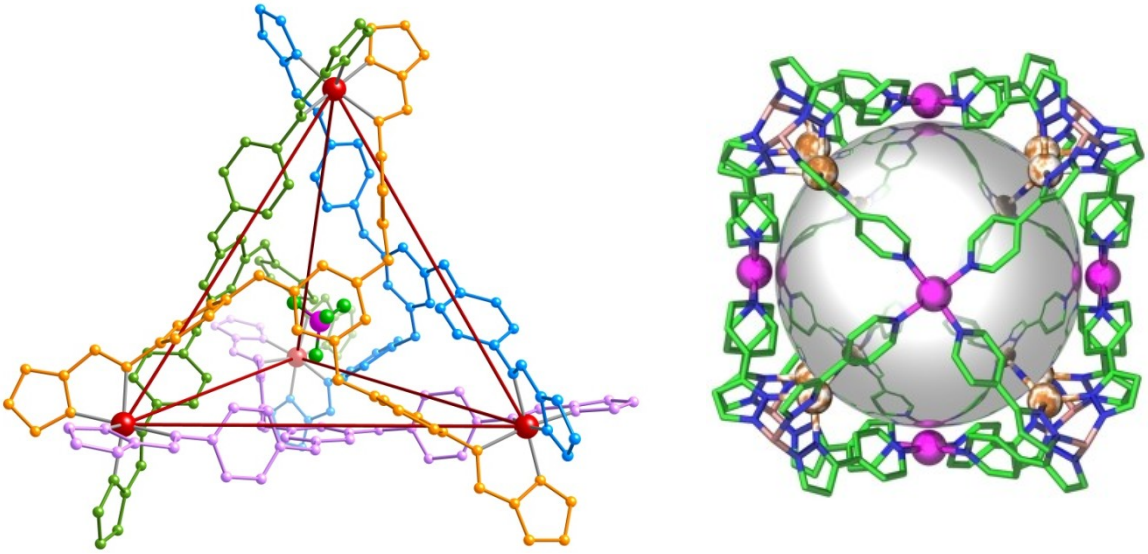

Fig 1.6.6 *Diagram of a SCO active tetrahedral cage* ***(left)***[219] *and a SCO and LIESST-active "nanoball"* ***(right)***[248]*. Images from references.*[219,249]

1.6.4 Potential Applications of Spin Crossover Complexes

SCO complexes are being investigated for applications where tuneable molecular bistability is required. In particular changes in the optical, magnetic and geometric properties of SCO complexes make them ideal for use in sensors and displays. Compounds that show abrupt SCO behaviour with thermal hysteresis may form the active components in data storage and molecular memory devices.[250] There are criteria which have to be met in order for a particular SCO system to be a candidate for potential memory applications. Five of these criteria were outlined by Kahn which consist of the following:[251]

(1) The spin transition must occur with a thermal hysteresis in order to promote a memory effect in the $T_c\uparrow$ - $T_c\downarrow$ range.

(2) The spin transition must be abrupt in both the heating and cooling modes.

(3) The thermal hysteresis loop must be as close as possible to room temperature, ideally with room temperature lying in the middle of the hysteresis loop.

(4) The nature of the spin state, either LS or HS, must be easily detected. The human eye is the most obvious detector and as such a pronounced thermochromic effect is most suitable for applications.

(5) The compound must be stable under normal conditions of use and must not pollute the environment.

One of the most important hurdles to overcome in the design of SCO compounds for application purposes, is having the spin transition occur near room temperature. Pioneering work conducted by Kahn designed a 1D coordination polymer utilising the 1,2,4-*1H*-triazole ligand.[250-252] Fully dried, the chain undergoes a smooth spin transition centred at 265 K with a narrow thermal hysteresis of 5 K. After the addition of one drop of water to 50 mg of the solid, the transition becomes more abrupt and is centred at higher temperatures with the $T_c\uparrow$ = 313 K and $T_c\downarrow$ = 296 K. This magnetic behaviour also occurs concurrently with a vivid colour change from deep purple in the LS state to colourless in the HS state (**Fig 1.6.7**). Advances continue to be made through the substitutions about the triazole backbone.[253-256] These coordination polymer systems also have the added benefit of being highly cooperative leading to abrupt transitions and thermal hysteresis.[250]

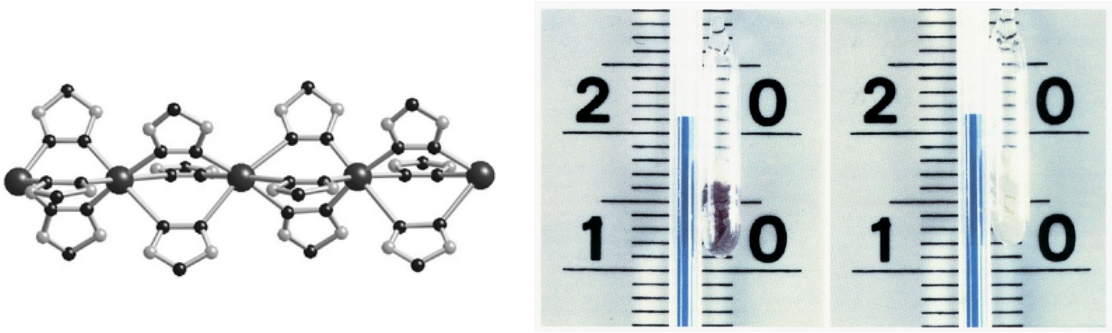

Fig 1.6.7 *Diagram showing the coordination of 1,2,4-triazole units to octahedral Fe(II) centres to form a 1D-coordination polymer (**left**). Colour change associated with thermal hysteresis for compound* $[Fe(htz)_3]^{2+}$ *(**right**). Image unchanged from reference.*[163,252]

In the design of functional materials, coordination polymers have seen particularly high levels of interest in recent years.[88,155,257] In particular, porous coordination polymers that exhibit functionality are vital in designing systems where the incorporation of guest molecules may be reported by the system, preferably to the naked eye. In light of this there has been a focus on incorporating SCO centres into porous coordination polymers. The 3D porous coordination polymer $\{Fe(pz)[Pt(CN)_4]\}_n$ (where pz = pyrazine) was shown by Real to undergo a spin transition with thermal hysteresis centred around room temperature ($T_c\downarrow$ = 285 K and $T_c\uparrow$ = 309 K).[258] Further investigations into this system found the spin state of the polymer to be dependent on the guest molecules within the pores of the polymer.[259]

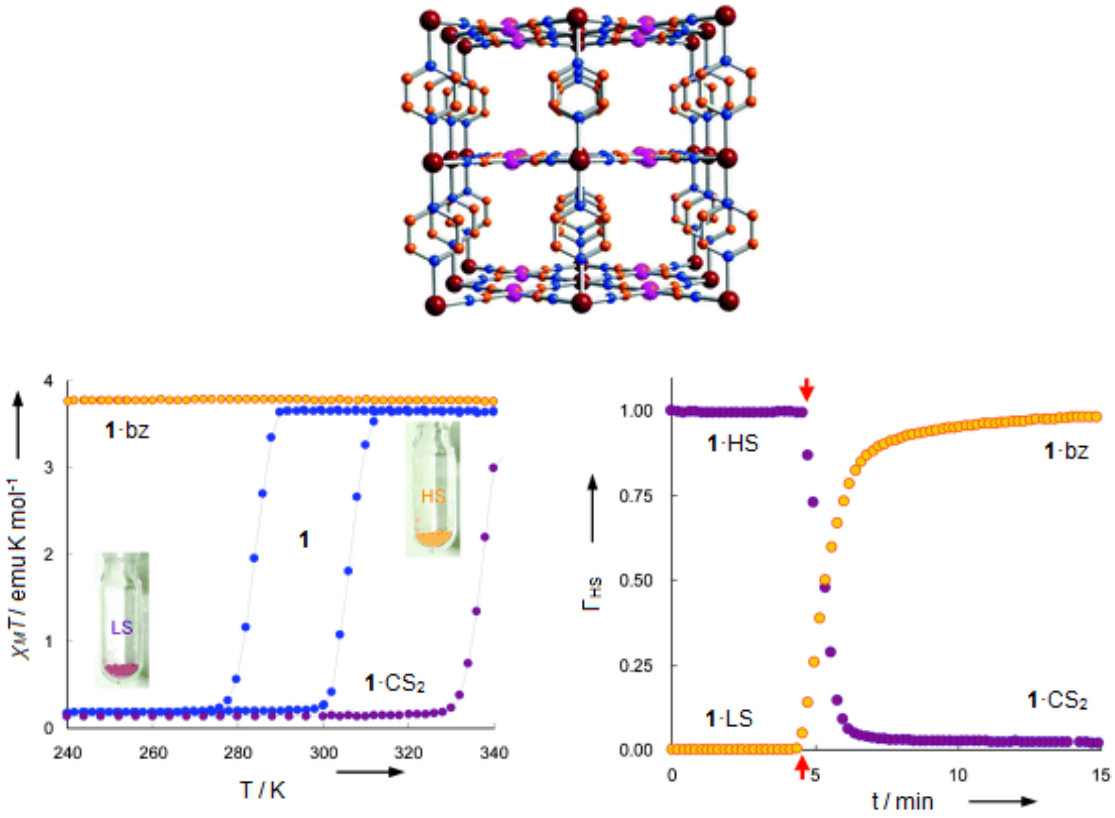

Fig 1.6.8 *The flexible porous coordination polymer* $\{Fe(pz)[Pt(CN)_4]\}_n$ ***(top)*** *showing the effect of guest inclusion on the spin state. Difference in spin states of guest-free polymer* ***(blue)****, polymer and benzene guest* ***(yellow)*** *and* CS_2 *guest* ***(purple)*** ***(left)****. Effect on the spin state after the addition of benzene* ***(yellow)*** *and* CS_2 ***(purple)*** *to the empty polymer* ***(right)****. Red arrows indicate time of addition of guest. Image modified from reference.*[259,260]

Benzene guest molecules were found to stabilise the HS state of the polymer such that the polymer remained paramagnetic over the measured temperature range (2-340 K) and the sample maintained the HS state after evacuation of benzene from the pore. The empty HS form was found to rapidly adsorb CS_2 molecules with a simultaneous conversion of the polymer to the LS state. As with the benzene clathrate, the CS_2 clathrate maintains the LS state even after evacuation of the pores. Interestingly, the polymer has a higher affinity for CS_2 and will gradually displace benzene molecules within the pore even in a saturated benzene atmosphere (**Fig 1.6.8**).

These two systems have also been investigated in nanotechnology with particular emphasis on particle size effects and the addition of these systems on to solid supports.[260] The groups of Letard [261,262] and Coronado [263,264] have succeeded in the synthesis of nanoparticles utilising the triazole ligand with particles sizes in the 70 nm range and 15 nm range respectively. The altering of particle size was shown to affect the SCO properties and thermal hysteresis loop

width. Along with the formation of nanoparticles there have been considerable advances in the tethering of these systems onto solid supports. Thin films may be formed by Langmuir-Blodgett techniques[265-268] or the simple mixing of SCO compounds with polymer matrices that can be attached to surfaces *via* spin and dip coating techniques.[269-271] A downside to these techniques is the incorporation of non-SCO entities within the matrix, altering the SCO properties of the final product. Methods that do not require additional components are ideal, with the growth of the SCO active 3D-coordination polymer $\{Fe(pz)[M(CN)_4]\}_n$ through stepwise adsorption reactions (also known as multi-layer sequential assembly or layer-by-layer assembly) being particularly successful.[272] This technique also lends itself well to incorporation with lithographic techniques as shown below in **Fig 1.6.9**.[273-277]

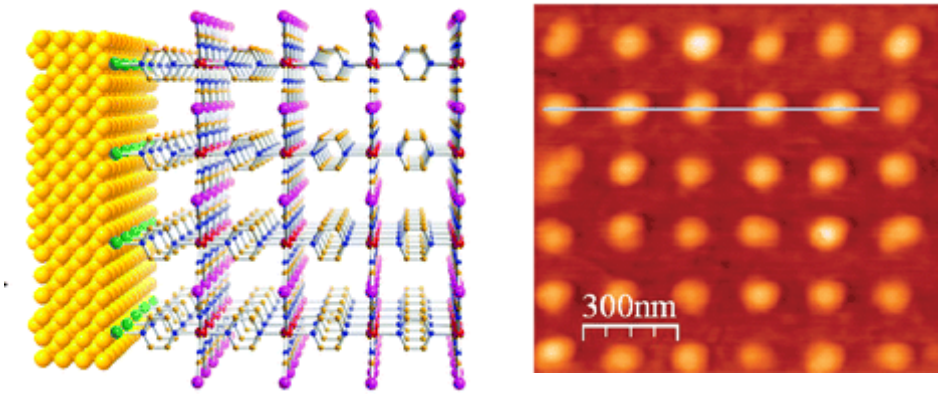

Fig 1.6.9 *The layering of $\{Fe(pz)[M(CN)_4]\}_n$ by multi-layer sequential assembly to give thin films* ***(left)***[272] *and nanoscale pattern of $\{Fe(pz)[M(CN)_4]\}_n$ designed using electron-beam lithiography* ***(right)***.[275] *Images unchanged from reference.*[260]

1.6.5 Elucidating Spin Crossover Behaviour: Methods and Techniques

During the present study, a variety of techniques were used to probe the SCO behaviour of novel Fe(II) complexes. A brief introduction into these techniques will be provided here, with particular emphasis on terminology that will be discussed later in the text.

Particular structural changes occur in Fe(II) coordination compounds during the transition between spin states. These changes can be followed *via* single-crystal X-ray diffraction at temperatures above and below the transition. This study stresses the relationship between molecular structure and SCO behaviour and as such only complexes that formed single crystals suitable for structural analysis *via* X-ray diffraction were employed. Particular focus has been placed on three crystallographic parameters which succinctly describe changes in the coordination

sphere between the LS and HS states.[278] Firstly, Fe(II) complexes undergo a significant expansion of the coordination sphere upon entering the HS state due to the greater antibonding character of the now occupied e_g orbitals. The average coordination bond length is often discussed in relation to SCO compounds with bond lengths below *ca.* 2.0 Å indicating a LS Fe(II) centre and conversely average coordination bond lengths around 2.2 Å are typical for Fe(II) in the HS state. Along with the expansion of the coordination bond lengths in the HS state, the coordination sphere also significantly deviates from octahedral geometry. This deviation can be measured through the Σ and Φ parameters illustrated in **Fig 1.6.10**. The Σ value is the sum of the angle deviations from the ideal value of 90° as measured through the 12 *cis* angles about the Fe(II) centre. As such, a perfect octahedral geometry will give an Σ value of 0. The Φ value indicates the trigonal distortion parameter and measures the average deviation of the 24 internal angles which make up the faces of the octahedron from their ideal angle of 60°.[279]

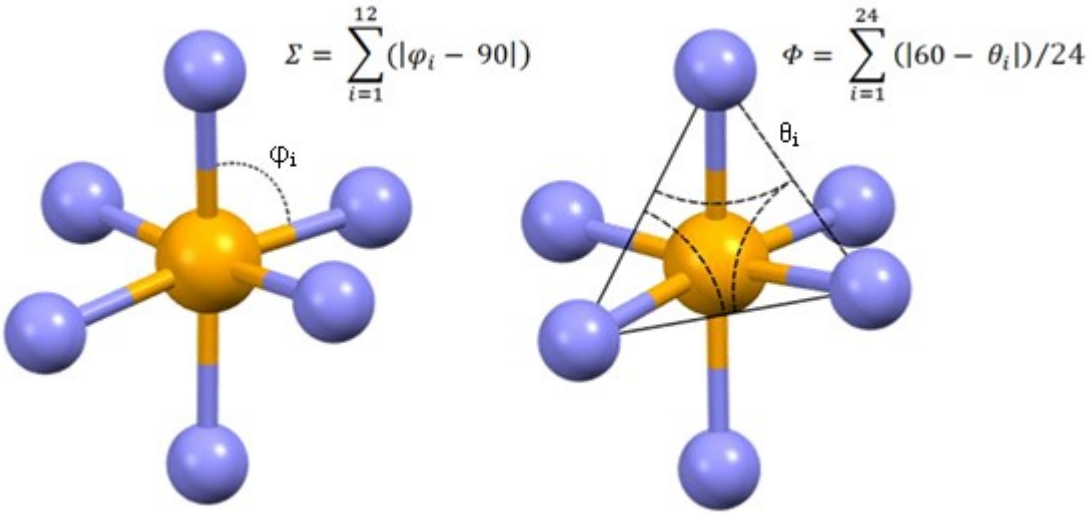

Fig 1.6.10 *Equations used to calculate the Σ and Φ parameters.*

Spin state transitions in Fe(II) occur with vivid colour changes. In particular the LS state has a characteristic absorbance in the visible region due to the $^1A_1 \rightarrow {}^1T_1$ transition, however this transition is often masked by a metal-ligand charge transfer transitions which commonly occur in the visible region in Fe(II) LS complexes. The corresponding transition in the HS state occurs at longer wavelengths (near infrared, NIR) with the absorbance now assigned to the $^5T_2 \rightarrow {}^5E$ transition.[280] As such thermal spin transitions may be monitored in solution through variable temperature UV-Visible spectroscopy and in the solid state using variable temperature surface reflectivity measurements. As the latter technique follows the reflectivity rather than the absorbance of these compounds the spectra are inverted with an increase in the surface reflectivity

in the NIR (*ca.* 900 nm) indicative of the formation of the LS state and increases in the reflectivity of the visible region indicative of the formation of the HS state.

Finally, Fe(II) compounds undergoing spin transitions also experience substantial changes in their magnetic properties. Fe(II) in the HS state has four unpaired electrons and as such is paramagnetic with S = 2. Conversely, the LS state is diamagnetic (S = 0) as all six electrons are paired. Due to these changes, the spin transition can be followed *via* magnetic susceptibility measurements using a superconducting quantum interference device (SQUID), a highly sensitive magnetometer which operates within the 1.8 – 400 K temperature range. ^{57}Fe Mössbauer spectroscopy is also powerful technique for tracking the spin state transition with Fe(II) in the HS and LS states showing different characteristic peaks.

1.7 Present Study

The present study aims to explore the SCO behaviour of Fe(II) complexes with imidazolylimine based ligands. Novel complexes synthesised during the course of this research have been fully characterised using appropriate techniques focusing on single crystal X-ray diffraction for structural analysis of the complexes. Examples which showed evidence of SCO were further analysed by magnetic susceptibility measurements, UV-Visible spectroscopy and surface reflectivity. Photomagnetic measurements were performed on selected samples to elucidate potential LIESST behaviours.

In order to maintain a concise narrative to this text, crystallographic refinement data and bonding parameters are not explicitly reported within the body of the text. Tables reporting crystallographic refinement information, coordination bond details and hydrogen bonding parameters are all provided in **Appendices I – III** with full crystallographic data supplied as electronic supplementary information in .cif format in the accompanying CD-ROM. **Appendix IV** includes further information on the compounds reported within the study which the reader will be directed to within the body of the text for further information.

Chapter 2 discusses the synthesis, characterisation and SCO behaviour of three closely related Fe(II) dinuclear triple helicates. Whilst maintaining a constant bridging group on the ligands, the coordination sites were subtly varied between pyridylimine, 2'–imidazolylimine and 4'–imidazolylimine. Structural similarities and differences, and the spin crossover behaviour of these complexes are discussed.

Continuing with the Fe(II) dinuclear triple helicates, Chapter 3 describes a new solvate of a previously reported helicate. This new compound displays remarkably different SCO behaviour to its predecessor. The subtle structural differences between the two compounds are explored with the

changes in SCO behaviour being linked to particular supramolecular interactions within the crystal lattice.

The study then moves away from the dinuclear helicates and focuses on a family of Fe(II) mononuclear compounds in Chapter 4. These mononuclear compounds utilise the same imidazolylimine coordination sphere as discussed in the previous chapters and may be thought of as "half" complexes to those described in Chapter 3. Whilst maintaining the imidazolylimine coordination sphere, the distant *para*-substituent is altered. The structures of these complexes are compared and the SCO behaviours of selected compounds are discussed.

Chapter 5 investigates the effect of electron-withdrawing substituents on Fe(II) mononuclear complexes, similar to those discussed in Chapter 4. The pyridylimine coordination sphere is also utilised in these ligands. The SCO behaviour of complex **5.5** is the main focus of this chapter with the spin crossover investigated both in solution and the solid state.

The preceding chapters will be summarised in Chapter 6 and this chapter also provides a discussion on possible avenues of further research related to this topic and all experimental data is included in Chapter 7.

CHAPTER TWO

Spin Crossover Behaviour in a Family of Dinuclear Triple Helicates

2.1 Introduction

Helicate assemblies have been widely investigated within the field of metallo-supramolecular chemistry for their self-assembly and self-recognition properties.[105,107,108] The formation of metallo-supramolecular helicates is of particular interest as through careful ligand design and metal choice, helical entities can be formed with particular physical properties. It is apparent that spin crossover (SCO) active metal centres could be easily incorporated into helicate assemblies although interestingly, there are few examples of helicates that display SCO behaviour.[120,176,217,221,281-285] There exists in the literature evidence for the potential for communication between the metal centres to occur within the helicate assembly, which may improve cooperativity within the SCO material.

Drawing on the knowledge that subtle changes to the metal coordination sphere are sufficient to alter the SCO behaviour of a given complex, it is vital to understand these changes at the molecular level. In helicate assemblies, interactions between donor atoms and metal centres primarily affect the overall structural properties of the complex. However, physical properties of the helicate species can vary depending on other factors remote from the coordination site. For example, helicates can invariably be compressed or extended along their helical axis depending at which conformation provides the lowest thermodynamic energy. This can result in diverse interactions within the crystal lattice through various supramolecular interactions.

This chapter will focus on a family of Fe(II) dinuclear triple helicates, formed from one of three homotopic ligands. These ligands all possess the same rigid backbone unit. The degree of flex within this backbone is limited due to the preferred *anti* conformation about the two central nitrogen atoms. However, there is some ability for the ligand to twist about the adjacent phenyl rings and the central N-N bond which maintains its single bond character following complexation. The ligand backbone also contains two methyl groups which create steric bulk within the ligand system. The incorporation of bulky substituents has been utilised with success in bringing the ligand field strength of $[FeN_6]$ coordination systems into the required energy domain for SCO.[208,209,211]

Whilst maintaining a constant backbone unit, the ligand binding group (head group) is varied to subtly change the ligand field strength. The pyridylimine motif has been shown to form low-spin (LS) complexes upon complexation with Fe(II)[204] and was used to form a LS analogue. Two isomeric imidazolylimine motifs featuring either 2'-imidazole or 4'-imidazole are known to coordinate to Fe(II) centres with weaker ligand field strengths, potentially resulting in SCO.[220,284,286,287] The imidazole ring also contains a hydrogen bond donor (N-H) which may be expected to form hydrogen bonding interactions with counter-anions within the crystal lattice.

2.2 Synthesis of Ligands: L2.1, L2.2, and L2.3

The three ligands within this family were all synthesised *via* simple imine condensation reactions between two equivalents of the respective aldehyde group (choice of either: 2-pyridinecarboxaldehyde, 2-imidazolecarboxaldehyde or 4-imidazolecarboxaldehyde) with the bridging group **L2A**. The formation of the diamine precursor involved the condensation of two equivalents of *m*-aminoacetophenone with one equivalent of hydrazine monohydrate (**Scheme 2.2.1**). The precursor **L2A** formed as yellow-brown needle crystals upon slow evaporation of the ethanol solution in good yield (90%).

The subsequent imine condensation steps with the appropriate aldehyde were performed in methanol/ethanol under reflux. The work-up procedures for each of the final ligands were different given the differing solubility of each ligand system. **L2.1** was isolated as a pale yellow oil which solidified over some days at room temperature; **L2.2** precipitated directly as a pale yellow powder which was found to be insoluble in common organic solvents and **L2.3** formed as a microcrystalline powder upon cooling.

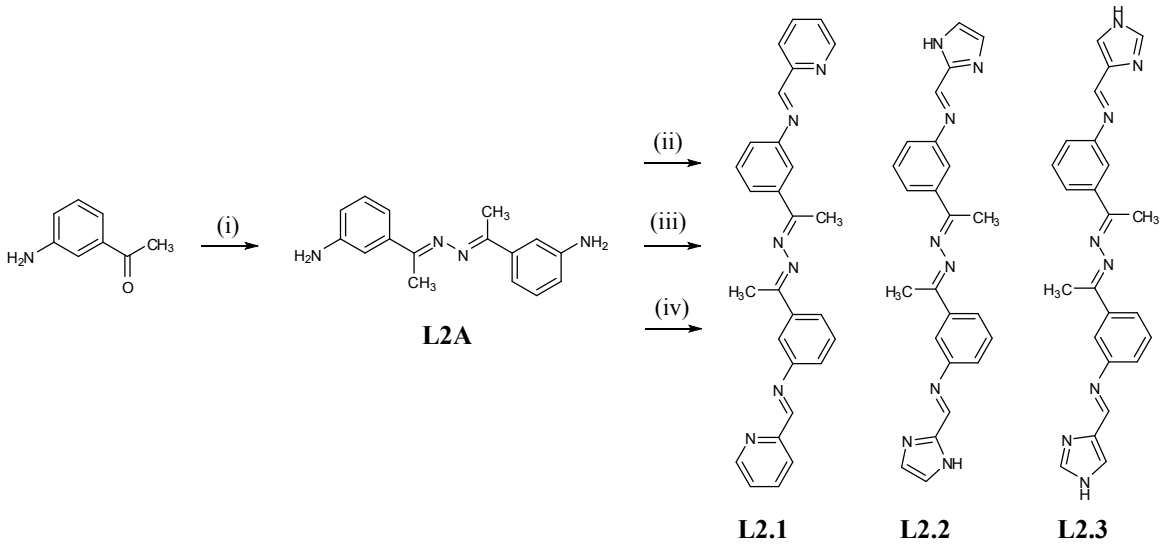

Scheme 2.2.1 *Synthesis of ligands* ***L2.1***, ***L2.2***, ***L2.3***. *Reagents and conditions: (i) 1.1 equivalents hydrazine monohydrate, 0.25 mL glacial acetic acid, EtOH, reflux 4 hr; (ii) 2 equivalents pyridine-2-carboxaldehyde, EtOH, reflux 4 hr; (iii) 2 equivalents imidazole-2-carboxaldehyde, MeOH, reflux 7 hr; (iv) 2 equivalents imidazole-4-carboxaldehyde, MeOH, reflux 4 hr.*

2.3 Complexation of L2.1 – Formation of a Low-Spin Dinuclear Triple Helicate

*2.3.1 Synthesis and Solution Studies of [Fe_2(**L2.1**)$_3$](BF_4)$_4$·2$CHCl_3$·3CH_3CN·5H_2O – **2.4***

The ligand **L2.1** contains two bidentate coordination sites separated by a rigid backbone spacer. It was anticipated that the ligand would preferentially form dinuclear complexes with octahedral metal centres in the ratio of 3L : 2M. In order to confirm this stoichiometry and to probe the interaction between the ligand and the Fe(II) metal centre, a UV-Visible spectroscopic titration experiment was conducted to follow the formation of **2.4**. In this experiment iron(II) tetrafluoroborate (1.084×10^{-3} mol L^{-1}) was added in 10 μL aliquots to a 3 mL acetonitrile solution of the ligand **L2.1** (6.410×10^{-5} mol L^{-1}). After each addition the UV-Visible spectrum was recorded. The absorbance spectrum of the free ligand revealed one major peak in the UV region with a maximum absorbance (λ_{max}) occurring at 261 nm ($\varepsilon = 35700 \pm 100$ L mol^{-1} cm^{-1}). This is consistent with the highly conjugated nature of the ligand system and can be attributed to a $\pi - \pi^*$ transition. As aliquots of the metal salt were added, a broad absorption band formed between 500 – 600 nm, with λ_{max} = 570 nm ($\varepsilon = 10700 \pm 100$ L mol^{-1} cm^{-1}). During the titration tight isosbestic points were observed at 243 and 357 nm indicating a direct transition from the free ligand to the [M_2L_3] complex. Upon coordination to the metal centre the $\pi - \pi^*$ transition at 261 nm undergoes a red-shift (bathochromic) of nearly 30 nm to reach a λ_{max} value of 287 nm at the end of the titration, as displayed in **Fig 2.3.1**.

By plotting the absorbance at 570 nm against the molar ratio ([$Fe(BF_4)_2$]/[**L2.1**]) it is clear that the stoichiometry for the formation of **2.4** was the anticipated 3L : 2M (**Fig 2.3.1-Inset**). Addition of further iron(II) tetrafluoroborate [$Fe(BF_4)_2 \cdot 6H_2O$] did not alter the absorbance once the optimal stoichiometry was reached. The accurate mass of the complex was determined by high-resolution electrospray mass spectrometry which clearly showed the [Fe_2**L2.1**$_3$]$^{4+}$ molecular ion at *m/z* 361.1213 (calculated *m/z* for $C_{84}H_{72}N_{18}Fe_2$ = 361.1225) with excellent agreement in the isotope pattern (**Fig 2.3.2**).

The intense deep purple colour and the formation of a substantial MLCT transition band during the UV-Visible titration of **2.4** suggested a [LS-LS] electronic configuration for the complex at room temperature.

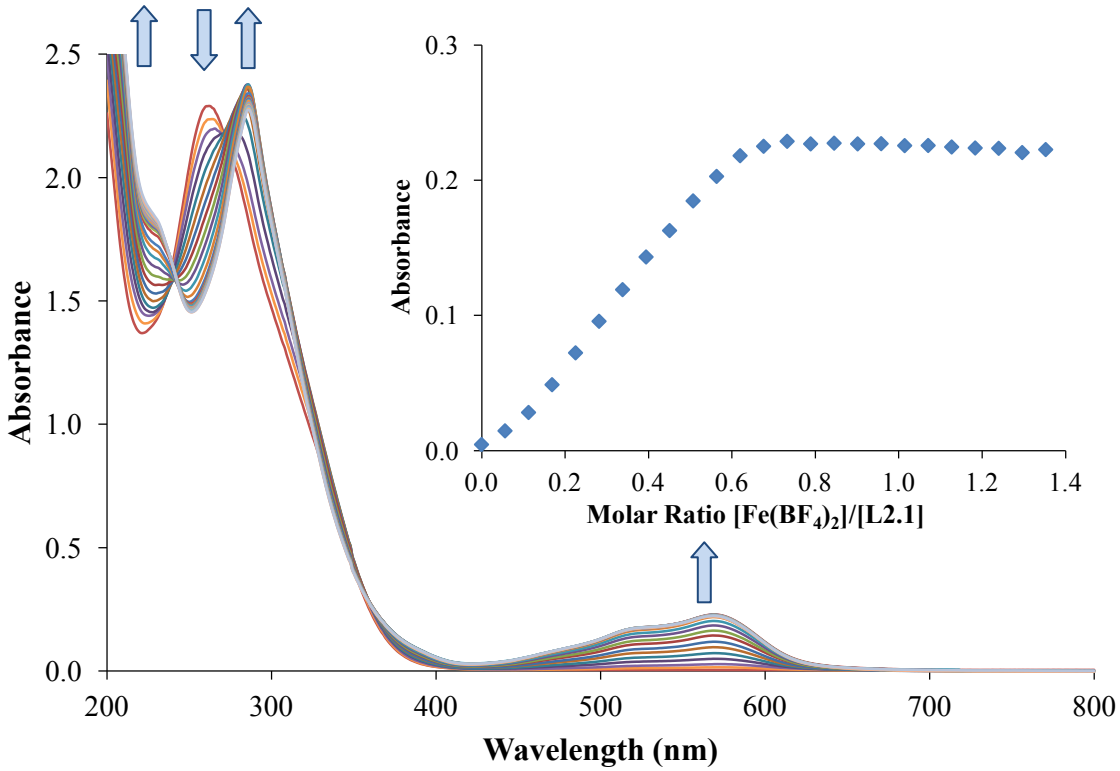

Fig 2.3.1 *UV-Visible spectroscopic titration plot of $Fe(BF_4)_2{\cdot}6H_2O$ (1.084×10^{-3} mol L^{-1}) against ligand* ***L2.1*** *(6.410×10^{-5} mol L^{-1}) in acetonitrile. Inset: Absorbance vs. molar ratio at 570 nm.*

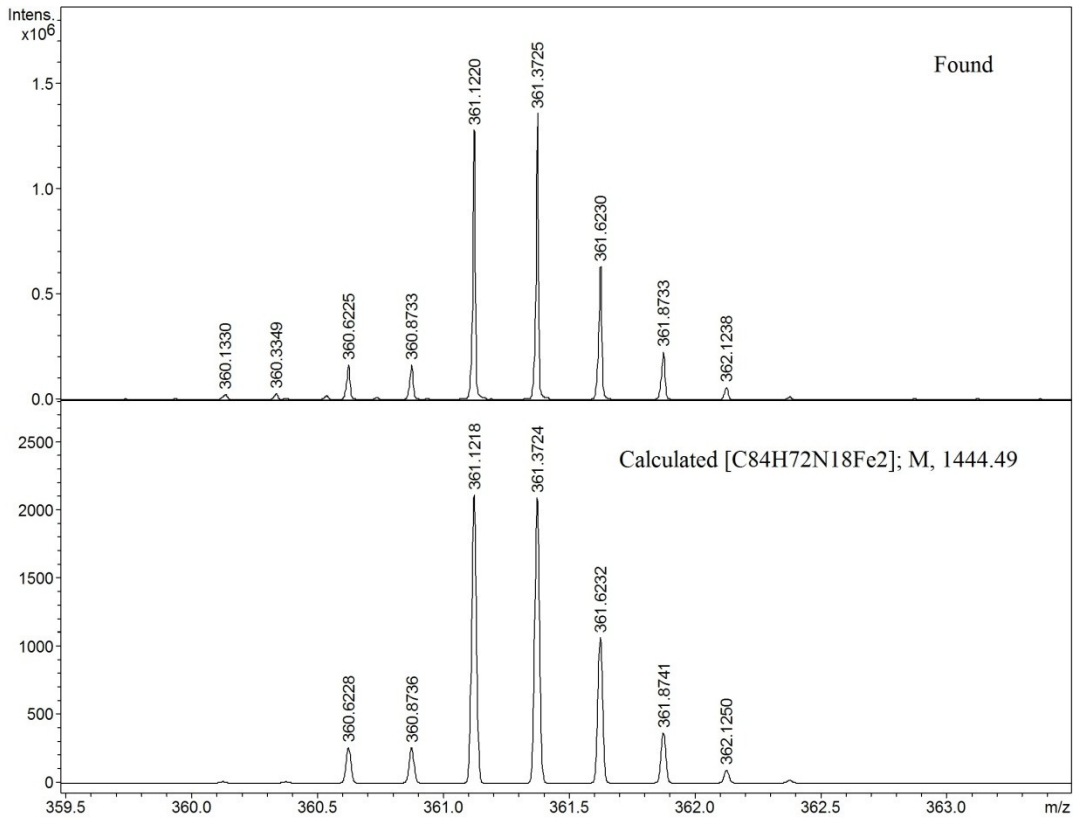

Fig 2.3.2 *Found (**top**) and calculated (**bottom**) electrospray ionization isotope distribution patterns for complex **2.4** in acetonitrile solution*

*2.3.2 Structural Analysis of Complex **2.4** via Single Crystal X-ray Diffraction*

In light of the spectroscopic studies which showed the formation of **2.4** in solution, the solid state structure was analysed through single crystal X-ray diffraction. Dark purple needle crystals of suitable quality were grown from the slow diffusion of chloroform into an acetonitrile solution of the complex. The data were solved and refined in the monoclinic space group *C*2/*c* (R-factor 7.92%). As anticipated, **2.4** was found to contain three ligands coordinated to two Fe(II) centres forming a dinuclear triple helicate with an Fe-Fe distance of 14.979(1) Å. The three ligands each twist through an angle of approximately 130° along the helical axis. Both ends of the helicate are identical due to a 2-fold rotation symmetry axis, which bisects the helicate. As such the helicate entity consists of two identical ligands running opposite one another as the 2-fold rotation symmetry axis runs through the middle of the helicate (perpendicular to the Fe-Fe plane). Only half of the third ligand is present in the asymmetric unit and the full ligand is generated by the symmetry axis described above. Two BF_4^- anions are present per asymmetric unit to balance the helicate charge, and both have some disorder. Solvent molecules were also present within the crystal lattice that were modelled as 1.5 molecules of acetonitrile, 1 molecule of chloroform (disordered over two positions), and 2.5 water molecules (disordered over five positions) per asymmetric unit. The crystal was racemic and contained both helical enantiomers.

The Fe(II) atoms are crystallographically identical with Fe-N coordination bond lengths within the range 1.971(4) to 1.994(4) Å with an average coordination bond distance of *ca.* 1.98 Å consistent with [LS-LS] electronic configuration at 120 K as expected. The geometry about the Fe(II) centre is octahedral and is only minimally distorted from ideal geometry with an Σ value (defined in **1.6.1)** of 59.1°. The ligands twist between the imine and phenyl planes in order to optimise C-H···π interactions between the three ligand strands. This results in torsion angles ranging from 58.0(5)° to 89.8(5)° with C-H···π(centroid) distances ranging from 2.6752(18) Å to 2.805(2) Å for these interactions. The ligands are also twisted slightly about the central N-N group. This segment only has limited flexibility as the adjacent methyl groups greatly favour the *anti* conformation. The N-N bond has single bond character with bond lengths of *ca.* 1.39 Å. The adjacent C-N bonds were considerably shorter characteristic of an imine bond.[288] Disorder about these methyl groups was observed with one pair of methyl groups modelled equally over two positions (*i.e.* with 50% occupancy in each position). This results in methyl-methyl torsion angles of 103.6(6)° and 170.5(6)° for the two positions. One of these positions points directly into the internal cavity of the helicate, whereas the other points outwards to yield the more favourable *anti* geometry. The structure and atom labelling scheme of **2.4** is illustrated below in **Fig 2.3.3**.

Inter-helical interactions between neighbouring cations within the crystal lattice are dominated by edge-to-face C-H···π interactions between helicates of opposite handedness with a

C-H···π (centroid) distance of 2.706(2) Å and an interplanar angle of 46.8(3)° These interactions form a 1D-network which extends along the crystallographic c-axis (**Fig 2.3.4**).

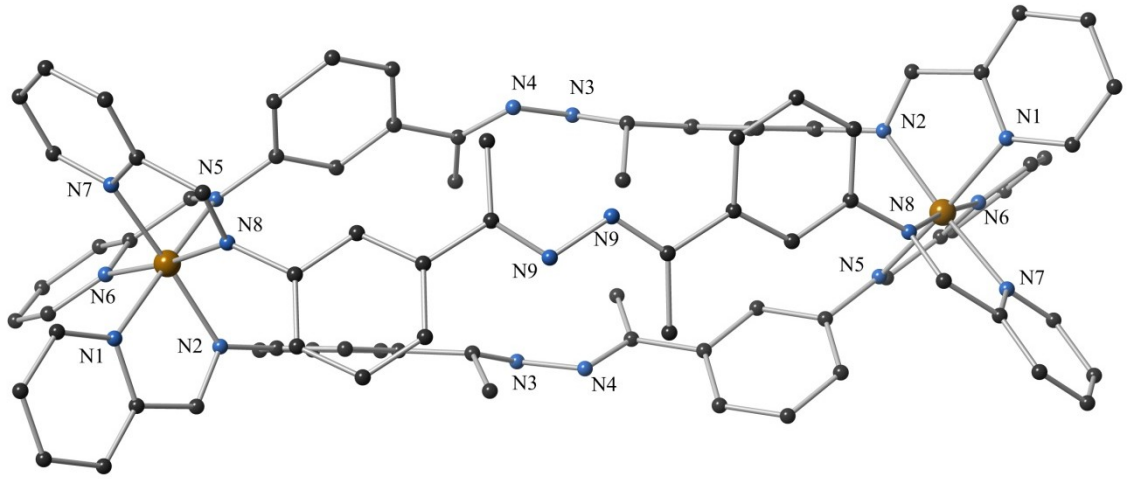

Fig 2.3.3 *Molecular structure and atom labelling scheme for complex* ***2.4*** *at 120 K. Hydrogen atoms, solvent molecules, disordered methyl groups and counter-anions have been omitted for clarity.*

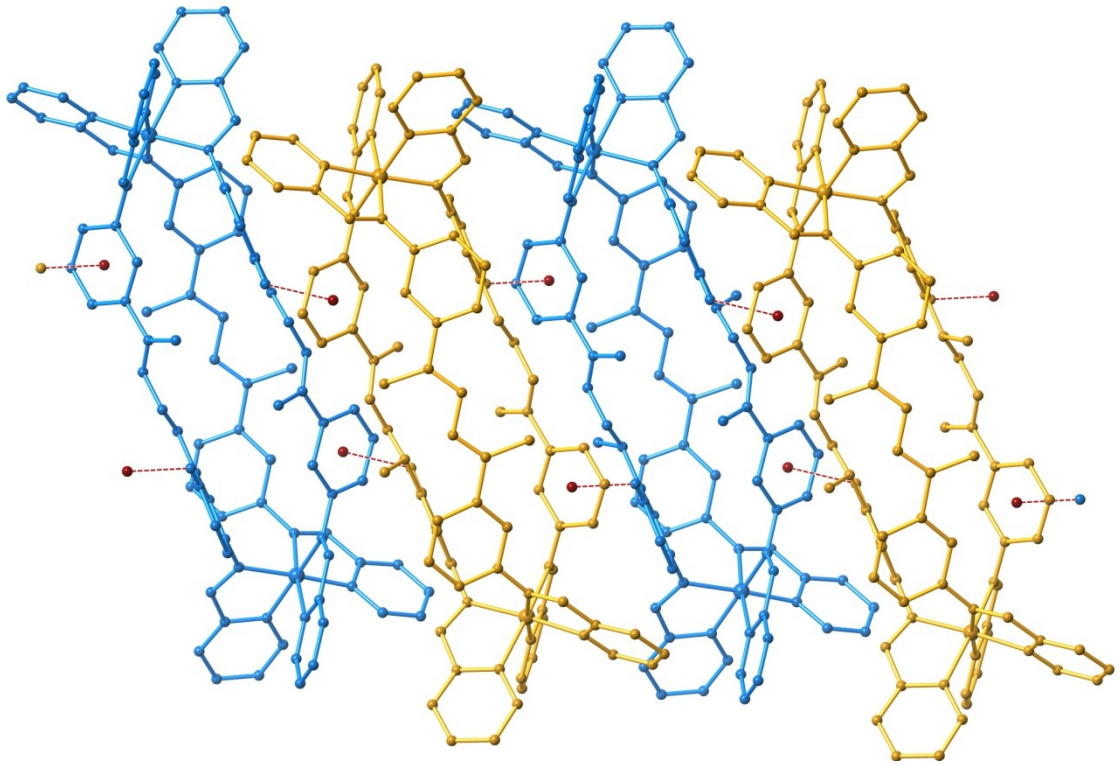

Fig 2.3.4 *Structure of complex* ***2.4*** *showing the edge-to-face C-H···π interactions between helicates of opposite handedness at 120 K. Right-handed helicates (**blue**), left-handed helicates (**yellow**). Counter-anions, solvent molecules and hydrogen atoms have been omitted for clarity.*

2.4 Complexation of L2.2 and L2.3 – Formation of Spin Crossover Dinuclear Triple Helicates

*2.4.1. Synthesis of [Fe_2(**L2.2**)$_3$](BF_4)$_4$·2.5CH_3CN – Complex **2.5** and Synthesis of [Fe_2(**L2.3**)$_3$](BF_4)$_4$·3$CHCl_3$·1.5CH_3CN·1H_2O – Complex **2.6***

The dinuclear triple helicate **2.5** was synthesised by mixing three equivalents of **L2.2** with two equivalents of $Fe(BF_4)_2·6H_2O$ in acetonitrile. Given the insoluble nature of the ligand the solution was stirred at room temperature for 3 hours. The resulting raspberry red solution was filtered and diethyl ether was diffused into the filtrate over several days, yielding thin dark red needle crystals suitable for structural analysis *via* single crystal X-ray diffraction.

A similar procedure was employed in the preparation of complex **2.6** through mixing three equivalents of **L2.3** with two equivalents of $Fe(BF_4)_2·6H_2O$ in acetonitrile. The resulting bright orange solution was filtered and crystals suitable for single crystal X-ray structural analysis were grown *via* a slow diffusion of chloroform into the reaction mixture. Large orange block crystals were obtained after a few days. Crystals with the same unit cell parameters could also be synthesised *via* a self-assembly process. Six equivalents of 4-imidazolecarboxaldehyde, three equivalents of **L2A**, and two equivalents of $Fe(BF_4)_2·6H_2O$ were reacted in acetonitrile and stirred at room temperature for 3 hours to give a bright orange solution. Single crystals were obtained *via* the method described above.

*2.4.2 Structural Determination of **2.5** and **2.6** via Single Crystal X-ray Diffraction*

The solid state structures of **2.5** and **2.6** were elucidated *via* single crystal X-ray diffraction, firstly at 120 K. In the case of **2.5** the diffraction data were solved and refined in the orthorhombic space group *Pccn* (R-factor of 7.46%). Conversely in **2.6**, the diffraction data were solved and refined in the triclinic space group *P-1* with the higher R-factor of 10.71%.

Both **2.5** and **2.6** form dinuclear triple helicates with geometric properties very similar to that observed in complex **2.4**. The Fe-Fe distances in **2.5** and **2.6** are 14.847(1) Å and 15.001(1) Å respectively with the ligands in both complexes undergoing a similar twist along the helical axis of *ca.* 130°. As observed in **2.4**, the six phenyl groups in both **2.5** and **2.6** rotate about the imine-phenyl bond in order to optimise intramolecular edge-to-face C-H···π interactions. The twisting is quite severe with some of the phenyl groups lying nearly perpendicular to the imidazolylimine bond. These interactions are similar in both complexes with C-H···π(centroid) distances in the range of 2.8111(2) – 3.050(2) Å for **2.5** compared with 2.849(2) – 3.100(2) Å in complex **2.6**. The

methyl groups adjacent to the central N-N bond rotate to occupy the least sterically encumbered position. Ideally, the methyl groups should adopt an *anti* conformation where methyl groups lie at 180° to one another. As observed in **2.4**, the three central N-N bonds rotate through angles of 134.9(4) – 154.5(5)° in **2.5** and 129.5(6) – 151.4(6)° in **2.6**. The smaller torsion angles (further distorted from the ideal 180°) correspond to the "internalisation" of the methyl groups within the complexes. Indeed, two of the six methyl groups present within both complexes point toward the internal space of the helicate causing the ligand opposite the internal methyl groups to "pucker" slightly to accommodate the steric bulk.

Although the geometric properties of the helicates are similar, there are some discrepancies between the two structures. The most obvious is the internal symmetry present in **2.5** that is not present in **2.6** resulting in both Fe(II) centres being crystallographically equivalent in **2.5** but non-equivalent in **2.6**. As such the helicate cation of **2.5** consists of one "full" ligand, one "half" ligand, and one Fe(II) centre in the asymmetric unit. The rest of the helicate results from a 2-fold rotation symmetry element, which bisects the complex perpendicular to the Fe-Fe axis. At 120 K the Fe-N coordination bond lengths lie within the range 1.942(5) – 2.016(4) Å and have an average bond length of *ca.* 1.98 Å consistent with an Fe(II) centre in the LS state.[1] In contrast, the Fe(II) centres in **2.6** are non-equivalent with Fe1 having coordination bond lengths which lie in the range 1.968(6) – 2.043(4) Å with an average bond length of *ca.* 2.01 Å, whereas the bond lengths about Fe2 lie in the range of 2.043(8) – 2.122(4) Å with an average bond length of *ca.* 2.09 Å. These bond lengths suggest that at 120 K the complex is in a mixed spin state with Fe1 in the LS state and Fe2 in a partially contracted high spin state [LS-HS]. The structural similarities between the three related complexes are illustrated in **Fig 2.4.1**.

Intrigued by the potential SCO behaviour indicated by the low temperature data, diffraction of **2.6** was conducted at 240 K. At 240 K, crystals of **2.6** remained yellow in colour compared to the deep red colour of the crystals at 120 K. This suggests that the complex is in the high spin state at this higher temperature. The crystallographic data was once again solved and refined in the triclinic space group *P-1* and the volume of the unit cell expands from 4984 $Å^3$ (120 K) to 5160 $Å^3$ (240 K), an increase of 3.5%. The bulk geometric characteristics of the helicate cation remain largely unchanged, however, closer inspection of the coordination bond lengths about both Fe(II) centres reveals a considerable increase to give an average coordination bond length of approximately 2.20 Å for both Fe(II) centres. This is consistent with both Fe(II) centres being in the high spin state at 240 K giving a [HS-HS] complex. During this process the intrahelical Fe-Fe distance increases to 15.223(2) Å and other changes to the helicate structure during SCO are illustrated in **Fig 2.4.2**. Subtle changes throughout the helicate can be attributed to the expansion of the coordination sphere in the HS state. A table containing the parameters Σ and Φ, for **2.4, 2.5**, **2.6-120 K**, and **2.6-240 K** are provided (**Table 2.4.1**) for the comparison of

coordination parameters in these three crystal structures. Tables of all coordination bond lengths and angles are provided as supplementary information in **A-II**.

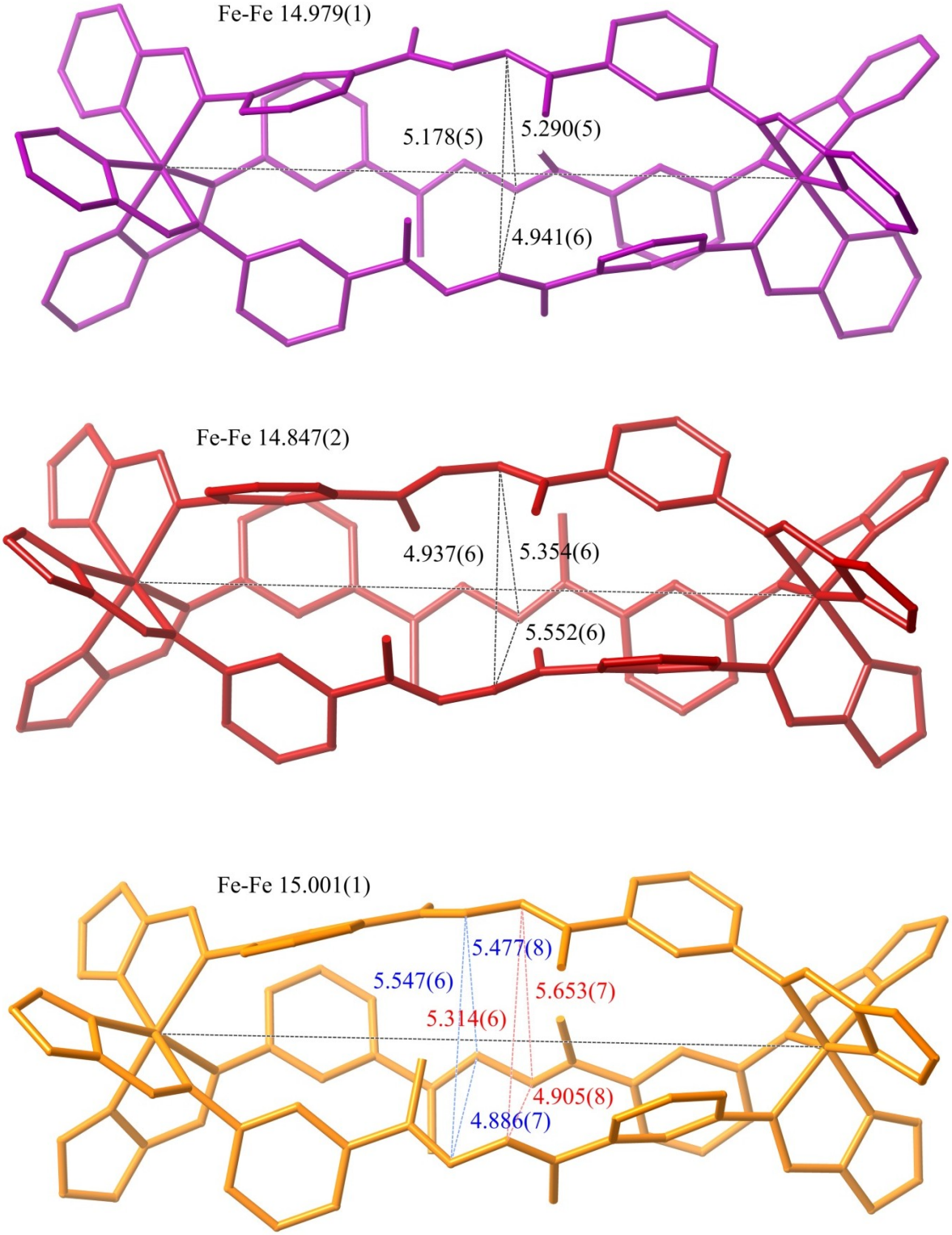

Fig 2.4.1 *Helicate structures of complexes* ***2.4 (purple)***, ***2.5 (red)***, *and* ***2.6 (orange)***, *showing selected geometric parameters at 120 K. All distances are in Å.*

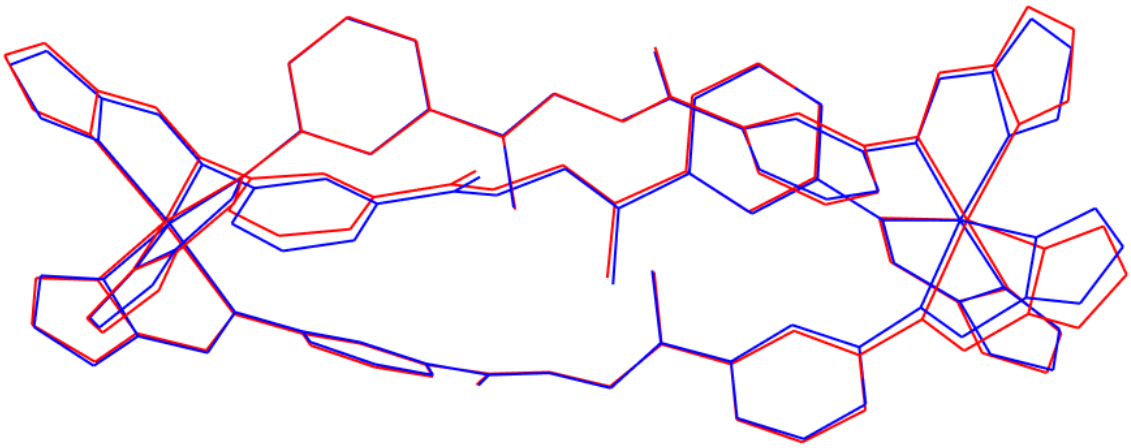

Fig 2.4.2 *Structural overlay of helicate* ***2.6*** *at 120 K (**blue**) and 240 K (**red**). Hydrogen atoms, solvent molecules and counter-anions have been omitted for clarity.*

	2.4	**2.5**	**2.6**			
Crystal Colour	Purple	Dark Red	Red		Yellow	
Temperature (K)	120	120	120		240	
Space Group	*C2/c*	*Pccn*	*P-1*		*P-1*	
Spin State	[LS-LS]	[LS-LS]	[LS-HS]		[HS-HS]	
Av. Fe-N Bond Length (Å)	1.98	1.98	**Fe1** 2.01	**Fe2** 2.09 Å	**Fe1** 2.20 Å	**Fe2** 2.19 Å
Σ (°)	50.0	63.3	66.0	77.8	88.3	89.0
Φ (°)	3.52	3.81	3.90	4.70	5.49	4.90

Table 2.4.3 *Selected geometric parameters for complexes* ***2.4***, ***2.5***, *and* ***2.6***.

Despite the similarities in helicate structure between the three complexes, all three structures show different crystal packing behaviour. In **2.5**, the imidazole N-H groups act as hydrogen bond donors towards the BF_4^- counter-anions. Two symmetry equivalent BF_4^- counter-anions bridge two complexes through hydrogen bonding interactions between N2-H2···F7 and N10-H10···F6, as shown in **Fig 2.4.4**. The other BF_4^- counter-anions hydrogen bond to the remaining hydrogen bond donor through N7-H7···F3 but no further hydrogen bonding occurs to this BF_4^-. A table outlining the hydrogen bonding parameters is provided as supplementary information in **A-III**. The hydrogen bonding interactions extend to form a 1D chain of helices parallel to the [1,1,0] crystallographic plane. Both helical enantiomers are present within the crystal lattice and the helices are inverted in an alternating fashion along the hydrogen bonding chain. The 2-fold screw

axis causes two of the hydrogen bonding chains to lie perpendicular to one another, so that a helicate effectively sits in the groove within the hydrogen bonding network, **Fig 2.4.5**. In this packing arrangement, solvent accessible channels exist which run parallel to the crystallographic c-axis. The equivalent of 2.5 acetonitrile molecules per helicate reside in this channel, with one lying directly on a 2-fold rotation symmetry axis. The channels are approximately 6 x 6 Å in diameter.

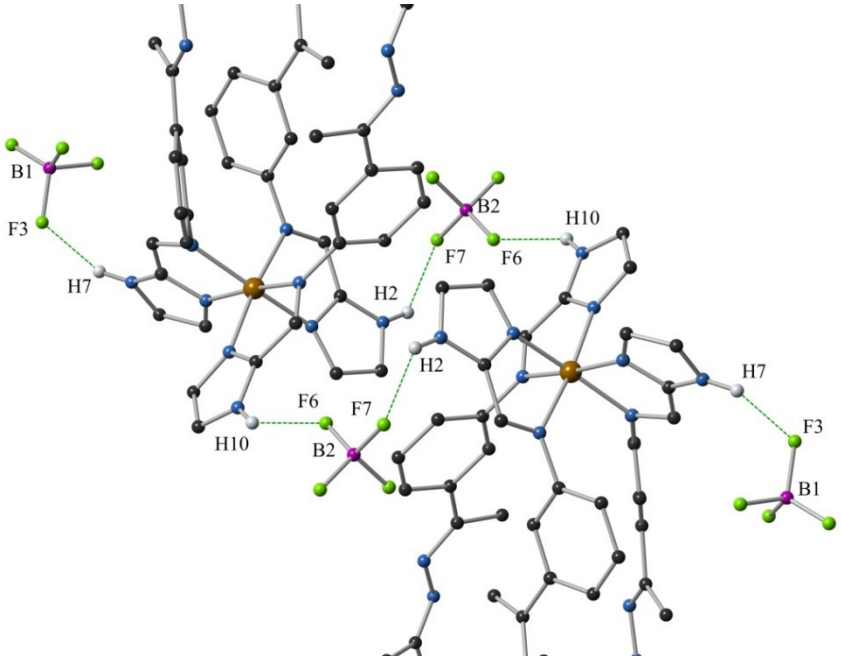

Fig 2.4.4 *'Cut-away' to the hydrogen bonding interactions between helicates in* ***2.5*** *at 120 K. Solvent molecules and hydrogen atoms not involved in hydrogen bonding have been omitted for clarity.*

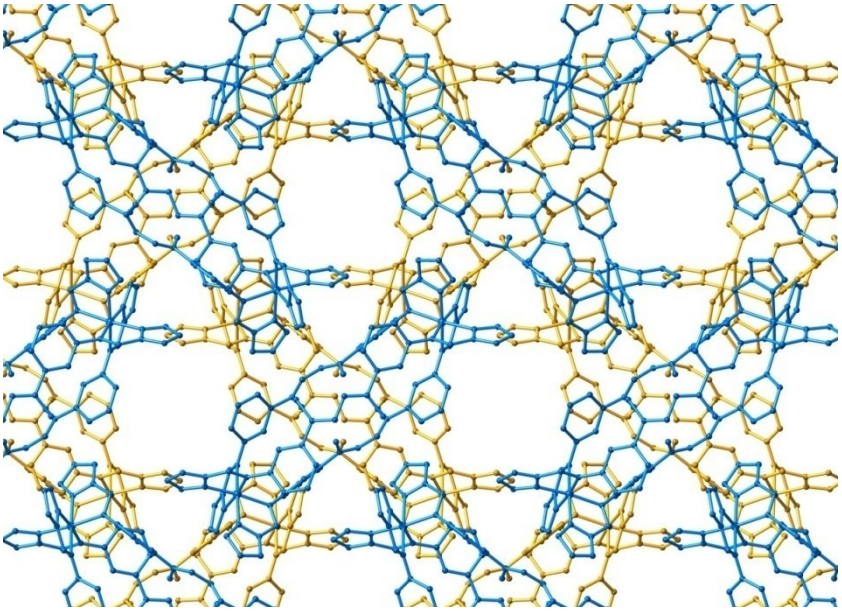

Fig 2.4.5 *Crystal packing diagram of* ***2.5*** *viewed along the crystallographic c-axis at 120 K. Helicates of opposite handedness are coloured separately (right-handed helicates,* ***blue****; left-handed helicates,* ***yellow****). Hydrogen atoms, counter-anions, and solvent molecules have been omitted for clarity.*

Solvent egress was found to readily occur, with thermogravimetric analysis reporting the loss of 5.4% mass (acetonitrile content equates to 5.9%) up to 140 °C. Microanalysis showed increased water content and loss of acetonitrile content, however, the sample was left to dry away from the mother liquor prior to analysis and as such solvent loss was not unexpected. The crystals appeared to maintain single crystallinity through gentle drying processes however, structural analysis of the dried compound *via* X-ray diffraction was unsuccessful with only weak diffraction of the sample observed.

The crystal lattice packing for **2.6** showed similar interhelical interactions to those observed in **2.4**. Inspection of the crystal lattice reveals interhelical edge-to-face C-H···π interactions that extend from each of the three ligand strands of the complex with C-H···π(centroid) distances of 2.699(2) Å and 2.717(2) Å respectively. These interactions form a 2D sheet, which extends parallel to both the crystallographic a- and b-axes, as shown in **Fig 2.4.6**. Layers of 2D-sheets are displaced from one another, such that no channels are observed within the crystal lattice. The BF_4^- counter-anions are all located towards the ends of the helicates and form hydrogen bonding interactions with the imidazole N-H moieties with D···A distances ranging between 2.75(2) Å and 3.00(1) Å. These interactions join the 2D-networks into the third dimension along the crystallographic c-axis (**Fig 2.4.7**). This crystal packing results in pockets within the crystal lattice that contain disordered solvent molecules which were modelled as 3 chloroform molecules disordered over four positions, 1.5 molecules of acetonitrile, and the equivalent of 1 water molecule in two partially occupied positions. Thermogravimetric and microanalyses showed varying solvent content with thermogravimetric analysis showing rapid loss of mass from the sample (*ca.* 13% at 200 °C). **2.6** was found to lose single crystallinity during drying procedures including standing in air over a few days, as such crystals were stored in their mother liquor and were filtered immediately prior to any further analysis.

The crystal packing at 240 K showed no major alterations to the interactions between helicates within the crystal lattice. Interhelical Fe-Fe distances between helicates within the 2D-sheet lie within the range 9.386(2) – 9.629(2) Å at 240 K compared with 9.331(1) – 9.398(1) Å at 120 K. The longer distances coincide with the interactions along the crystallographic a- and b-axes which is also observed in the expansion of the unit cell along these axes.

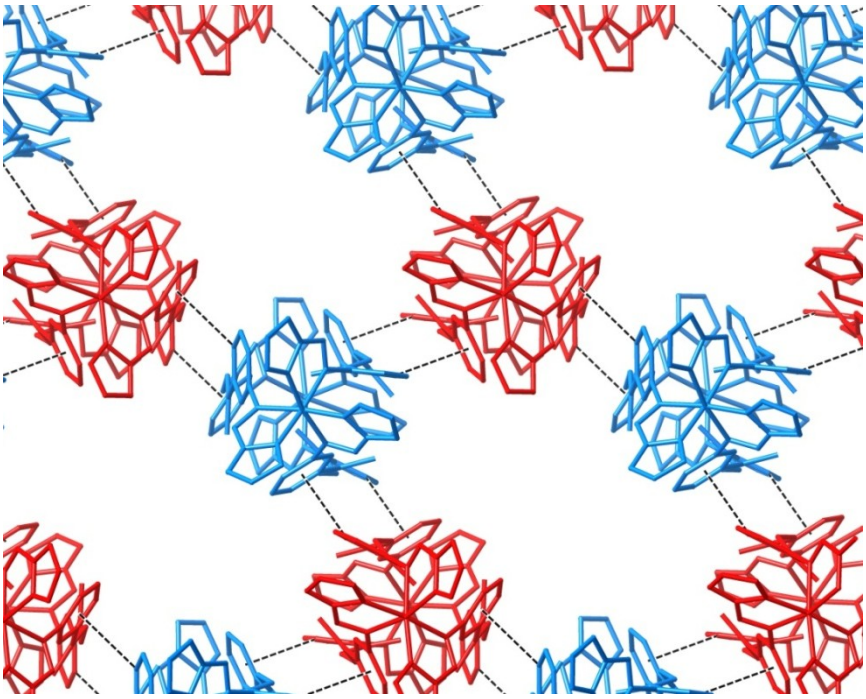

Fig 2.4.6 *Crystal packing diagrams for complex* ***2.6*** *at 120 K showing the 2D-network comprising of edge-to-face C-H···π interactions as viewed along the helical axis.*

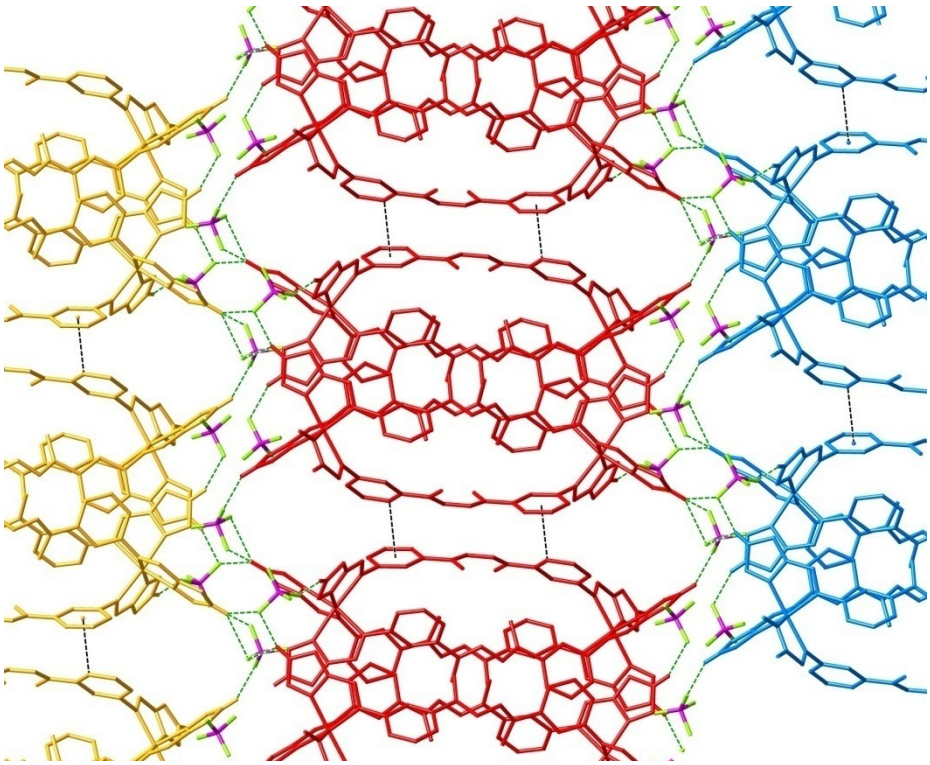

Fig 2.4.7 *Hydrogen bonding interactions between helicate ends in* ***2.6*** *at 120 K, as viewed along the crystallographic a-axis with the 2D-networks are coloured separately.*

*2.4.3. Variable Temperature UV-Visible Spectroscopy of **2.5***

The study of SCO in solution provides contrasting but complementary insights into the behaviour of these systems. In the solid state, weak interactions between SCO centres within the crystal lattice often dominate SCO behaviour with the chemist being driven serendipitously to systems with interesting behaviour rather than through thoughtful design. By observing the SCO process in solution, the effects of crystal packing interactions are minimised and the SCO behaviour is mainly determined by the ligand field strength, solvent choice, and anion (and/or guest) interactions.

During the synthesis of **2.5**, it was observed that an acetonitrile solution of the complex displayed significant thermochromic behaviour on gentle heating changing in colour from raspberry red at room temperature to a pale peach when heated to 60 °C. As no high temperature structural data for **2.5** could be acquired due to crystal instability, this complex was ideal for variable temperature UV-Visible spectroscopic analysis to probe the SCO properties of **2.5** in solution. To accomplish this, a nitromethane solution of **2.5** at a concentration of 3.773×10^{-4} mol L^{-1} was prepared. **2.5** is only sparingly soluble in the solvents acetonitrile and nitromethane and as such the solvent nitromethane was employed due to its higher boiling point. Once prepared, 2 mL of the solution were added to a quartz cuvette and the solution cooled to 273 K. The solution was left to thermally equilibrate after which the absorbance spectrum of the sample was collected between 400 – 800 nm. A broad absorbance band in the visible region with a λ_{max} = 540 nm (ε = 3030 ± 100 L mol^{-1} cm^{-1}) was clearly visible. This is typical of LS Fe(II) complexes and is due to the metal-to-ligand charge transfer (MLCT) transition.[280] The temperature was then increased in 1 K increments to reach a final temperature of 353 K and spectra were collected at each temperature once thermally equilibrated. As the temperature increased a decrease in the absorbance of the 540 nm band was observed, with a tight isosbestic point at 425 nm, consistent with a thermal spin crossover from the [LS-LS] state to the [HS-HS] state. Combined spectra are shown in **Fig 2.4.8**. Gradual SCO processes in solution may occur over a range of 150 K and as such the full LS to HS crossover is not observed in the 80 K range employed in this experiment. This is illustrated in **Fig 2.4.8-Inset** with no plateaus in absorbance being observed.

From these results it was possible to ascertain the thermodynamic parameters for the partial SCO in solution and fitting the concentration parameters to **Equation 2.4.7**.[165,289,290] Calculations to this end were performed and ΔH = 30.17 kJ mol^{-1}, ΔS = 96.02 kJ mol^{-1}, and $T_{1/2}$ = 314 K were found to give the best fit. The derivation of **Equation 2.4.7** is provided as supplementary information in **A-IV.1.1**. The fit was not as good as anticipated, with the extreme temperature values at either end of the experiment deviating from the fit curve. It is postulated that as both ΔS and ΔH are dependent on temperature, at the extremes in the experiment the temperature dependence plays a more significant role.

For a species without any ligand dissociation behaviour the ΔH values typically do not exceed 30 kJ mol^{-1} and have ΔS values below 130 kJ mol^{-1}.[165] The ΔH for **2.5** at 30.17 kJ mol^{-1} is within experimental error to this value and ΔH may be increased due to the dinuclear nature of the complex. Indeed, it was reported by Purcell[291] and later Toftlund,[292,293] that torsional modes have a significant contribution to the SCO process. Encumbered torsional motion was postulated to result in higher energy SCO pathways. Given the helicate nature of **2.5** it is not surprising that the SCO centres do not twist as freely as comparable mononuclear systems, which may go some way to explain the thermodynamic parameters. Also important to note, is the possibility of ligand dissociation processes to be involved during the SCO process. Tight isosbestic points were observed in the UV-Visible experiment indicating the direct conversion of [LS-LS] species into the [HS-HS] species.

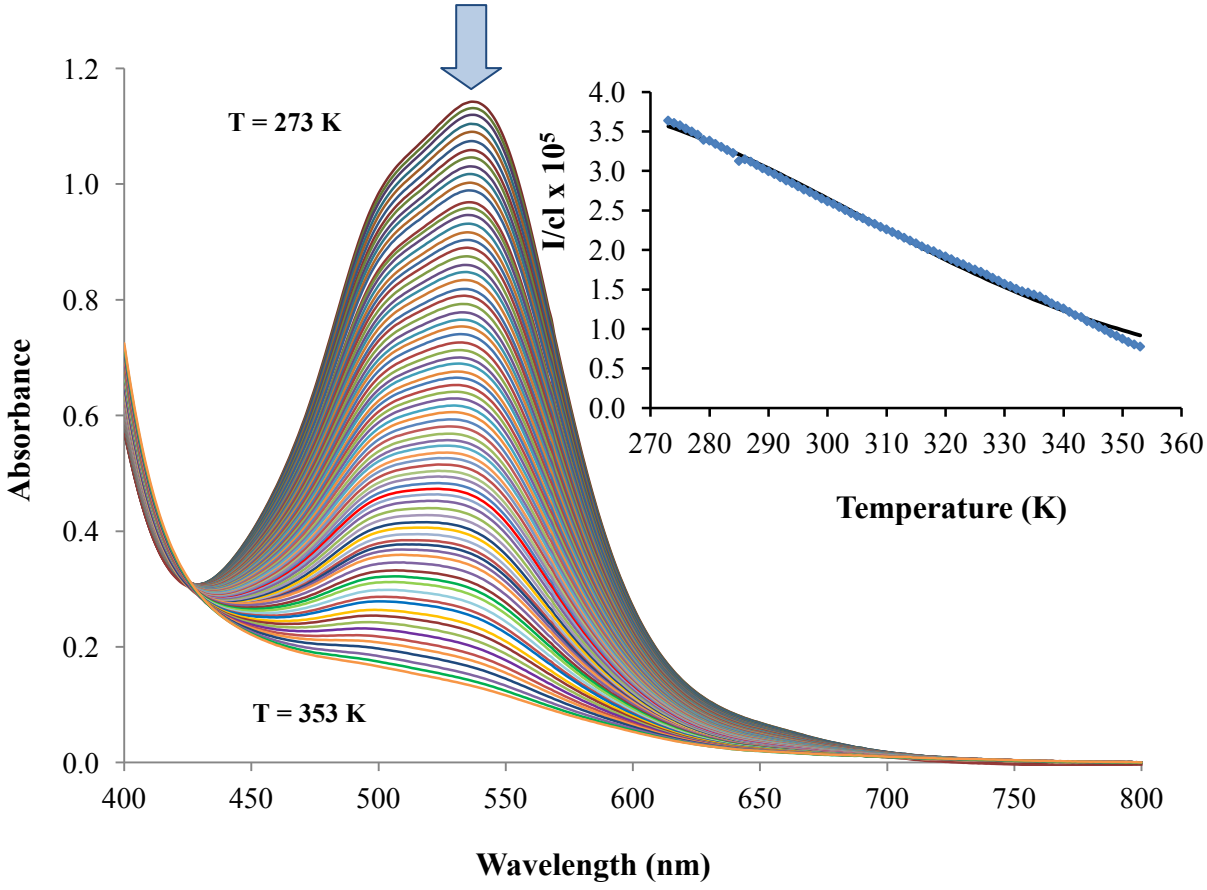

Fig 2.4.8 *Graph showing the temperature dependence of complex* ***2.5*** *(3.773 x 10^{-4} mol L^{-1}nitromethane).* ***Inset****: Integrated absorbance data (****blue****) vs. temperature with curve showing fit (****black****).*

$$\frac{A}{cl} = \frac{\varepsilon_L[exp(\Delta S/R)]^{T_{1/2}/T} + \varepsilon_H exp(\Delta S/R)}{[exp(\Delta S/R)]^{T_{1/2}/T} + exp(\Delta S/R)}$$

Equation 2.4.7 *Definitions of parameters: A = Absorbance; c = total concentration of solution; l = path length (1 cm); $\varepsilon_L/\varepsilon_H$ = molar absorptivity coefficient for the LS and HS state respectively; S = entropy of the SCO; T = temperature; $T_{1/2}$ – temperature at which concentrations of HS and LS states are equal; R = gas constant 8.314 J mol^{-1} K$^{-.1}$*

*2.4.4 Variable Temperature Surface Reflectivity Measurements of **2.5** and **2.6***

Given the vivid thermochromic behaviour exhibited around room temperature by **2.5** in solution, variable temperature surface reflectivity measurements were performed on a microcrystalline sample of **2.5** to investigate the solid-state optical properties. Due to the intense dark colour of **2.5** the sample was diluted with solid $BaSO_4$. The first experiment measured the reflectivity during cooling from 270 K – 10 K with a scan rate of 4 K min^{-1}, followed by a return heating run at the same rate. The measurements were conducted under weak white-light irradiation of 0.4 mW cm^{-2} from the spectroscopic source. As the temperature decreased from 270 K to 10 K, there was a corresponding increase in the reflectivity of the near infrared region (NIR, > 800 nm) and decrease in the visible component (400 – 700 nm) resulting in tight isosbestic points about 459 nm and 758 nm. Selected reflectivity spectra as a function of temperature during cooling are illustrated in **Fig 2.4.8**. The return heating mode is provided as supplementary information in **A-IV.1.2a**. To better visualise this behaviour, the thermal evolution of the [LS-LS] state (illustrated by the reflectivity at 900 ± 5 nm; R_{900}) was analysed. At 270 K the reflectivity at 900 nm is 0.65 and increases with S-shaped behaviour typical of SCO, to a value of 0.75 as the temperature decreases to *ca.* 170 K. Further reductions in the temperature result in no change to R_{900}. The return heating run follows the same trace as the initial cooling run, indicative of reversible SCO behaviour (**A-IV.1.2b**).

Additional surface reflectivity measurements were also used to investigate potential light-induced SCO behaviour in **2.5**. The compound was cooled to 10 K and irradiated with white light for 80 minutes. The effect of the white light excitation was a decrease of R_{900} from 0.75 to 0.70 after the irradiation (**A-IV.1.2c**). In order to optimise these conditions, a series of light excitations using 14 different LED sources at wavelengths ranging from 365 to 1050 nm, were performed. During these experiments, the 530 nm light was found to be efficient. With these optimal parameters, the sample was cooled to 10 K and irradiated with 0.8 mW cm^{-2} green light (530 nm) for 80 minutes. After the irradiation, the sample showed a significant decrease in R_{900} from 0.76 to 0.69 consistent with LIESST behaviour. Thermal relaxation occurred as the sample was heated above 60 K (**Fig 2.4.9**). Despite the improved light-activation behaviour with green light, the initial

reflectivity value for the [HS-HS] species at 270 K (0.65) was not reached, even though the compound showed full light saturation behaviour within approximately 3 minutes of 530 nm irradiation (**A-IV.1.2d**).

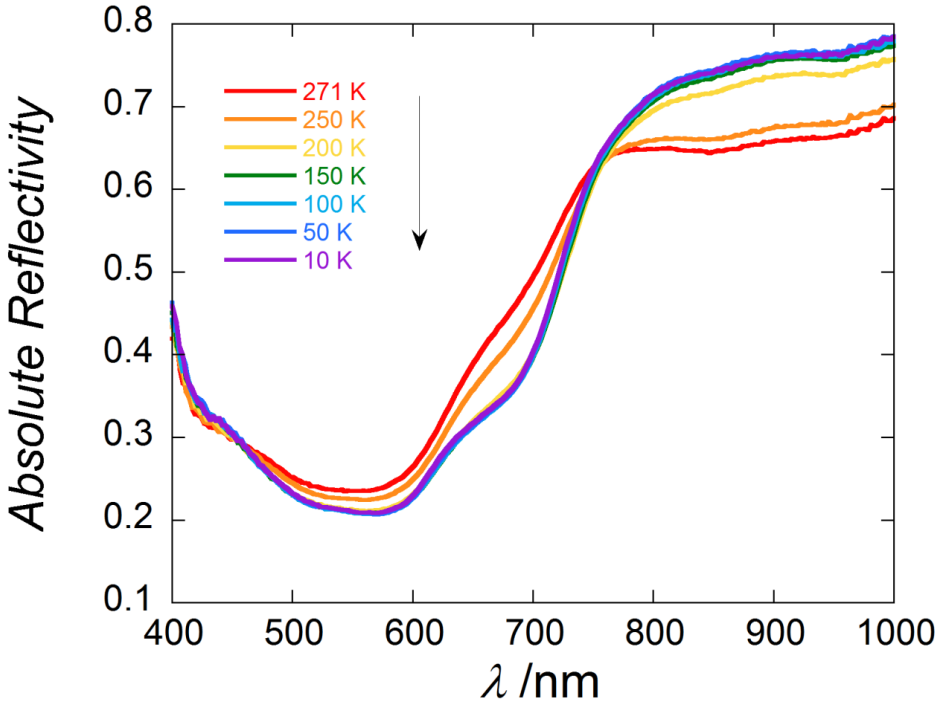

Fig 2.4.8 *Selected surface reflectivity measurements of* ***2.5*** *collected with a white light spectroscopic source (0.4 mW cm^{-2}) as a function of temperature during cooling mode between 270 – 10 K.*

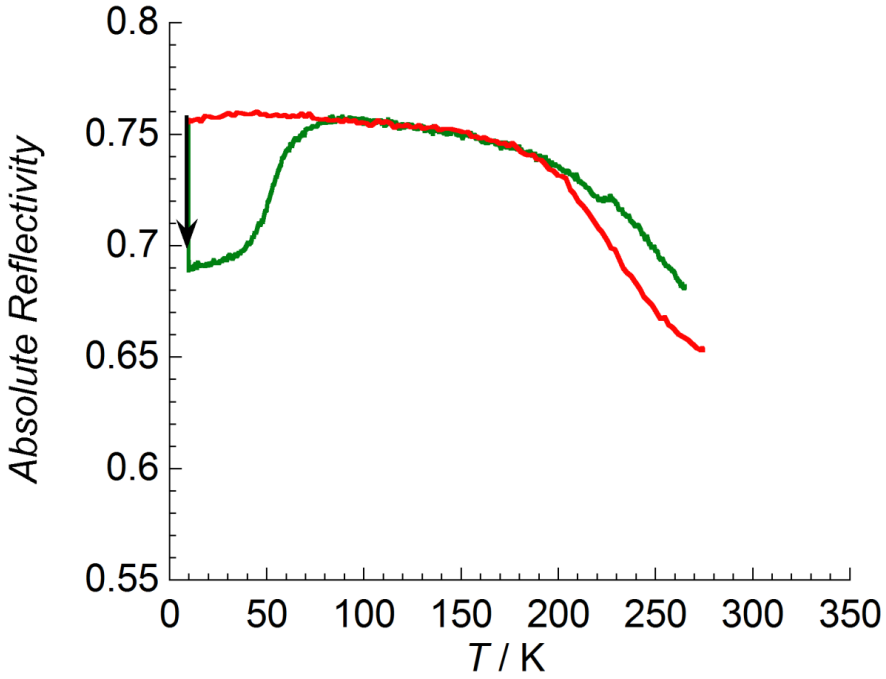

Fig 2.4.9 *Thermal evolution of the reflectivity signal recorded at λ = 900 nm ± 5 nm recorded during cooling mode, 270 – 10 K (**red trace**) and after green light irradiation (530nm, 0.8 mW cm^{-2}, 80 minutes) during heating mode, 10 – 270 K (**green trace**).*

As thermally induced SCO behaviour was observed crystallographically in **2.6**, variable temperature surface reflectivity measurements were performed to examine the SCO behaviour of **2.6** in the solid-state. The reflectivity of the compound was measured on a freshly filtered crystalline sample, in the temperature range from 10 K to 270 K with a scanning rate of 4 K min^{-1} in the presence of a 0.4 mW cm^{-2} white light source. As the temperature decreases during the cooling run (270 K to 10 K), the reflectivity of the NIR region increases as the reflectivity in the visible region decreases. This results in an isosbestic point around 760 nm, consistent with a transition from the [HS-HS] state to the [LS-LS] over the temperature range, with fully reversible behaviour. Selected reflectivity spectra, as a function of temperature (cooling), are illustrated in **Fig 2.4.10** (heating mode provided in **A-IV.1.3a**).

By probing the reflectivity at 900 nm, the thermal evolution of the [LS-LS] state can be monitored. As the sample cooled from 270 K to approximately 220 K, the reflectivity at 900 nm (R_{900}) remained constant at 0.17. Further cooling resulted in an increase in R_{900} to a maximum value of 0.23 at approximately 80 K, a signature of the thermal spin crossover phenomenon. The SCO occurs over a *ca.* 100 K range from 200 – 100 K. Inspection of R_{900} during the return heating run showed reversible SCO behaviour (**A-IV.1.3b**).

To investigate the effects of light on the SCO properties of **2.6**, the sample was cooled to 10 K and was then illuminated with white light. These experiments showed photo-excitation of the [LS-LS] state into the [HS-HS] state between 10 K and 100 K under white light irradiation. In order to fully probe this effect, the sample was irradiated with white light for 5 hours. After this period of time the sample was fully excited into the [HS-HS] state (**A-IV.3c**).

In a subsequent experiment the same sample as previously studied was irradiated with light of 14 different LED sources to investigate the optimal excitation wavelengths for **2.6**. From this experiment green light of 530 nm was identified (**A-IV.1.3d**). The sample was cooled to 10 K and excited with 530 nm light for 2 hours. After this time the spectra were measured and showed the excitation of the sample into the [HS-HS] state (**Fig 2.4.11**). There is a substantial increase in the excitation of the sample by 530 nm light than the excitation seen with white light under these conditions (**A-IV.1.3e**). Impressed by the photoexcitation of **2.6** a reverse LIESST experiment was completed where the sample was excited using 530 nm green light and then with near infrared light (wavelength 850 nm) of the same power. Unfortunately, under these conditions the sample showed no signs of reverse-LIESST behaviour with 850 nm light (**A-IV.1.3f**).

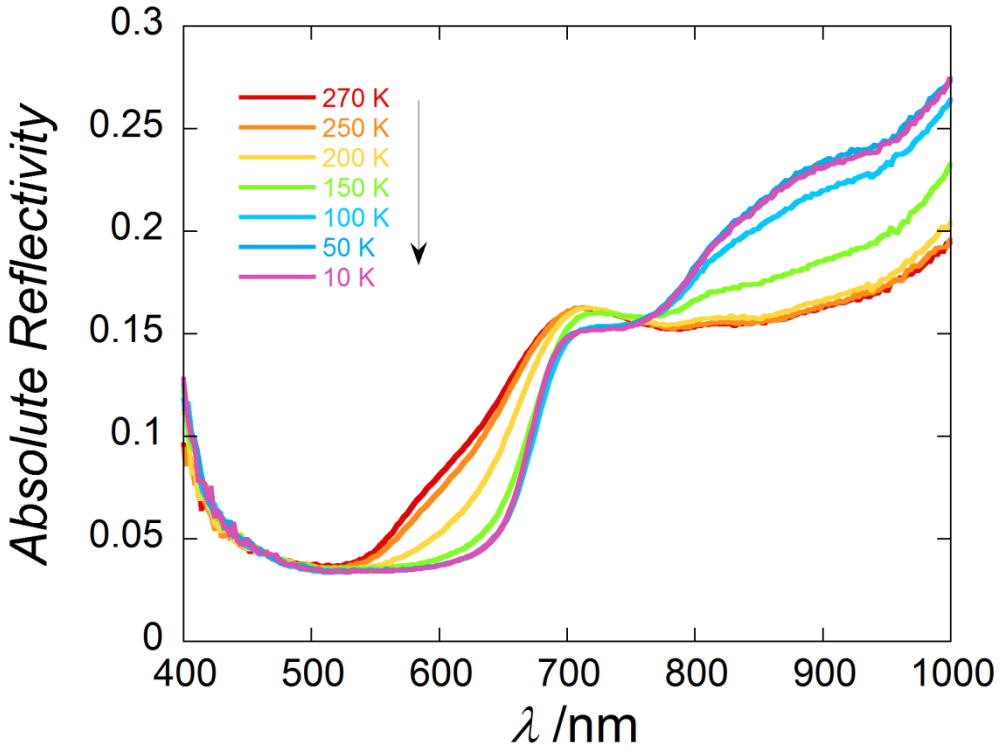

Fig 2.4.10 *Selected surface reflectivity measurement of complex* ***2.6*** *collected at a scan rate of 4 K min^{-1} with a white light spectroscopic source (0.4 mW cm^{-2}) as a function of temperature during cooling mode between 270 – 10 K.*

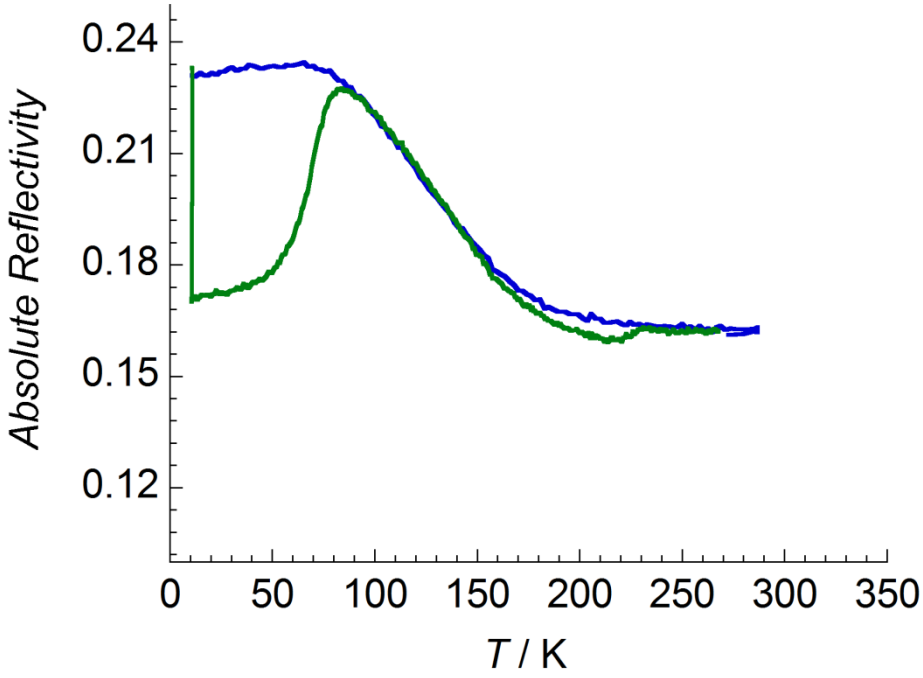

Fig 2 .4.11 *Thermal evolution of the reflectivity signal recorded at λ = 900 nm ± 5 nm recorded during cooling mode, 270 – 10 K (****blue trace****) and after green light irradiation (530nm, 0.8 mW cm^{-2}, 240 minutes) during heating mode, 10 – 270 K (****green trace****).*

*2.4.5 Magnetic Susceptibility Measurements of Complexes **2.5** and **2.6***

To further elucidate the nature of the SCO behaviour in the solid-state, dc magnetic susceptibility experiments were undertaken on **2.5** and **2.6**. Given the significant solvent content within the crystal lattice for both samples, freshly filtered crystalline samples were used and a small amount of the mother liquor was carefully added to the crystalline sample to prevent solvent loss. The magnetic susceptibilities were measured within the temperature range of 1.8 – 300 K.

The variable temperature magnetic susceptibility for **2.5** was measured with a χT product of 0.07 cm^3 K mol^{-1} at 50 K, consistent with the [LS-LS] species with a slight paramagnetic impurity estimated at *ca.* 1% of the total sample. As the temperature increased the χT product remained constant up to a temperature of 240 K at which point the χT product began to increase up to a maximum value of 1.07 cm^3 K mol^{-1} at 300 K, indicating the initiation of SCO. A maximum χT value of 1.07 cm^3 K mol^{-1} is consistent with *ca.* 18% conversion to the HS state at room temperature. The sample was subsequently cooled and the SCO behaviour was shown to be reversible. (**Fig 2.4.12**)

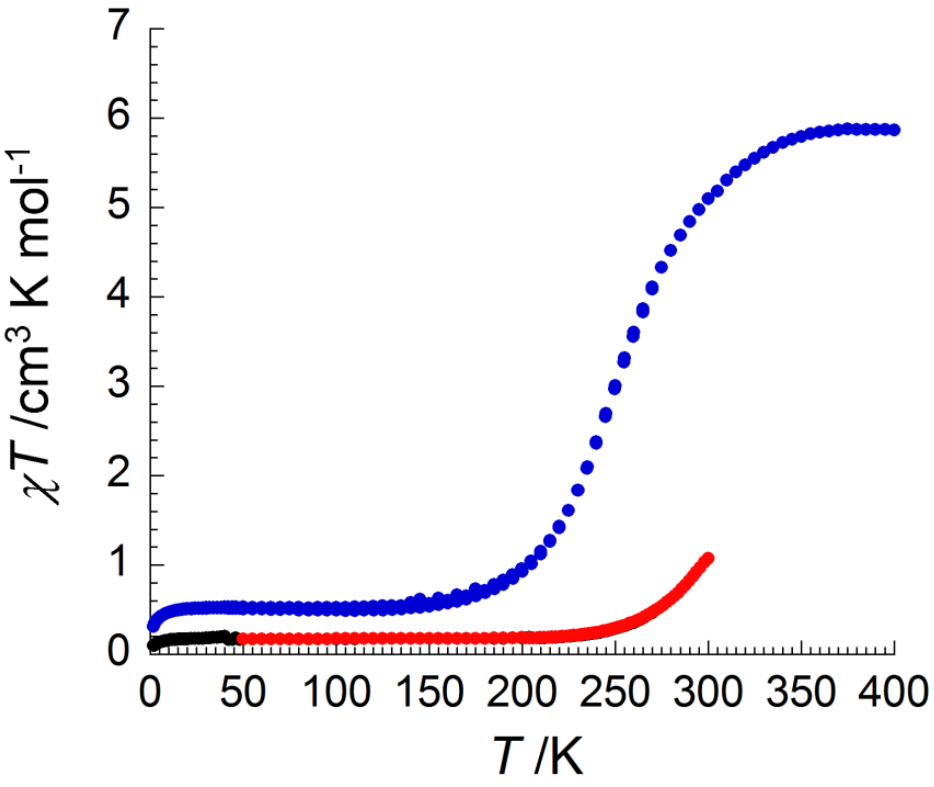

***Fig 2.4.12** Magnetic susceptibility measurements of complex **2.5** (crystals layered with a small amount of mother liquor) under a magnetic field of 1T. Red circles – initial heating mode 50 K – 300 K; black circles – cooling mode 300 K – 1.8 K, Blue circles – cooling mode dried sample (M_R-Dried 1726.4 g mol^{-1}).*

As **2.5** was prone to solvent loss, variable temperature magnetic susceptibility measurements were performed after the sample had been dried under vacuum at 50 °C overnight. The dried sample shows a significant shift in the magnetic susceptibility curve to give a SCO process with a $T_{1/2}$ of *ca.* 250 K. (**Fig 2.4.12**)

The magnetic susceptibility of complex **2.6** was also measured due to the promising results from the solid state crystallography and surface reflectivity measurements. Once again due to the considerable solvent content of the crystals, the crystalline sample was prepared in a sealed straw with a small amount of the mother liquor to limit solvent loss. The magnetic susceptibility of **2.6** was measured as the sample cooled to 1.8 K under a magnetic field of 0.1 T. At 270 K the χT product is 6.6 cm^3 K mol^{-1}, consistent with the [HS-HS] state and remains constant down to a temperature of *ca.* 200 K. As the sample is further cooled, the χT product decreases to a minimum value of *ca.* 0.6 cm^3 K mol^{-1} following a gradual SCO process with a $T_{1/2}$ of *ca.* 140 K. The χT product for the [LS-LS] state of **2.6** is expected to be zero, the residual component is likely to be due to a small paramagnetic impurity within the crystalline sample. This impurity is estimated at 8% of the Fe(II) centres within the sample. The SCO behaviour is reversible with the heating run following the same curve as the cooling mode. Given the contraction in the coordination spheres of both Fe(II) centres in the crystal structure at 120 K, and the crystallographically inequivalent nature of both Fe(II) centres, a gradual spin transition where the [LS-LS] state is not fully occupied at 120 K, is consistent with the crystallographic evidence (**Fig 2.4.13**).

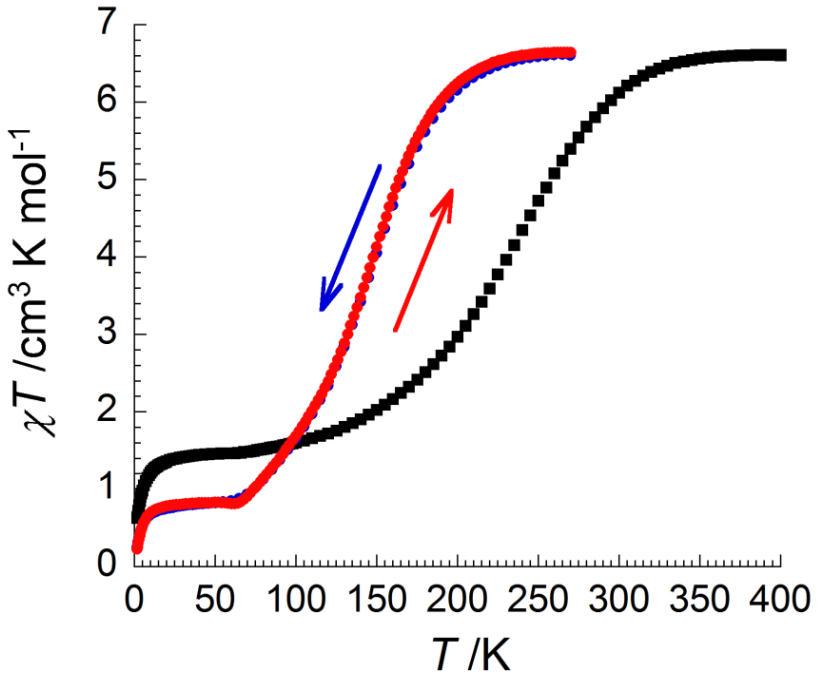

Fig 2.4.13 *Magnetic susceptibility measurements of* ***2.6*** *using crystals layered with a small amount of mother liquor (cooling mode at 0.1 T –* ***blue****; heating mode at 1 T –* ***red****) and after drying at 50°C under vacuum for 7 days (* M_R*-Dried 1726.4 g* mol^{-1} ***black squares****).*

As with **2.5**, the sample was dried (50 °C under vacuum, seven days) to analyse the changes in SCO behaviour following solvent loss. The dried sample shows an increase in the SCO curve, pushing the $T_{1/2}$ to approximately 250 K.

*2.4.6 Photomagnetic Measurements for **2.5** and **2.6***

Given the magnetic susceptibility and surface reflectivity data, the photomagnetic properties of the complex **2.5** were investigated. A crystalline sample of **2.5** was cooled to 10 K, where the χT product decreased to almost zero consistent with the data from the previous experiments. The compound was then irradiated with white light (3 mW cm^{-2}) for 4 and a half hours after which time the χT value had increased slightly (*ca.* 0.35 cm^3 K mol^{-1}). Further heating of the compound showed a relaxation of the excited state back into the LS state above approximately 60 K. The photomagnetic activation of **2.5** is illustrated in **Fig 2.4.14** below. Attempts to improve the photoexcitation by altering the light source and power were unsuccessful. It is likely that the photoexcitation is situated on the outer edges of the bulk sample and this type of photoexcitation has been observed previously in related compounds.[219]

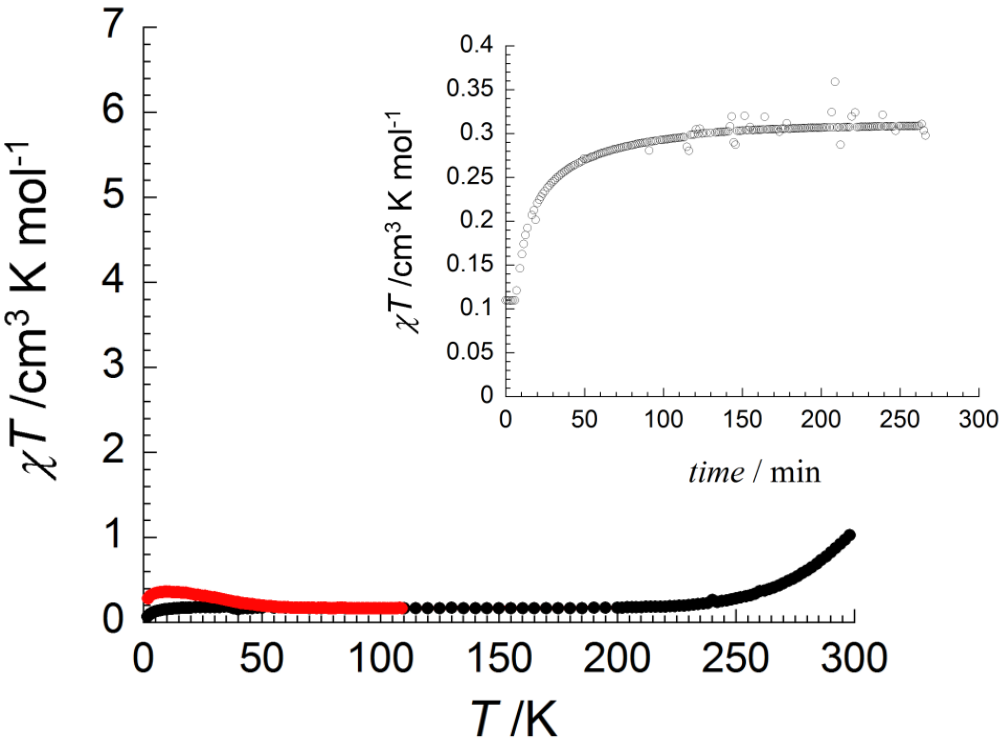

Fig 2.4.14 *χT vs. T plot for complex **2.5** after white light irradiation for a period of 270 minutes (**red dots**) and in the dark (**black dots**). Time dependence on the χT product with white light irradiation at 10 K under 1T (**Inset**). Scan rate 0.4 K min^{-1}; Light irradiation, 3 mW cm^{-2}.*

Photomagnetic measurements were also performed on complex **2.6**. The compound was cooled to 10 K in a SQUID magnetometer at a rate of 0.4 K min^{-1} under a magnetic field strength of 1 T and dark conditions. Subsequently the sample was irradiated with 3 mW cm^{-2} white light for 3 hours to ensure saturation of the compound. The sample showed photoexcitation under these conditions with approximately 70% conversion of the Fe(II) centres to the [HS-HS] state. As the sample was heated at 0.4 K min^{-1}, the excited species undergoes thermal relaxation back into the [LS-LS] state with complete relaxation of the sample by 70 K (**Fig 2.4.15**). Although surface reflectivity measurements show full excitation of the compound into the high spin state, this was not observed in the photomagnetic measurements. The exact cause of this is uncertain however, the photoactivation was shown to be considerably improved under a green light source, which was not available during the photomagnetic measurements. It may be that the excitation into the [HS-HS] state would be possible with green light irradiation. It is also possible that only a portion of the Fe(II) centres within the complex undergo photoexcitation due to inadequate penetration of light into the bulk sample during the photomagnetic measurements leaving a pocket of unexcited sample.

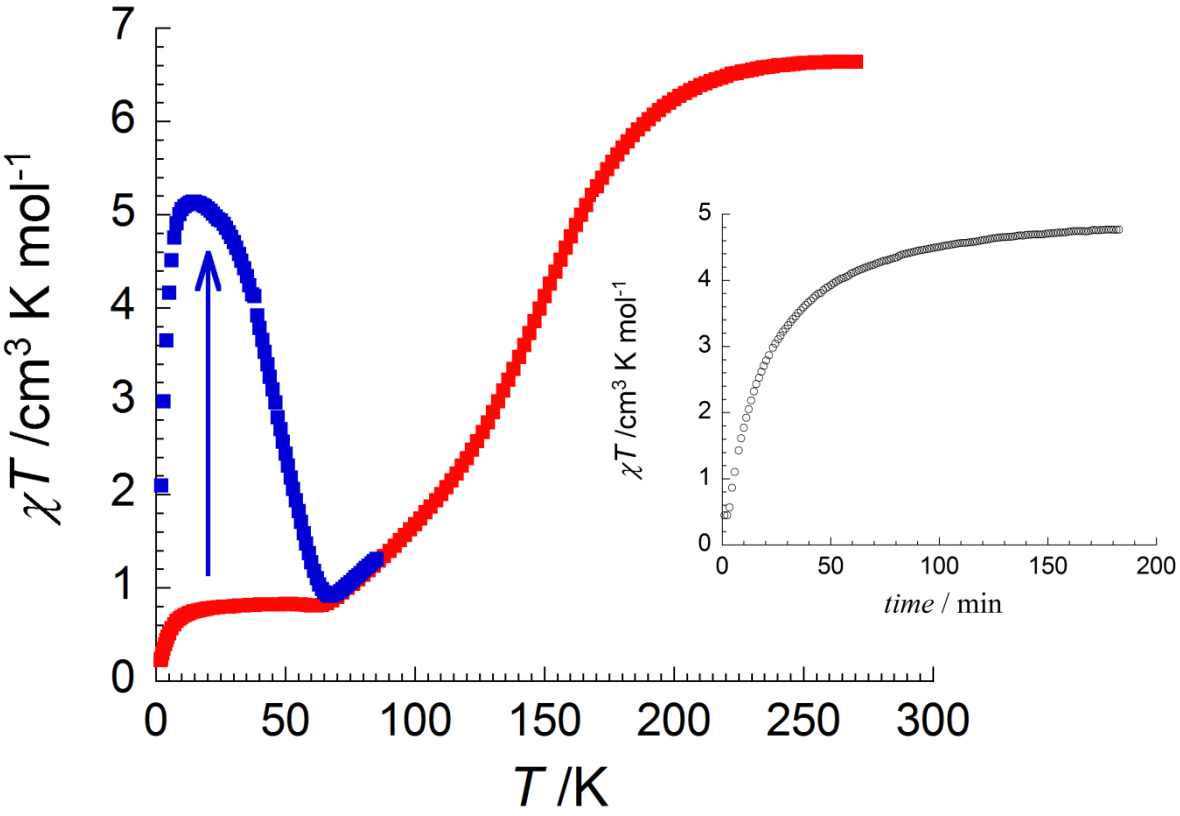

Fig 2.4.15 *χT vs. T data for complex* ***2.6*** *measured after white light irradiation 180 minutes in the heating mode (**blue dots**) and during cooling mode in the dark (**red dots**). Time dependence on the χT product with white light irradiation at 10 K under 1T (**Inset**). Scan rate = 0.4 K* min^{-1}*;White light irradiation, 3 mW* cm^{-2}*.*

2.5 Discussion and Conclusions

From the analysis of complexes **2.4 – 2.6** above, several conclusions may be drawn in regards to their SCO behaviour. Firstly, it was pleasing to note that all three complexes share remarkably similar helicate properties, despite each complex crystallising in a different space group. By altering the coordinating functionality from pyridylimine (**2.4**) to 2-imidazolylimine (**2.5**) to 4-imidazolylimine (**2.6**) the SCO properties of these three materials were shown to vary significantly. No evidence of SCO behaviour was observed for complex **2.4** and was found to be exclusively [LS-LS] as expected. Both **2.5** and **2.6** were found to undergo SCO; excitingly, for complex **2.5** this occurs above room temperature in both solution and the solid state with a weak LIESST effect. Complex **2.6** undergoes gradual SCO with the $T_{1/2}$ centred at a lower temperature of *ca.* 140 K with partial LIESST-behaviour observed.

The differing LIESST behaviour between these two complexes is consistent with the inverse energy gap law, where compounds with higher $T_{1/2}$ values (and therefore a more stable LS state) have fast thermal relaxation into the LS state even at 10 K. This leads to weak LIESST behaviour when compared to similar compounds with lower $T_{1/2}$ values, as shown with **2.5** and **2.6**.

Careful analysis of the supramolecular interactions present within the crystalline state revealed similar motifs between the three structures. The incorporation of a hydrogen bond donor motif in the form of the imidazole N-H group did enable hydrogen bonding networks to form within the solid state for both complexes **2.5** and **2.6**. In both cases, the BF_4^- counter anion acts as the hydrogen bond acceptor and helicate cations are linked through these interactions. The interactions between helicates in complex **2.5** largely consisted of 1D-hydrogen bonding chains of helicate cations that lie orthogonal to one another where two helicates of opposite handedness cross over one another. This particular crystal packing motif results in a solvent containing channel of approximately 6 x 6 $Å^3$ which lies parallel to the crystallographic c-axis.

The interhelical interactions in a crystalline sample of complex **2.6** are extensive with both edge-to-face C-H$\cdots\pi$ interactions forming a 2D network and hydrogen bonding interactions extended that network into the third dimension. These abundant interactions however, do not cause an abrupt spin transition to occur with the SCO behaviour in complex **2.6** taking place over an approximately 100 K temperature range (200 – 100 K). This may be due to the hydrogen-bonding and C-H$\cdots\pi$ interactions being simply too far away from the SCO centre and as such subtle adjustments occur within the ligand to accommodate the expanded HS coordination sphere. The solvent containing pockets within the crystal may also allow the helicates to accommodate the change in spin state without communicating the change throughout the crystal lattice. In light of these complex interactions, altering the SCO behaviour of these systems through anion modification is likely to be highly advantageous.

Other important solid-state interactions effecting SCO were apparent when both **2.5** and **2.6** were dried. Interestingly, the dried compounds displayed opposite behaviour with the SCO curve in **2.5** shifting to lower temperatures indicating that the [HS-HS] state is favoured in the dried state, whereas in **2.6** the dried compound SCO curve moves to higher temperatures consistent with stabilisation of the [LS-LS] state. Unfortunately attempts to structurally analyse dried samples through single crystal X-ray diffraction were unsuccessful with both complexes showing crystal instability even under gentle drying procedures. Given the pockets of solvent molecules within the crystal lattice of **2.6** there is no simple method of egress of the solvent, suggesting that fracturing of the crystal lattice occurs as the solvent is lost. This crystal "fracturing" may in fact allow neighbouring helicates to pack more closely together causing a relativity higher density than in the solvated phase. This higher density about the SCO centres would destabilise the [HS-HS] state, coincidentally stabilising the [LS-LS] state and pushing the SCO curve to higher temperatures. **2.6-Dried** also undergoes a more gradual SCO process, suggesting that the intermolecular interactions within the solid-state are minimised during the drying procedure. In contrast, **2.5** contains solvent accessible channels which promote a simple method of egress of solvent molecules from the crystal lattice, however, whether the lattice structure remains intact upon solvent loss is unclear at this stage.

This rapid solvent loss was also observed during the surface reflectivity measurements on **2.5**. A comparison between the reflectivity measurements and the initial magnetic susceptibility measurements do not agree, presumably due to solvent loss over the course of the experiment. Indeed, the reflectivity measurements show a shift in the SCO to lower temperatures similar to the magnetic behaviour observed in the dried sample. **2.6** showed no such loss of solvent during the surface reflectivity experiments with the magnetic susceptibility and surface reflectivity being in good agreement.

The room temperature SCO behaviour of complex **2.5** warrants further discussion. The *tris*-[2'-imidazolylimine] coordination sphere has been previously shown to give rise to SCO materials with $T_{1/2}$ values around 150 K[120,218] and as such an increase in the $T_{1/2}$ to above room temperature is particularly fascinating. Although SCO behaviour is determinant upon a number of factors, some potential interactions can be postulated to cause the stabilisation of the [LS-LS] state for this system. Careful investigation of the helicate structure in the solid state reveals six edge-to-face C-H$\cdots\pi$ interactions, which are present in all three helicates with similar distances. It is tempting to suggest that it is these interactions which act to stabilise the [LS-LS] species resulting in a shift in the $T_{1/2}$ to higher temperatures. That the SCO behaviour is similar in the solution studies also suggests that it is interactions within the helicate that are stabilising the [LS-LS] state, rather than interhelical interactions relating to crystal packing interactions.

In conclusion, the self-assembly of helicate species provides a simple and effective means to access materials suitable for SCO. The two imidazolylimine isomeric coordination spheres provide both interesting supramolecular interactions within the solid state and also maintain the ideal ligand field for SCO behaviour. Although in this study only the BF_4^- counter anion was used for ease of comparison, further studies into the effects of differing anions on these systems would be beneficial.

CHAPTER THREE

Partial Spin Crossover Behaviour in an Fe(II) Dinuclear Triple Helicate

3.1 Introduction

Dinuclear helicates have been under-represented in the literature for spin crossover (SCO) compounds compared with the significant volume of mononuclear compounds that display SCO behaviour. Previous work within the Kruger group showcased the formation of an Fe(II) dinuclear triple helicate $[Fe_2(\mathbf{L3.1})_3](ClO_4)_4 \cdot 2CH_3CN$ (**3.2·CH$_3$CN**) which displayed asymmetric SCO from the [HS-HS] state into the [LS-LS] state with a $T_{1/2}$ of 158 K.[120] The structure for this compound was elucidated though single crystal X-ray diffraction and was found to consist of three ligands connecting two Fe(II) centres where the ligands twist about the Fe-Fe axis giving rise to the helical nature of this compound. At the data collection temperature of 150 K the coordination bond lengths about the Fe(II) centres were 2.00(2) Å Fe1 and 1.99(2) Å for Fe(II) giving rise to a formally [LS-LS] species. Careful investigation of the crystal lattice revealed no significant interhelical interactions but the compound did exhibit some intrahelical interactions of the formation of C-H···π bonds between four of the six phenyl rings within the helicate (**Fig 3.1.1**).

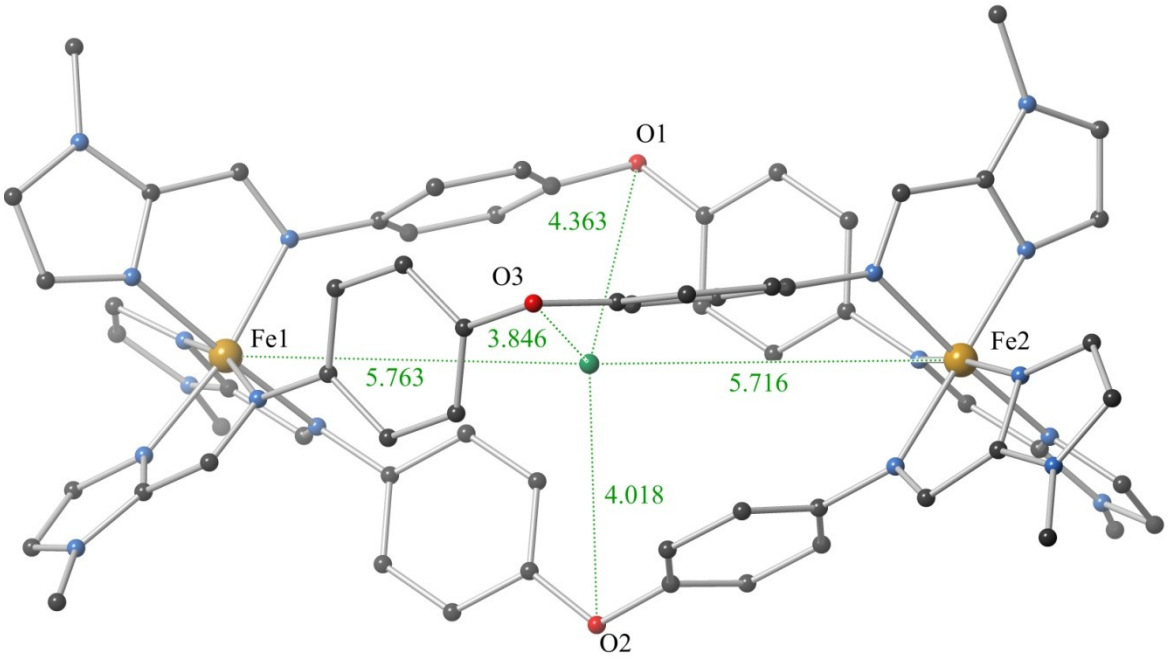

Fig 3.1.1 *Molecular structure for* ***3.2·CH$_3$CN*** *with pertinent geometric distances to the centre point (green sphere; distances in Å). Counter-anions, hydrogen atoms, and solvent molecules have been omitted for clarity.*

Magnetic susceptibility measurements were performed and confirmed the presence of SCO with some thermal hysteresis present between the cooling and heating phases; the cooling phase exhibiting a one-step SCO with a $T_{1/2}$ of 140 K and the return heating phase exhibiting two-step

SCO behaviour with $T_{1/2}$ values at 147 K and 166 K. This asymmetric SCO behaviour was found to be consistently reproducible. LIESST behaviour was also investigated through irradiating the sample with white light at 10 K. The compound was successfully excited into the [HS-HS] state. The thermal relaxation for this compound was interesting in that there appears to be meta-stable states as shown in **Fig 3.1.2**, however, this behaviour is not fully understood at this stage.

Interestingly, attempts to repeat the synthesis of this compound led to the isolation of a related compound containing different crystallised solvent content (**3.2·H_2O**) that showed unexpected and markedly different magnetic behaviour to that of **3.2·CH_3CN**. Comparisons between the two compounds will be discussed in depth within this chapter particularly focussing on potential structural features involved in the differing magnetic behaviour.

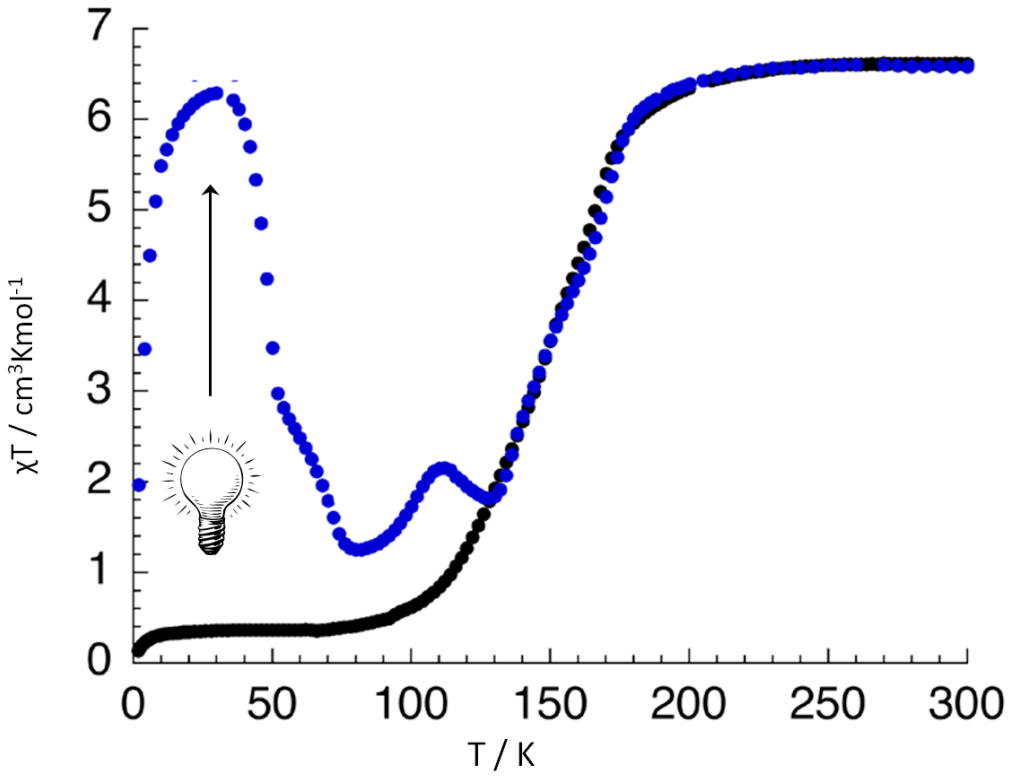

Fig 3.1.2 *Variable temperature magnetic susceptibility measurements for* ***3.2·CH_3CN*** *during cooling (**black dots**) and after white light irradiation at 10 K (**blue dots**).*

3.2 Ligand Synthesis

The ligand **L3.1** was synthesised following the preparation provided by Kruger[120] with two equivalents of 1-methyl-imidazole-2-carboxaldehyde reacting with one equivalent of 4,4'-oxydianiline (**Scheme 3.2.1**). The methanol reaction solution was stirred at room temperature overnight to give a clear solution. The excess methanol solvent was removed *via* rotary evaporation to give a pale yellow oil which was subsequently dissolved in dichloromethane, dried over anhydrous $MgSO_4$ and the organic solvent removed *via* rotary evaporation. The ligand was precipitated by adding a small amount of acetonitrile to the oil to give the ligand as an off-white powder.

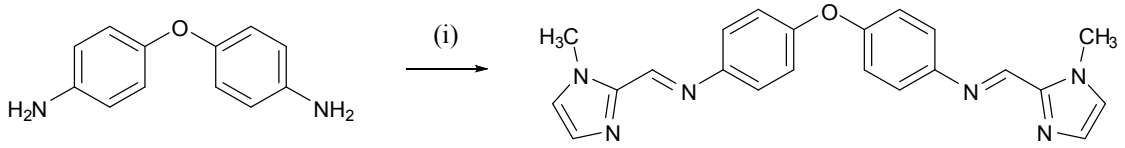

L3.1

Scheme 3.2.1 *Synthesis of ligand* ***L3.1****. Reagents and conditions: (i) 2 equivalents N-methyl-imidazole-2-carboxaldehyde, MeOH, room temperature 18 hrs.*

3.3 Synthesis and Structural Characterisation of $[Fe_2(3.1)_3](ClO_4)_4 \cdot xH_2O$ – $3.2 \cdot H_2O$

Thin red needle crystals suitable for X-ray structural analysis *via* synchrotron radiation, were synthesised through a slow diffusion of diethyl ether into an acetonitrile solution containing three equivalents of the ligand with two equivalents of $Fe(ClO_4)_2 \cdot 6H_2O$. As anticipated, the structure of **$3.2 \cdot H_2O$** consists of three crystallographically unique ligands coordinated about two pseudo-octahedral Fe(II) centres to form a dinuclear triple helicate. Both enantiomers of the helicate are expressed within the lattice generating a racemic crystal. Initial comparisons between the two helicates, **$3.2 \cdot CH_3CN$** and **$3.2 \cdot H_2O$**, show few structural differences. Both helicates consist of three crystallographically unique ligands connecting the two Fe(II) centres through the coordinating imine and imidazole nitrogen atoms. The intra-helical Fe-Fe distance of 11.45(3) Å is the same in both helices and the helical twist of the ligands about the Fe-Fe axis in **$3.2 \cdot H_2O$** is approximately 171° with a range of torsion angles between 170.0(8) and 172.2(8)° measured between the N_{imid}-Fe bonds at either end of the coordinating ligand. This is slightly less than the helical twist observed in **$3.2 \cdot CH_3CN$** with an average value of *ca.* 178° (ranging from 175.0(2) to

179.1°). The molecular structure of **3.2·H_2O** is shown below in **Fig 3.3.1**. Along with the greater helical twist in **3.2·CH_3CN** there are other subtle deviations between the two structures. Four of the phenyl rings within both structures twist in order to optimise edge-to-face C-H···π interactions however, these are generally weaker in **3.2·H_2O** as illustrated in **Fig 3.3.2**. The phenyl rings in **3.2·H_2O** do not undergo as severe twisting as occurs in **3.2·CH_3CN** with imine-phenyl torsion angles lying within the range 35(3) – 66(2)° for **3.2·H_2O** compared with 55.6(4) – 74.4(4)° in **3.2·CH_3CN**. Presumably, other stabilising forces are at play in **3.2·H_2O**. Indeed, perusal of the intermolecular interactions about the helicate reveals that neighbouring phenyl rings in adjacent complexes align, appearing to optimise three face-to-face π-π stacking interactions. On closer inspection, two of the interactions have centroid-centroid distances of 4.080(15) Å, too long to be considered as providing any significant attractive interaction. However, the third interaction with a centroid-centroid distance of 3.606(17) Å and a mean interplanar angle of 0.0(15)°, is indicative of a stabilising offset face-to-face π-π interaction. There are no corresponding interhelical interactions within the crystal lattice of **3.2·CH_3CN**.

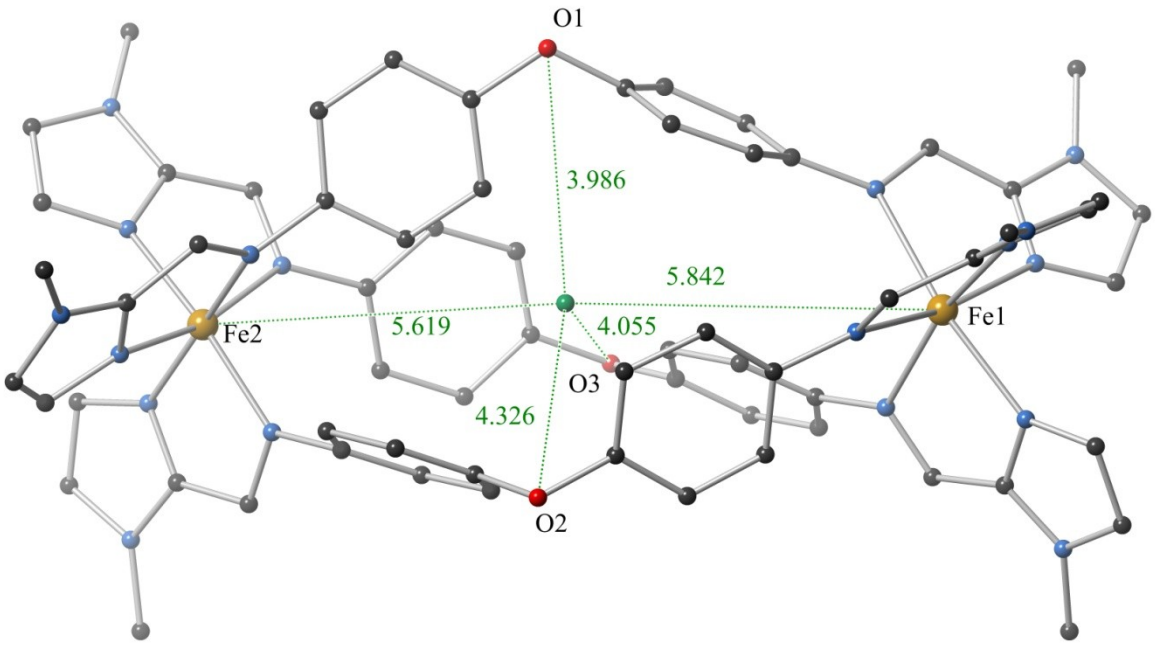

Fig 3.3.1 *Molecular structure scheme for **3.2·H_2O** showing pertinent geometric distances to the centre point (green sphere; all distances in Å). Hydrogen atoms, solvent molecules and counter-anions have been omitted for clarity.*

Comparison of the Fe-N_6 coordination sphere in both **3.2·CH_3CN** and **3.2·H_2O** reveals contrasting spin behaviour in the two complexes. At 150 K both Fe(II) centres in **3.2·CH_3CN** are in the LS state with an average coordination bond length of *ca.* 2.00 Å and 1.99 Å for Fe1 and Fe2

respectively. Conversely, in **3.2·H_2O** one Fe(II) centre remains in the HS state with average coordination bond lengths of *ca.* 2.18 Å and 1.96 Å for Fe1 and Fe2 respectively. Selected geometric parameters for the Fe-N coordination sphere are provided in **Table 3.3.3**. Examination of the crystal lattice interactions in **3.2·H_2O** reveals that two helicates of opposite handedness "pair up" with both the HS Fe(II) centres stacking on top of one another, shifting the helicates sideways relative to each other, compared with similar packing modes in **3.2·CH_3CN** (**Fig 3.3.4**). The face-to-face π-π interaction discussed previously connects the two helicates and it is tempting to suggest that it is this π-π interaction that effectively holds one of the Fe(II) centres in the HS state. The other Fe(II) centre is not involved in any interactions with adjacent helicates and as such is free to contract into the LS state forming the [LS-HS] species at 150 K. In **3.2·CH_3CN** adjacent helicates are situated in line with each other. As discussed previously there are no apparent inter-helicate interactions involved in **3.2·CH_3CN** and as such both Fe(II) centres are able to freely contract into the LS state.

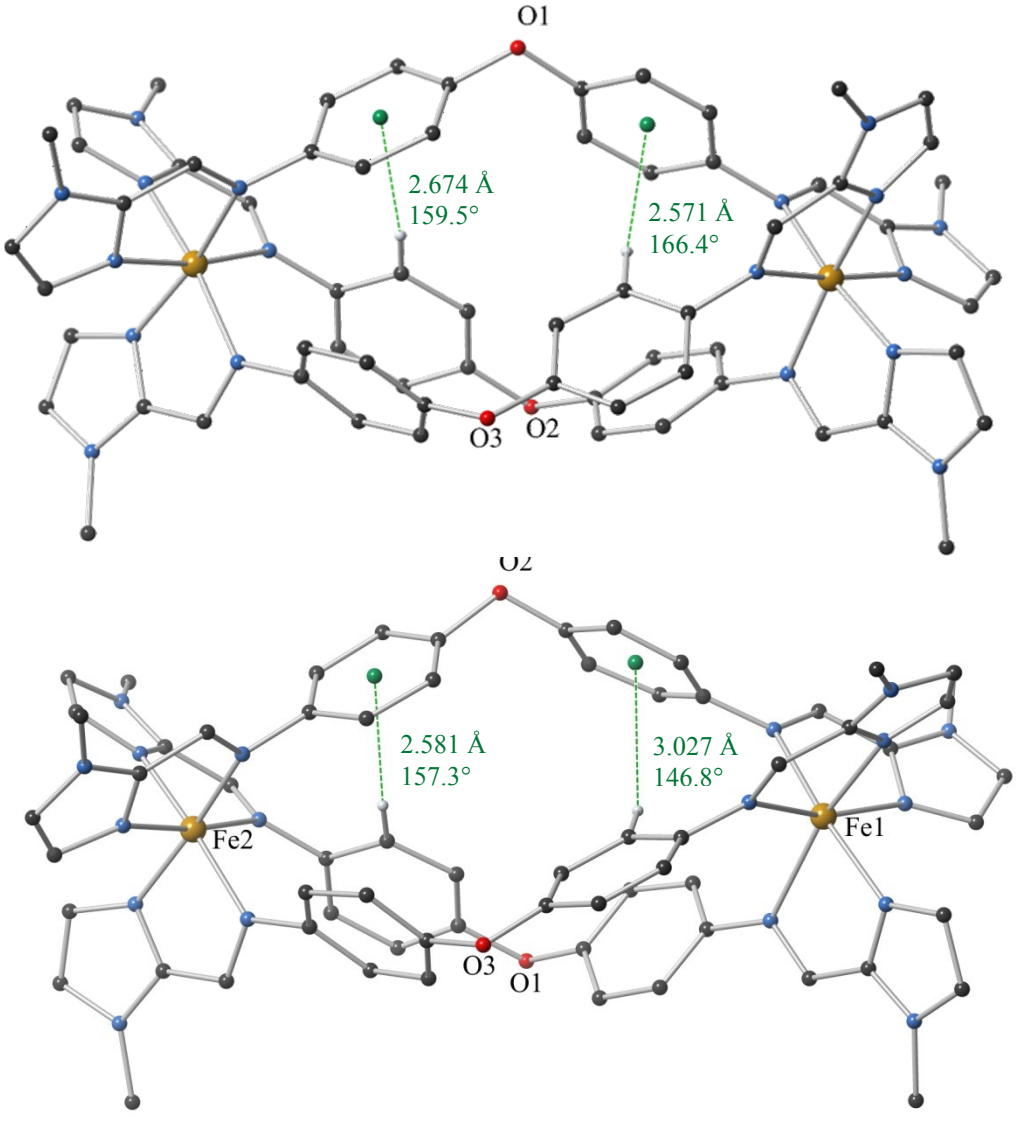

Fig 3.3.2 *Selected intramolecular C-H···π interactions in* ***3.2·CH_3CN (top)*** *and* ***3.2·H_2O (bottom)****.*

The influence of the different solvents within each crystal lattice warrants further discussion. The data for both complexes were solved and refined in the related monoclinic space groups $P2_1/c$ and $P2_1/n$ for **3.2·H$_2$O** and **3.2·CH$_3$CN** respectively. Crystal packing effects lead to some variations between the two structures, in particular the presence of solvent containing channels down the crystallographic c-axis in **3.2·H$_2$O**.

Although the data collected for **3.2·H$_2$O** was of relatively poor quality due to very thin needle crystals, the residual electron density within the crystal lattice were assigned as partially occupied water molecules over four sites. Two of the sites were refined with 50% occupancy, with the remaining two sites refined as having 25% occupancy. Given that the water solvent molecules form a believable hydrogen bonding network with the perchlorate counter-anions, that if fully occupied would have the form $(ClO_4)_2(H_2O)_4$. Further analysis on the compound *via* thermogravimetric and microanalyses were consistent with the hydrated compound.

When both structures are viewed down their respective crystallographic b-axes the difference in the packing of both of these compounds is apparent. In **3.2·CH$_3$CN** the helicate cations overlay each other down the b-axis whereas in **3.2·H$_2$O** the helicates pack in order to optimise the face-to-face π-π interaction and so are displaced from one another. The water molecules in **3.2·H$_2$O** are situated in channels that run along the crystallographic c-axis which goes some way in explaining the variable nature of the water within this structure. Water molecules have a mode of egress into and out of the structure with little alteration to the rest of the crystal lattice. Comparisons in crystal packing between the two complexes are illustrated in **Fig 3.3.5 – Fig 3.3.7**.

Compound	**3.2·CH$_3$CN**		**3.2·H$_2$O**	
Temperature	150 K		150 K	
Space Group	$P2_1/n$		$P2_1/c$	
Spin State	[LS-LS]		[HS-LS]	
Av. Fe-N Bond Length (Å)	Fe1 2.00	Fe2 1.99	Fe1 2.18	Fe2 1.96
Σ (°)	65.2	64.2	85.3	62.3
Φ (°)	4.12	4.09	5.39	4.23

Table 3.3.3 *Selected geometric parameters for complexes* ***3.2·CH$_3$CN*** *and* ***3.2·H$_2$O****.*

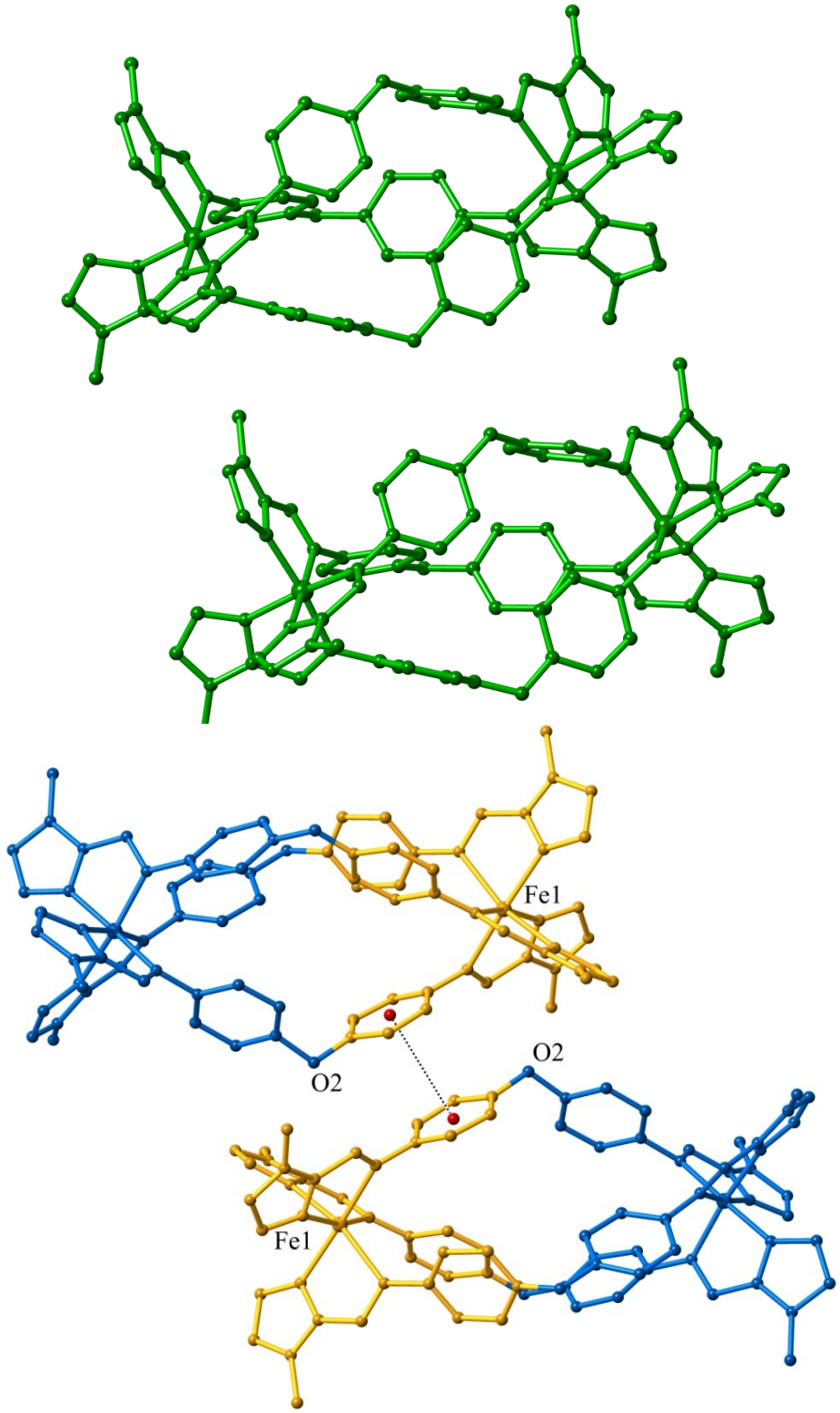

Fig 3.3.4 *Interhelical interactions in* ***3.2·CH$_3$CN*** *(above) and* ***3.2·H$_2$O*** *(below) with the HS helicate half coloured in yellow and the LS helicate half coloured in blue. Hydrogen atoms, counter-anions and solvent molecules have been omitted for clarity.*

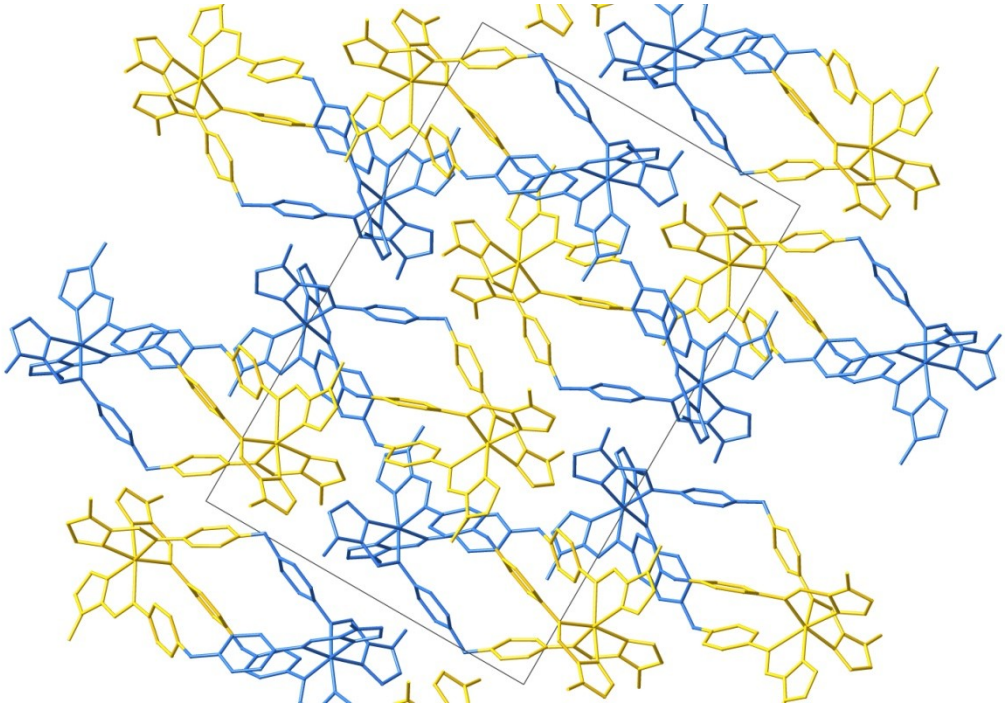

Fig 3.3.5 *Packing diagram of* ***3.2·H_2O*** *as viewed along the crystallographic a-axis and rotated so that helicates lie in the same direction as* ***3.2·CH_3CN*** *in* ***Fig 3.3.6*** *below. Hydrogen atoms, solvent molecules and counter-anions have been omitted for clarity.*

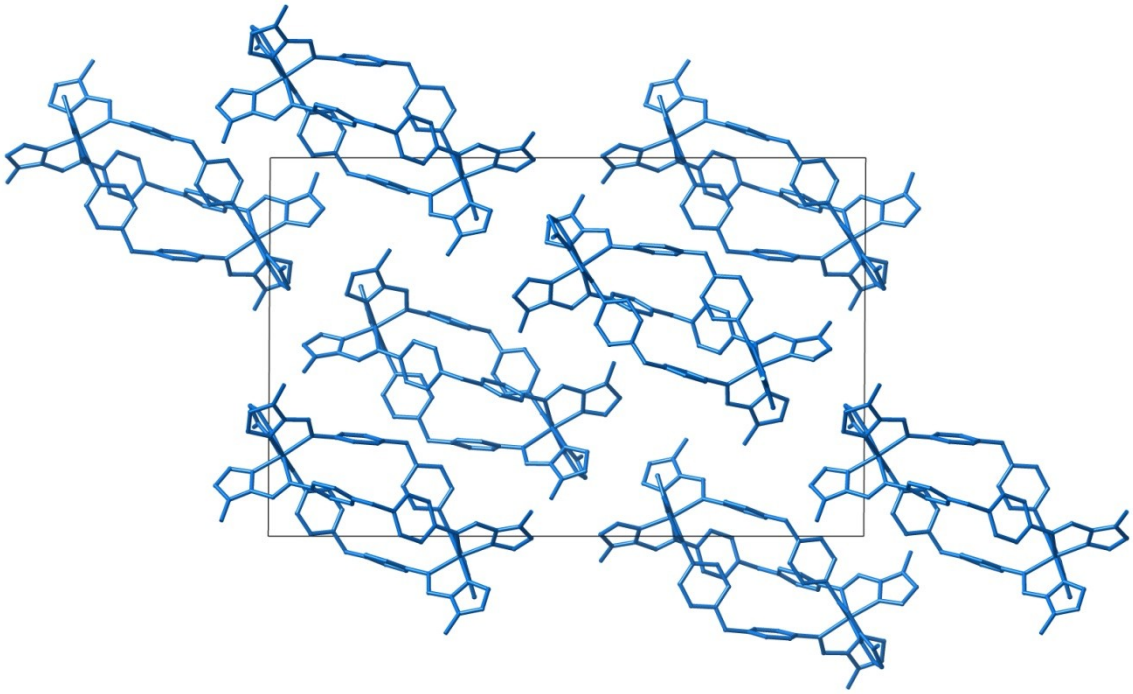

Fig 3.3.6 *Packing diagrams for* ***3.2·CH_3CN*** *viewed along the crystallographic b-axis to compared with* ***3.2·H_2O*** *(above). Hydrogen atoms, counter-anions and solvent molecules have been omitted for clarity.*

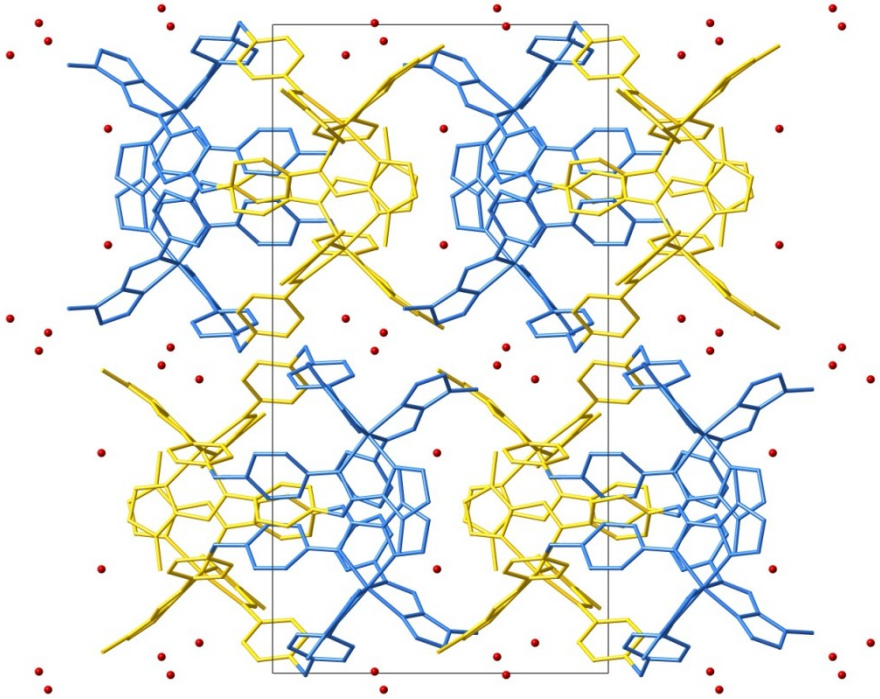

Fig 3.3.7 *Packing diagram for* ***3.2·H$_2$O*** *as viewed along the crystallographic c-axis showing water containing solvent channels. Water molecules are shown as red spheres. Hydrogen atoms and counter-anions have been omitted for clarity.*

3.4 Magnetic Susceptibility Measurements and Mössbauer Spectroscopy

Through the structural analysis of **3.2·H$_2$O** it was observed that one Fe(II) remained in the HS state to give a [HS-LS] structure at 150 K. In contrast, the magnetic and structural behaviour of **3.2·CH$_3$CN** showed a completed contraction to the [LS-LS] state at this temperature. In order to fully elucidate the different magnetic behaviour, variable temperature magnetic susceptibility measurements were carried out. To this end, the magnetic susceptibility of a crystalline sample of **3.2·H$_2$O** was measured between 2 K and 300 K over multiple heating and cooling cycles.

During the initial heating run from 2 – 300 K (white circles **Fig 3.4.1**) the magnetic susceptibility *vs.* temperature plot shows a curve typical of that for a gradual "half" SCO process from the [HS(Fe1)-LS(Fe2)] system to the [HS-HS] form. The onset of this behaviour occurs at *ca.* 200 K and the μ_{eff} value increases over a 100 K temperature range with the [HS-HS] form not fully isolated at the maximum temperature of 300 K. The broad SCO has a $T_{1/2}$ of *ca.* 265 K. During the return cooling run (300 – 2 K; white circles **Fig 3.4.1**) the transition back to the [HS-LS] form occurs at lower temperatures, with the [HS-HS] form remaining occupied from 300 – 260 K. As the temperature decreases further the μ_{eff} value decreases over an approximately 100 K temperature

range, rejoining the [HS-LS] plateau at around 180 K. The sharp decrease in the μ_{eff} below 30 K is often observed in magnetic susceptibility plots of formally HS species and is due to the zero-field splitting of the quintet ($^5T_{2g}$) state.

The apparent thermal hysteretic behaviour observed during the first cycle was probed further through performing additional heating and cooling cycles on the sample (red circles **Fig 3.4.1**). The second heating and cooling cycle revealed further shifting of the SCO curve to lower temperatures, with a $T_{1/2}$ value of *ca.* 240 K with approximately 12 K difference between the heating and cooling runs. Due to the changing nature of the SCO during previous runs this behaviour is assigned to solvent loss within the crystal rather than thermal hysteresis. Indeed, the sample was subsequently left to sit in the magnetometer under vacuum at room temperature for 2 hours after which time a third cycle was run. After this period the SCO curve had further shifted to lower temperatures ($T_{1/2}$ *ca.* 200 K) however, the thermal hysteresis is no longer apparent, with both the heating and cooling modes tracing the same path (left red circles **Fig 3.4.1**). It is postulated that the sample is now fully desolvated.

Of particular interest is that the sample can be rehydrated by leaving the crystalline sample for some weeks under ambient conditions. Variable temperature magnetic susceptibility experiments were performed upon this rehydrated sample and the results closely mirror those of the initial "pristine" sample (green circles **Fig 3.4.1**).

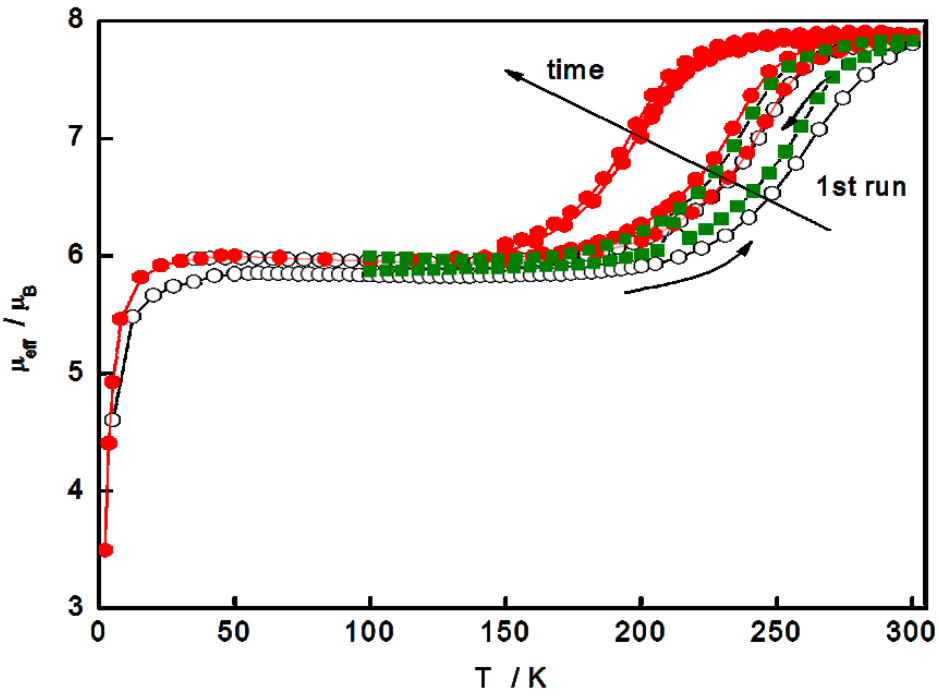

Fig 3.4.1 *Magnetic susceptibility plot for* ***3.2·H$_2$O****: White dots – first cycle (2-300-2 K); red dots – second/third cycles (2-300-2 K; third cycle after 2 hrs under vacuum at room temperature); green dots – sample after being left under ambient conditions for some weeks.*

Indeed, the sample appears to show no degradation during this dehydration/rehydration process with the sample still maintaining its crystalline appearance. No attempt was made to prevent water loss from the crystalline material and the crystallography was performed on crystals that were "aged" in that they were stored dry and not in their mother liquor.

To further confirm the magnetic behaviour of **3.2·H_2O**; Mössbauer spectroscopy was performed on a crystalline sample of the compound at 295 K and 4 K. The spectrum collected at 295 K is poorly resolved but shows the presence of two peaks relating to the [LS-HS] and [HS-HS] forms. The presence of some LS character is not unexpected as inspection of the magnetic susceptibility measurements shows that the initial curve has not reach the full [HS-HS] form at this temperature. The Mössbauer data shows the two peaks in a ratio of approximately 1:3 [LS-HS] : [HS-HS]. The low temperature data at 4.5 K is considerably better resolved and shows peaks consistent with the [LS:HS] form rather than a 1:1 mixture of [LS:LS] and [HS-HS] forms (**Fig 3.4.2**).

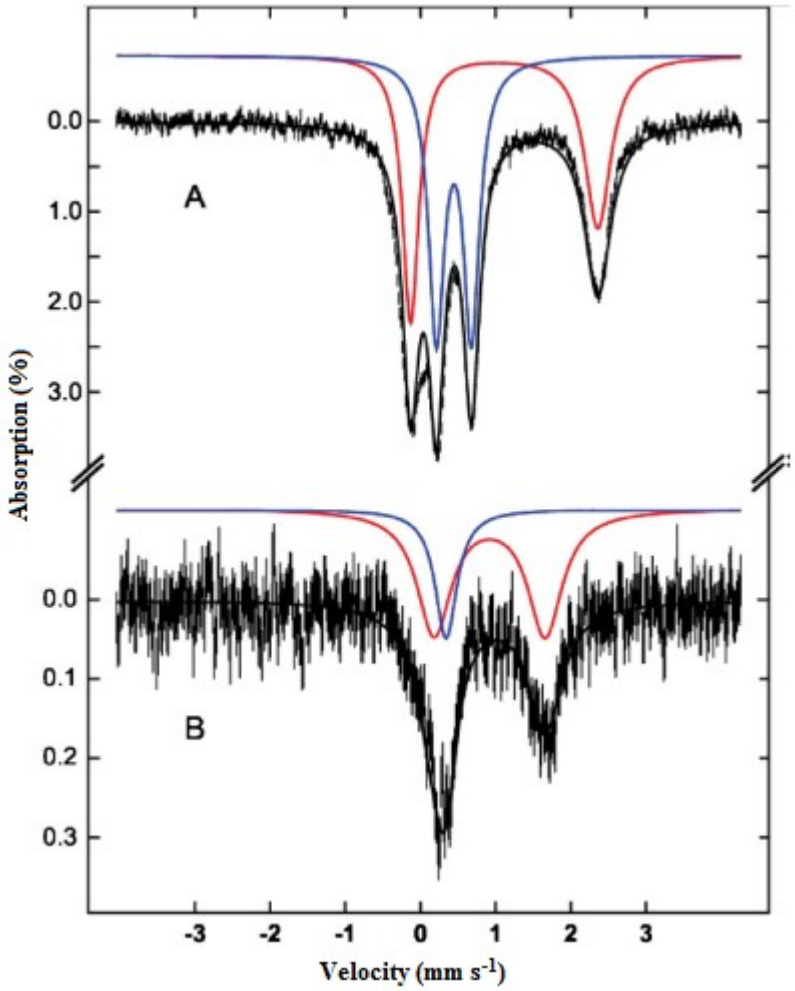

Fig 3.4.2 *Mössbauer Spectra of* ***3.2·H_2O*** *at 4.5 K (top) and 295 K (bottom) with HS fractions coloured in red and LS fractions coloured in blue.*

The Mössbauer parameters show a large change for the HS site between 4.5 K and 295 K, particularly the change in ΔE_Q from 1.48 mm s^{-1} at 295 K to 2.49 mm s^{-1} at 4.5 K (**Table 3.4.2**). This considerable change in the ΔE_Q suggests that there is a modification of the coordination geometry around Fe1 as the temperature is lowered even though Fe1 remains in the high spin state. The exact nature of this modification is difficult to determine without further high temperature structural data. However, as Fe2 contracts into the LS state the ligands within the helicate will shift to accommodate the change, subtly altering the coordination sphere about Fe1 even though spin crossover does not occur at this centre.

T (K)	Spin State	δ(mm/s)	ΔE_Q (mm/s)	Γ_L (mm/s)	Γ_R (mm/s)	I (%)
4.5	HS	1.11	2.49	0.27	0.42	50
	LS	0.45	0.47	0.26	0.26	50
295	HS	0.92	1.48	0.55	0.55	75
	LS	0.34	0	0.35	0.35	25

Table 3.4.2 *Mössbauer parameters for* ***3.2·H₂O****.*

3.5 Thermogravimetric Analysis of 3.2·H₂O

The variable water content of **3.2·H₂O** was analysed through careful thermogravimetric analysis in order to confirm the dehydration/rehydration behaviour postulated to explain the variable magnetic behaviour. As this complex contained the potentially explosive perchlorate anion, extreme care was taken during these experiments. Small quantities of the complex were analysed and samples were not heated above 100 °C. As such, no issues were encountered.

An initial experiment was performed on an air-dried sample of **3.2·H₂O**. The sample was heated at 1 °C min^{-1} to 100 °C and maintained at this temperature for 120 minutes (lower blue trace **Fig 3.5.1**). During this experiment there was total weight loss of *ca.* 4.08% which corresponds to a loss of four water molecules (calc. 4.15%) with the onset of mass loss occurring immediately from 20 °C. The sample was then left overnight open to the atmosphere and a second experiment was conducted where the sample was heated at 1°C min^{-1} to 100 °C and maintained at 100 °C for 120 minutes as with the previous experiment. There was a total weight loss of *ca.* 2.51% which corresponds to a loss of 2.5 water molecules (calc. 2.64%) (green trace **Fig 3.5.1**).

Experiments to this end were also conducted on the sample recovered for the magnetic susceptibility measurements after being exposed to air for some weeks. The results show a similar

weight loss profile to those of the "pristine" sample and the sample maintain visual appearance of crystallinity after thermogravimetric analysis.

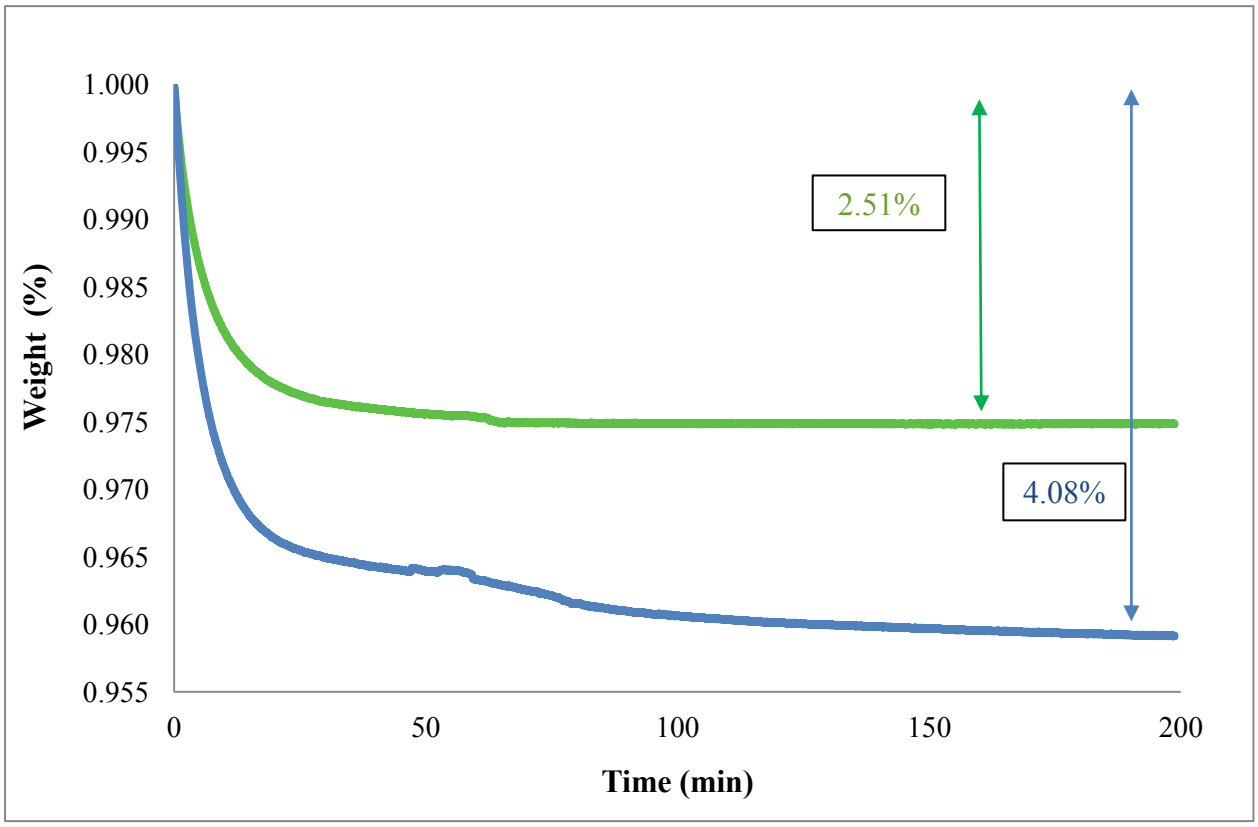

Fig 3.5.1 *Thermogravimetric analysis of* ***3.2·H$_2$O*** *showing the loss of water from an air-dried sample of* ***3.2·H$_2$O*** *(**blue trace**) and the loss of water after the initial sample had been left to rehydrate under atmospheric conditions overnight (**green trace**).*

3.6 Conclusion

The comparison between the two dinuclear triple helicates **3.2·CH$_3$CN** and **3.2·H$_2$O** revealed remarkably different magnetic behaviour, with **3.2·H$_2$O** only undergoing a partial SCO to the [LS-HS] state compared with the full transition to the [LS-LS] observed in **3.2·CH$_3$CN**. This behaviour is attributed to the intermolecular face-to-face π-π interaction between two adjacent high-spin "halves" which occur in **3.2·H$_2$O**. It is postulated that it is this interaction which stabilises the HS state of one of the Fe(II) centres within the dinuclear triple helicate, effectively preventing the contraction into the [LS-LS] state.

The SCO behaviour of **3.2·H$_2$O** was also found to depend on the water content of the sample with dehydration of the sample resulting in a shift in the SCO curves to lower temperatures.

Interestingly, the sample is able to be rehydrated under ambient conditions with the magnetic behaviour returning to that of the pristine sample. Variable SCO behaviour relating to reversible guest inclusion is a fascinating area of research, and **3.2·H_2O** joins a small but fast growing family of complexes which display this behaviour.[294]

Comparisons between the complexes discussed in the preceding chapters clearly illustrate the effectiveness and versatility of dinuclear triple helicates as SCO compounds. The dinuclear triple helicates discussed here have different flexibilities associated with the differing bridging group employed. The flexible oxy-bridging unit in **L3.1** results in greater helical twisting upon complexation with Fe(II) (in both solvates of **3.2**) when compared to the rigid hydrazine bridging unit in complexes **2.4** – **2.6**. Also, the rigid unit is unable to flex to the same extent as the oxy-bridge and as such the helicates **2.4** – **2.6** are narrower, possibly promoting the intra-helical C-H···π interactions that are present between all six phenyl rings in **2.4** – **2.6**, but only occur between four of the six rings in **3.2·CH_3CN** and **3.2·H_2O**. This interaction is postulated to stabilise the [LS-LS] state therefore increasing the $T_{1/2}$ of **2.5** relative to **3.2·CH_3CN** and **3.2·H_2O**.

CHAPTER FOUR

Spin Crossover Behaviour Within a Family of Mononuclear Fe(II) Complexes with Imidazolylimine Based Ligands

4.1 Introduction

Impressed with the varied magnetic behaviour of the dinuclear triple helicates discussed in previous chapters; the study moved to the synthesis, structural characterisation and magnetic analysis of a series of related ligands with only one binding domain.

In this chapter the spin crossover (SCO) behaviour of members within a family of mononuclear Fe(II) imidazolylimine complexes will be discussed in detail; with particular focus given to the supramolecular interactions present that affect SCO. Subtle alterations to the above complexes such as change in the counter-anion, electronic properties of the ligand, and solvent effects within the crystal lattice will be discussed in detail. Surprisingly, few ligands of this type have been reported in the literature.[218,295]

The ligands employed in this study incorporate some features important to the analysis and study of SCO. By changing the head group moiety from the methyl-imidazole, utilised previously in Chapter Three, to an unsubstituted imidazole provides the resulting complex with hydrogen bond donor capabilities, through the now accessible imidazole N-H group as observed in **2.5** and **2.6**. By incorporating hydrogen bonding entities within the ligand design, greater cooperativity between metal centres within the crystal lattice may occur.

Previous research within the Kruger group focused on the synthesis, characterisation and magnetic properties of a mononuclear Fe(II) complex utilising the ligand **L4.1** ($[Fe(\mathbf{L4.1})_3](ClO_4)_2$ – complex **4.6**). This system can be thought of as "half" of the complex described in Chapter Three. This research has since been published[218] and for convenience the pertinent details will be discussed briefly here. The complex **4.6** consists of three crystallographically unique **L4.1** units, coordinating in a meridional manner about the Fe(II) centre. Interestingly, complexes join together in pairs through hydrogen bonding between two imidazole N-H and perchlorate anions. No further intermolecular interactions are observed. Structural data for complex **4.6** was collected at both 116 K and 292 K to monitor the structural changes that occur during the SCO process. In particular, the Fe-N bond lengths increase by *ca.* 10% at the higher diffraction temperature. As such, variable temperature magnetic susceptibility measurements were completed on **4.6** and confirmed reversible SCO behaviour with a $T_{1/2}$ of 158 K. The compound was also found to show LIESST behaviour with red light irradiation of the sample at 10 K inducing the full HS-state of the complex. For further information the reader is directed to the published article and to **Fig 4.1.1** and **4.1.2** which show the molecular structure, hydrogen bonding interactions and the magnetic susceptibility behaviour of **4.6**.

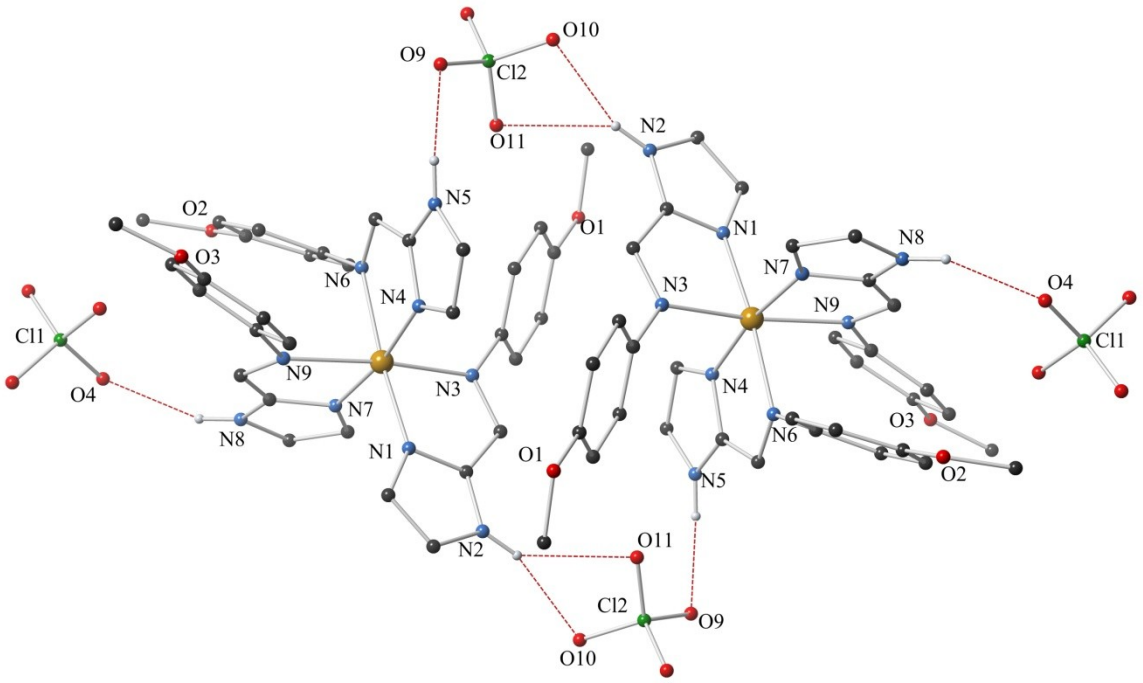

Fig 4.1.1 *Molecular structure and atom labelling scheme for complex* ***4.6*** *at 116 K showing the hydrogen bonding interactions between two adjacent molecules within the crystal lattice. Hydrogen atoms not involved in hydrogen bonding interactions have been omitted for clarity.*

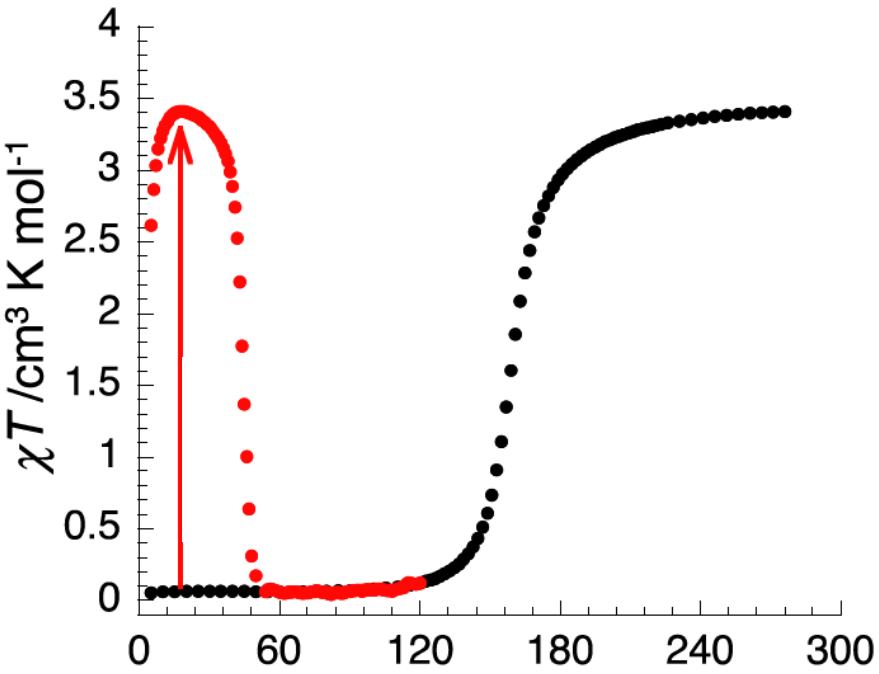

Fig 4.1.2 *χT vs. T plot for* ***4.6*** *after red light activation for 3.5 hours (**red dots**), and under dark conditions (**black dots**). Measurements performed under a 0.5 T magnetic field with a scan rate of 0.4 K min^{-1}.*

4.2 Ligand Design and Synthesis

Two isomeric imidazole aldehydes (*1H*-imidazole-2-carbaldehyde and *1H*-imidazole-4-carbaldehyde) were combined with various *para*-substituted anilines with different electronic properties. These ligand systems form mononuclear complexes with Fe(II), essentially forming "half" structures of the dinuclear triple helicates discussed in the previous chapters. The family of ligands involved in this study are shown in **Fig 4.2.1.**

All of the ligands were synthesised *via* a simple one-step imine condensation reaction between the aldehyde "head group" and the *para*-substituted aniline "tail group" and all were isolated with good yields (*ca.* 70 – 85%). Single crystals suitable for structural analysis *via* X-ray diffraction were obtained for the novel ligands **L4.2** and **L4.3**, discussion of the structural characteristics of these ligands are provided as supplementary information in **A-IV.2.1** and **A-IV.2.2**.

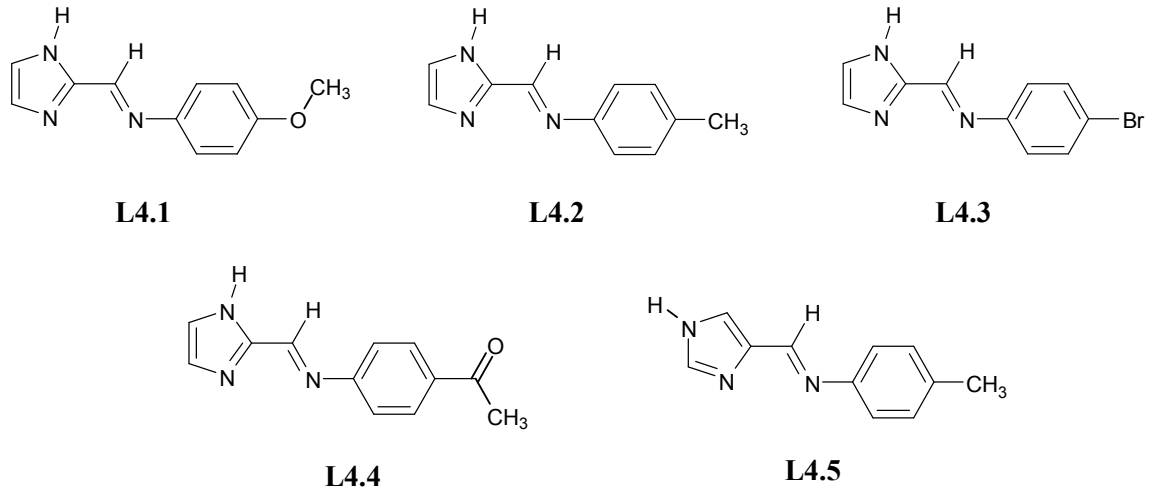

Fig 4.2.1 *Ligands described in Chapter 4.*

4.3 Synthesis and Structural Characterisation of Mononuclear Fe(II) Complexes

*4.3.1 Synthesis and Structural Characterisation of [Fe(**L4.1**)$_3$](BF$_4$)$_2$ – Complex **4.7***

Given the impressive photomagnetic behaviour of **4.6**, the ClO_4^- counter-anion was exchanged with BF_4^-, an anion with similar size, electronic and geometric properties, in order to investigate the effect of the counter-anion on the SCO of these systems. As such, three equivalents of ligand **L4.1** were dissolved in dichloromethane and treated with one equivalent of $Fe(BF_4)_2 \cdot 6H_2O$

dissolved in a small amount of acetonitrile. The resulting bright red solution was gently heated at 60 °C for one hour and subsequently filtered. The filtrate was then carefully layered with diethyl ether and allowed to stand in a sealed vessel for one week after which time red plate crystals of **4.7** formed suitable for structural analysis *via* single crystal X-ray diffraction. In the case of complex **4.7** the crystals were isostructural to those obtained for **4.6**. The X-ray diffraction data for **4.7** at 120 K were solved and refined in the triclinic space group *P-1* with an R-factor of 4.46%. The complex consists of three ligand units coordinating in a meridional fashion about the Fe(II) centre. The ligands coordinate in a bidentate manner through the imidazole and imine nitrogen atoms leading to a N_6 coordination sphere. The Fe-N coordination bond lengths lie in the range 2.024(2) – 2.110(2) Å with an average coordination bond length of *ca.* 2.06 Å and an Σ value of 79.7°. All of the geometric parameters are consistently larger than those observed in **4.6** and are within the expected range for an Fe(II) centre transitioning between the HS and LS states.[278]

Each of the ligands undergoes some twisting between the imine and phenyl ring planes. The three crystallographically non-identical ligands have torsion angles ranging from 30.9(3)° to 60.0(3)°. The two larger torsion angles at -51.3(3)° and 60.0(3)° for C4-N3-C5-C6 and C15-N6-C16-C17 respectively, allow a relatively strong edge-to-face C-H···π interaction to form, similar to that observed in complex **4.6**. The C-H···π (centroid) interaction has a distance of 2.829(1) Å and an angle of 25.37(16)°. Not only does this twisting of one of the ligand strands optimise the edge-to-face C-H···π interaction, but it also creates an offset face-to-face π-π interaction between the imidazole head group and an adjacent methoxy-benzene "half" with a centroid-centroid distance of 3.6263(12) Å and an interplanar angle of 21.01(8)°.

As discussed previously with the ClO_4^- analogue, two adjacent complexes are linked together through hydrogen bonding interactions. The intermolecular Fe-Fe distance in **4.7** is slightly shorter than that observed in **4.6** at 7.4265(6) Å and is attributed to the subtle differences in the hydrogen bonding between the two analogous complexes. These hydrogen bonding interactions are illustrated in **Fig 4.3.1** below and the hydrogen bonding parameters are provided in detail as supplementary information in **A-III**.

Given the similar structural characteristics of **4.6** and **4.7**, single crystal X-ray diffraction data were collected at 220 K to investigate potential SCO behaviour in **4.7**. From the analysis of these two diffraction data sets there is a noticeable expansion of the unit cell at the higher temperature. In particular the unit cell volume increases by *ca.* 3.2% at 220 K. Upon closer inspection of the coordination sphere there are significant increases to the Fe-N coordination bond lengths with an average bond length of *ca.* 2.19 Å at 220 K, corresponding to an approximately 6% increase at 220 K compared with the average bond lengths at 120 K.

The octahedral distortion parameter Σ also increases from Σ = 79.67° to Σ = 98.86° at the higher temperature. All of these crystallographic parameters show smaller changes than would typically be expected for SCO behaviour in an Fe(II) complex, possibly suggesting that the LS state may not be fully isolated at 120 K. The important geometric parameters at both 120 K and 220 K are provided in **Table 4.3.2** and the structural changes in **4.7** during SCO are illustrated in **Fig 4.3.3**.

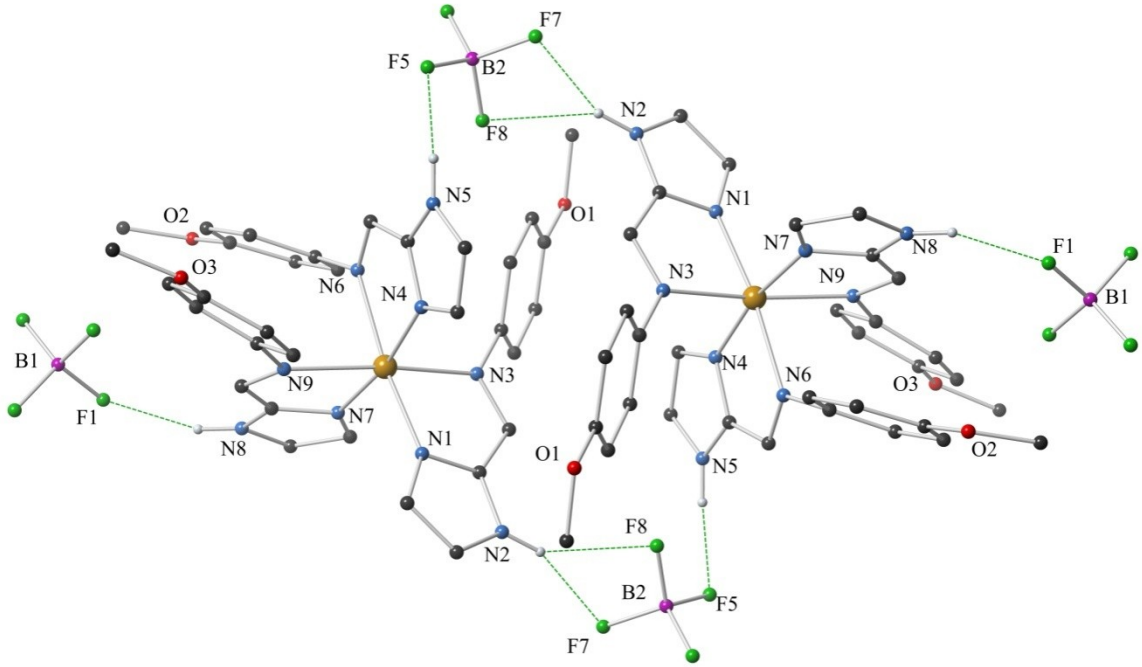

Fig 4.3.1 *Molecular structure and atom labelling scheme for complex* ***4.7*** *(120 K) showing the hydrogen bonding interactions between two complexes within the crystal lattice. Hydrogen atoms not involved in hydrogen bonding have been omitted for clarity.*

	4.7 – 120 K	**4.7 – 220 K**
Space Group	*P-1*	*P-1*
Unit Cell Volume (Å^3)	1812.09(19)	1870.70(11)
Av. Fe-N Bond Length (Å)	2.06	2.19
Σ (°)	79.7	98.9
Φ (°)	4.84	6.05

Table 4.3.2 *Selected geometric parameters for the Fe-N coordination bonds in* ***4.7*** *at 120 K and 220 K*

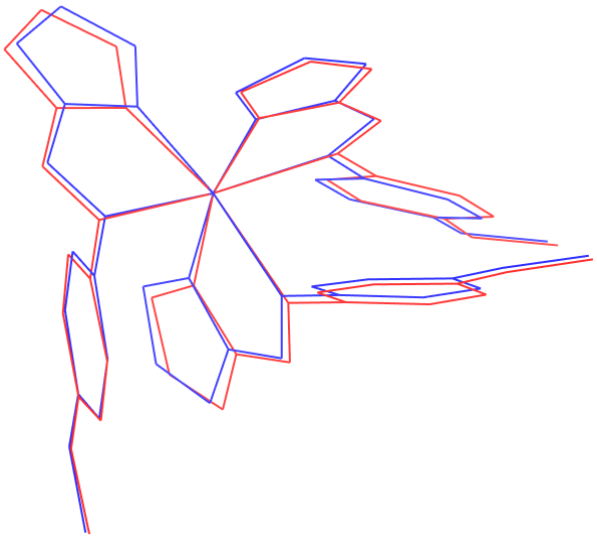

Fig 4.3.3 *Structural overlay of complex **4.7** at 120 K (**blue**) and 220 K (**red**). Hydrogen atoms and counter-anions have been omitted for clarity.*

*4.3.2 Synthesis and Structural Characterisation of [Fe(**L4.1**)$_3$](ClO$_4$)$_2$·CH$_3$CN – Complex **4.8***

As this study was being conducted, monoclinic crystals of the [Fe(**L4.1**)$_3$](ClO$_4$)$_2$ complex were isolated from the reaction of three equivalents of **L4.1** suspended in dichloromethane with one equivalent of Fe(ClO$_4$)$_2$·6H$_2$O dissolved in a small amount of acetonitrile. The resulting red-brown solution was filtered and carefully layered with diethyl ether. Interestingly, even though the crystallisation technique was the same as that employed for the formation of complex **4.7**, the structural outcome was remarkably different. As such this second crystallographic phase with the form ([Fe(**L4.1**)$_3$](ClO$_4$)$_2$·CH$_3$CN (Complex **4.8**) was carefully analysed.

The X-ray diffraction data for **4.8** at 120 K were solved and refined in the monoclinic space group *P2$_1$/c*. As anticipated, the structure consists of three bidentate ligands coordinated about a central Fe(II) atom. The coordination bonds are once again from the imidazole and imine nitrogen atoms on the three ligands. Interestingly though, the average coordination bond length of **4.8** at 120 K is *ca.* 2.21 Å which is consistent with Fe(II) in the HS state. The presence of a HS Fe(II) centre at 120 K is unexpected when compared to the related compound structures of both **4.6** and **4.7** which both contain Fe(II) centres in the LS state at 120 K. The structure of **4.8**, along with the hydrogen bonding interactions to the counter-anions and solvent molecule are illustrated in **Fig 4.3.4**.

Careful investigation of the crystal structure reveals the inclusion of an acetonitrile solvent molecule within the crystal lattice of **4.8**. This solvent molecule forms a hydrogen bond to one of

the imidazole N-H moieties. The other two imidazole N-H moieties form hydrogen bonds to the ClO_4^- counter-anions which do not extend further in the crystal lattice.

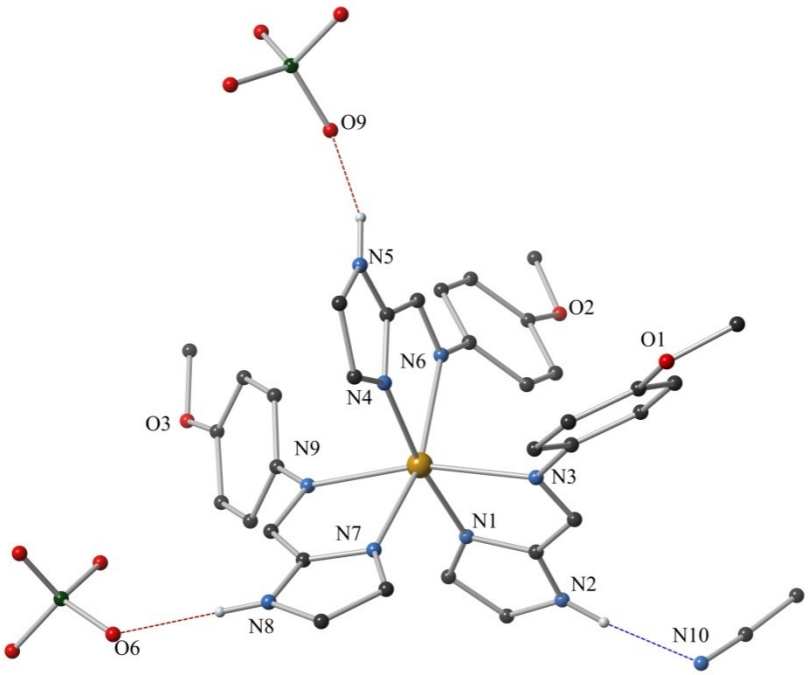

Fig 4.3.4 *Molecular **s**tructure and atom labelling scheme for **4.8** at 120 K. Hydrogen atoms not involved in hydrogen bonding interactions have been omitted for clarity.*

Along with the simple inclusion of a solvent molecule within the crystal lattice the complexes were found to order differently within the lattice compared with the packing in both **4.6** and **4.7**. The complexes form sandwich-type dimer interactions, where two of the methoxy tail groups intercalate between the two tail groups on an adjacent complex. The methoxy group forms strong C-H···π interactions with the two neighbouring phenyl rings. These C-H···π(centroid) interactions are at a distance of 2.6671(14) and 3.0546(14) Å respectively. This sandwich effect significantly lengthens the Fe-N_{imine} bond lengths of the ligands involved to 2.267(3) Å and 2.323(3) Å. As the SCO process involves the contraction of the coordination sphere it is not surprising that the intercalation of the ligand tails prevents this due to steric hindrance. On viewing the space-filling diagram it is clear to see that the structure has very little room in which to contract as illustrated in **Fig 4.3.5**.

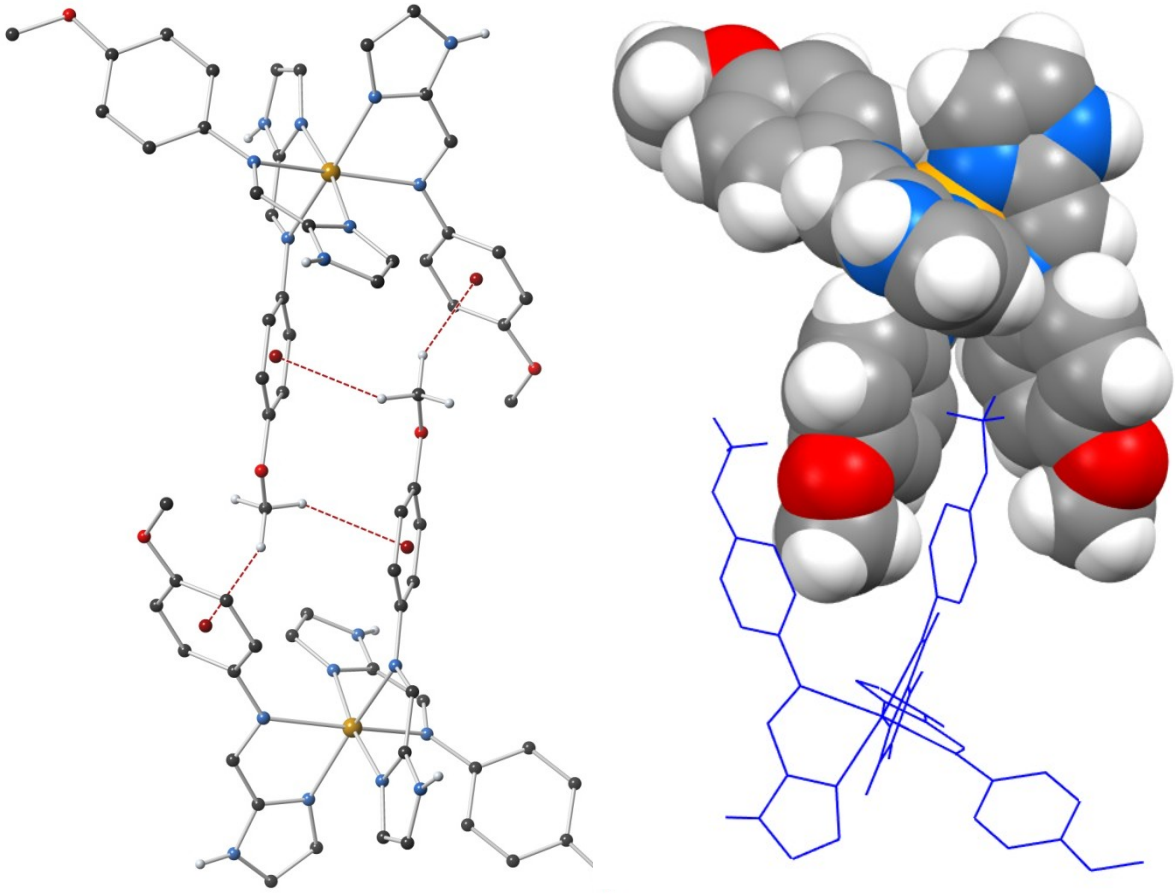

Fig 4.3.5 *Molecular structure and packing diagram of* ***4.8*** *at 120 K, showing the C-H···π interactions between the intercalating methoxy tails.*

	4.8 – 120 K
Space Group	$P2_1/c$
Unit Cell Volume (Å^3)	3874.1(2)
Av. Fe-N Bond Length (Å)	2.21
Σ (°)	87.8
Φ (°)	6.16

Table 4.3.6 *Selected geometric parameters for the Fe-N coordination bonds in* ***4.8*** *at 120 K.*

*4.3.3 Synthesis and Structural Analysis of [Fe(**L4.2**)$_3$](BF$_4$)$_2$·CH$_3$CN·0.5H$_2$O – Complex **4.9***

Subtle changes to the steric and electronic properties of ligands have been shown to affect the SCO behaviour of the resulting complexes.[1,204] To this end, the *para*-methyl substituted ligand **L4.2** was explored. Three equivalents of **L4.2** were suspended in dichloromethane with one equivalent of

$Fe(BF_4)_2 \cdot 6H_2O$, dissolved in a small amount of acetonitrile. The resulting red solution was gently refluxed and the solution was filtered when cool. Red block crystals suitable for structural analysis by X-ray diffraction were obtained *via* a slow diffusion of diethylether into the reaction solution. The crystallisation technique employed here was kept consistent with that used in the crystallisation of complexes **4.7** and **4.8** in an attempt to maintain similar crystallisation environments for solid state analysis.

The diffraction data for **4.9** at 120 K were solved and refined in the triclinic space group *P-1* with similar unit cell parameters to complex **4.6** and **4.7**. The structure is comprised of three bidentate **L4.2** ligands in an octahedral geometry about an Fe(II) centre with the imidazole and imine nitrogen atoms acting as the donor atoms, the structure of which is outlined below in **Fig 4.3.7.** The Fe-N average coordination bond length is *ca.* 2.07 Å. The average bond length shows significant contraction from the typical average Fe-N bond length associated with a HS Fe(II) centre of *ca.* 2.2 Å, but are longer than those typically observed with LS Fe(II) of *ca.* 1.9 Å. Interestingly, positional disorder was observed about one of the imidazole head groups. This disorder was modelled as the imidazole head group residing equally between two positions. Only two of the five atoms within the imidazole ring appear to be disordered with the other three atom locations being modelled with full occupancy. Analysis of the *cis* angles within the Fe-N coordination sphere shows an Σ value of 83.3°, approximately 14% larger than the Σ value for complex **4.6** for the low temperature data collection. The larger than anticipated geometric coordination parameters in combination with the disorder about one of the imidazole head groups could imply that the SCO is incomplete at the diffraction temperature of 120 K.

The asymmetric unit of **4.9** also contains two crystallographically independent BF_4^- counter-anions. One of the BF_4^- counter-anions is well defined and is involved in hydrogen bonding between neighbouring complexes, the other BF_4^- counter-anion is positionally disordered. The solvent content was modelled crystallographically as one molecule of acetonitrile with a half occupied water molecule within the asymmetric unit. The water molecule was assigned as such due to the plausible hydrogen bonding interactions that may occur between the BF_4^- and water molecule and also the hydrated nature of the metal salt used during the synthesis provided a reasonable source of water during the formation of the complex. Thermogravimetric analysis on a freshly filtered sample showed rapid loss of mass consistent with loss of crystallised acetonitrile, however, microanalysis on a crystalline sample removed from mother liquor for approximately one week showed increased water content. As such the solvent content is expected to vary under different drying conditions.

Individual complexes within the crystal lattice are connected in pairs through hydrogen bonding interactions with the counter-anion, similar to the interactions observed in **4.6** and **4.7**. This interaction gives an intermolecular Fe-Fe distance of 7.678(1) Å. The third imidazole head group weakly interacts with the disordered BF_4^- entity and does not contribute to any further

hydrogen bonding networks. A comparison of the hydrogen bonding information for **4.9** is provided in **A-III**.

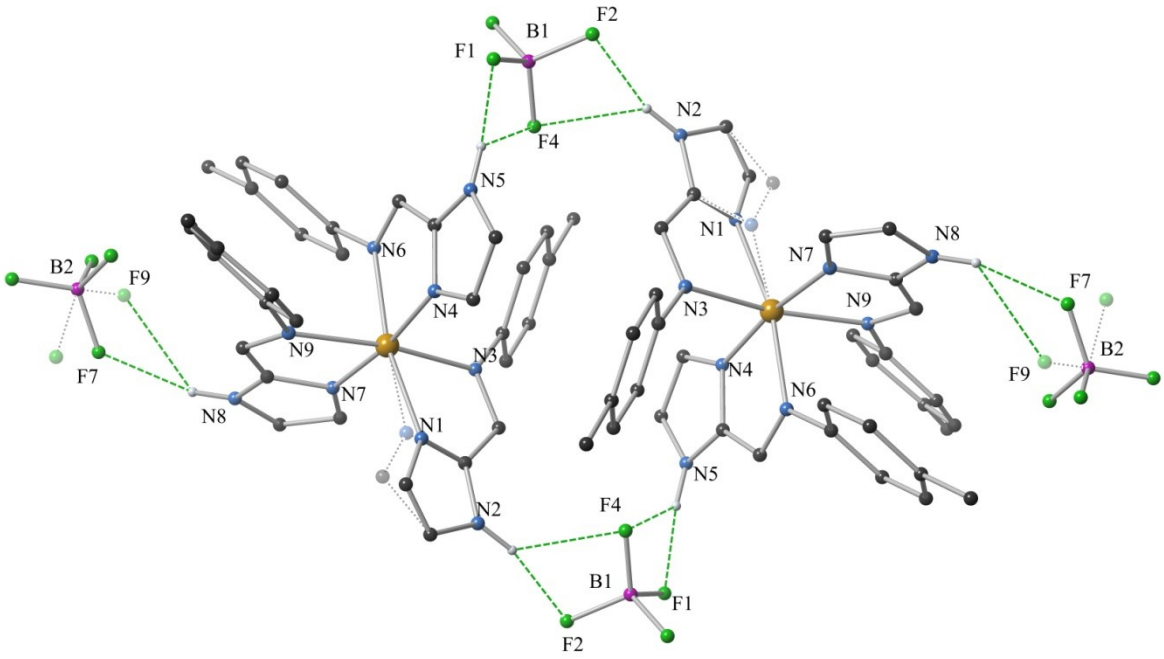

Fig 4.3.7 *Molecular structure and atom labelling scheme for complex* ***4.9*** *at 120 K showing the hydrogen bonding interactions between two complexes within the crystal lattice. Hydrogen atoms not involved in hydrogen bonding and solvent molecules have been omitted for clarity.*

Further crystallographic data were collected at 220 K in order to probe the structural changes in **4.9** during SCO. Diffraction data collected at 220 K reveals that the unit cell has expanded in volume by approximately 4.6% with an increase in the lengths of all three cell axes. Of great interest is the expansion of the Fe-N bond lengths about the Fe coordination sphere at the higher temperature. The Fe-N bond lengths have increased to the range 2.120(3) – 2.237(2) Å with an average bond length of *ca.* 2.18 Å, an increase of 5.3%. The Σ value also increases to 102° which is consistent with SCO to the HS state. The structural changes within **4.9** are illustrated in **Fig 4.3.8** and the geometric coordination parameters at both 120 K and 220 K are provided in **Table 4.3.9**.

The crystal packing at 220 K is comparable to that from the low temperature collection with some adjustment to the distances involved in order to accommodate the expanded coordination sphere. The pairing up of two adjacent molecules through the hydrogen bonding interactions still occur at 220 K with a slight increase in the intermolecular distance to 7.780(1) Å.

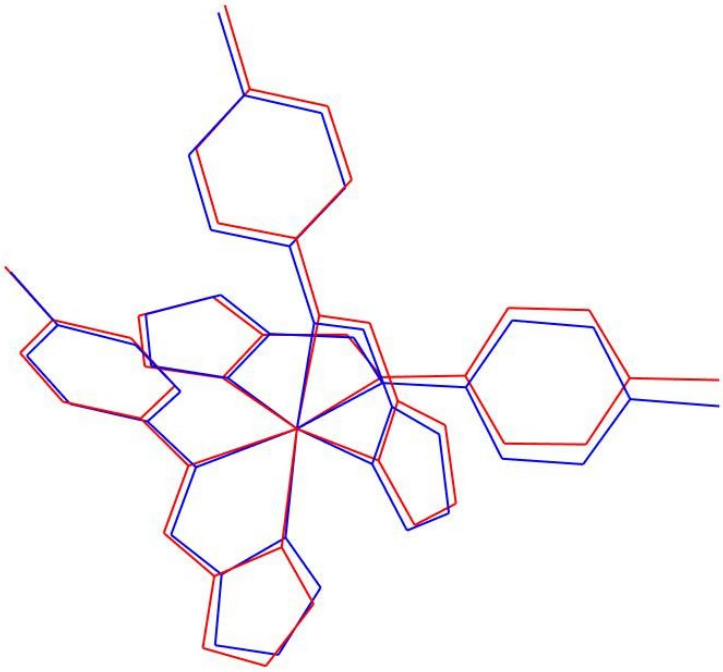

Fig 4.3.8 *Structural overlay of complex* ***4.9*** *at 120 K* ***(blue)*** *and 220 K* ***(red)****. Hydrogen atoms, solvent molecules and counter- anions have been omitted for clarity.*

	4.9 – 120 K	**4.9 – 220 K**
Space Group	*P-1*	*P-1*
Unit Cell Volume ($Å^3$)	1881.6(2)	1969.4(3)
Av. Fe-N Bond Length (Å)	2.07	2.18
Σ (°)	83.3	101.6
Φ (°)	5.25	6.11

Table 4.3.9 *Selected geometric parameters for the Fe-N coordination bonds in* ***4.9*** *at 120 K and 220 K*

*4.3.4 Synthesis and Structural Analysis of [Fe(**L4.2**)$_3$](ClO$_4$)$_2$·CH$_3$CN·0.5H$_2$O – Complex **4.10***

As with the BF_4^- analogue analysed in **Section 4.3.3**, complex **4.10** was synthesised by mixing three equivalents of **L4.2** dissolved in dichloromethane with one equivalent of $Fe(ClO_4)_2.6H_2O$ dissolved in a small amount of acetonitrile. The resulting red solution was gently refluxed for 1 hour. Red plate crystals suitable for X-ray analysis were obtained from the slow diffusion of diethyl ether into the reaction solution. The ClO_4^- analogue is isostructural with the BF_4^- complex and consists of three ligands arranged in a meridional fashion about a pseudo-octahedral Fe(II)

centre. The Fe(II) centre is in the LS state with Fe-N coordination bond lengths in the range 1.957(2) – 2.030(2) Å to give an average coordination bond length of *ca.* 1.99 Å

Both the BF_4^- and ClO_4^- complexes crystallise in the triclinic space group *P-1* with one meridional cation, one molecule of acetonitrile, a half occupied water molecule, and even both structures show one anion being well ordered and the other being disordered over two positions. Upon initial inspection of the hydrogen bonding network of **4.10** the complex forms the same hydrogen bound dimers to those observed previously utilising the **L4.1** ligand, and the BF_4^- analogue **4.9**. As with the previous examples, two of the imidazole N-H moieties act as hydrogen bond donors toward two of the perchlorate oxygen atoms. This results in an inter-complex Fe-Fe distance of 7.6263(7) Å at 120 K. The final imidazole N-H group forms a hydrogen bond to the disordered ClO_4^- anion and does not form any further hydrogen bonding networks. The hydrogen bonding interactions are illustrated in **Fig 4.3.10**, and the crystallographic hydrogen bonding parameters are provided in **A-III**.

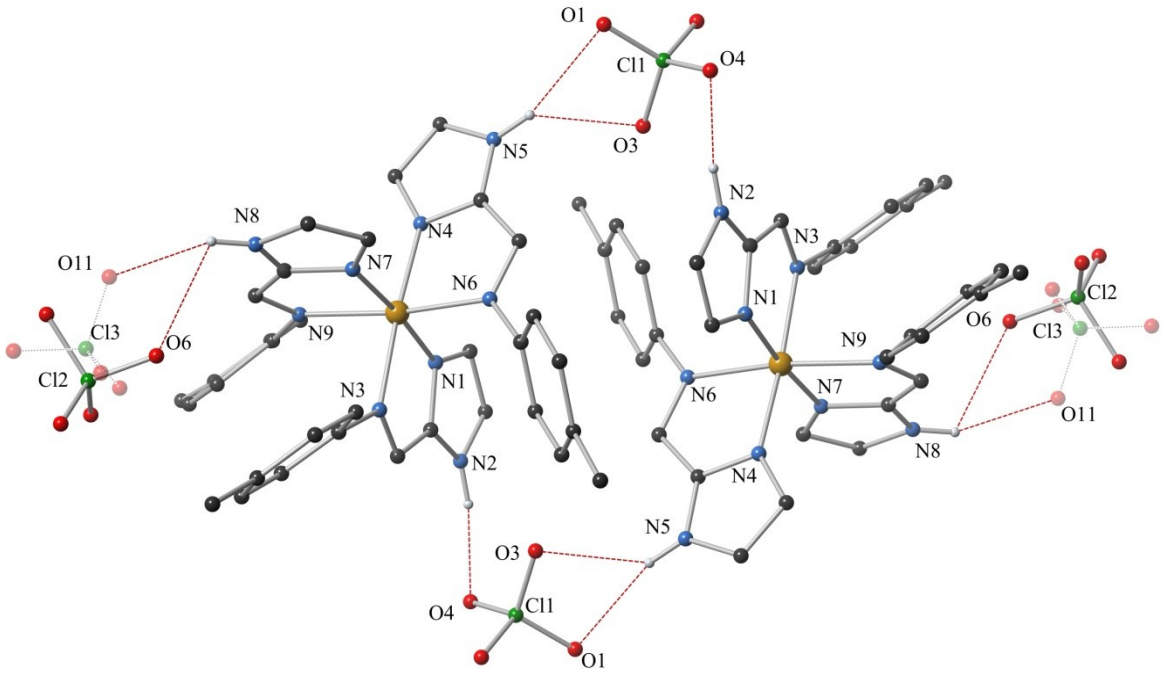

Fig 4.3.10 *Molecular structure and atom labelling scheme for complex* ***4.10*** *at 120 K showing the hydrogen bonding interactions between two complexes within the crystal lattice. Hydrogen atoms not involved in hydrogen bonding and solvent molecules have been omitted for clarity.*

The structure of **4.10** was also analysed at 220 K to follow the structural changes associated with SCO. As with the previous examples, there is an approximately 4.6% increase in the unit cell volume at the higher diffraction temperature. The Fe-N coordination bond lengths also show an approximately 9% expansion in the average Fe-N bond length to *ca.* 2.17 Å at the higher

diffraction temperature. The substantial increase in coordination bond lengths along with an approximately 60% increase in the Σ value are indicative of the complex undergoing SCO into the HS state by 220 K. The geometric parameters at both 120 K and 220 K are provided in **Table 4.3.11** below.

	4.10 – 120 K	**4.10 – 220 K**
Space Group	*P-1*	*P-1*
Unit Cell Volume ($Å^3$)	1903.51(13)	1990.99(15)
Av. Fe-N Bond Length (Å)	1.99	2.17
Σ (°)	67.8	112.9
Φ (°)	4.29	5.93

Table 4.3.11 *Selected geometric parameters for the Fe-N coordination bonds in* ***4.10*** *at 120 K and 220 K.*

*4.3.5 Synthesis and Structural Analysis of [Fe(**L4.3**)$_3$](ClO$_4$)$_2$·CH$_2$Cl$_2$ – Complex **4.11***

To further study the effects of subtle ligand alteration on SCO, the *para*-bromo substituted ligand **L4.3** was employed. To this end, three equivalents of **L4.3** were suspended in dichloromethane, and an acetonitrile solution containing one equivalent of $Fe(ClO_4)_2 \cdot 6H_2O$ was added. Upon mixing, the solution turned bright red and after heating the solution at reflux for one hour the mixture was filtered and layered with diethylether. Red plate crystals suitable for structural analysis *via* X-ray diffraction formed after a few days.

The crystallographic data were solved and refined in the triclinic space group *P-1* with a R-factor of 3.95% and as with the previous structure the complex consists of three bidentate ligands coordinating to a central Fe(II) ion in a meridional fashion. The structure of **4.11** is shown in **Fig 4.3.12**. The ligands coordinate through the imidazole nitrogen and imine nitrogen atoms leaving the other imidazole nitrogen protonated, creating hydrogen bonding networks as discussed below. The central Fe(II) has an average bond length of *ca.* 2.20 Å and an Σ value of 82.4° which is consistent with the complex being in the HS state at 120 K. (**Table 4.3.13**). As with the previous examples the ligands are not perfectly flat and all three ligands show varying degrees of distortion about the imine-phenyl bonds. The torsion angles lie within the range 31.3(6)° to 52.5(6)° and the twisting does not appear to optimise any edge-to-face C-H···π interactions between phenyl rings within the same molecule as observed in the previous complexes.

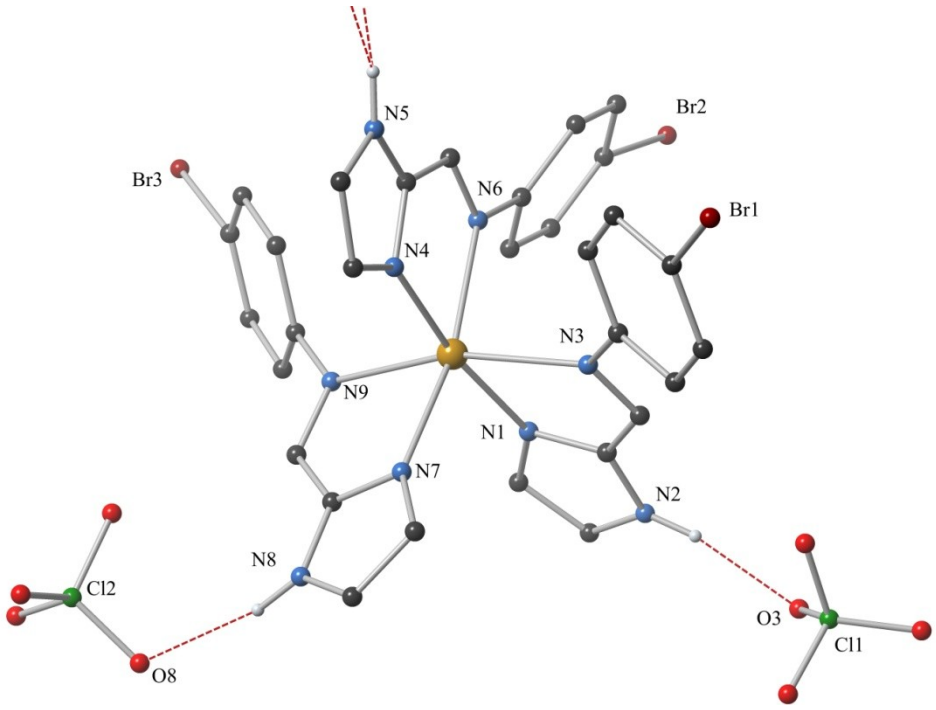

Fig 4.3.12 *Molecular structure and atom labelling scheme for complex* ***4.11*** *at 120 K. Solvent molecules and hydrogen atoms not involved in hydrogen bonding have been omitted for clarity.*

There does appear to be some edge-to-face C-H···π interactions between neighbouring molecules. Two of the bromo-benzene units on adjacent complexes are in close proximity forming an edge-to-face C-H···π interaction with a C-H···π (centroid) distance of 2.672(2) Å. There does not appear to be any strong face-to-face π···π interactions between neighbouring complexes, although the C-H···π interaction described above appears to create an overlap between two aryl rings in the adjacent complexes. However, with a centroid-centroid distance of 4.309(2) Å and an interplanar angle of 152.7(2) °, the contact is too long to be considered as providing any great stabilising force to the system. The N-H moieties on the imidazole rings are able to hydrogen bond to neighbouring perchlorate counter-anions to create a 2D-hydrogen bonding network with donor-acceptor distances less than 3.1 Å. These interactions are illustrated in **Fig 4.3.14** and crystallographic hydrogen bonding parameters are provided in **A-III**.

	4.11 - 120 K
Space Group	*P-1*
Unit Cell Volume (Å^3)	2008.61(13)
Av. Fe-N Bond Length (Å)	2.20
Σ (°)	82.4
Φ (°)	5.58

Table 4.3.13 *Selected geometric parameters for the Fe-N coordination bonds in* ***4.11*** *at 120 K.*

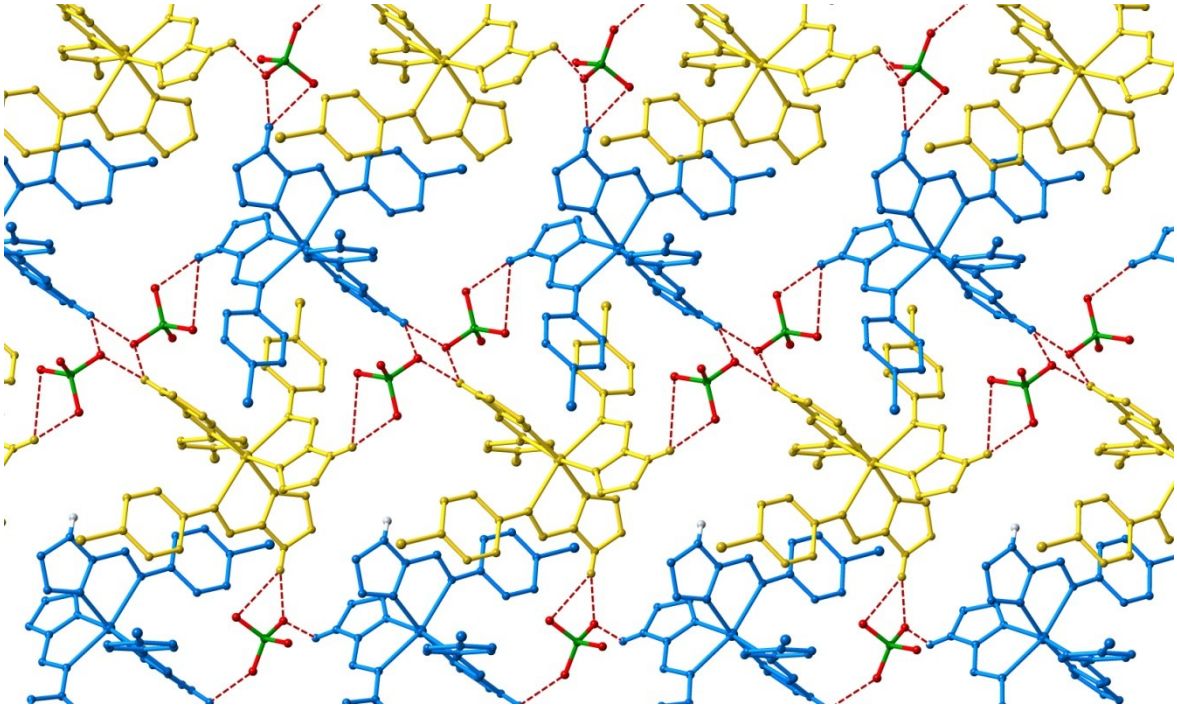

Fig 4.3.14 *Packing diagram of complex* ***4.11*** *at 120 K showing the hydrogen bonding interactions between complexes within the crystal lattice. Hydrogen atoms not involved in hydrogen bonding and solvent molecules have been omitted for clarity.*

*4.3.6 Synthesis and Structural Analysis of [Fe(**L4.4**)$_3$](BF$_4$)$_2$ – Complex **4.12***

The complex **4.12** was synthesised by reacting three equivalents of the ligand **L4.4**, suspended in dichloromethane, with one equivalent of $Fe(BF_4)_2 \cdot 6H_2O$ dissolved in a small amount of acetonitrile. The resulting bright orange solution was heated gently at reflux for one hour and upon cooling the solution was promptly filtered and carefully layered with diethyl ether. Orange plate crystals suitable for structural analysis *via* X-ray diffraction formed after a few days.

The crystallographic data for complex **4.12** were solved and refined in the triclinic space group *P-1* with an R-factor of 5.62%. As with the other members of this family, **4.12** forms a meridional structure with three **L4.4** ligands coordinated about a central Fe(II) ion. At the diffraction temperature of 120 K the Fe(II) centre is in the HS state with an average coordination bond length of *ca.* 2.19 Å. The structural diagram and geometric parameters are shown in **Fig 4.3.15** and **Table 4.3.16**, respectively. The three ligands are all crystallographically inequivalent and have slight distortion from planarity about the imine-phenyl bond. The torsion angles for the three ligands about this centre are within the range 28.5(4)° - 56.5(4)°. The torsion values are very

similar to those measured for complex **4.11** which does not form any intramolecular edge-to-face or face-to-face π-π interactions. Unsurprisingly, given this similarity, **4.12** also exhibits no intramolecular interactions within the cationic structure. However, the ligand (**L4.4**) has two potential sites for hydrogen bond formation, the imidazole N-H moiety, which has been discussed in great detail with other members of this system, and the carbonyl oxygen moiety. As these systems form very robust hydrogen bonding networks within the crystal lattice it is important that these variations in ligand design be discussed.

In **4.12**, the imidazole N-H moieties are involved in hydrogen bonding interactions to both the counter anions, and the carbonyl moiety. Isolating the hydrogen bonding network involving only the carbonyl oxygen moiety reveals a 2D-sheet hydrogen bonding network with the imidazole N-H moiety within the crystal lattice. This sheet involves two of the three oxygen atoms within each complex, and links one enantiomer through the network. Two of these sheets are then joined through hydrogen bonds between counter-anions, essentially forming a double-layered sheet. Only one BF_4^- anion acts through this hydrogen bond with the second counter-anion bolstering the hydrogen bonding interaction within the 2D-sheet described initially. The donor-acceptor distances for all of these interactions are below 3.1 Å, and further hydrogen bonding parameters are provided as supplementary information in **A-III**. The hydrogen bonding network is illustrated below in **Fig 4.3.17**.

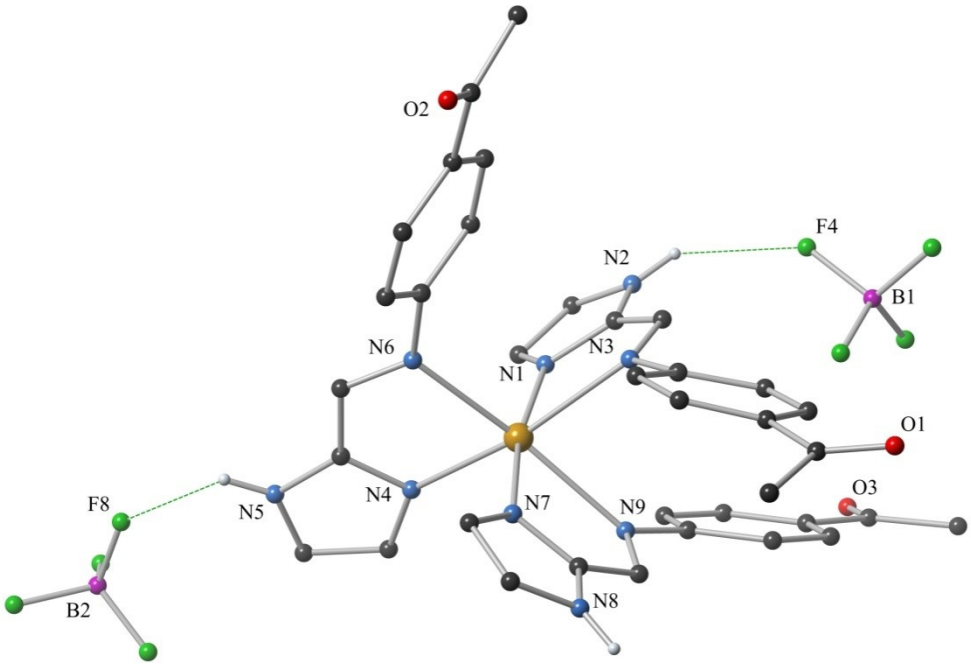

Fig 4.3.15 *Molecular structure and atom labelling scheme for complex **4.12** at 120 K. Hydrogen atoms not involved in hydrogen bonding have been omitted for clarity.*

	4.12 -120 K
Space Group	*P-1*
Unit Cell Volume ($Å^3$)	1907.9(2)
Av. Fe-N Bond Length (Å)	2.19
Σ (°)	110.3
Φ (°)	6.87

Table 4.3.16 *Selected geometric parameters for the Fe-N coordination bonds in* ***4.12*** *at 120 K.*

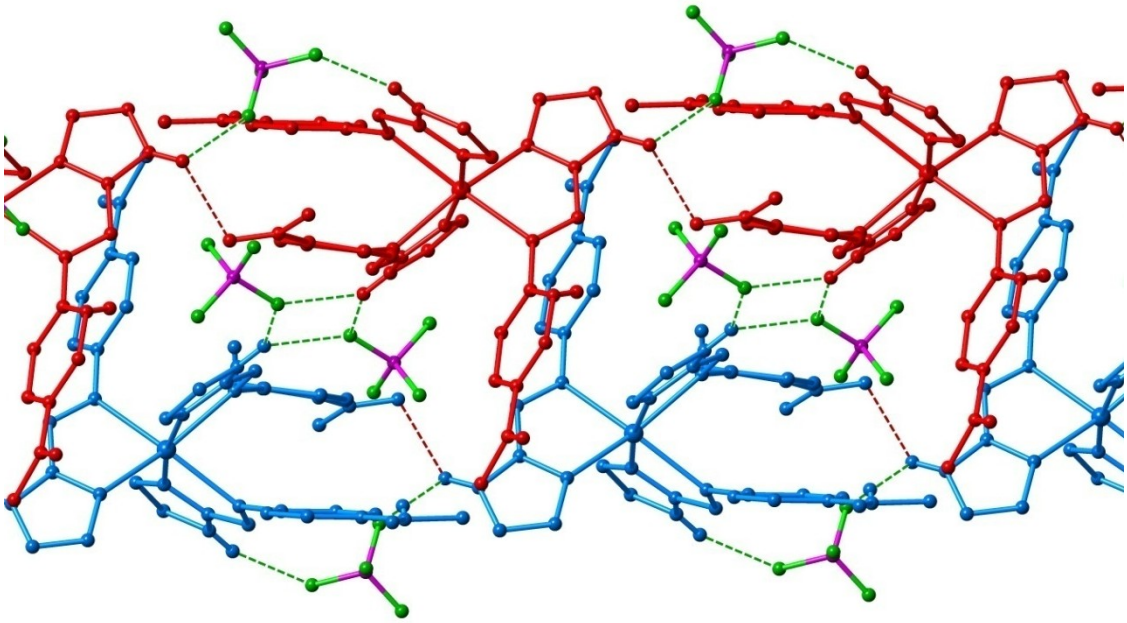

Fig 4.3.17 *Packing diagram of complex* ***4.12*** *at 120 K showing the hydrogen bonding interactions between 2D-hydrogen bonding sheets (****red****/****blue****) as viewed along the crystallographic a-axis. Hydrogen atoms not involved in hydrogen bonding and solvent molecules have been omitted for clarity.*

*4.3.7 Synthesis and Structural Analysis of [Fe(**L4.5**)$_3$](BF$_4$)$_4$·CH$_3$CN – Complex **4.13***

To further inspect the effect of various head groups on these mononuclear systems an isomer of **L4.2** was synthesised. Ligand **L4.5** only differs from **L4.2** through the relative position of the imine bond – the imine joins the imidazole functionality through the 4'-position rather than the 2'-position. This will very subtly change the electronic nature of the head group. The crystallographic data for complex **4.13** were solved and refined in the triclinic space group *P-1* and show a meridional arrangement of three bidentate ligands about a central pseudo-octahedral Fe(II) centre. The ligand **L4.5** coordinates through the imidazole and imine nitrogen atoms to the central Fe(II) ion. This Fe(II) centre is in the HS state with an average coordination bond length of 2.19(1) Å at the collection temperature of 120 K. A diagram displaying the structure of **4.13** is provided in **Fig 4.3.18**. In order to compare this to the 2' isomer which exhibits SCO to the LS state at 120 K, careful consideration of the crystal lattice structure is required.

Interestingly, due to the altered position of the N-H hydrogen bond donor group the hydrogen bonding network is quite different to that observed in the isomeric complex **4.9**. In complex **4.13** a 1D hydrogen bonding polymer forms through connecting BF_4^- counter anions rather than the pairing up of molecules that occurs in **4.9** (**Fig 4.3.19**). The acetonitrile molecule within the asymmetric unit does not appear to cause any extension of the coordinating bond lengths about the Fe(II) with all of the coordinating imidazole bonds lying in the range 2.142(1) – 2.147(1) Å. Unlike complex **4.8**, which also shows exclusively high spin behaviour, there are no obvious steric interaction that may be preventing the complex from contracting to the LS state. By eliminating these causes the HS character of this molecule is likely due to the weaker field ligand strength of the 4' ligand with respect to the 2' ligand. Given that the dinuclear triple helicates discussed in Chapter 2 showed that this subtle change within the coordination sphere corresponded to a nearly 100 K shift in the $T_{1/2}$ of similar complexes, it is not surprising that this complex is HS and shows no structural evidence of SCO (**Table 4.3.20**).

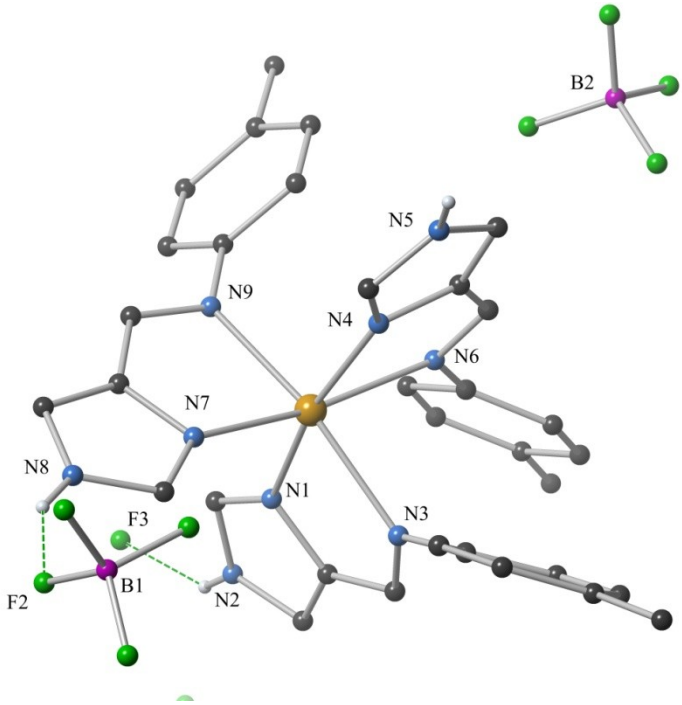

Fig 4.3.18 *Molecular structure and atom labelling of complex* ***4.13*** *at 120 K. Hydrogen atoms not involved in hydrogen bonding interactions, solvent molecules and counter-anions have been removed for clarity.*

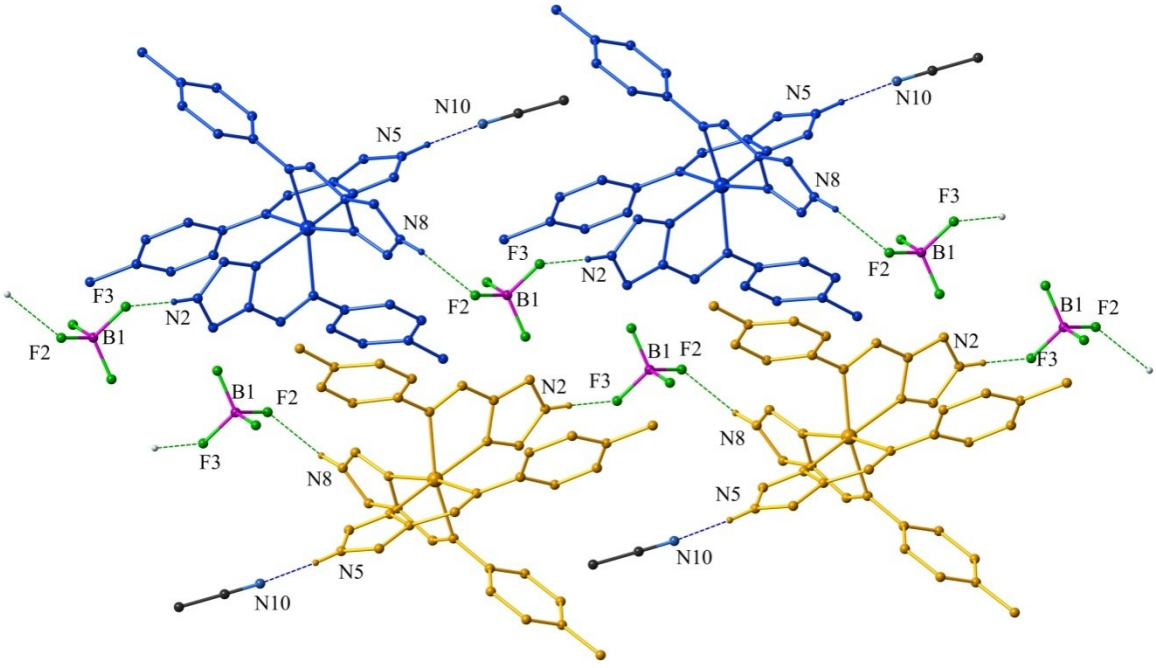

Fig 4.3.19: *Packing diagram of complex* ***4.13*** *at 120 K showing the hydrogen bonding interactions between complexes within the crystal lattice. Hydrogen atoms and counter-anions not involved in hydrogen bonding have been omitted for clarity. The complexes arrange in layers of the Δ-isomer* ***(blue)*** *and the Λ-isomer* ***(yellow)****.*

	4.13 -120 K
Space Group	*P-1*
Unit Cell Volume ($Å^3$)	1929.63(15)
Av. Fe-N Bond Length (Å)	2.19
Σ (°)	96.9
Φ (°)	5.91

Table 4.3.20 *Selected geometric parameters for the Fe-N coordination bonds in* ***4.13*** *at 120 K.*

4.3.8 Discussion and Trends

During this study, a series of Fe(II) mononuclear complexes were synthesised utilising the ligands **L4.1** – **L4.5**. The ligands in this series all coordinate to Fe(II) centres in a bidentate manner, with three ligands arranged in a meridional fashion about the six-coordinate metal ion in the solid-state. The same crystallisation procedure was used to isolate complexes **4.7** – **4.13** in an attempt to maintain similar crystal lattice environments. Unfortunately, this attempt was ultimately unsuccessful with a variety of different crystal packing motifs being observed within the study.

This is illustrated particularly well with the comparison between complexes **4.6** – **4.8**. Once again all three of these complexes contain three *para*-methoxy substituted ligands (**L4.1**), coordinated in a meridional fashion about the Fe(II) centre. Changing the counter-anion from ClO_4^- (**4.6**) to BF_4^- (**4.7**) does little to alter the structural properties of the complex. Both complexes display crystallographic evidence of SCO with low temperature diffraction data showing significant contraction of the coordination sphere compared with the high temperature diffraction data. Indeed, only minor changes are observed between the two structures, the most noticeable of which are the consistently shorter hydrogen bond lengths observed in **4.7** compared to the ClO_4^- analogue **4.6** and the longer average coordination bond length observed in **4.7** at low temperature. The difference in the coordination bond lengths between the two structures can be easily attributed to SCO that is not fully complete at 120 K in complex **4.7**. Other crystallographic geometric parameters (Σ and Φ) are also larger in **4.7** suggesting that the Fe(II) centre is not fully LS at 120 K.

Mononuclear Fe(II) complexes formed with the ligand **L4.1** (**4.6** – **4.8**) showed interesting structural diversity. While **4.6** and **4.7** were isostructural, complex **4.8** revealed remarkably different crystal packing behaviour within the solid state. Bulk structural changes occur within the crystal lattice including a crystal system change from triclinic to monoclinic and the inclusion of an acetonitrile solvent molecule which is involved in a hydrogen bonding interaction to one of the imidazole head groups. Rather than forming hydrogen bonding dimers as observed in **4.6** and **4.7**,

in complex **4.8** two complexes intercalate, with the methoxy-benzene tail group becoming encased by the other complex forming C-H···π interactions between the methoxy unit and the adjacent phenyl rings. It is this interaction which appears to be responsible for the elongated Fe-N coordination bond lengths, and as such the HS nature of the complex at 120 K.

Complexes **4.9** and **4.10** also explore the subtle effects of the counter-anion on the SCO behaviour, along with altering the *para*-substituent from methoxy to methyl, subtly altering the electronic properties of the ligand. Both **4.9** and **4.10** are isostructural with each other and share similar solid state structures with **4.6** and **4.7**. There is the inclusion of acetonitrile molecule within the crystal lattices of both **4.9** and **4.10** which is not present in either **4.6** or **4.7**, however, this solvent molecule only forms a weak interaction to the imidazole N-H moiety (donor-acceptor distance is greater than 3.1 Å in both **4.9** and **4.10**) and does not appear to result in any considerable changes in the arrangement of complexes within the crystal lattice. Indeed, **4.9** and **4.10** both form pairs of complexes through hydrogen bonding interactions in a similar manner to **4.6** and **4.7**. The counter-anion that is not involved in this interaction is disordered in both complexes **4.9** and **4.10** slightly affecting the hydrogen bonding interactions to the imidazole head group, however, this is not perpetuated through the lattice. Both complexes also show significant contraction of the coordination sphere at 120 K, consistent with a crossover of the Fe(II) centre into the LS state. A similar difference between the BF_4^- and ClO_4^- anions is observed with **4.9** appearing to not fully contact into the LS state at 120 K whereas the coordination bond lengths for **4.10** are consistent with a fully isolated LS state at 120 K.

The last three complexes were all found to be HS at the diffraction temperature of 120 K. In order to ascertain whether there was potential for SCO behaviour, acetonitrile solutions of the three complexes were immersed in liquid N_2. Only **4.11** showed a vivid colour change consistent with SCO. There were no apparent colour changes for either **4.12** or **4.13** suggesting that the complexes would remain exclusively in the HS state, as such no further analysis was completed on these two complexes. Interestingly, all three of these complexes also show different crystal packing motifs despite the method of crystallisation being held constant. The three complexes show the formation of linear hydrogen-bonding networks (either 1D-chains or 2D-sheets) are preferred over the dimer formations found in complexes **4.6**, **4.7**, **4.9**, **4.10**.

In summary, the complexes **4.7**, **4.9**, **4.10**, and **4.11** showed potentially interesting SCO behaviour and as such the magnetic behaviour of these complexes were analysed *via* variable temperature magnetic susceptibility measurements and will be discussed in the following section.

4.4 Variable Temperature Magnetic Susceptibility Measurements

*4.4.1 Variable Temperature Magnetic Susceptibility Measurements of Complex **4.7***

Intrigued by the structural data for **4.7**, variable temperature magnetic susceptibility measurements were performed in order to fully elucidate its SCO behaviour. The magnetic susceptibility was measured in both heating and cooling modes under a 1 T magnetic field. At room temperature the χT product is approximately 3.6 cm^3 K mol^{-1} which is in good agreement with a HS Fe(II) centre. Upon cooling, the χT value remains constant to a temperature of approximately 180 K. At this temperature the sample undergoes SCO to the LS state, illustrated by the *S*-shaped curve of χT *vs.* *T* typical of a SCO process (**Fig 4.4.1**). At 80 K the SCO is complete and the χT value lies very close to zero cm^3 K mol^{-1} as anticipated for a LS Fe(II) centre. A very small paramagnetic signal is observed at *ca.* 0.1 cm^3 K mol^{-1}, which is likely to be due to a small paramagnetic impurity within the bulk crystal sample. This paramagnetic impurity is estimated at 2.9% of the bulk sample. The $T_{1/2}$ for the SCO is approximately 123 K (see **Fig A-IV.2.3**) and both the cooling and heating modes trace the same curve indicating that the SCO is reversible.

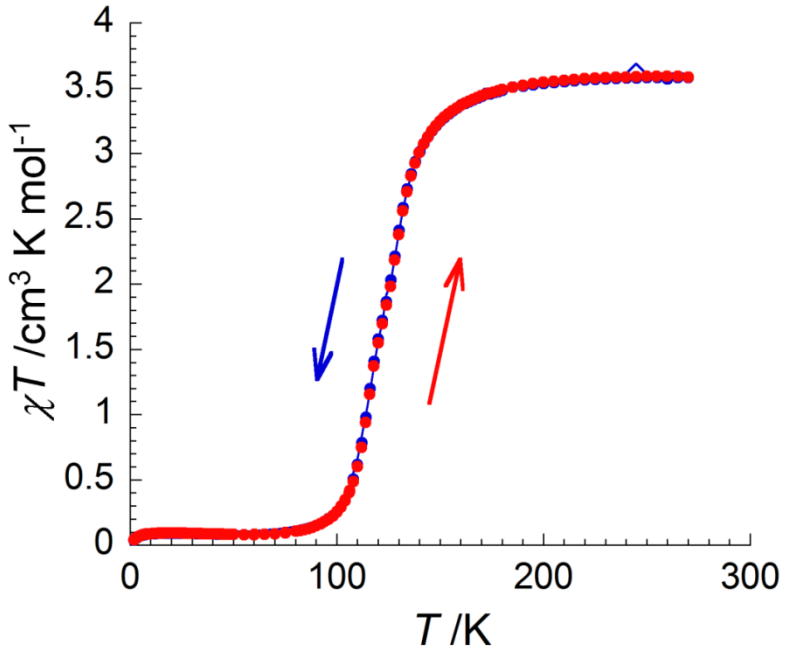

***Fig 4.4.1** Variable temperature magnetic susceptibility measurement for complex **4.7** as measured under a 1 T magnetic field in cooling mode (**blue dots**) and heating mode (**red dots**).*

*4.4.2 Variable Temperature Magnetic Susceptibility Measurements for Complex **4.8***

The crystallographic structural analysis of complex **4.8** indicated that the Fe(II) centre remained in the HS state at 120 K, despite both of the related complexes **4.6** and **4.7** showing SCO. In light of this intriguing behaviour, variable temperature magnetic susceptibility measurements were completed in order to fully elucidate the magnetic properties of this complex. Initial magnetic susceptibility measurements at 250 K have a χT value of 3.4 cm^3 K mol^{-1}, consistent with an Fe(II) centre in the HS state. As the temperature decreases there is no corresponding change in the magnetic moment. The decrease in χT value below 30 K is typical for exclusively HS systems and is likely due to zero field splitting effects experienced by HS Fe(II) centres. This indicates that the system remains HS at all temperatures and does not undergo SCO, consistent with the crystallographic data. The χT *vs.* T plot is illustrated in **Fig 4.4.2**.

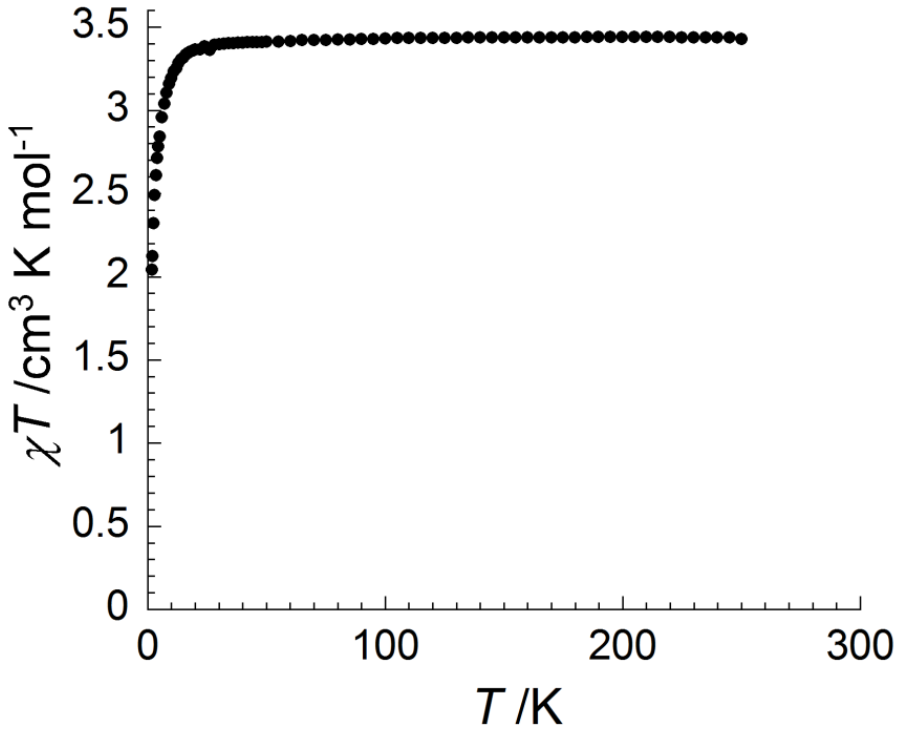

***Fig 4.4.2** Variable temperature magnetic susceptibility measurements for complex **4.8**, measured in cooling mode.*

*4.4.3 Variable Temperature Magnetic Susceptibility Measurements for Complex **4.9***

Given the crystallographic evidence for potential SCO behaviour with **4.9**, variable temperature magnetic susceptibility measurements were undertaken. These measurements show unusual

behaviour in that approximately 50% of the sample undergoes SCO to the LS state quite readily with a $T_{1/2}$ of *ca.* 199 K. After this point approximately 35% of the remaining sample undergoes a gradual conversion into the LS state, with a $T_{1/2}$ of *ca.* 76 K. The χT value plateaus at approximately 0.5 cm^3 K mol^{-1} indicating a residual paramagnetic impurity of *ca.* 15%. In order to probe this dynamic behaviour the magnetic moment of the sample was measured during a full cooling and heating cycle (270 K – 1.8 K – 270 K) at 0.7 K min^{-1} (black and red traces in **Fig 4.4.3**). After this period the sample was quickly cooled to 15 K and then reheated to 270 K at 0.7 K min^{-1}. From the data the cooling and heating modes track out the same curve and show no hysteretic properties. The fast cool down quenches a portion of the sample in the HS state, as indicated by the increase χT value to *ca.* 0.7 cm^3 K min^{-1} as shown by the green trace in **Fig 4.4.4**. As the sample is heated after the quenching has occurred, the SCO behaviour of the sample alters with the complex undergoing a lower energy crossover to the HS state between 70 K and 170 K. After approximately 180 K the remaining Fe(II) centres in the sample convert to the HS state in the same manner observed during the initial scan. The sample was subsequently cooled again to 1.8 K with the SCO behaviour returning to a similar process to that observed during the initial cooling and heating cycle, but with a greater portion of the sample remaining in the HS state due to the quenching process.

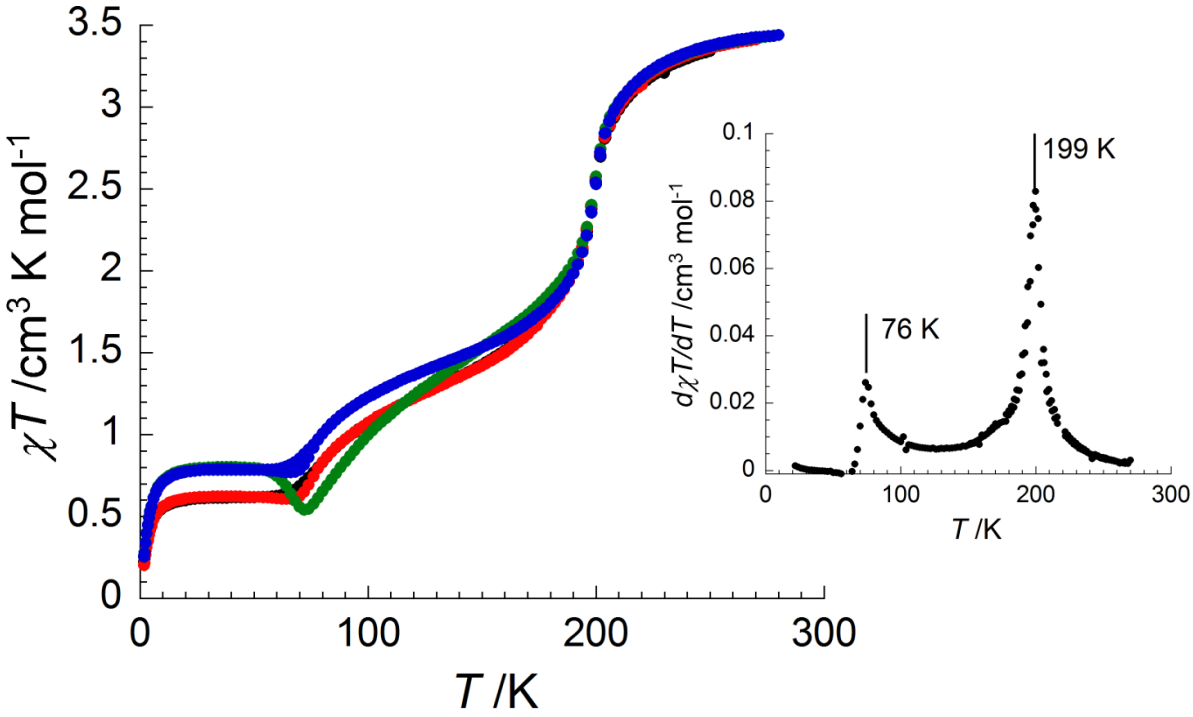

Fig 4.4.3 *Variable temperature magnetic susceptibility measurements for* ***4.9*** *measured at a scan rate of 0.7 K* min^{-1} *over multiple heating and cooling runs. Initial cooling run 270 K – 1.8 K at 0.1 T (**black trace**); return heating run at 1 T (**red trace**); heating mode to 270 K after the sample was quenched at 15 K (**green trace**); cooling mode after the sample was quenched at 15 K (**blue trace**). **Inset**: Derivative plot showing the two-step nature of the SCO behaviour.*

Given the inclusion of solvent molecules within the crystal lattice that were not present in **4.6** or **4.7**, a second measurement was competed using crystals layered with a small amount of mother liquor. This technique was employed to minimise the effect of solvent loss on the sample during the experiment, the results of which showed the same behaviour as for the freshly filtered sample.

*4.4.4 Variable Temperature Magnetic Susceptibility Measurements for Complex **4.10***

In order to fully characterise the magnetic properties of **4.10**, variable temperature magnetic susceptibility measurements were undertaken for freshly filtered crystals in both cooling and heating modes at a sweep rate of 0.7 K min^{-1}. At 270 K the χT value is *ca.* 3.5 cm^3 K mol^{-1}, consistent with Fe(II) in the HS state. As the temperature decreases the χT value decreases with a slightly atypical curve. This curve is indicative of a two step crossover with approximately half the sample undergoing SCO with a $T_{1/2}$ of 184 K and the remaining portion of the sample converts to the LS state with a $T_{1/2}$ of 158 K. This is shown in the second derivative inset plot below (**Fig 4.4.4**). Fortunately, the ClO_4^- analogue **4.10** is considerably better behaved than **4.9** with the entire sample entering the LS state below 90 K with very few paramagnetic impurities. The heating mode traces the same curve as that for the cooling mode showing that this behaviour is reversible including the two-step behaviour of the bulk sample.

Given that crystal lattice interactions have been found to have a marked effect on SCO behaviour, the sample was gently dried at 50 °C under vacuum for 7 days. Thermogravimetric analysis confirms the loss of *ca.* 4% mass of the sample consistent with the loss of the acetonitrile solvent within the crystal lattice. The variable temperature magnetic susceptibility experiment was repeated on the desolvated compound with a scan rate of 0.7 K min^{-1}. At 270 K the χT value is *ca.* 3.8 cm^3 K mol^{-1} consistent with Fe(II) in the HS state. The χT value stays constant as the temperature decreases to 100 K. At this temperature a very sharp spin transition occurs to the LS state. The LS state is fully occupied with a χT value approaching 0 cm^3 K mol^{-1} by approximately 80 K. The heating mode shows a narrow thermal hysteresis with a loop width of approximately 10 K and the transition back into the HS state is also particularly sharp.

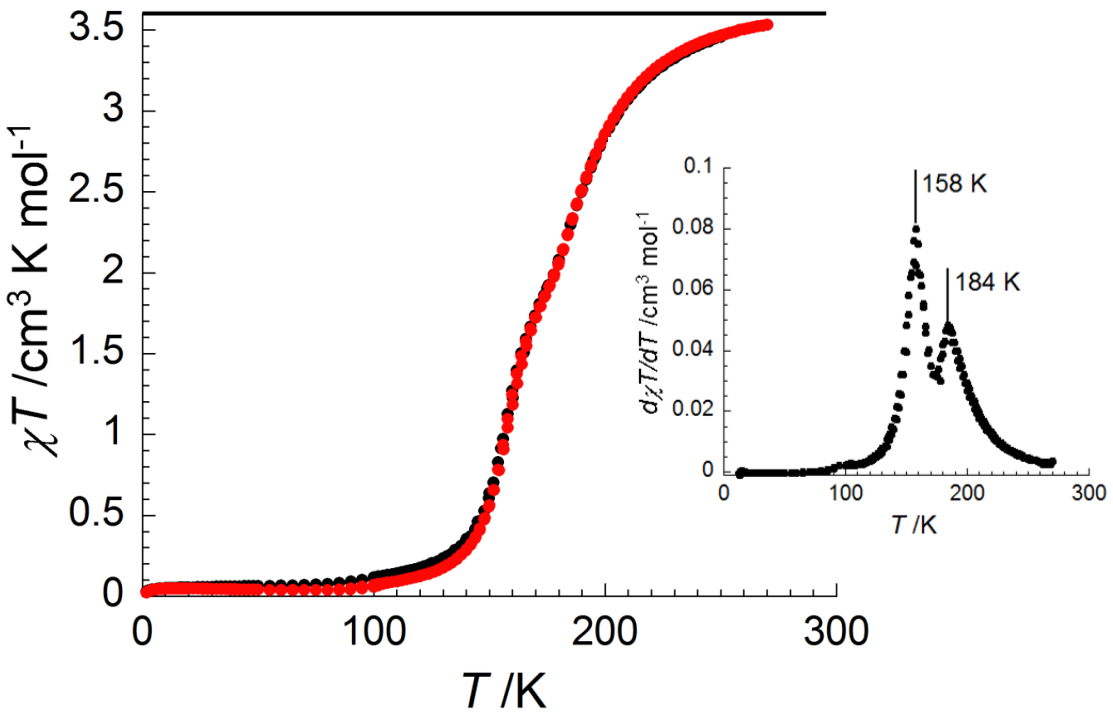

Fig 4.4.4 *Variable temperature magnetic susceptibility measurements for* ***4.10*** *showing cooling mode from 270 – 1.8 K under a 0.1 T magnetic field (**black dots**) and the return heating mode under a 1 T magnetic field (**red dots**). Measured with a scan rate of 0.7 K min^{-1}.*

Inset: *Derivative plot showing the two step nature of the SCO behaviour.*

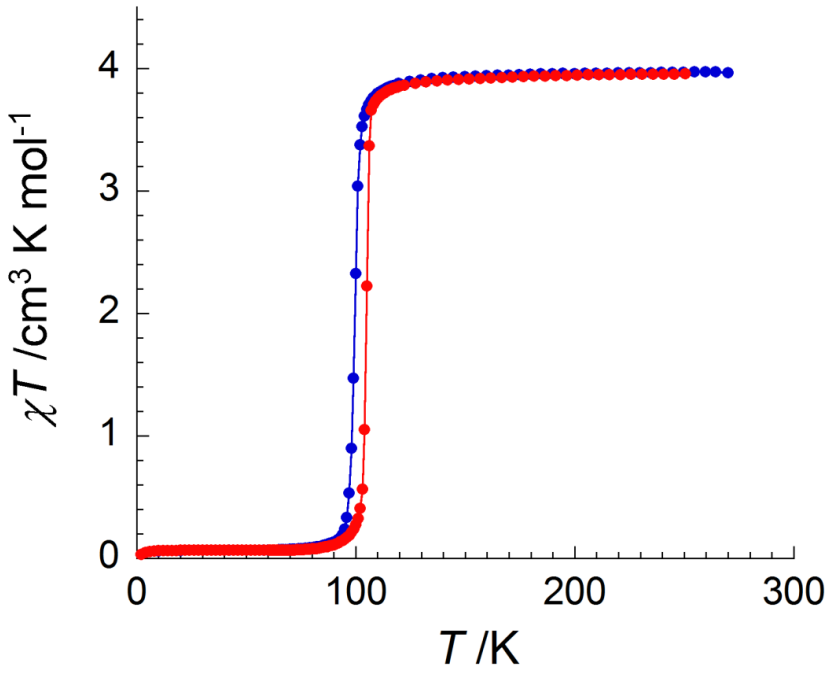

Fig 4.4.5 *Variable temperature magnetic susceptibility measurements on* ***4.10-Dried*** *measured with a scan rate of 0.7 K min^{-1} and under a 1T magnetic field from 270 – 1.8 K during cooling mode (**blue dots**) and heating mode (**red dots**).*

*4.4.5 Magnetic Susceptibility Measurements for Complex **4.11***

Complex **4.11** utilising the *para*-bromo substituted ligand **L4.3**, was found to be HS at 120 K through structural determination *via* single crystal X-ray diffraction. However, immersion of an acetonitrile solution of the complex in liquid N_2 causes a significant colour change consistent with SCO behaviour. In light of this, variable temperature magnetic susceptibility measurements were undertaken to elucidate to potential for SCO to occur below the X-ray diffraction temperature. The results of this experiment revealed partial SCO behaviour which varies depending on the nature of the crystalline material. The initial measurements were performed on a freshly filtered sample and the χT value at 250 K was approximately 3.7 cm^3 K mol^{-1}, as anticipated for Fe(II) centre in the HS state. As the temperature was decreased, the χT value decreased in a gradual fashion until reaching a plateau at approximately 3.1 cm^3 K mol^{-1}. This can be described as SCO in less than 10% of the overall bulk sample. Given that some time had progressed between the synthesis of the complex and the subsequent magnetic measurements, the sample was recrystallised and the experiment repeated. As the crystals contain the highly volatile solvent dichloromethane, the second sample was prepared with the crystals layered with a small amount of mother liquor in attempt to halt the loss of solvent from within the crystal lattice. The second repetition of the experiment provided similar results with the sample still showing a gradual decrease in the χT value from approximately 3.7 cm^3 K mol^{-1} at 250 K to approximately 2.2 cm^3 K mol^{-1} at 80 K.

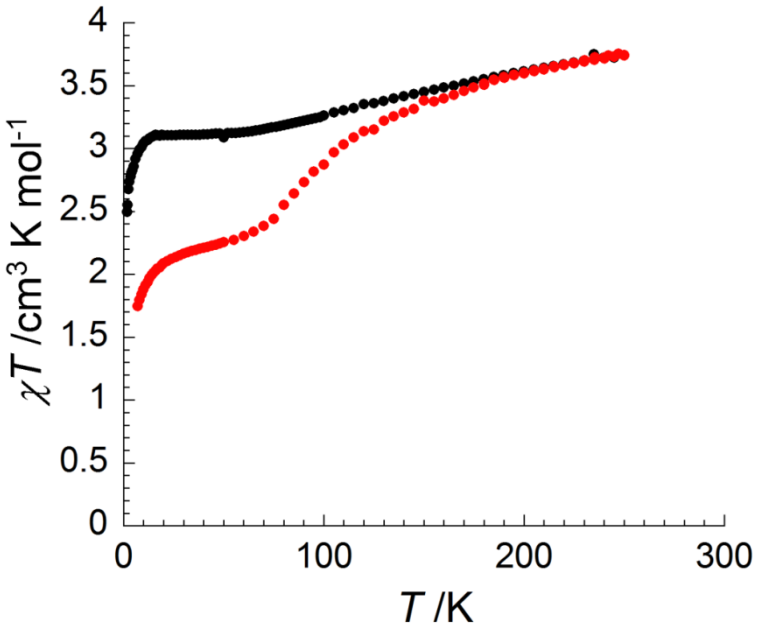

***Fig 4.4.9** Variable temperature magnetic susceptibility measurements for **4.11** in the cooling mode from 250 – 1.8 K, showing the SCO behaviour for a freshly filtered sample (**black dots**), and a recrystallised sample of **4.11**, with the crystals layered with mother liquor during the experiment to prevent solvent loss (**red dots**).*

4.4.6 Summary

From the magnetic susceptibility data discussed in this section a variety of different SCO behaviours were exhibited. Complex **4.7** showed very similar SCO behaviour to the analogous compound **4.6**, with the $T_{1/2}$ shifted approximately 30 K lower than the ClO_4^- complex. **4.8** exhibited purely HS behaviour, consistent with the crystallographic evidence for this complex. Interestingly, complexes **4.9** and **4.10** both exhibited two-step behaviour with the process being particular dynamic in complex **4.9**. Due to the complexity of this behaviour no further analysis was completed on this complex. Drying complex **4.10** resulted in a significant change in the SCO behaviour, with the two-step transition being replaced with an abrupt spin transition with a thermal hysteresis width of approximately 10 K centred about 100 K. Finally, **4.11** did show partial SCO behaviour consistent with the thermochromic behaviour observed in acetonitrile solution. However, the behaviour is particular susceptible to solvent loss and as such no further analysis was undertaken.

Given the impressive SCO behaviour exhibited by **4.7** and **4.10-Dried**, these two complexes were further analysed to investigate the photo-induced SCO properties of these complexes.

4.5 Variable Temperature Surface Reflectivity Measurements

*4.5.1 Variable Temperature Surface Reflectivity Measurements of Complex **4.7***

Given the reversible SCO behaviour observed for complex **4.7**, surface reflectivity measurements were conducted in order to investigate any light induced spin crossover behaviour. The initial experiment consisted of measuring the reflectivity of approximately 5 mg of freshly filtered crystals during a cooling run at 4 K min^{-1} from 270 K to 10 K, followed by a return heating run to 270 K at the same rate. The measurements were conducted under weak white-light irradiation of 0.4 mW cm^{-2} from the spectroscopic source. As the temperature decreases from 270 K to 100 K, the reflectivity in the visible region around 600 – 700 nm also decreases while the near infrared (NIR, > 800 nm) component increases leading to the presence of an isosbestic point at 768 nm; consistent with SCO from the HS to the LS state. Selected reflectivity spectra as a function of temperature in the cooling mode are illustrated in **Fig 4.5.1**. The thermal SCO occurs with a $T_{1/2}$ of approximately 120 K and is reversible, as seen previously in the magnetic susceptibility experiments even after multiple experimental runs on the same sample. Further selected reflectivity spectra illustrating the heating mode are provided in **A-IV.2.4a**.

By probing the NIR component at 900 nm it is possible to investigate the evolution of the reflectivity of the LS state with varying temperature. The reflectivity at 900 ± 5 nm (R_{900}) shows a constant value of approximately 0.17 while cooling from 270 K to 150 K. The sample is further cooled and the reflectivity at 900 nm increases to *ca.* 0.28, a signature of the thermally induced SCO behaviour observed both magnetically and crystallographically (reflectivity plot for R_{900} is provided in **A-IV.2.4b**). There is a slight decrease in the reflectivity below 60 K due to a small photoexcitation contribution of the sample. This contribution is small under the low power light conditions for the experiment (0.4 mW cm^{-2}).

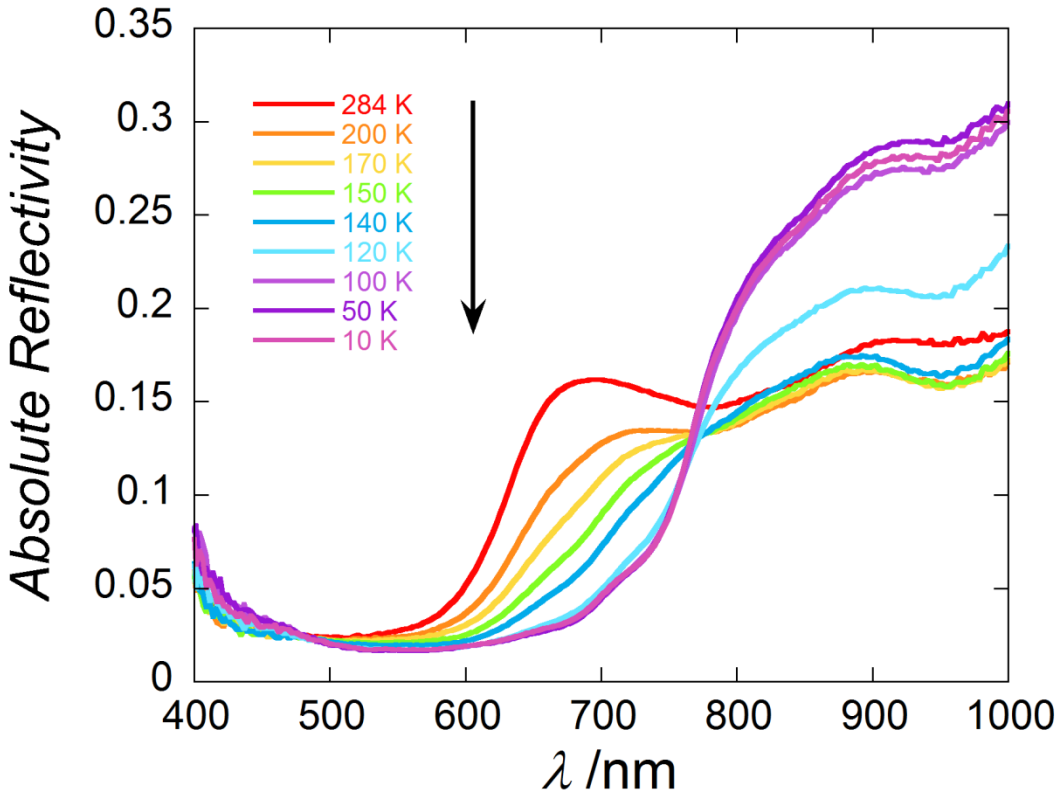

Fig 4.5.1 *Selected variable temperature surface reflectivity measurements for* ***4.7*** *in cooling mode between 270 K and 10 K, at a rate of 4 K* min^{-1} *and under a spectroscopic white light source of 0.4 mW* cm^{-2}.

In order to further probe the light excitation behaviour of complex **4.7**, an experiment was conducted where the sample was cooled from 270 K – 10 K at 4 K min^{-1} and irradiated with 0.4 mW cm^{-2} white light for 180 minutes at 10 K. The sample was then heated at 4 K min^{-1} to investigate the thermal relaxation of the excited state. Inspection of the R_{900} curve under these conditions showed a significant decrease in the reflectivity at 10 K from 0.28 to 0.18 after irradiation with white light, illustrating that **4.7** is sensitive to white light with photoexcitation of the complex into the HS state. This excitation is close to, but not fully complete under these

conditions with the HS state analysed at the beginning of the experiment having a reflectivity of 0.16. As the temperature is increased after light activation the sample undergoes thermal relaxation back into the LS state by 70 K. The variable temperature surface reflectivity plot for this experiment is provided as supplementary information in **A-IV.2.4c**.

Impressed by the photoexcitation of this compound under white light, an experiment was conducted to optimise the conditions using 14 different LED light probes, which ranged from 365 to 1050 nm. For each wavelength, the measurements were conducted at 10 K with light irradiation (0.8 mW cm^{-2}) for 5 minutes. This experiment showed the greatest change in reflectivity occured with red light of 625 nm (**Fig A-IV.2.4d**). Using this information, the sample was irradiated at 10 K with 0.8 mW cm^{-2} red light (625 nm). After this irradiation, the sample showed a significant decrease in the reflectivity from 0.28 to 0.16, with red light being considerably more active than the white light previously tested (**Fig 4.5.2**). Under red light irradiation the sample reached saturation after approximately 90 seconds versus nearly 180 minutes for white light irradiation (both saturation curves are provided in **A-IV.2.4e**). The thermal relaxation of the sample once again occurs as the sample is heated to 90 K as observed with the white light photoactivation.

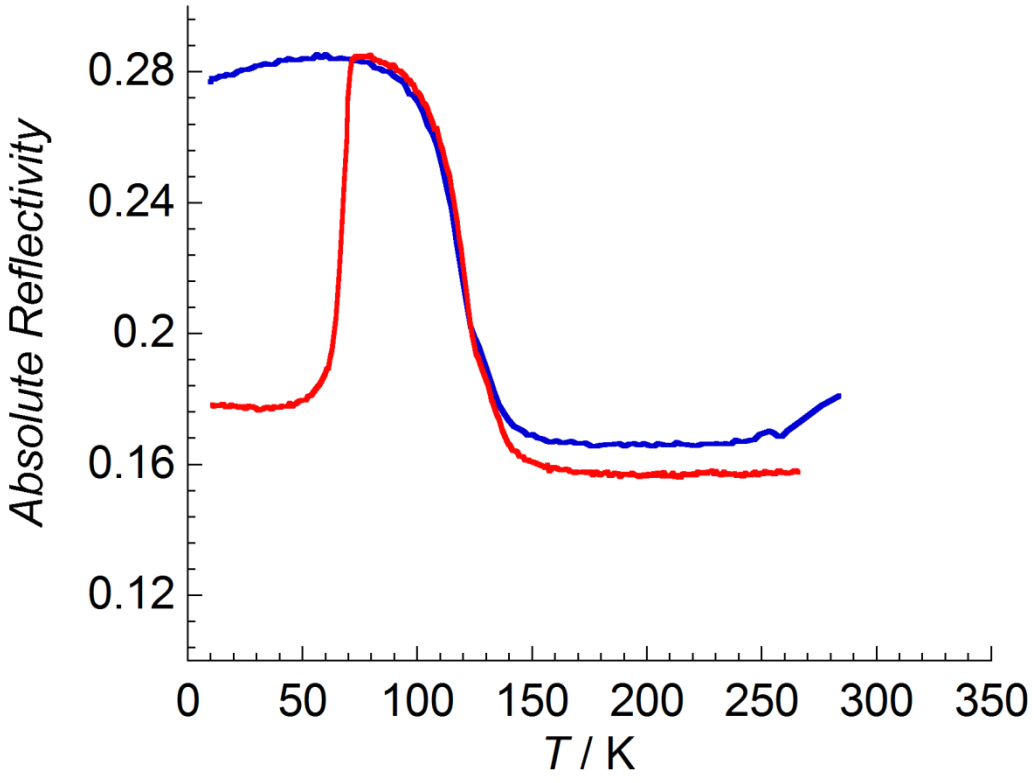

Fig 4.5.2 *Thermal evolution of reflectivity signal for* ***4.7*** *recorded at λ = 900 ± 5 nm for the cooling mode 270 – 10 K (**blue trace**) and heating mode after red light irradiation at 10 K (**red trace**). Measured with a scan rate of 4 K min^{-1} and 0.8 mW cm^{-2} red light source of 625 nm at 10 K for 180 minutes.*

*4.5.2 Variable Temperature Surface Reflectivity Measurements for Complex **4.10-Dried***

The optical properties of **4.10-Dried** were examined in order to more fully characterise the SCO behaviour of this compound. The surface reflectivity of a crushed crystalline sample was measured under a weak light irradiation of 0.4 mW cm^{-2} and a scanning rate of 4 K min^{-1}. As observed in the previous example as the temperature decreases from 270 K down to 100 K, the reflectivity in the NIR region increases while the visible component decreases (**Fig 4.5.3**) resulting in a tight isosbestic point around 810 nm. These changes are consistent with thermal SCO behaviour as exhibited in both the magnetic susceptibility and crystallographic studies.

In order to more closely investigate the photo-induced SCO behaviour of **4.10–Dried**, surface reflectivity measurements were carried out under light irradiation conditions. Cooling the sample from 270 – 140 K under light irradiation of 0.4 mW cm^{-2} shows that the absolute reflectivity of the HS state at 700 nm (R_{700}) stays relatively constant at 0.34. Between 140 and 110 K the reflectivity quickly decreases to 0.23 indicative of an abrupt SCO from the HS state to the LS state. A small plateau occurs in the LS state as the temperature cools to around 60 K and as the sample is further cooled the reflectivity increases back to 0.25, consistent with a small contribution of photoexcitation of the sample into the HS state (**Fig A-IV.2.5a**).

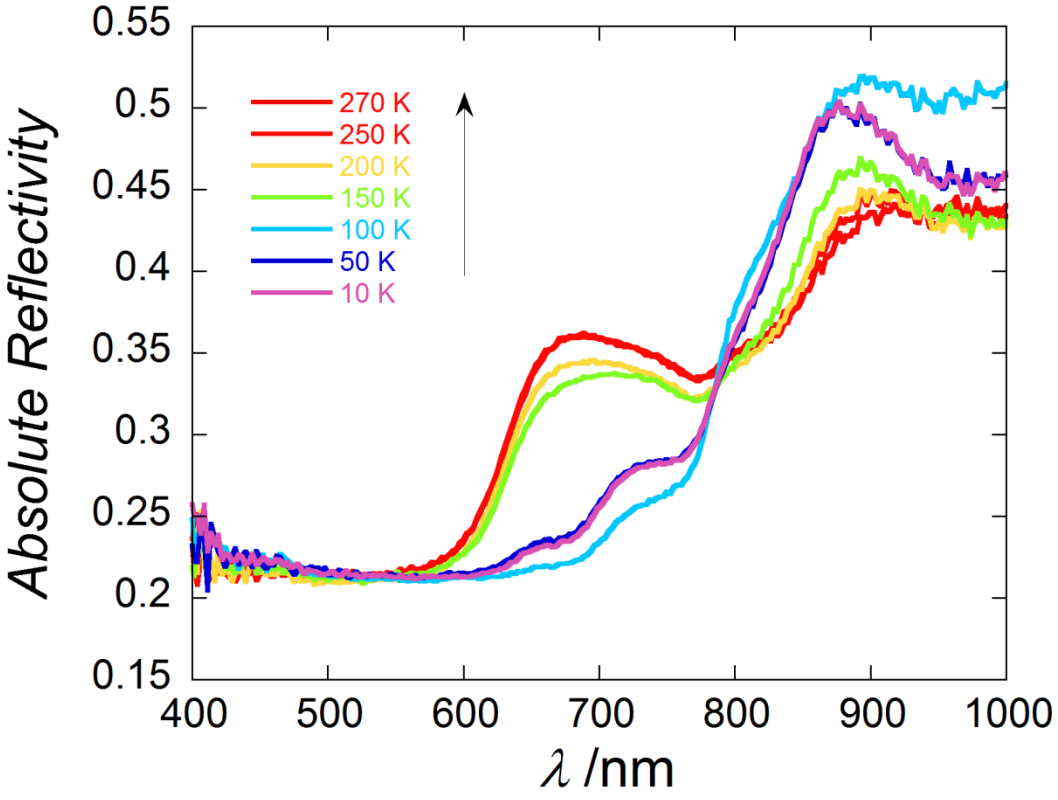

***Fig 4.5.3** Selected variable temperature surface reflectivity measurements for **4.10-Dried** in heating mode between 270 K and 10 K, at a rate of 4 K min^{-1} and under a spectroscopic white light source of 0.4 mW cm^{-2}.*

The reflectivity at 700 nm (R_{700}) is in good agreement with the magnetic susceptibility curve as illustrated in **Fig 4.5.4**. Irradiation with a 0.4 mW cm^{-2} white light source for 210 minutes at 10 K revealed the same increase in the absolute reflectivity indicative of full photoexcitation into the HS state (**Fig 4.5.5**) with the sample becoming saturated after approximately 60 minutes of white-light irradiation. (**A-IV.2.5b**).

To optimise the photoexcitation behaviour of this complex, the sample was irradiated with a series of 14 LED light sources ranging from 365 – 1050 nm. As with the complex **4.7**, red light of wavelength 625 nm was found to be the most active (**Fig A-IV.2.5c**). Upon irradiation of the sample with 625 nm light of 0.8 mW cm^{-2} power for 2 hours, the sample undergoes full excitation into the HS as shown in **Fig A-IV.2.5d**. Although red light was successful for photoinduced SCO behaviour, the white light conditions were used for subsequent measurements.

In summary, both complexes **4.7** and **4.10** exhibit impressive photo-induced SCO behaviour and as such their photomagnetic behaviours were analysed further the results of which are discussed in the following section.

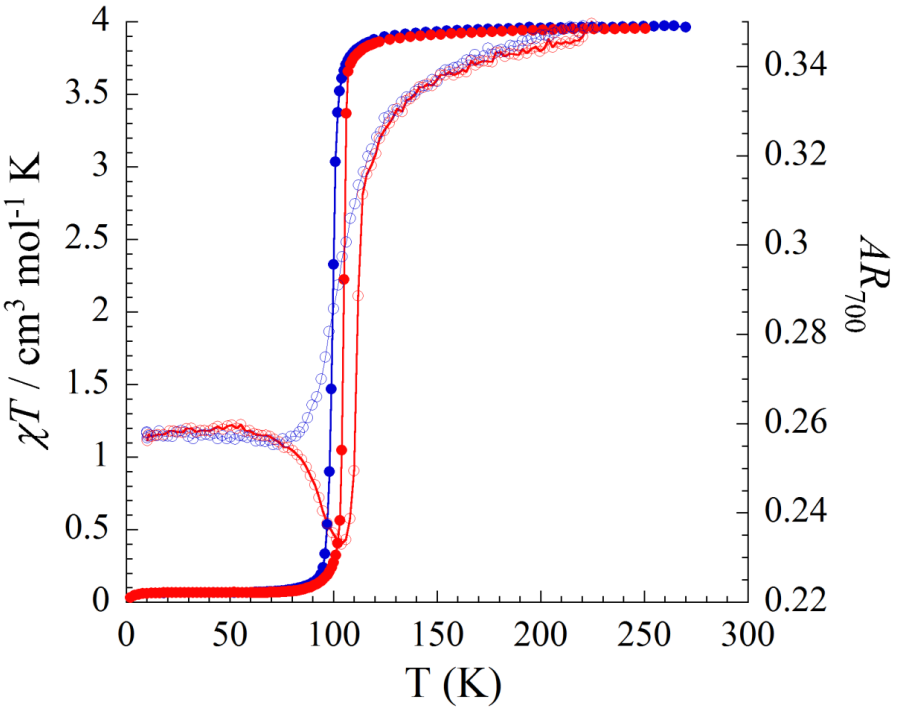

Fig 4.5.4 *Overlay of the magnetic susceptibility data for* ***4.10-Dried*** *with the reflectivity at 700 nm. Magnetic susceptibility data cooling mode (**blue filled circles**) and heating mode (**red filled circles**); Reflectivity data in cooling mode (**blue open circles**) and heating mode (**red open circles**). Scan rate 4 K min^{-1} and white light spectroscopic source (0.4 mW cm^{-2}).*

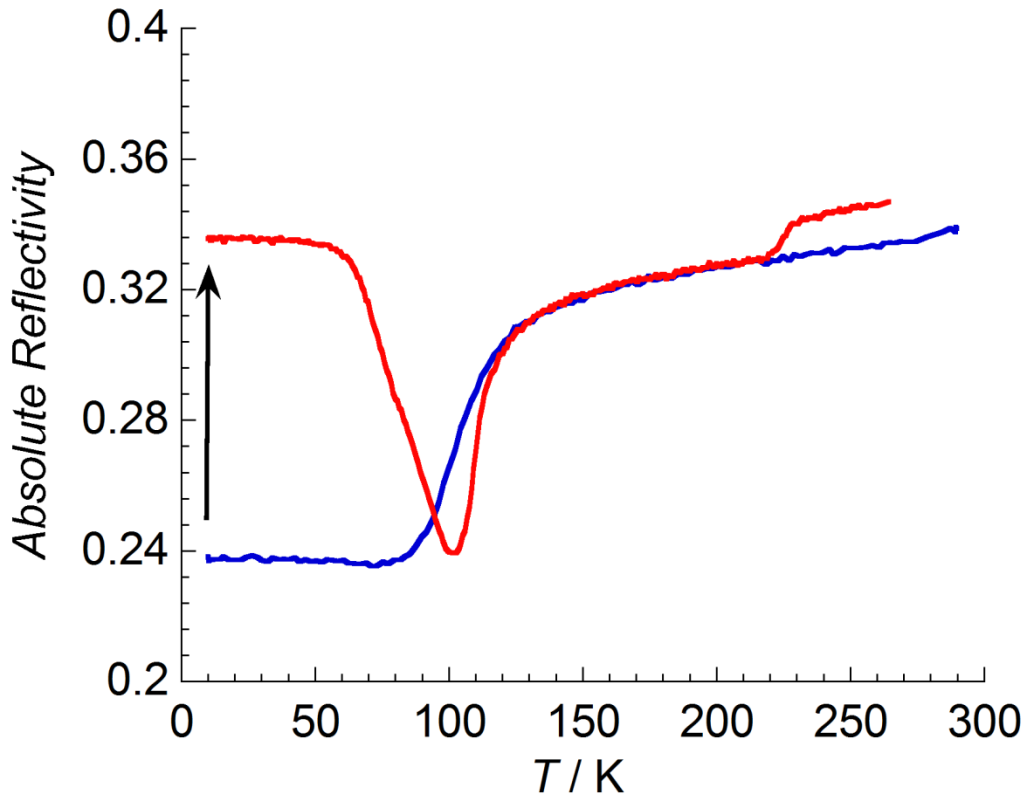

Fig 4.5.5 *Thermal evolution of the reflectivity signal of* ***4.10-Dried*** *recorded at λ = 700 ± 5 nm during cooling mode (**blue trace**) and after white light irradiation at 10 K during heating mode (**red trace**). Measured with a scan rate of 4 K min^{-1} and 0.4 mW cm^{-2} white light at 10 K for 3.5 hours.*

4.6 Photomagnetic Measurements of Complexes 4.7 and 4.10

*4.6.1 Photomagnetic Behaviour of Complex **4.7***

Intrigued by the impressive light activation of **4.7** during the surface reflectivity measurements; photomagnetic measurements were performed on the compound. In order to fully probe the LIESST behaviour, the sample was cooled to 1.8 K and subsequently irradiated with 0.3 mW cm^{-2} white light for 180 minutes. Upon white light irradiation the χT value increase dramatically to 3.9 cm^3 K mol^{-1} consistent with light-induced SCO behaviour. Indeed, the χT value is slightly larger than the initial HS state observed at room temperature which can be attributed to the magnetic anisotropy of the HS state at low temperature. Increasing the temperature at a sweep rate of 0.4 K min^{-1} results in the complete thermal relaxation of the sample to the LS state by 60 K. Reverse-LIESST experiments were also conducted, however, attempts to photo-induce the LS state using NIR light were unsuccessful.

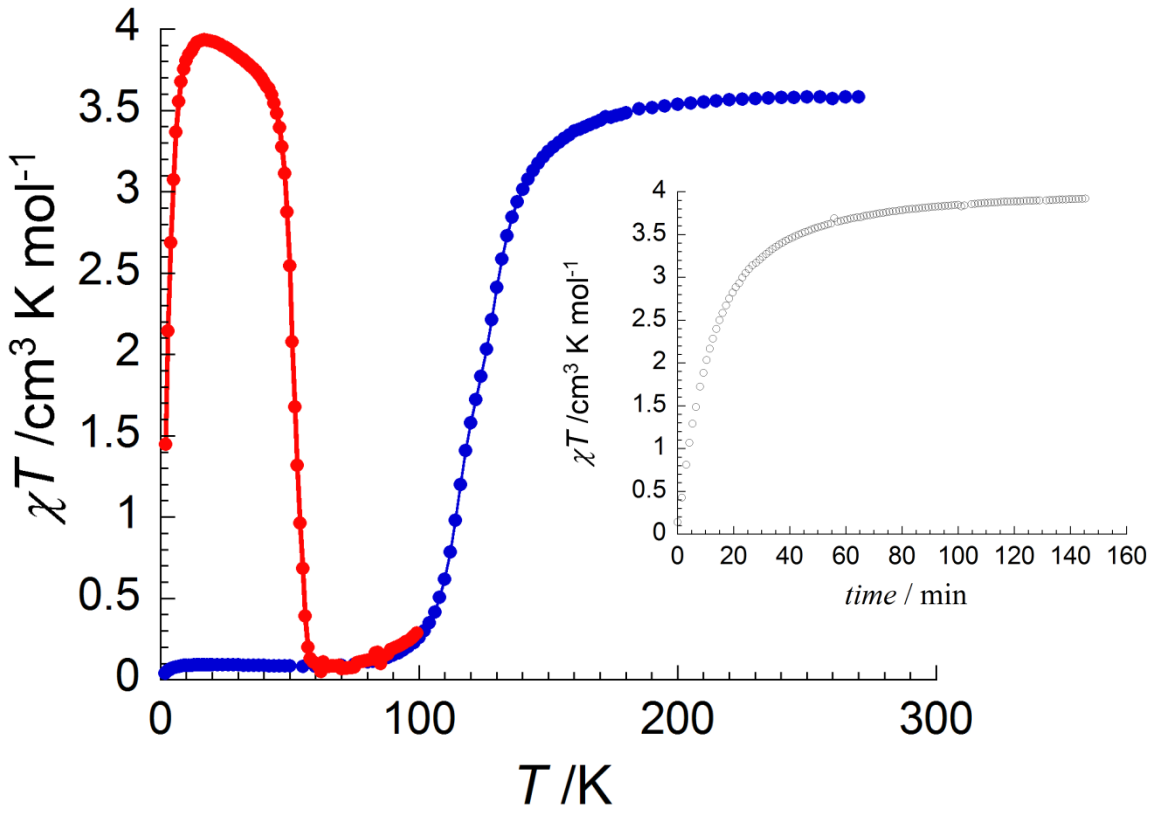

Fig 4.6.1 *χT vs. T plot of* ***4.7*** *in cooling mode under dark conditions (**blue dots**) and under white light irradiation (**red dots**) under 1 T. Measured with scan rate 0.4 K min^{-1} and white light 0.3 mW cm^{-2} at 10 K for 180 minutes.* ***Inset:*** *Time dependence on the χT product with white light irradiation at 10 K under 1 T.*

*4.6.2 Photomagnetic Behaviour of Complex **4.10***

In order to investigate the LIESST properties of **4.10**, photomagnetic measurements were performed on a freshly filtered sample of crystalline material. Initially the photomagnetic measurements were performed on a solvated sample with a scan rate of 0.4 K min^{-1} under 1 T (**Fig 4.6.2**). At 270 K the compound has a χT value of 3.5 cm^3 K mol^{-1}, consistent with a single Fe(II) centre in the HS state. As the temperature decreases the χT value also decreases in a gradual two-step manner with approximately half the sample undergoing a SCO with a $T_{1/2}$ of approximately 180 K. A slight plateau forms before the remainder of the sample transitions into the LS state by 90 K. As anticipated from the optical experiments, a photomagnetic effect is clearly observed when the sample is irradiated with white light. The χT product under 0.5 T starts at 1.8 cm^3 K mol^{-1} and increases to around 3.9 cm^3 K mol^{-1} after approximately 3.5 hours of light irradiation. The higher χT value can be attributed to the paramagnetic complexes aligning within the magnetic field and becoming "frozen" in that configuration. As the temperature increases

above 20 K the χT value decreases as the sample thermally relaxes back to the LS state. At 80 K the χT value is 0.0 cm^3 K mol^{-1} consistent with the compound being fully converted to the LS state.

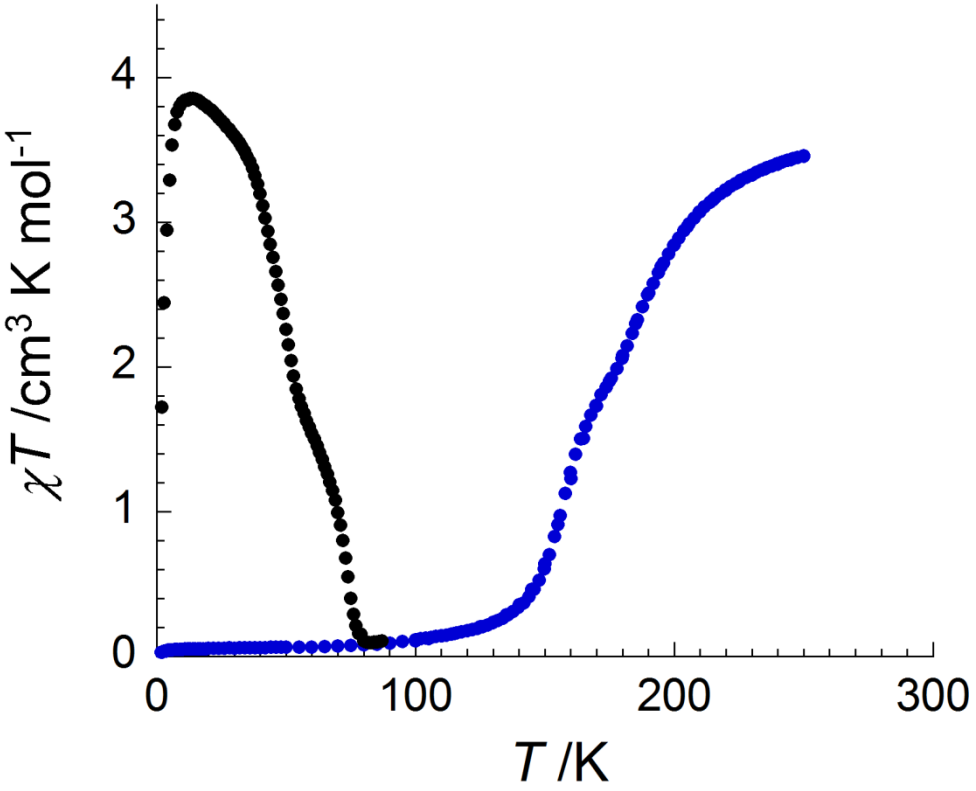

Fig 4.6.2 *χT vs. T plot of* ***4.10-solvated*** *under dark conditions (**blue dots**) and under white light irradiation (**black dots**). Measured with scan rate 0.4 K min^{-1} and white light irradiation of 0.3 mW cm^{-2} over 210 minutes.*

From the magnetic susceptibility measurements it was apparent that the magnetic behaviour altered significantly as the sample dried. In order to compare the LIESST behaviour of both the solvated and the dried compounds a further photomagnetic experiment was completed on a fully dried sample (**Fig 4.6.3**). The dried sample was irradiated with 3mW cm^{-2} white light at 10 K for approximately 210 minutes and during this time the χT moment increased from 1.6 to 3.8 cm^3 K mol^{-1}. This value is equal to that observed at 270 K and indicates that white light excites all the Fe(II) centres into the HS state. Increasing the temperature at a sweep rate of 0.4 K min^{-1} under 1 T, the χT value remains constant to a temperature of approximately 60 K. The complete relaxation of the photo-induced high spin state is observed between 60 – 80 K. Further heating of the sample after white light irradiation shows the χT *vs.* T plot aligning with the original magnetic susceptibility measurements in the heating mode.

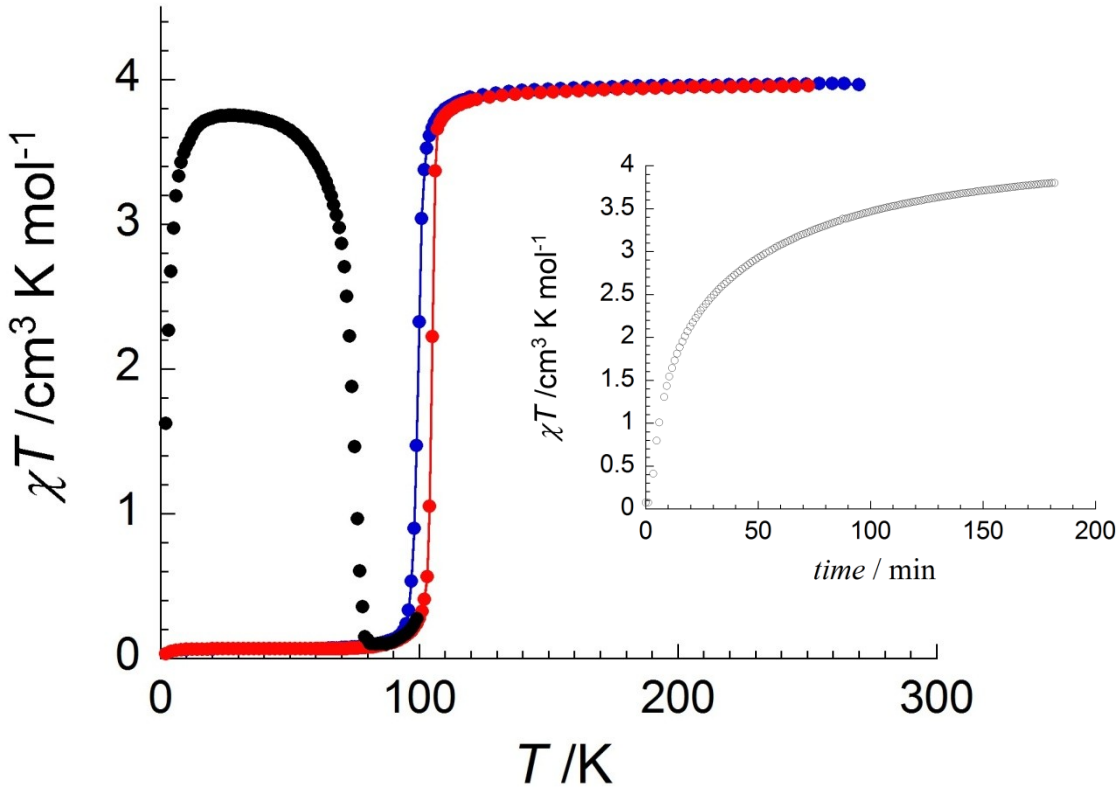

Fig 4.6.3 *χT vs. T plot of* ***4.10-Dried*** *under dark conditions (cooling mode –* ***blue dots****, and heating mode –* ***red dots****) and under white light irradiation (****black dots****). Measured with scan rate 0.4 K min^{-1} and white light irradiation of 0.3 mW cm^{-2} over 210 minutes.* ***Inset****: Time dependence on the χT product with white light irradiation at 10 K under 1 T.*

4.7 Discussion and Conclusions

There is typically some difficulty in assigning structural effects to SCO behaviour as the behaviour is controlled by a complex variety of interactions. The first series of closely related complexes **4.6 – 4.8** provide an interesting insight into these particular relationships. While all three of these complexes are *tris*-chelated complexes utilising ligand **L4.1**, there are some significant changes to the SCO behaviour. The effect of altering the anion from ClO_4^- to BF_4^- was explored in complexes **4.6** and **4.7**. Given the isomorphous nature of both complexes in the solid state any changes in the SCO behaviour may be related to subtle differences within the crystal lattice due to the difference in anions. The variable temperature magnetic susceptibility measurements showed similar behaviour between the two complexes with SCO of the BF_4^- analogue having a $T_{1/2}$ approximately 30 K lower than the ClO_4^- analogue. It is tempting to assign this behaviour to the stronger hydrogen bonding interactions in **4.7** compared to the same hydrogen bonding interactions in **4.6**. The direct comparison between the higher temperature crystal structures for the two complexes in

the HS state show the BF_4^- analogue (**4.7**) has donor-acceptor hydrogen bond lengths within the range 2.829(3) Å to 3.039(3) Å which are consistently shorter than the same bonds in **4.6** (2.922(4) Å to 3.128(4) Å). This is in line with the greater polarising nature of the B-F bond compared to that of the Cl-O bond creating a better electrostatic interaction for the hydrogen bond, thus increasing hydrogen bond strength in the BF_4^- analogue. This stronger hydrogen bond may subtly influence the coordination sphere about the Fe(II) centre and act to stabilise the HS state of **4.7**. The shift in the $T_{1/2}$ values may result from the restriction of the contraction of the metal centre into the LS state. Unfortunately, although the data was of good quality, the X-ray crystallography technique only detects electron density. The locations of hydrogen atoms are modelled based on the residual electron density and as such the systematic error within these values is high. Therefore there is a degree of hesitation in the assignment of the magnetic behaviour to the hydrogen bonding structural difference. In the prediction's favour however, are that other hydrogen bonding compounds of similar N_6 coordination modes show a remarkably similar difference in $T_{1/2}$ between isostructural ClO_4^- and BF_4^- compounds (BF_4^- analogues have a $T_{1/2}$ consistently around 30 K lower than the ClO_4 analogues.[234,296,297]

The loss of SCO behaviour in the related structure **4.8**, shows the sensitive nature of SCO systems to interactions within the crystal lattice. In the solid state, the methoxy-benzene tail units intercalate, creating a steric clash preventing the contraction of the coordination sphere. The methoxy moiety forms C-H···π interactions with the adjacent complex, resulting in the considerable lengthening of the Fe-N_{imine} bond to *ca.* 2.3 Å.

Complexes using the *para*-methyl substituted **L4.2** were synthesised in order to analyse subtle electronic changes to the ligand and how this may affect the SCO behaviour of the resulting complex. Attempts were made to ensure crystallisation conditions were kept consistent between both sets of complexes however, although isostructural to each other, complexes **4.9** and **4.10** were found to contain crystallised solvent molecules that were absent in **4.6** and **4.7**. The crystal lattice structures of both **4.9** and **4.10** share many similar features to the solid-state structures exhibited in **4.6** and **4.7**, yet the SCO behaviour follows a two-step transition rather than the typical one-step SCO behaviour observed in **4.6** and **4.7**. Typically, two-step behaviour is indicative of two crystallographically inequivalent Fe(II) centres being present within the crystal lattice,[173,178,298] however, neither **4.9** nor **4.10** displayed any evidence of crystallographically inequivalent Fe(II) centres. Both complexes show some disorder within the counter-anions and **4.9** also showed disorder in one of the imidazole head groups at 120 K. The disorder in **4.9** was isolated to these entities and no other evidence that the crystallographic space group was incorrect was found. The two-step SCO behaviour is unlikely to be attributed to multiple crystalline phases in the bulk sample as phase purity was measured by testing the unit cell parameters of a representative sample of the compound. Powder X-ray diffraction was not used to determine phase purity as the sample was prone to solvent loss as confirmed by thermogravimetric and micro-analyses. All unit cell

parameters were within statistical variation and matched the initial crystallography. No visible discrepancies were observed between the crystals of the same batch, all crystals were red plate shaped crystals of relatively uniform size.

The cause of the unusually dynamic SCO behaviour exhibited by **4.9** is difficult to ascertain at this stage. There is some precedence in the literature for mononuclear complexes with single unique Fe(II) centres to display two-step spin crossover behaviour.[299,300] Research conducted by Matouzenko and co-workers[299] showed similar two-step behaviour to that exhibited by **4.9** and **4.10**. The behaviour was attributed to disorder within the crystal lattice, with both the counter-anions and atoms within the primary coordination sphere being disordered. It is tempting to attribute the two-step dynamic behaviour of **4.9** and **4.10** to the disorder apparent within the crystal structures. As both complexes are directly hydrogen bonding to the disordered counter-anions this may go some way to explain the two-step behaviour, with the subtly different locations of the counter-anions within the crystal lattice influencing the SCO behaviour of the metal centre. Further detailed crystallographic analysis will be required to determine the exact cause of this behaviour.

The ClO_4^- analogue **4.10** is considerably better behaved than **4.9** and also exhibits the two-step behaviour shown above with $T_{1/2}$ values of 184 and 158 K, respectively. Interestingly, when dried the SCO behaviour becomes abrupt and includes a small (*ca.* 10 K) thermal hysteresis loop, centred around 100 K. Unfortunately, structural analysis *via* single crystal X-ray diffraction on the dried sample was unsuccessful due to the complex losing single crystallinity during the drying process and as such it is difficult to ascribe this differing behaviour to any particular structural effect. However, in attempt to gain some understanding into this behaviour a sample of **4.10-Dried** was analysed *via* X-ray powder diffraction (**Fig 4.7.1**). The powder diffraction revealed that the structure of the dried sample deviates from the solvated form. This is consistent with the loss of single crystallinity on drying and it is apparent from the magnetic data that the loss of solvent enables the crystal lattice to adopt a more cooperative phase, resulting in the abrupt SCO behaviour observed with this compound.

The final SCO-active complex, **4.11**, showed only partial SCO behaviour which appeared susceptible to solvent loss. Thermogravimetric analysis confirmed the rapid release of crystallised solvent at room temperature. Using a freshly recrystallised sample, with the crystals layered with mother liquor, improved the SCO behaviour although it still remained partial and gradual.

In conclusion, this simple family of mononuclear Fe(II) complexes with imidazolylimine ligands was shown to produce a wide range of SCO behaviour. Simple alteration of the anion resulted in an approximately 30 K shift in the $T_{1/2}$, inclusion of crystallised solvent molecules resulted in bulk changes to the crystal lattice causing loss of SCO behaviour (**4.8**) or causes multi-step transitions (**4.9** and **4.10**). Drying the latter complex resulted in an abrupt transition with thermal hysteresis. These interesting SCO behaviours along with the impressive photoactivation of **4.7** and **4.10**, offer a rich avenue of further research.

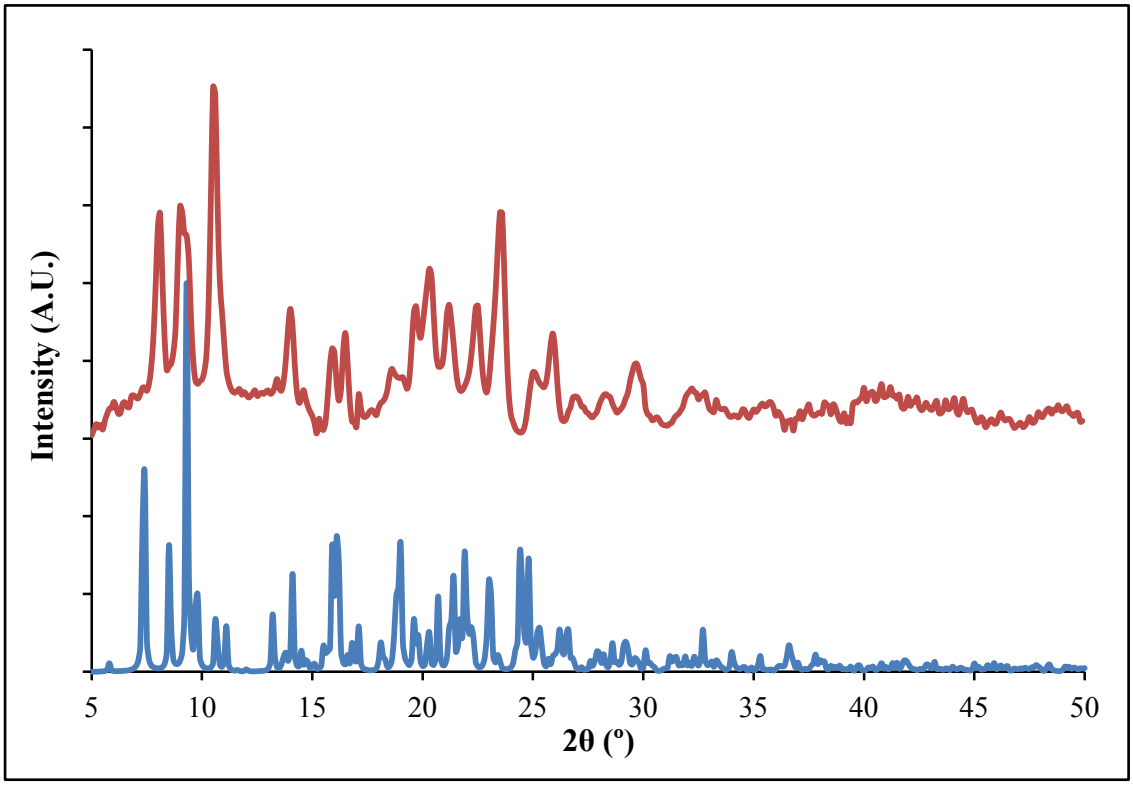

Fig 4.7.1 *X-ray powder diffraction of* ***4.10-Dried (red)*** *and* ***4.10-HS (blue)*** *at 120 K.*

CHAPTER FIVE

Investigations into the Spin Crossover Behaviour of

$[Fe(\mathbf{L})_2(CH_3CN)_2]X_2$ Compounds

5.1 Introduction

The research explored in this chapter follows closely on from that described in Chapter 4, through the investigation of the effects of more electron-withdrawing *para*-substituents on spin crossover behaviour in mononuclear Fe(II) systems.

5.2 Ligand Synthesis

The ligands discussed within this chapter were synthesised *via* a simple one-step imine condensation reaction between the aldehyde (choice of either pyridine-2-carbaldehyde or *1H*-imidazole-2-carbaldehyde) and the particular *para*-substituted amine, with electron-withdrawing substituents (either *p*-nitroaniline or *p*-aminobenzonitrile). The syntheses of the ligands described within this chapter are similar to those described in Chapter 4, however, with generally longer reaction times to compensate for the lower reactivity of the amine groups.

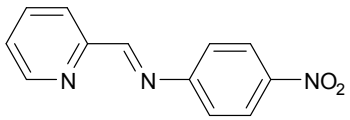

L5.1

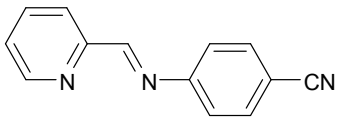

L5.2

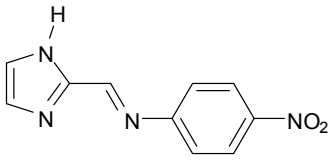

L5.3

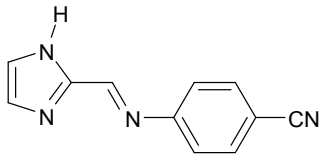

L5.4

Scheme 5.2.1 *Ligands described in Chapter 5*

5.3 Synthesis and Structural Characterisation of Mononuclear Fe(II) Complexes

*5.3.1 Synthesis and Characterisation of [Fe(**L5.1**)$_2$(CH$_3$CN)$_2$](BF$_4$)$_2$ – Complex **5.5***

Three equivalents of **L5.1** were reacted with one equivalent of $Fe(BF_4)_2 \cdot 6H_2O$ in acetonitrile and the resulting raspberry red solution was carefully layered with diethyl ether and left to stand for a few days, after which time large black block crystals formed. Attempts to subject the crystals to structural analysis *via* single crystal X-ray diffraction were met with immediate degradation of the crystals upon immersion in the liquid nitrogen stream. In order to investigate the structure of this compound, X-ray diffraction was completed at approximately room temperature (293(2) K). At this temperature the crystals gave good quality data which were solved and refined in the monoclinic space group *C*2/*c* (R-factor 5.73%). The data revealed one Fe(II) centre coordinating to two crystallographically equivalent **L5.1** ligands in a bidentate fashion through the pyridine and imine nitrogen atoms. The remaining two coordination sites about the octahedral metal centre are occupied by coordinating acetonitrile molecules that are situated in a *cis* arrangement. The asymmetric unit contains half the molecule and one counter-anion with the central Fe(II) atom residing on a 2-fold rotation symmetry element. There were no non-coordinating solvent molecules observed within the crystal lattice as illustrated below in **Fig 5.3.1**.

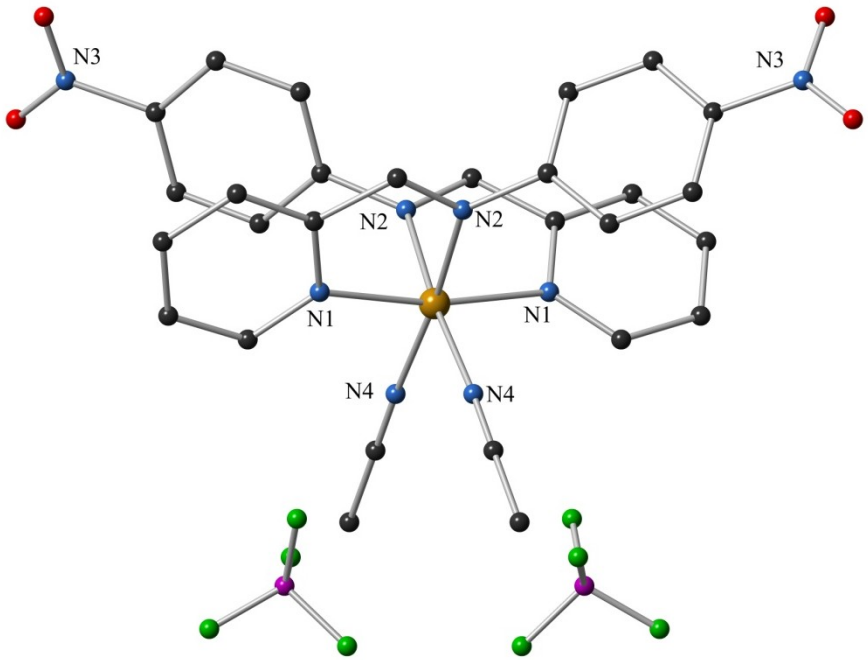

***Fig 5.3.1** Molecular structure and atom labelling scheme for **5.5**.*
Hydrogen atoms have been omitted for clarity.

	5.5
Space Group	*C2/c*
Temperature (K)	293(2)
Crystal Colour	Black
Av. Fe-N Bond Length (Å)	1.98
Σ (°)	45.9
Φ (°)	2.82

Table 5.3.2 *Selected geometric parameters for the Fe-N coordination bonds in* ***5.5****.*

The inclusion of coordinating acetonitrile was somewhat surprising for this family of compounds given that no evidence of *bis* coordinating modes were found with the ligands discussed in the previous chapter. However, it is common within the literature for SCO systems to contain two coordinating thiocyanate anions with bidentate ligands of a similar nature. Interestingly, examples of SCO compounds with *cis* coordinating acetonitrile molecules are rare in the literature with work by Bryliakov and similar work by Company and Costas being notable examples.[301,302]

At the data collection temperature of 293 K the Fe(II) centre is in an octahedral geometry with the two bidentate ligands having coordinating angles of 80.06(8)° between the Fe-N_{imid} and Fe-N_{imine} bonds, and an Σ value of 45.9°. The coordinating acetonitrile molecules arranged in a *cis* fashion with a coordinating angle of 89.21(9)°. The coordinating bond lengths about the Fe(II) centre range from 1.945(2) Å to 1.993(2) Å, consistent with Fe(II) in the LS state at 293 K. Other geometric parameters for the coordinating Fe-N bonds are provided in **Table 5.3.2**.The ligands twist significantly about the imine-phenyl bond with a torsion angle of 71.2(3)°. This distortion appears to optimise a face-to-face π-π interaction between the two ligands within the complex with a centroid-centroid distance of 3.6845(16) Å and an interplanar angle of 27.04(9)°. Of particular interest is the lack of displacement of the aromatic rings relative to one another. Usually in face-to-face π-π interactions ring "slippage" occurs where one ring shifts relative to the other to optimise the electrostatic interaction between the electron rich π system and the electron poor σ system (*i.e.* the hydrogen atoms). In **5.5**, both pyridine and nitrobenzene aromatic systems are π-deficient[303] and this has been observed to increase the stability of aligned face-to-face π-π interactions.[38,304] Although interactions of this type are uncommon, there is precedence within the literature.[38]

Perusal of the intermolecular interactions throughout the crystal lattice also reveal weak edge-to-face C-H···π interactions between the nitrobenzene "half" and the pyridine head group on adjacent molecules. However, with a C···π(centroid) distance of 3.913(3) Å and angle 30.3(2)°, this interaction is unlikely to be providing any significant stabilising force. Further interactions between molecules can be attributed to non-classical hydrogen bonding between a polarised C-H

bond situated on the pyridine head group and the *para*-nitro substituents on adjacent complexes to form a 1D-hydrogen bonding network along the crystallographic [101] plane. With a donor-acceptor distance of 3.162(4) Å, the interaction can be considered to be providing a moderate stabilising force to the crystal lattice (**Fig 5.3.3**).

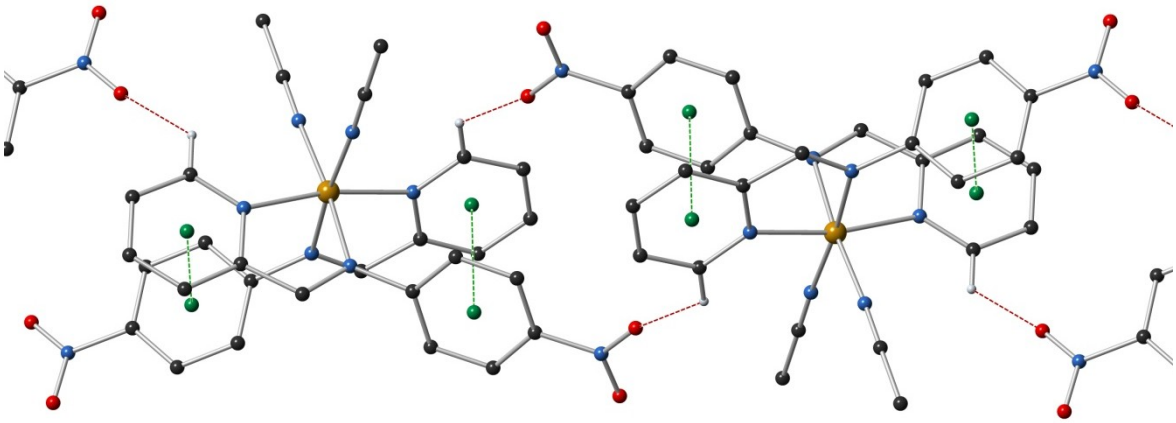

Fig 5.3.3 *Diagram showing the 1D-hydrogen bonding network and face-to-face π-π interactions in* ***5.5****, as viewed along the crystallographic c-axis. Counter-anions and hydrogen atoms not involved in hydrogen bonding have been omitted for clarity.*

The rapid loss of single crystallinity upon immersion of crystals of **5.5** under liquid N_2 stream is particularly intriguing. This behaviour is typically ascribed to a first order phase transition that has been reported to occur in compounds undergoing a spin transition. As the crystallographic data shows that the sample is in the LS state at room temperature the phase transition cannot be due to a spin transition into the LS state. Unit cell parameters were measured as the crystal was cooled in 10 K increments from 240 K to 150 K with the visible loss of crystallinity and subsequent loss of diffraction occurring at 220 K.

*5.3.2 Synthesis and Characterisation of [Fe(**L5.2**)$_2$(CH$_3$CN)$_2$](BF$_4$)$_2$·2CH$_3$CN – Complex **5.6***

Three equivalents of the ligand **L5.2** were reacted with one equivalent of $Fe(BF_4)_2 \cdot 6H_2O$ in acetonitrile. The resulting dark purple solution was filtered and carefully layered with diethyl ether. The sample was left in the freezer over one week after which time a purple oil had formed which upon further standing yielded dark purple crystals suitable for structural analysis using X-ray crystallography. The data were solved and refined in the monoclinic space group *C*2/*c* (R-factor

3.43%) with the complex consisting of two **L5.2** ligand units and two coordinating acetonitrile molecules, despite three equivalents of ligand being added to the reaction mixture. The counter anion BF_4^- was found to be disordered within the asymmetric unit and rotates through two positions with occupancies refined at 75% and 25% for the two positions. Acetonitrile solvent was also found within the crystal lattice and was well defined with full occupancy.

The complex **5.6** shows similar structural properties to those discussed in the previous section for **5.5** and the structure is shown below in **Fig 5.3.4**. Interestingly this system shows no evidence of the phase transition that occurred in the previous example. As such the data collection could take place at 120 K. At this temperature the Fe(II) centre is in a LS configuration with coordinating bond lengths ranging from 1.938(1)Å to 1.973(1)Å with an average of 1.957(3)Å. As was observed in the previous example the Fe(II) centre lies on a two-fold rotational axis and half the molecule is observed within the asymmetric unit. The **L5.2** ligands coordinate in a bidentate fashion through the pyridine and imine nitrogen atoms with a bite angle of 81.06(6)°. The Fe(II) centre being in the LS state has an octahedral geometry with only minor distortion (Σ = 48.9). As was the case with **5.5** the **L5.2** ligands also undergo some quite significant distortion away from planarity about the imine – phenyl ring bond. The torsion angle of 61.0(2)° is less than that observed previously and as such the face-to-face π-π interaction between the pyridine and phenyl rings is significantly longer than the analogous interaction in **5.5** at 3.8908(11) Å with an interplanar angle of 40.73(6)°.

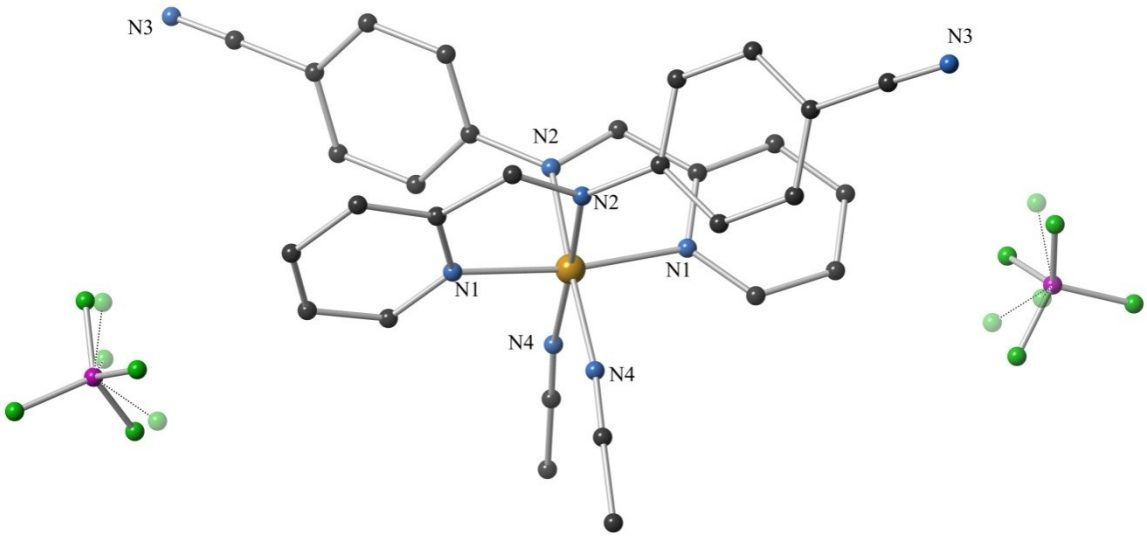

Fig 5.3.4 *Molecular structure and atom labelling scheme for* ***5.6****. Hydrogen atoms and solvent molecules have been omitted for clarity.*

	5.6
Space Group	*C*2/*c*
Temperature (K)	113(2)
Crystal Colour	Purple
Av. Fe-N Bond Length (Å)	1.96
Σ (°)	48.9
Φ (°)	3.00

Fig 5.3.5 *Selected geometric parameters for the Fe-N coordination bonds in* ***5.6****.*

The two coordinating acetonitrile molecules are once again in a *cis* configuration with a coordination angle of 85.08(6)°. These two acetonitrile molecules do not coordinate in a perfectly "straight on" manner instead they approach the Fe(II) centre at an angle of 167.9(1)° instead of the expected 180°. The two non-coordinating solvent acetonitrile molecules lie in line with the coordinating acetonitrile molecules which may account for the slight distortion from the optimal geometry.

Intermolecular interactions within the crystal lattice are minimal with no hydrogen bonding or aromatic interactions observed between complexes. The packing of molecules within the crystal lattice differs considerably for that observed in **5.5** as illustrated in **Fig 5.3.6**.

*5.3.3 Synthesis and Characterisation of [Fe(**L5.3**)$_2$(CH$_3$CN)$_2$](ClO$_4$)$_2$·CH$_3$CN – Complex **5.7***

The complex **5.7** was synthesised by reacting three equivalents of the ligand **L5.3** with one equivalent of $Fe(ClO_4)_2 \cdot 6H_2O$ in acetonitrile. The bright orange solution was heated at reflux for one hour to ensure full dissolution of both reactants. After cooling, the solution was filtered and bright red plate crystals suitable for structural determination by X-ray diffraction formed by layering the filtered solution with diethyl ether and leaving the resulting mixture to stand, sealed, over some weeks.

As with the previous examples, the crystallographic data of **5.7** were solved and refined in the monoclinic space group *C*2/*c* with an R-factor of 5.82%. The crystals were stable at the collection temperature of 113 K and the structure was found to contain two **L5.3** ligands coordinating in a bidentate fashion about a central Fe(II) centre through the imidazole and imine nitrogens, along with two coordinating acetonitrile molecules in a *cis* geometry.

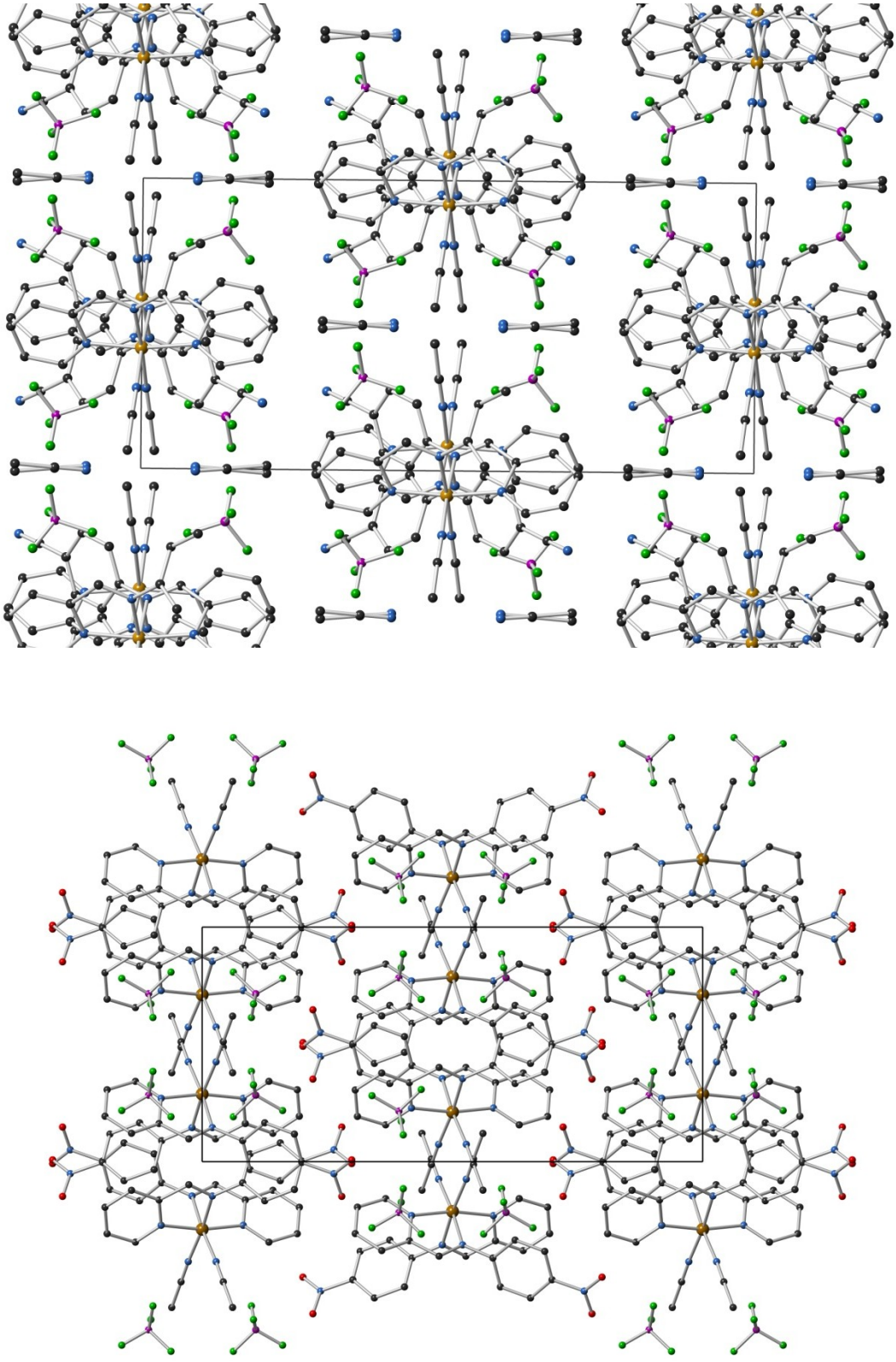

Fig 5.3.6 *Crystal packing comparisons between* ***5.6*** *(**top**) and* ***5.5*** *(**bottom**) as viewed along their respective crystallographic c-axes. Hydrogen atoms and disordered counter-anion components have been omitted for clarity.*

The perchlorate counter anions were well refined and showed no disorder within the crystal lattice (**Fig 5.3.7**). There was found to be some electron density about a crystallographic special position which was refined as an acetonitrile molecule with 50% occupancy giving a total occupancy of one acetonitrile molecule per complex.

As discussed previously even though three equivalents of the ligand were initially added the *bis* isomer crystallises exclusively, in this case however, there was evidence of the *tris* species forming in solution through mass spectrometry with a small peak measured at *m/z* 903.1456 consistent with $[FeL_3+H^+](ClO_4)_2$. No peaks were found to be consistent with the *bis* complex and unsurprisingly there was a large peak associated with the free ligand suggesting that the complex fragments under electrospray conditions. The evidence that the *tris* form is observed to some degree in solution suggests that the *bis* and *tris* forms are in equilibrium and the *bis* form is preferred under these particular crystallisation conditions. Attempts to crystallise the *tris* form using solvents other than acetonitrile were unfortunately unsuccessful.

By moving to a known weaker field head group in the form of the imidazole entity causes the compound to exhibit a purely HS state for the central Fe(II) centre with an average bond length of *ca.* 2.18(6) Å. The angles about the Fe centre are also further distorted from an octahedral geometry as anticipated with the bond angles about the Fe(II) centre giving $\Sigma = 73.6$ (**Table 5.3.8**). No evidence was observed for SCO in this compound and the exclusively HS structure is unsurprising given the relatively weaker ligand strength of the ligand along with the acetonitrile co-ligands.[202] Immersion of an acetonitrile solution of **5.7** into liquid N_2 showed no colour change, consistent with the complex remaining in the HS state even at low temperature.

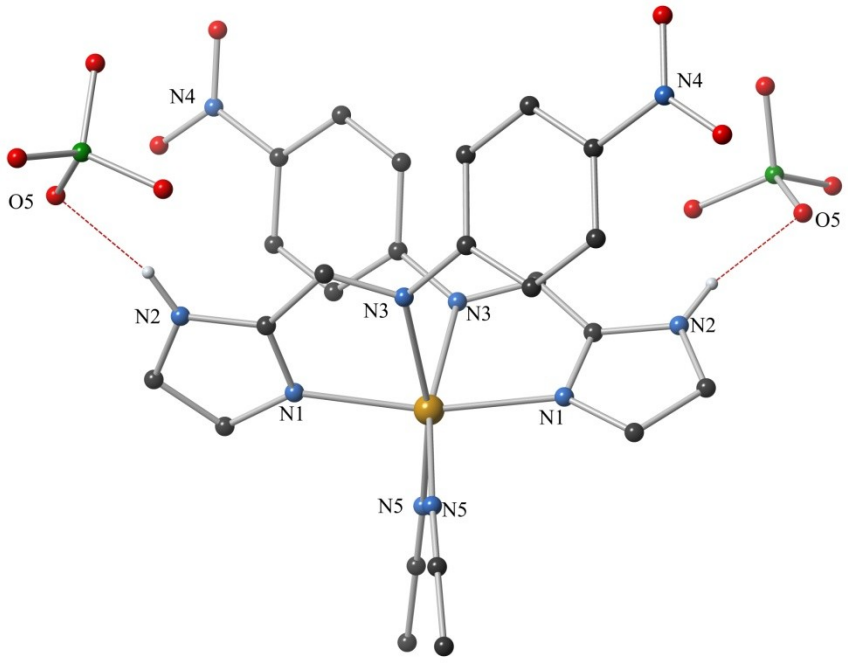

Fig 5.3.7 *Molecular structure and atom labelling scheme for* ***5.7****. Solvent molecules and hydrogen atoms not involved in hydrogen bonding have been omitted for clarity.*

	5.7
Space Group	*C2/c*
Temperature (K)	113(2)
Crystal Colour	Red
Av. Fe-N Bond Length (Å)	2.18
Σ (°)	73.6
Φ (°)	4.44

Table 5.3.8 *Selected geometric parameters for the Fe-N coordination bonds in* ***5.7****.*

The imidazole head group contains a hydrogen bond donor which has been shown previously in this study to form hydrogen bonding networks. In this case the imidazole N-H moiety forms a relatively strong hydrogen bond to the counter-anion with a [D-H···A] distance of 1.96(9) Å, however no further hydrogen bonds occur to make a network. The imidazole and phenyl rings are further displaced with an overlapping centroid-centroid distance of 4.234(2) Å and an interplanar angle of 42.53(15)°. At this distance, stabilisation due to face-to-face π-π stacking is likely to be minimal.

Perusal of the crystal packing reveals few stabilisation interactions with contacts exceeding defined distances. A weak hydrogen bond between the imidazole N-H and the nitro-group on a neighbouring complex is observed, however, with a D-H···A distance of 2.73(3) Å and contact angle of 106(6)° this is once again more likely to be due to convenience in crystal packing rather than a driving stabilising factor. The crystal lattice shows solvent containing channels that occur parallel to the crystallographic c-axis with the acetonitrile solvent molecule being refined at 50% occupancy about a two-fold rotation axis. The channels are approximately 4.6 Å wide at the closest imidazole-imidazole distance, and the disordered acetonitrile molecule sits on either side of the channel (**Fig 5.3.9**).

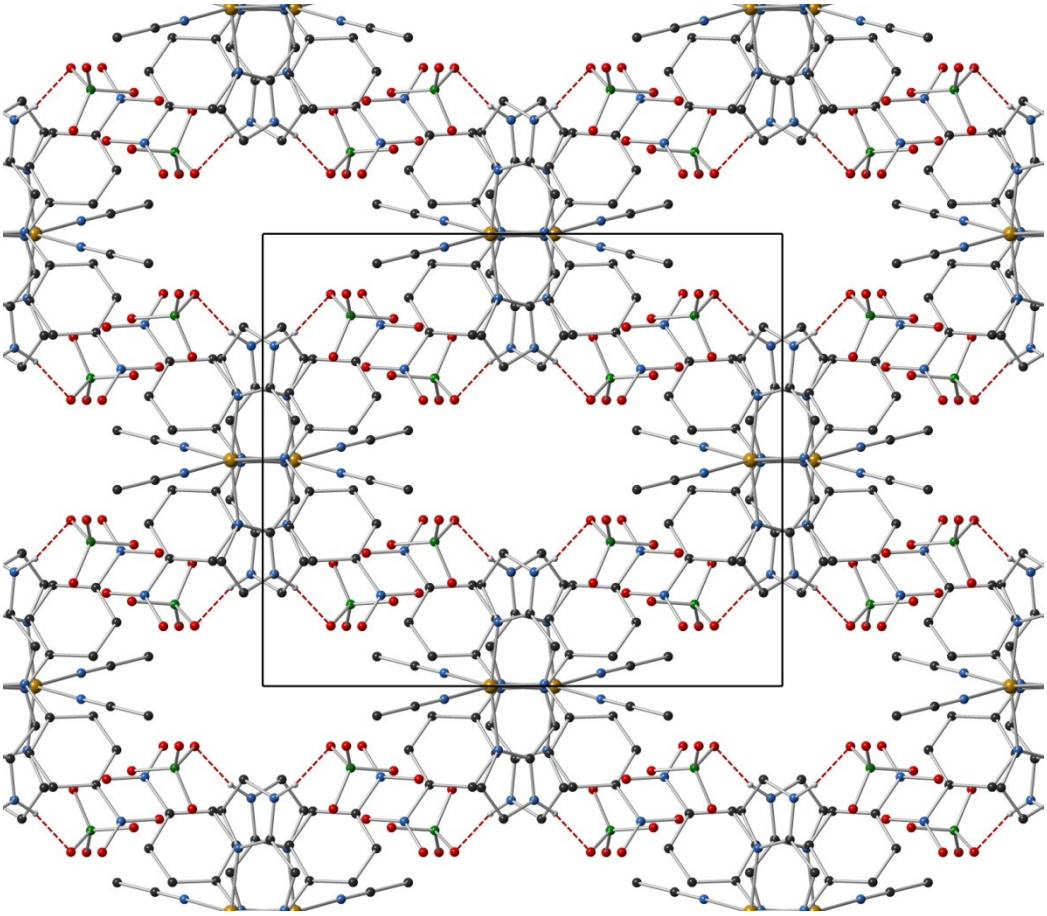

Fig 5.3.9 *Packing diagram of* ***5.7*** *as viewed along the crystallographic c-axis showing solvent containing channels. Hydrogen atoms not involved in hydrogen bonding and solvent molecules have been omitted for clarity.*

*5.5.2 Synthesis and Characterisation of [Fe(**5.4**)$_2$(CH$_3$CN)$_2$](ClO$_4$)$_2$·CH$_3$CN – Complex **5.8***

The complex **5.8** was synthesised through the reaction of three equivalents of **L5.4** with one equivalent of Fe(ClO$_4$)$_2$·6H$_2$O in acetonitrile. The resulting red-orange solution was filtered and carefully layered with diethyl ether. After a few days standing in a sealed vessel at 0 °C red plate crystals formed suitable for structural analysis *via* X-ray crystallography.

The X-ray crystallographic data collected were solved and refined in the monoclinic space group *C*2/*c* with half the complex present in the asymmetric unit. The central Fe(II) atom is situated on a two-fold rotation symmetry element and is coordinated to one bidentate **L5.4** ligand, and one coordinating acetonitrile molecule as has been seen for the other members of this family. The total complex consists of the Fe(II) centre in a pseudo-octahedral geometry coordinating to two **L5.4** ligands through the imidazole and imine nitrogen atoms. The rest of the coordination

sphere is filled by the two coordinating acetonitrile molecules arranged in a *cis* fashion. The perchlorate counter-anions are well defined and an acetonitrile solvent molecule is found within the asymmetric unit to give the equivalent of one acetonitrile molecule disordered over two symmetry related positions per complex (**Fig 5.3.10**).

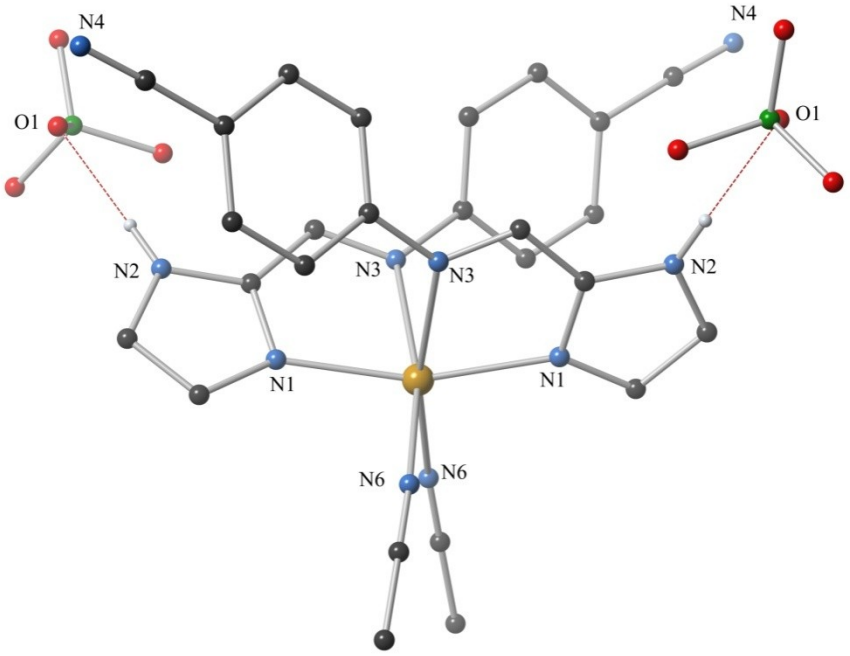

Fig 5.3.8 *Molecular structure and atom labelling scheme for* ***5.8****. Solvent molecules and hydrogen atoms not involved in hydrogen bonding have been omitted for clarity.*

	5.8
Space Group	*C*2/*c*
Temperature	113(2) K
Crystal Colour	Red
Av. Fe-N Bond Length (Å)	2.18
Σ (°)	77.7
Φ (°)	4.49

Table 5.3.11 *Selected geometric parameters for the Fe-N coordination bonds in* ***5.8****.*

The Fe(II) centre is in the HS state with an average bond distance of *ca.* 2.18 Å and as with **5.7** no evidence of SCO was observed upon immersion a solution of the compound in liquid N_2. The geometry about the Fe(II) centre is distorted from an ideal octahedral geometry as is typical for Fe(II) centres in the HS state, the complex was found to have an Σ value of 77.7 as described in **Table 5.3.11**. The **L5.4** ligands subtend about the central Fe(II) atom with a bite angle of 75.55(6)° and the coordinating acetonitrile molecules do not bind to the Fe atom in a linear fashion but with an approach angle of 164.7°. As observed in **5.**7 the overlap between the imidazole and phenyl rings within the complex are too long to be providing any significant stabilisation with a centroid-centroid distance of 3.9296(14) Å and an interplanar angle of 33.11(9)°. The compound shows similar crystal packing behaviour to that of the nitro analogue discussed above with solvent containing channels present with approximate width of 4.6 Å (**Fig 5.3.12**).

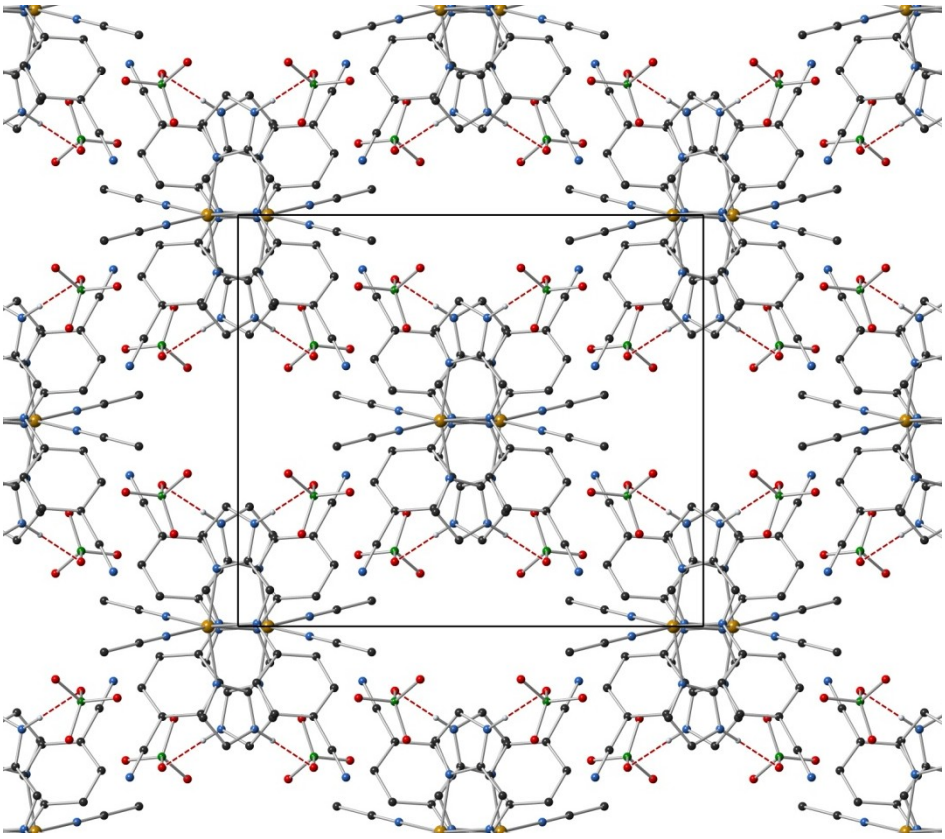

Fig 5.3.12 *Packing diagram of* ***5.8*** *as viewed along the crystallographic c-axis. Hydrogen atoms not involved in hydrogen bonds and solvent molecules have been omitted for clarity.*

5.4 Spin Crossover Behaviour of Complex 5.5

*5.4.1 Variable Temperature UV-Visible Spectroscopy of Complex **5.5***

To investigate the potential spin-crossover characteristics of complex **5.5** the complex was dissolved in acetonitrile at a concentration of 4.071 x 10^{-4} mol L^{-1}. 3 mL of the sample was cooled to 274 K and subsequently heated in 2 K increments to a maximum temperature of 343 K. The UV-Visible spectra were recorded between 400 – 800 nm after thermal equilibration at each temperature setting. The combined spectra are shown below in **Fig 5.4.1**. Initially at 274 K, a broad absorption band with a λ_{max} = 543 nm (ε = 2430 L mol^{-1} cm^{-1}) occurs, typical of the $^1A_1 \rightarrow {}^1T_1$ transition for Fe(II) complexes in the LS state. As the temperature increases, the absorbance of this band decreases to reach a minimum value at *ca.* 330 K. Full transition into the HS state is clearly observed in the plot of maximum absorbance at 543 nm as a function of temperature (**Inset Fig 5.4.1**).

Thermodynamic parameters were elucidated from the fit of **Equation 2.4.7** to the data with ΔH = 74.4 kJ mol^{-1}, ΔS = 246.6 J mol^{-1} and $T_{1/2}$ = 299 K. These parameters are significantly higher than those observed for the dinuclear triple helicate **2.5** and are likely to be attributed to ligand dissociation processes occurring simultaneously with SCO. The exact nature of this dissociation process in **5.5** is not understood at this stage. Work conducted by Bryliakov showed thermodynamic parameters of *ca.* ΔH = 40 kJ mol^{-1} and *ca.* ΔS = 137 J mol^{-1} for the dissociation of one acetonitrile molecule from the complex $[Fe(BPMEN)(CH_3CN)_2](ClO_4)_2$.[301] In this example it is likely that both acetonitrile molecules are undergoing ligand exchange processes.

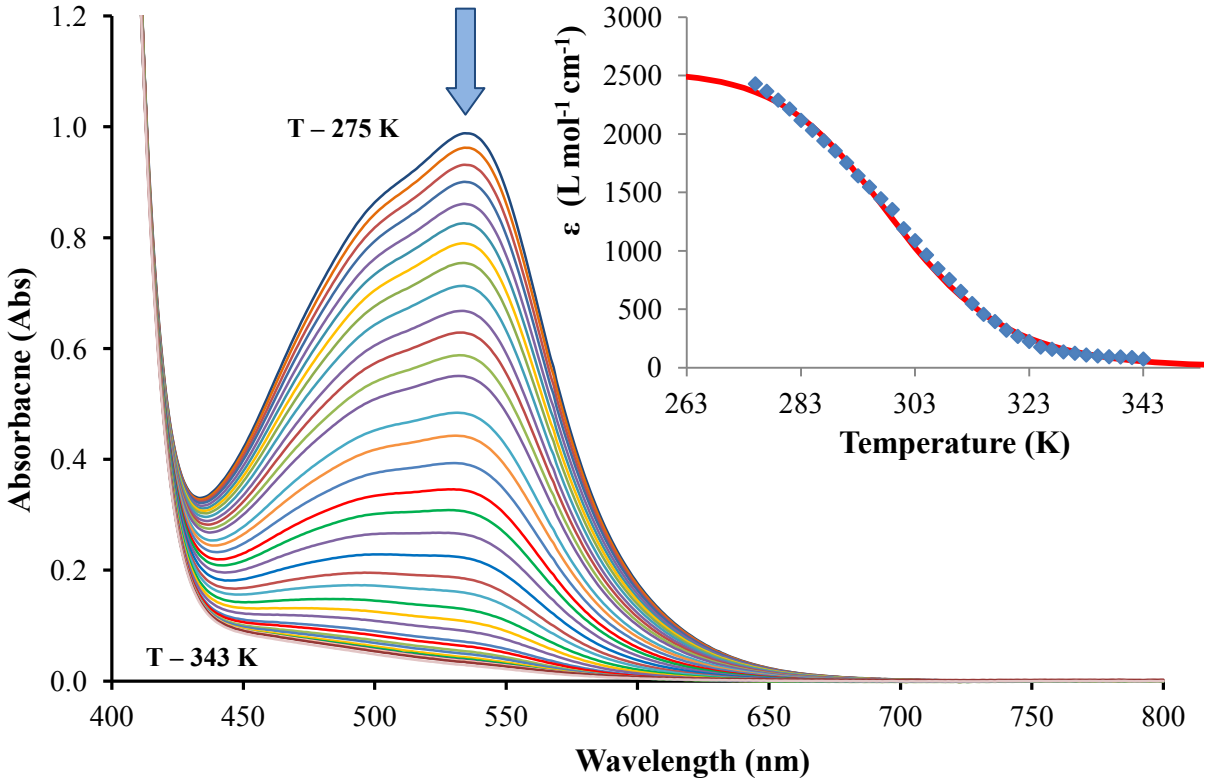

Fig 5.4.1 *Graph showing the temperature dependence of the absorbance of complex* ***5.5*** *(4.071 x 10^{-1} molL^{-1}acetonitrile). Inset: Absorbance data (**blue**) vs. temperature with curve showing fit (**red**).*

5.4.2 Variable Temperature Magnetic Susceptibility Measurements

Given the SCO behaviour of **5.5** observed in solution, the solid state magnetic properties were also investigated. Some care was taken in selecting appropriate experimental conditions for this sample given the sensitive nature of the crystals to a phase transition at 220 K and solvent loss within the crystal above 100 °C. As such the sample was cooled from 300 K under a magnetic field of 2 T. The χT value decreased immediately from 0.45 cm^3 K mol^{-1} to a value of 0.1 cm^3 K mol^{-1}, consistent with SCO to the LS state by *ca.* 240 K. This is consistent with the behaviour observed during the solution studies. For an Fe(II) centre in the LS state one would expect a χT value of 0 cm^3 K mol^{-1}, the slightly elevated value of the χT product in **5.5** is likely due to some paramagnetic impurity within the crystal lattice and is estimated at 3% of the crystalline sample (assuming a maximum χT value of 3.5 cm^3 K mol^{-1}). The sample was further cooled to 1.8 K with no noticeable changes in the magnetic moment around the phase transition temperature of 220 K.

The return heating run shows the LS plateau being extended to approximately 280 K after which point the χT value increases slightly to 0.16 cm^3 K mol^{-1} (**Fig 5.4.2**). The temperature was not increased past 330 K due to potential solvent loss with excess heating. Because of these limitations the exact nature of the increase in χT value is difficult to ascertain. It may be attributed to the phase transition at 220 K where the new phase may increase the stability of the LS state, pushing the SCO to higher temperatures or solvent loss from the crystalline material may be occurring, potentially altering the magnetic properties of the compound. It is apparent that the system characterised as **5.5** crystallises in a metastable state and shows SCO behaviour near room temperature. This system undergoes a very dynamic first-order phase transition which results in the shattering of the crystalline material around 220 K. The exact nature of this new species is as yet not understood but may have a higher $T_{1/2}$ by nearly 50 K.

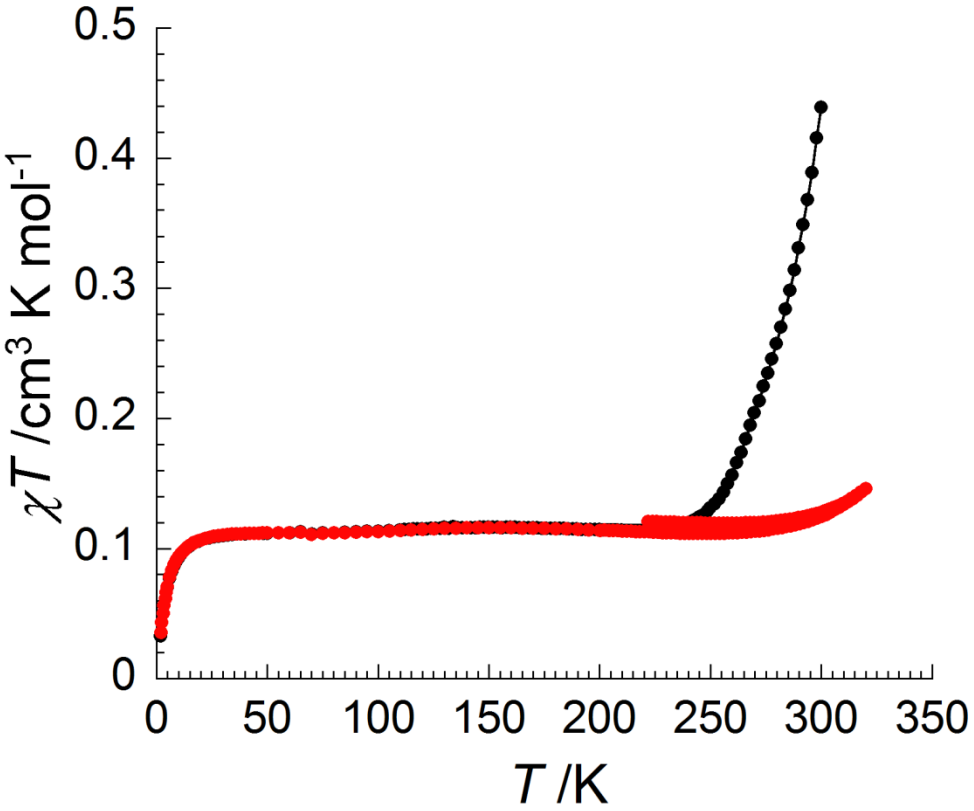

Fig 5.4.2 *Variable temperature magnetic susceptibility measurements of complex* ***5.5*** *under a magnetic field of 2T showing cooling mode (****black circles****, 300 – 1.8 K) and heating mode (****red circles****, 1.8 – 320 – 220 K).*

5.5 Discussion and Conclusions

In this study a series of mononuclear Fe(II) complexes with electron-withdrawing *para*-substituents were synthesised. Interestingly, although there was some evidence of the *tris*-species forming in solution, all four of the complexes studied within this series crystallised in the *bis*-form with two coordinating acetonitrile molecules. This isolation of the *bis*-bidentate form provides an ideal base for subsequent ligand exchange that may be able to "tune" the spin crossover properties of the given complex. Unfortunately, attempts to synthesise complexes where the acetonitrile molecules had been displaced by other nitrile containing ligands such as isothiocyanate, benzonitrile, adiponitrile and acryonitrile were unsuccessful.

Only **5.5** showed evidence of SCO behaviour with the other three complexes remaining HS (or LS) during changes in temperature. **5.5** showed intriguing behaviour with apparent thermal SCO in solution occurring around room temperature. The large thermodynamic parameters observed during this experiment are consistent with the sample undergoing ligand exchange and as such the thermochromic behaviour is not due to SCO alone as the system is in a more complex chemical equilibrium. The magnetic susceptibility measurements on **5.5** in the solid state also showed SCO behaviour, however, the LS state appears to be favoured as within the solid-state only *ca.* 13% of the sample is in the HS state at 300 K compared with 50% in the solution studies ($T_{1/2}$ = 299 K in solution). From this information it could be postulated that as the sample undergoes SCO in solution, the rate of the ligand dissociation process is increased as the temperature increases. Although this phenomenon is not considered a true spin crossover transition[305] this particular system may provide some intriguing insights into the effect of ligand dissociation on SCO behaviour in competitive solution environments.

Other interesting behaviour exhibited by **5.5** was an apparent phase transition observed below 220 K which at this stage is not understood. The metastable state which readily crystallises at room temperature undergoes significant alterations within the crystal lattice resulting in rapid degradation of the crystal around 220 K. This new phase remains in the LS state past the SCO onset temperature of 250 K with a small increase in χT observed above 300 K. Given the propensity for this sample to lose solvent with heating, it is at the stage unknown whether the magnetic behaviour is due to the new phase having a more stable LS state and therefore increasing the onset temperature of the SCO behaviour, or whether solvent loss in occurring within the sample and is contributing to the increase in magnetic susceptibility.

This intriguing system will provide the basis for further study and potential avenues of research will be indicated in Chapter Six: Final Conclusions and Future Work.

CHAPTER SIX

Conclusions and Future Work

6.1 Conclusions and Final Thoughts

The results discussed in the preceding chapters have illustrated varying spin crossover behaviour within a family of Fe(II) complexes with imidazolylimine (or in one example, pyridylimine) based ligands.

Chapter 2 discussed a series of three dinuclear triple helicates which differed only in the coordinating group. All three of these helicate species shared similar geometric properties and pleasingly, two of these helicates exhibited SCO behaviour. Complex **2.5**, with the 2'-imidazoylimine coordination sphere showed SCO behaviour above room temperature and was carefully analysed in both solution and the solid state. Complex **2.6** utilising the isomeric 4′-imidazolylimine ligand, showed gradual SCO behaviour that was able to be structurally monitored through variable temperature X-ray diffraction. The compound also showed impressive LIESST behaviour under green light irradiation, however, the fully photo-induced [HS-HS] state was not isolated during photomagnetic measurements under white light irradiation. Complex **2.5** showed weak LIESST behaviour consistent with the more stable LS state and higher $T_{1/2}$.

The considerable effects of crystal packing interactions on SCO behaviour were clearly illustrated in Chapter 3 where the solvate **3.2·H_2O** was shown to have remarkably different magnetic properties to the previously reported **3.2·CH_3CN**. Variable temperature magnetic susceptibility measurements on **3.2·H_2O** showed SCO behaviour in only one Fe(II) centre within the helicate ([HS-LS] state) compared with full SCO into the [LS-LS] state observed in **3.2·CH_3CN**. The behaviour is attributed to a face-to-face π-π interaction between the HS "halves" of two neighbouring helicates in **3.2·H_2O** that is absent in the crystal lattice of **3.2·CH_3CN**, effectively stopping one of the Fe(II) centres from contracting to the LS state.

The study then moved to the analysis of Fe(II) mononuclear SCO compounds that were essentially "half" complexes of the dinuclear triple helicates discussed in the previous chapters. Through subtle alterations to the *para*-substituent of these ligands a wide variety of SCO behaviour was observed, with crystal packing in the solid state once again being a dominant feature in altering the magnetic behaviour. LIESST behaviour in two of these complexes was also observed, with **4.10-Dried** showing an abrupt spin transition with a narrow thermal hysteresis centred around 100 K, along with full excitation into the HS state after white light irradiation at low temperatures.

Finally, Chapter 5 continued with the theme set out in Chapter 4 using ligands with electron-withdrawing *para*-substituents. These complexes did not form *tris*-species with two ligands and two coordinating acetonitrile molecules the preferred coordination mode. As such, three of the complexes discussed within this chapter did not display any SCO behaviour remaining exclusively in the HS or LS state. However, one complex did show SCO behaviour centred above room temperature and this behaviour was analysed both through variable temperature UV-Visible solution studies and variable temperature magnetic susceptibility measurements.

In summary, the imidazolylimine coordination motif has been shown in this thesis to form SCO compounds which possess various modes of SCO behaviour and cover a wide range of temperatures, with the $T_{1/2}$ values of *ca.* 100 K to above room temperature being observed. The ease in modification of these systems through different combinations of aldehydes and substituted amines, makes these complexes ideal for further research.

6.2 Future Work

6.2.1 Further Studies of Mononuclear Spin Crossover Complexes

In this initial study, only a select few ligands were synthesised and resulted in the formation of mononuclear complexes with Fe(II). Due to the ease of the synthesis of these compounds, other ligands with other substituents may be synthesised and their resulting complexes also studied. By creating a library of similar complexes, attempts to study and understand trends amongst the series will be greatly improved. Ligands with different electronic and steric environments are currently being investigated within the Kruger group, in particular the coordination chemistry of **L6.1** is being explored. **L6.1** will be interesting to compare with the *para*-substituted analogue (**L4.4**) and also with the closely related dinuclear ligand **L2.2**. The proposed complex [Fe(**L6.1**)$_3$]X_2 may form either the *meridional* isomer (as observed in **4.12**) or the *facial* isomer (as observed in the dinuclear triple helicate **2.5**), both of which will provide further insights into the behaviour of the complexes studied within this text. It will be interesting to observe whether the intra-ligand C-H···π interactions observed in **2.5** will be conserved in the mononuclear complex (therefore favouring formation of the *facial* isomer) as this motif should result in the complex displaying SCO behaviour above room temperature (as observed in **2.5**). If the *meridional* form is preferred, then the direct comparison between the *para*-analogue **4.12** and the resulting similarities or differences between the SCO behaviour may be discussed.

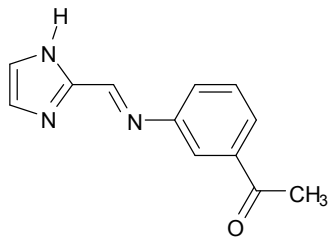

L6.1

6.2.2 Ligand Exchange Mechanism in Complex 5.5

The interesting solution based SCO behaviour exhibited by **5.5** warrants further investigation. From the research covered within this thesis, it was apparent that ligand exchange occurred simultaneously with SCO as the solution was heated. As such, the thermochromic behaviour of **5.5** cannot be strictly defined to a SCO process (discussed in Chapter 5). However, this system may be useful in using ligand exchange to promote a change in spin state, with the associated colour change reporting the binding event.

Further studies into the precise nature of the ligand exchange behaviour in solution would be beneficial. Possible methods of investigation would involve comparing the thermodynamic parameters from repeated variable temperature UV-Visible spectroscopic experiments with a varying amount of acetonitrile. For example, during initial studies of **5.5** it was noted that performing the synthesis in nitromethane or dichloromethane resulted in bright purple solutions, a colour consistent with Fe(II) in the LS state in the systems described within this thesis. No crystalline product was able to be obtained from either the dichloromethane or nitromethane preparations and the method was abandoned in favour of the acetonitrile method. It would be interesting to observe the change in thermodynamic parameters and $T_{1/2}$ value (if any changes occur) as the concentration of acetonitrile solution is decreased, *i.e.* performing the experiment in acetonitrile and comparing the data to a similar experiment performed in 9:1 parts acetonitrile to nitromethane and so on to finally performing the experiment in nitromethane. This work is currently being undertaken as part of a Masters project within the Kruger group.

Also of particular interest and a closely related study would involve the analysis of the magnetic susceptibility of **5.5** in solution, once again further investigating the nature of the SCO process in solution. This work will form part of future collaborations with the Clérac research group at the Université de Bordeaux.

6.2.3 Spin Crossover Thin Films

A driving force in the research of SCO compounds is to optimise their behaviour to be of use as the active components in molecular sensors, optical displays and memory devices.[306-308] Materials science is of particular importance in designing and analysing SCO compounds with suitable behaviour for particular applications. The formation of nanoparticles, gels, liquid crystals and 3D-coordination polymers that display SCO behaviour are also undergoing extensive research to fabricate devices. However, these techniques are not directly applicable to the SCO systems developed and discussed within this thesis. As such, this section will briefly discuss the formation

of SCO thin films with the view of incorporating the SCO complexes presented here within thin films in the future.

One important facet of SCO behaviour is the interaction between SCO centres within the solid state. In particular the formation of compounds that show abrupt spin transitions with thermal hysteresis are important for potential memory device applications.[250] However, the techniques used for synthesising thin films often involve the inclusion of other molecules within the film or significant modifications to the SCO complex. As the SCO properties of a compound heavily rely on the interactions between the SCO centres, this may cause the SCO behaviour of the compound to not be carried over to the thin film.

Some of the common techniques used to form thin films are unlikely to be applicable for use with the complexes discussed within this thesis. Langmuir-Blodgett films mainly require the SCO complex to be amphiphilic which would require significant alterations to the complexes discussed within this text. The complexes discussed here are also unlikely to be stable enough for vacuum deposition.

For initial studies, thin film formation *via* the spin coating technique would be the most suitable for the SCO compounds discussed within this text. Spin coating is cost effective and has been shown by Matsuda[309] to form thin films of the compound $[Fe(dpp)_2](BF_4)_2$ (dpp = 2,6-di(pyrazollyl)pyridine). The crystalline sample underwent an abrupt spin transition with a $T_{1/2}$ of 259 K, compared with the thin film which displayed reversible SCO behaviour with a $T_{1/2}$ of *ca.* 260 K, similar to the crystalline state but with less cooperativity as expected.

Preliminary studies into the formation of SCO thing films are currently being conducted through collaborations at the University of Canterbury with Prof. Alison Downard (Chemistry) and Dr. Mark Staiger (Mechanical Engineering).

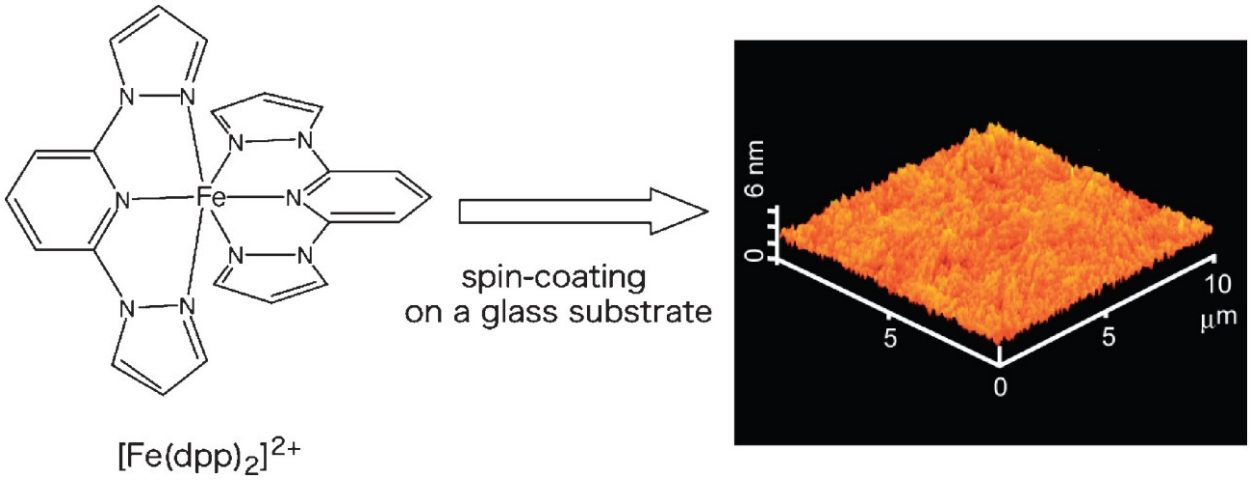

Fig 6.2.1 *Atomic force microscopy image of a spin-deposited SCO thin film, fabricated from* $[Fe(dpp)_2](BF_4)_2$ *conducted by Matsuda. Image from reference.*[309]

CHAPTER SEVEN

Experimental Data and Methods

7.1 Materials and Methods

7.1.1 General Information

Unless otherwise specified, all reagents and starting materials were reagent grade, purchased from standard suppliers and used as received. Water was purified by reverse omosis *in-house*. Where anhydrous solvents were required, the HLPC-grade solvent was either distilled from standard drying agents or dried by passing over a sealed column of activated alumina. Melting points were recorded on an Electrothermal Melting Point Apparatus and are uncorrected. Elemental analyses were carried out by Campbell Microanalytical Laboratory, University of Otago, New Zealand. Except where otherwise specified, all reactions were carried out in air.

7.1.2 Infrared Spectroscopy

All infrared spectra were recorded on a Perkin-Elmer Spectrum One FTIR instrument operating in diffuse reflectance mode with samples prepared as KBr mulls (denoted KBr), or in transmittance mode with liquid samples pressed between KBr discs (neat). The following abbreviations are used: vs: very strong, s: strong, m: medium, w: weak, sh: sharp, br: broad.

7.1.3 Thermogravimetric Analysis

Thermogravimetric analyses were carried out on an Alphatech SDT Q600 TGA/DSC apparatus. All samples were heated on alumina crucibles under N_2 flow of 100 mL min^{-1}. Ramp heat cycles consist of heating at 1 °C per minute. Due to the potentially explosive nature of perchlorate salts any samples containing perchlorate were not heating above 100 °C.

7.1.4 Nuclear Magnetic Resonance

All spectra were recorded on Varian INOVA 500, Varian Unity 300, or 400 instruments, operating at 500, 400, and 300 MHz, respectively, for ^{1}H, and 125, 100, 75MHz for ^{13}C. All samples were dissolved in commercially available deuterated solvents d_6-DMSO, $CDCl_3$, CD_3CN, CD_3OD or D_2O. Spectra were referenced to the residual solvent peaks and/or TMS. COSY and HSQC experiments were employed where required, using standard Varian pulse sequences.

7.1.5 UV-Visible Spectroscopy

UV-Visible spectra were recorded on a Varian CARY UV-Visible spectrometer in the range 200 – 800 nm unless otherwise stated. Experiments using nitromethane were recorded in the range 400 – 800 nm. Samples were measured in quartz curvettes of path length 1 cm and approximate capacity of 3 mL. UV-Visible complexiometric titrations were carried out by dissolving the free ligand in 10 mL spectroscopic grade solvent (commonly acetonitrile) at the concentration specified and recording the spectra of the free ligand and following each addition of 10 μL of metal solution in the same solvent. All concentrations were chosen such that the total change in volume of the solvent did not exceed 5% and the maximum absorbance did not exceed 2.5

7.1.6 Mass Spectrometry

Mass spectra were recorded by Dr. Marie Squire and Dr. Meike Holzenkaempfer on either a DIONEX Ultimate 3000 or Bruker MaXis 4G spectrometer, both of which were operated in high resolution positive ion electrospray mode. Samples were dissolved and diluted to the required concentration in appropriate HPLC grade solvents – generally acetonitrile or methanol.

7.1.7 X-ray Crystallography

Refinement data and hydrogen bond parameters are presented in Appendix 1. X-ray crystallographic data collection and refinement was carried out with either a Bruker APEXII instrument, using graphite-monochromated Mo Kα (λ = 0.71073 Å) radiation, or an Oxford Agilent SuperNova instrument with focused microsource Cu Kα (λ = 1.5418 Å) radiation and ATLAS CCD area detector. All structures were solved using direct methods or charge splitting with SHELXS[310] and refined on F^2 using all data by full matrix least-squares procedures with SHELXL-97[311] within the program OLEX-2.[312] Non-hydrogen atoms were refined with anisotropic displacement parameters. Hydrogen atoms were included in calculated positions, or were manually assigned from residual electron density where appropriate, with isotropic displacement parameters 1.2 times the isotropic equivalent of their carrier atoms. The functions minimised were $\Sigma w(F^2_o - F^2_c)$, with $w = [\sigma^2(F^2_o) + aP_2 + bP]^{-1}$, were $P = [\max(F_o)^2 + 2F^2_c]/3$. Graphical representations of crystallographic data were prepared using the CrystalMaker, OLEX-2, Mercury software packages. Crystallographic data for all compounds is included in .cif format as electronic supplementary information.

7.1.8 Powder X-ray Powder Diffraction

X-ray powder diffraction data were collected using an Oxford-Agilent SuperNova instrument using Cu Kα (λ = 1.5418 Å) radiation and an ATLAS CCD area detector. Samples were dried at 60 °C overnight and stored under vacuum prior to analysis. Approximately 5 mg of sample were prepared for analysis by grinding with a minimal quantity of Paratone-N oil and applying a sample of *ca.* 0.5 mm in diameter to a thin glass fibre mounted on a goniometer head. The sample was centred directly in the X-ray beam path and the diffraction data were recorded using four averaged 360° scans in Φ with 150 second exposure time per rotation frame. The diffraction data were integrated radially and a background correction was manually applied to approximate the absorbance due to the fibre and oil.

7.1.9 Magnetic Susceptibility

Magnetic susceptibility measurements were conducted by Prof. Rodolphe Clérac and Mathieu Rouzieres at the Université de Bordeaux and were obtained with the use of a Quantum Design SQUID magnetometer MPMS-XL. This magnetometer works between 1.8 and 400 K for dc applied fields ranging from −7 to 7 T. Measurements were performed on a polycrystalline sample of approximately 10 mg introduced in a polyethylene bag (3 × 0.5 × 0.02 cm). Some samples were measured with a small amount of mother liquid layered over the crystalline sample to reduce the influence of solvent loss. Samples where this technique was employed were not heated above a temperature of 300 K.

The magnetic susceptibility measurements in Chapter Three were conducted by Prof. Keith Murray and Dr. Boujemaa Moubaraki at Monash University and were obtained using a Quantum Design SQUID magnetometer, PPMS 5 under a dc magnetic field of 1 T. The sample was contained in a gelatine capsule held at the centre of a drinking straw. Diamagnetic corrections for the ligand contribution were obtained using Pascal's constants.

7.1.10 Photomagnetic Measurements

The photo-magnetic experiments were performed with different sources coupled through an optical fibre directed into the magnetometer cavity. Powdered samples of approximately 5mg were packed in a thermo-formed straw maintained at 3 cm to the optical fibre. For all experiments, the magnetic data were corrected for the sample holder and the diamagnetic contribution.

7.1.11 Surface Reflectivity

The surface reflectivity measurements have been performed with a home built system. The temperature range is from 10 to 270 K. The spectrometric range runs from 400 − 1000 nm. The light for spectrometry is a halogen-tungsten light source (Leica CLS 150 XD tungsten halogen source adjustable from 0.05 mW cm^{-2} to 1 W cm^{-2}). The measurements were calibrated by a NIST traceable standard for reflectance (sphereOptics, ref 45 SG3054).

7.2 Synthesis of Chapter Two Compounds

*7.2.1. 3,3' – 1,1'-(hydrazine-1,2-diylidine)bis(ethan-1-yl-1ylidene)dianiline – **L2A***

m-Aminoacetophenone (1.0 g, 7.3 mmol) was dissolved in 20 mL ethanol with a few drops of glacial acetic acid. To this solution was added hydrazine monohydrate (0.2 mL, 4.1 mmol) and the resulting solution was refluxed for 4 hours and left to cool to room temperature slowly.

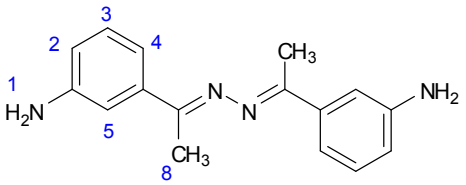

The product formed as a yellow-brown crystalline solid on cooling. Yield 0.87 g (3.3 mmol, 90%); m.p. 130 – 132 °C; δ_H (400 MHz; d_6-DMSO) 7.17 (1H, s, H_5) 7.10 (1H, t, J = 8 Hz, H_3) 7.04 (1H, d, J = 8 Hz, H_2) 6.66 (1H, d, J = 8 Hz, H_4) 5.18 (2H, s, H_1) 2.19 (3H, s, H_8); δ_C (125 MHz; d_6-DMSO) 157.11, 148.61, 138.65, 128.81, 115.42, 114.39, 111.68, 14.76; *m/z* (HR-ESMS) 267.1607 [M + H^+] calculated for $C_{16}H_{19}N_4$ 267.1604; υ_{max} (KBr) cm^{-1} 3411 m, 3374 m, 3299 m, 3203 m, 3025 m, 1937 w, 1851 w, 1772 w, 1570 s, 1486 s, 1448 s, 1361 s, 1319 s, 1238 s, 1163 m, 1079 m, 1049 m, 994 m, 871 s, 789 s, 693 s, 615, 538 m, 515 m, 501 m, 468 s.

*7.2.2 3,3'(1,1'-(hydrazine-1,2-diylidene)bis(ethan-1-yl-1-ylidene))bis-((1H-imidazol-2-yl)methylene)aniline – **L2.1***

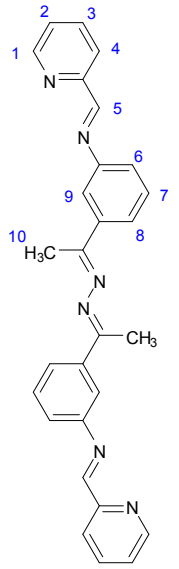

Pyridine-2-carboxaldehyde (0.5 g, 4.7 mmol) was added to **L2A** (0.5 g, 1.9 mmol) dissolved in 10 mL ethanol and heated at reflux for 4 hours. After this time the yellow solution was left to cool to room temperature and the excess solvent was removed *via* rotary evaporation to give a yellow oil. The residue was then dissolved in 10 mL dichloromethane and washed 3 times with 5 mL distilled water. The organic layers were combined and dried over anhydrous $MgSO_4$. The organic component was filtered and the solvent removed *via* rotary evaporation to give a pale yellow oil which solidified over some days at room temperature to give the product as an off-white solid. Yield 0.76 g (1.7 mmol, 88%) ; m.p. 106 – 110 °C; δ_H (400 MHz; CD_3CN) 8.68 (1H, d, J = 8 Hz, H_1) 8.62 (1H, s, H_5), 8.17 (1H, d, J = 8 Hz, H_4) 7.93 – 7.79 (3H, m, H_3/H_6/H_9) 7.50 – 7.41 (2H, m, H_2/H_7) 7.34 (1H, d, J = 8 Hz, H_8) 2.31 (3H, s, H_{10}); δ_C (100 MHz; CD_3CN) 162.96, 158.75, 155.94, 152.60, 151.16, 140.99, 138.27, 130.69, 126.85, 126.21, 123.55, 122.70, 120.70, 15.68 *m/z* (HR-ESMS) 445.2147 [M + H^+] calculated for $C_{28}H_{25}N_6$ 445.2135; υ_{max} (KBr) cm^{-1} 1567 m, 1469 m, 1423 m, 1288 m, 989 m, 903 m, 791 s, 772 s, 739 s, 683 vs, 617 m, 520 m.

*7.2.3. 3,3'(1,1'-(hydrazine-1,2-diylidene)bis(ethan-1-yl-1-ylidene))bis-((1H-imidazol-2-yl)methylene)aniline – **L2.2***

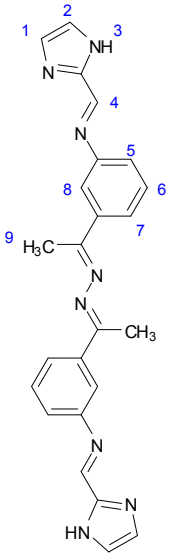

Imidazole-2-carboxaldehyde (200 mg, 2.0 mmol) was added to **L2A** (280 mg, 1.0 mmol) in 20 mL of methanol. The resulting suspension was heated at reflux for two hours. After approximately 30 minutes the imidazole-2-carboxaldehyde had fully dissolved and at completion of the reaction a pale yellow powder formed. The powder was filtered and air dried overnight to the give the product as a fine insoluble yellow powder. Yield 420 mg, 1.0 mmol, 99%; m.p. 250 – 254 °C; δ_H compound insoluble in common deuterated solvents; *m/z* (HR-ESMS) 423.2041 [M + H^+] calculated for $C_{24}H_{23}N_8$ 423.2046 ; υ_{max} (KBr) cm^{-1} 2897 br, 1940 w, 1743 w, 1625 s, 1574 s, 1441 s, 1387 s, 1361 s, 1293 s, 1270 s, 1190 m, 1152 m , 1135 m, 1112 s , 1075 m, 1000 s, 972 s, 915 s, 873 s, 813 m, 792 s, 777 s, 752 s, 718 w, 686 s, 645 w, 624 w, 584 w, 527 w, 507 w.

*7.2.4 3,3'-(1,1'-(hydrazine-1,2-diylidene)bis(ethan-1-yl-1-ylidene)bis(N-((1H-imidazol-4-yl)methylene)aniline **L2.3***

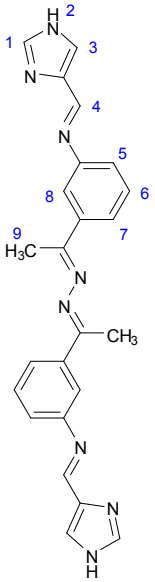

Imidazole-4-carboxaldehyde (40 mg, 0.42 mmol) was added to an ethanolic solution (3 mL) of **L2A** (50 mg, 0.19 mmol). The resulting suspension was heated gently at 60 °C for 15 minutes to allow reactants to dissolve and the pale yellow solution was stirred at room temperature for 3 hours. After this time the product formed as a pale yellow precipitate. Yield 65 mg (0.15 mmol, 79%); m.p. 197 – 199 °C; δ_H (400 MHz; d_6-DMSO) H_2 exchanges with d_6-DMSO solvent; 8.53 (1H, s, H_4) 7.86 (1H, s, H_8) 7.76 (1H, d, J = 8 Hz, H_5) 7.71 (2H, s, H_1/H_3) 7.48 (1H, t, J = 8 Hz, H_6) 7.30 (1H, d, J = 8Hz, H_7) 2.29 (3H, s, H_9); *m/z* (HR-ESMS) 423.2036 [M + H^+] calculated for $C_{24}H_{23}N_8$ 423.2040; υ_{max} (KBr) cm^{-1} 1628 s, 1598 s, 1462 w, 1294 m, 1094 m, 1006 m, 865 m, 785 s, 697 s, 625 s.

*7.2.5 Synthesis of Fe_2(**L2.1**)$_3$]$(BF_4)_4 \cdot 2CHCl_3 \cdot 3CH_3CN \cdot 5H_2O$ – **2.4***

The components pyridine-2-carboxaldehyde (50 µL, 0.47 mmol), **L2A** (60 mg, 0.23 mmol), and $Fe(BF_4)_2 \cdot 6H_2O$ were mixed with continuous stirring in 5 mL acetonitrile at room temperature. A purple solution formed after 5 minutes and the reaction mixture was stirred for a further 30 minutes to ensure complete self assembly of components. The reaction mixture was filtered and the filtrate was diffused with chloroform to give block purple crystals suitable for structural analysis *via* single crystal X-ray diffraction. Yield 32 mg (0.014 mmol; 19%) Found (%): C, 54.1; H, 4.10; N, 13.1; $C_{84}H_{72}B_2N_{16}F_{16}Fe_2 \cdot CHCl_3$ requires (%): C, 54.0; H, 3.89; N, 13.3; m.p. > 250 °C; δ_H (400 MHz; CD_3CN) 8.85 (1H, s, H_5) 8.53 (1H, d, J = 8 Hz, H_1) 8.40 (1H, t, J = 8 Hz, H_3) 8.14 (1H, d, J = 8 Hz, H_8) 7.75 (1H, t, J = 8 Hz, H_2) 7.35-7.40 (2H, m, H_4/H_7) 5.66 (1H, d, J = 8 Hz, H_6) 5.43 (1H, s, H_9) 3.26 (3H, d, H_{10}); UV-Vis λ_{max} (ε) 570 nm (10700 ± 100 L mol^{-1} cm^{-1}); *m/z* (HR-ESMS) 361.1213 [$Fe_2L_3^{4+}$] calculated for $[C_{84}H_{72}N_{18}Fe_2]^{4+}$ 361.1225; υ_{max} (KBr) cm^{-1} 1574 m, 1557 m, 1472 m, 1441 m, 1365 m, 1300 m, 1237 m, 1190 w, 1169 w, 1033 vs, 886 s, 810 s, 768 s, 700 s, 520 s.

*7.2.6 Synthesis of [Fe_2(**L2.2**)$_3$](BF_4)$_4$·2.5MeCN – **2.5***

$Fe(BF_4)_2·6H_2O$ (25 mg, 0.07 mmol) was added to a suspension of **L2.2** (40 mg, 0.10 mmol) in 3 mL acetonitrile. The reaction mixture was stirred at room temperature for 2 hours over which time the reactants fully dissolved and a raspberry red solution formed. The reaction mixture was filtered and thin red needle crystals suitable for single crystal X-ray diffraction formed *via* a slow diffusion of diethyl ether into the filtrate. Yield 15 mg (0.009 mmol, 27%), Found (%): C, 46.9; H, 4.40; N. 17.90; $C_{72}H_{66}B_4N_{24}F_{16}Fe_2·CH_3CN·0.5Et_2O·8H_2O$ requires (%): C, 46.8; H, 4.66; N, 18.0; m.p. > 250 °C; UV-Vis (ε) 540 nm (3030 L mol^{-1} cm^{-1}) υ_{max} (KBr) cm^{-1} 3276 br, 1612 w, 1573 w, 1435 m, 1364 w, 1051 br s, 163 br, 692 s, 518 m, 454 br.

*7.2.7 Synthesis of [Fe_2(**L2.3**)$_3$](BF_4)$_4$·3$CHCl_3$·1.5CH_3CN·1H_2O – **2.6***

$Fe(BF_4)·6H_2O$ (35 mg, 0.10 mmol) dissolved in 1 mL acetonitrile was added dropwise to **L2.3** (60 mg, 0.15 mmol) dissolved in 3 mL acetonitrile. The resulting mixture was stirred at room temperature for 30 minutes after which time a bright orange solution had formed. The solution was subsequently filtered and single crystals were generated by the slow diffusion of $CHCl_3$ into the acetonitrile solution producing large orange block crystals. This product could also be formed *via* self-assembly by mixing the individual components (imidazole-4-carboxaldehyde, **L2A**, and $Fe(BF_4)_2·6H_2O$) in a 6:3:2 ratio in acetonitrile. The identity of crystals isolated by this method was confirmed by performing unit cell checks on representative samples. Yield 29 mg (0.017 mmol, 30%); Found (%): C, 46.0; H, 3.78; N, 17.9; $C_{72}H_{66}$ $B_4N_{24}F_{16}Fe_2·2CH_3CN·2CHCl_3$ requires (%): C, 45.8; H, 3.64; N, 17.8; m.p. > 250 °C; *m/z* (HR-ESMS) complex fragments; υ_{max} (KBr) cm^{-1} 3316 br, 1619 m, 1595 m, 1573 w, 1437 w, 1365 w, 1295 m, 1005 s br, 993 m, 800 m, 746 s, 692 s, 614 s, 520.

7.3 Synthesis of Chapter Three Compounds

*7.3.1 4,4' – oxybis(1-methyl-1H-imidazol-2-yl)methylene)aniline – **L3.1***

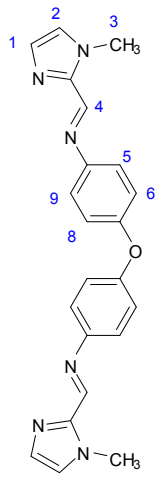

Following preparation provided by Kruger.[120] *1*-Methyl-2-imidazolecarboxaldehyde (220 mg, 1.96 mmol) and 4,4'-oxydianiline (200 mg, 0.97 mmol) were stirred in methanol (10 mL) for 18 hours. The pale yellow solution was evaporated to dryness; the oil obtained was dissolved in dichloromethane. The organic solution was dried over $MgSO_4$, filtered and the solvent was removed. The residue obtained was recrystallised from acetonitrile. The off-white solid that formed was collected by filtration. Yield: 215 mg (0.56 mmol, 58%); Found (%) C, 68.47; H, 5.44; N, 21.53 $C_{22}H_{20}N_6O$ requires (%): C, 68.72; H, 5.25; N, 21.87; mp: 154-156 °C; δ_H (400 MHz; d_6-DMSO] 8.52 (s, 1H, H_4), 7.43 (s, 1H, H_1), 7.37 (d, 2H, J = 8.8 Hz, H_6), 7.16 (s, 1H, H_2), 7.08 (d, 2H, J = 8.8 Hz, H_5), 4.05 (s, 3H, H_3); δ_C (100 MHz; d_6-DMSO) 155.3, 150.5, 146.3, 142.8, 129.7, 126.5, 122.8, 119.4, 35.2; *m/z* (HR-ESMS) 385.1765 [M + H^+] calculated for $C_{22}H_{21}N_6O$ 385.1777.

*7.3.2 Synthesis and Characterisation of $[Fe_2(\mathbf{3.1})_3](ClO_4)_2 \cdot xH_2O$ – **3.2·H₂O***

Ligand **L3.1** (92 mg, 0.24 mmol) was dissolved in methanol (5 mL) and a methanolic (5 mL) solution of iron perchlorate hexahydrate (60 mg, 0.17 mmol) was added dropwise. A dark-orange precipitate formed instantly. The reaction mixture was stirred for at room temperature for 15 minutes and the product collected by filtration and recrystallised from MeCN following the slow diffusion of diethylether, and the thin red-needles were collected and air dried. Yield: 190 mg, 68 %; Found (%): C, 46.25; H, 3.79; N, 14.58; $Fe_2C_{66}H_{60}N_{18}O_{18}Cl_4 \cdot 3H_2O$ requires (%): C, 46.17; H, 3.88; N, 14.69; *m/z* (ESMS) 316.0958 [$Fe_2L_3^{4+}$] calculated for $[C_{66}H_{60}N_{18}O_3Fe_2]^{4+}$ 316.0944; υ_{max} (KBr) cm^{-1} 3511 br, 1628 m, 1495 s, 1448 m, 1328 m, 1295 m, 1243 s, 1245 s, 1080 s, 927 m, 903 m, 865 m, 776 m, 664 m, 593 m, 532 m, 508 m, 473 m, 455 m.

7.4 Synthesis of Chapter Four Compounds

*7.4.1 Synthesis of (1H-imidazol-2-yl)methylene)-4-methoxyaniline – **L4.1***

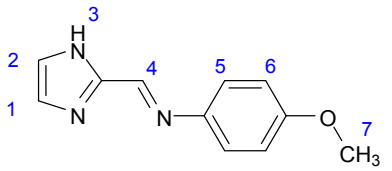

Following preparation given by Kruger.[218] *p*-Anisidine (300 mg, 2.5 mmol) was dissolved in 10 mL methanol and added to a suspension of imidazole-2-carboxaldehyde (240 mg, 2.5 mmol) in 10 mL methanol. The reaction mixture was heated at reflux for 4 hours after which time a colourless solution had formed. The reaction mixture was left to cool to room temperature slowly and after approximately 30 minutes long grey needle crystals formed. Crystals suitable for X-ray structural analysis were obtained *via* the slow evaporation of the reaction mixture. Characterisation data consistent with reference. Yield 340 mg (1.7 mmol, 70%); m.p. 178 - 179 °C; δ_H (500 MHz, $CDCl_3$) 8.49 (1H, s, H_4), 7.26 (1H, s, H_1/H_2), 7.21 (2H, d, J = 8.5Hz, H_5) 7.06 (1H, s, H_1/H_2), 6.90 (2H, d, J = 8.5Hz, H_6), 3.82 (3H, s, H_7); δ_C (126 MHz, $CDCl_3$) 159.2, 148.0, 145.8, 143.1, 131.5, 122.6, 119.0, 114.8, 55.8; *m/z* (HR-ESMS) 224.0794 [M + Na^+] calculated for $C_{11}H_{11}N_3O_3Na$ 224.0794 ; υ_{max} (KBr) cm^{-1} 2891 br, 2036 m, 1625 s, 1504 s, 1391 m, 1245 s, 1112 m, 832 m, 539 br s.

*7.4.2 Synthesis of (1H-imidazol-2-yl)methylene-4-methylaniline – **L4.2***

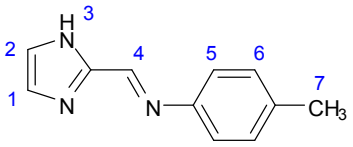

p-Toluidine (520 mg, 4.9 mmol) was dissolved in 20 mL ethanol. To this solution imidazole-2-carboxaldehyde (480 mg, 5.0 mmol) was added and the resulting suspension was heated at reflux for 4 hours at which point the imidazole-2-carboxaldehyde had fully dissolved resulting in a yellow solution. The solution was left to cool to room temperature to give the product as a white crystalline solid. Yield 710 mg (3.8 mmol, 78%); m.p. decomposes at 185 °C; δ_H (500 MHz; d_6-DMSO) H_3 exchanges with solvent, 8.39 (1H, s, H_4) 7.25 (2H, br s, H_1/H_2) 7.21 (4H, d, H_5/H_6) 2.32 (3H, s, H_7); δ_C (100MHz; d_6 -DMSO [D_6]) 149.54, 148.19, 145.08, 135.78, 129.92, 120.96, 20.66; *m/z* (HR-ESMS) 186.1027 [M + H^+], calculated for $C_{11}H_{12}N_3$ 186.1026; υ_{max} (KBr) cm^{-1} 2917 br, 1631 m, 1506 m, 1438 m, 1306 m, 1214 m, 1154 m, 1115 s, 960 s, 932 s, 799 m, 765 m, 535m, 490 m.

*7.4.3 Synthesis of (1H-imidazol-2-yl)methylene-4-bromoaniline – **L4.3***

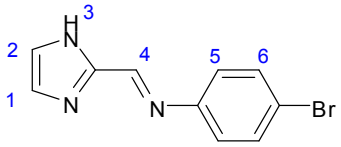

p-Bromoaniline (520 mg, 3.0 mmol) was dissolved in 20 mL ethanol. Imidazole-2-carboxaldehyde (290 mg, 3.0 mmol) was suspended in 20 mL ethanol and added to the aniline solution. The resulting mixture was heated at reflux for 2 hours at which time the imidazole-2-carboxaldehyde had fully dissolved and a pale yellow solution had formed. The reaction mixture was allowed to slowly cool to room temperature and the excess solvent removed *via* rotary evaporation to give the product a pale yellow crystalline product suitable for single crystal X-ray diffraction. Yield 620 mg (2.5 mmol, 83%); m.p. 204-205 °C; δ_H (500 MHz; d_6-DMSO) H_3 exchanges with solvent, 8.41 (1H, s, H_4) 7.59 (2H, d, J = 8.5 Hz, H_6) 7.29 (2H, s, H_1/H_2) 7.25 (2H, d, J = 8.5 Hz, H_5); δ_C (100 MHz, [D_6] DMSO) 150.90, 149.74, 144.54, 123.64, 131.95, 123.00, 118.53; *m/z* (HR-ESMS) 249.9970 [M + H^+] calculated for $C_{10}H_9N_3Br$ 249.9974; υ_{max} (KBr) cm^{-1} 2879 br s, 2865 m, 2357 m, 1911 br, 1713 m, 1631 m, 1580 m, 1631 s, 1580 m, 1548 m, 1488 s, 1453 s, 1438 s, 1413 m, 1347 m, 1314 m, 1205 m, 1168 m, 1114 m, 1098 m, 1072 m, 1006 m, 960 m, 869 s, 834 s, 782 s, 699 m, 635 m, 559 m, 528 s, 480 m, 453 m.

*7.4.4 Synthesis of (4-((1H-imidazol-2-yl)methyleneamino)phenyl)ethanone – **L4.4***

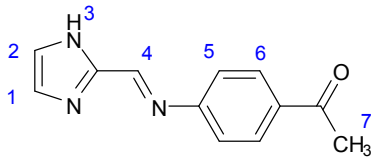

p-Aminoacetophenone (580 mg, 3.9 mmol) dissolved in 20 mL ethanol was added to imidazole-2-carboxaldehyde (370 mg, 3.9 mmol). The suspension was then heated at reflux for 4 hours after which time an insoluble white precipitate had formed. The solid was filtered and air dried overnight to give the product. Yield: 640 mg (3.0 mmol, 78%); m.p. 204 - 205 °C; δ_H compound insoluble in common deuterated solvents; *m/z* (HR-ESMS) 214.0974 [M + H^+] calculated for $C_{12}H_{12}N_3O$ 214.0975; υ_{max} (KBr) cm^{-1} 3234 br, 3159 br, 3036 m, 1665 s, 1603 s, 1512 m, 1480 m, 1442 m, 1364 m, 1308 m, 1280 s, 1231 m, 1186 s, 1131 m, 1098 m, 1068 m, 962 m, 932 m, 897 m, 869 m, 855 m, 830 m, 816 m, 759 m, 702 m, 677 m, 638 m, 595 m, 518 m, 489 m.

*7.4.5 Synthesis of (1H-imidazol-4-yl)methylene-4-methylaniline – **L4.5***

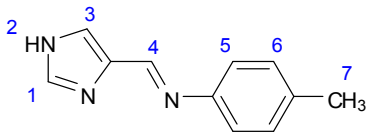

Imidazole-4-carboxaldehyde (200 mg, 2.1 mmol) and *p*-toludiene (230 mg, 2.1 mmol) were heated at reflux in 20 mL methanol for 4 hours. The resulting pale yellow solution was then cooled to room temperature and the sample was concentration to approximately ¼ of the initial volume *via* rotary evaporation. A cream fibrous microcrystalline product was formed as the solution cooled. Yield 340mg (1.8mmol, 88%); m.p. decomposes at 160 °C; δ_H (500 MHz; d_6-DMSO) 8.43(1H, s, H_4) 7.83 (1H, s, H_1) 7.64 (1H, s, H_3) 7.18 (2H, d, J = 8Hz, H_6) 7.10 (2H, d, J = 8Hz, H_5) 2.29 (3H, s, H_7); δ_C (100 MHz; d_6-DMSO) 134.43, 129.49, 120.42, 20.31; *m/z* (ESMS) 186.1027 [M + H^+] calculated for $C_{11}H_{12}N_3$ 186.1026; ν_{max} (KBr) cm^{-1} 2831 br, 1632 m, 1505 m, 1438 m, 1353 m, 1305 m, 1226 m, 1199 m, 1147 m, 1088 m, 980 m, 878 m, 842 m, 737 m, 716 m, 622 m, 539 m, 495 m.

*7.4.6 Synthesis of [Fe(**L4.1**)$_3$](BF$_4$)$_2$ – **4.7***

$Fe(BF_4)_2 \cdot 6H_2O$ (20 mg, 0.05 mmol) dissolved in 0.5 mL acetonitrile was added to a solution of **L4.1** (35 mg, 0.17 mmol) dissolved in 3 mL dichloromethane. The resulting bright red solution was gently heated at reflux for 1 hour. After this time the solution was left to cool to room temperature and filtered. The filtrate was then carefully layered with approximately 2 mL diethyl ether. Red plate crystals suitable for single crystal X-ray diffraction formed after a few days. Yield 15 mg (0.018 mmol, 72%); Found (%): C, 47.4; H, 3.8; N, 15.1; $C_{33}H_{33}B_2N_9O_3F_8Fe$ requires (%): C, 47.6; H, 4.0; N, 15.1; m.p. 165 - 166 °C; *m/z* (HR-ESMS) complex fragments; υ_{max} (KBr) cm^{-1} 3313 br, 2926 m, 1613 m, 1558 m, 1507 s, 1444 s, 1346 w, 1301 m, 1249 s, 1212 m, 1170 m, 1112 s, 1069 s, 1015 br s, 953 s, 889 m, 834 m, 806 m, 765 m, 548 m, 517 m, 491 m.

*7.4.7 Synthesis of [Fe(**L4.1**)$_3$](ClO$_4$)$_2$·CH$_3$CN – **4.8***

$Fe(ClO_4)_2 \cdot 6H_2O$ (25 mg, 0.7 mmol) dissolved in 0.5 mL acetonitrile was added to a solution of **L4.1** (40 mg, 0.20 mmol) dissolved in 3 mL dichloromethane. The resulting bright red solution was gently heated at reflux for 1 hour. After this time the solution was left to cool to room temperature and filtered to remove any undissolved reactants once cooled. The filtrate was then carefully layered with approximately 2 mL diethyl ether. Red plate crystals suitable for single crystal X-ray diffraction formed after a few days. Yield 18 mg (0.02 mmol, 57 %); Found (%): C, 44.68; H, 3.99; N, 14.32; $C_{33}H_{33}N_9O_{11}Cl_2Fe \cdot 1.5H_2O$ requires (%): C, 44.76; H, 4.10; N, 14.24; *m/z*

(HR-ESMS) complex fragments; υ_{max} (KBr) cm^{-1} 3270 br, 2933 m, 2253 m, 2050 m, 1611 m, 1581 m, 1507 s, 1466 m, 1442 s, 1340 w, 1305 m, 1248 s, 1209 m, 1170 m, 1117 br, 1031 m, 958 m, 925 m, 889 m, 833 m, 807 m, 771 m, 624 s, 552 m, 507 m, 471 m.

*7.4.8 Synthesis of [Fe(**L4.2**)$_3$](BF$_4$)$_2$·1CH$_3$CN·0.5H$_2$O – **4.9***

L4.2 (60 mg, 0.31 mmol) was suspended in 3 mL dichloromethane and $Fe(BF_4)_2.6H_2O$ (40 mg, 0.11 mmol) dissolved in a small amount of acetonitrile. The resulting red solution was refluxed gently (60 °C) for 1 hour after which time the solution was cooled to room temperature and carefully layered with 2 mL of diethyl ether and left to stand for a week. Red block crystals suitable for structural determination *via* X-ray crystallography were collected after one week. Yield 45 mg (0.06 mmol, 55%); Found (%): C, 46.0; H, 4.30; N, 14.7; $C_{33}H_{33}B_2N_9F_8Fe·4H_2O$ requires (%): C, 46.2; H, 4.82; N, 14.7%; m.p. 168-170 °C; *m/z* (ESMS) 305.6098 [FeL_3^{2+}] calculated for $[C_{33}H_{33}N_9Fe]^{2+}$ 305.6099; υ_{max} (KBr) cm^{-1} 2930 br, 1621 w, 1555 w, 1510 m, 1468 m, 1441 s, 1349 w, 1216 w, 1084 br s, 892 m, 803 m, 515 m.

*7.4.9 Synthesis of [Fe(**L4.2**)$_3$](ClO$_4$)$_2$·CH$_3$CN·0.5H$_2$O – **4.10***

L4.2 (110 mg, 0.60 mmol) was dissolved in 3 mL dichloromethane and $Fe(ClO_4)_2·6H_2O$ (80 mg, 0.20 mmol) dissolved in a few drops of acetonitrile was added to the ligand solution. The solution turned red immediately and was heated gently at reflux for 1 hour. The solution was filtered while hot and left to cool to room temperature after which time the filtrate was layered carefully with 2 mL diethyl ether. Red block crystals suitable for single crystal X-ray diffraction formed after approximately one week. Yield 65 mg (0.4 mmol, 40%) ; Found (%): C, 48.95; H, 4.08; N, 15.55; $C_{33}H_{33}N_9O_8Cl_2Fe$ requires (%): C, 48.91; H, 4.10; N, 15.55; *m/z* (HR-ESMS) complex fragments; υ_{max} (KBr) cm^{-1} 3262 br, 1615 m, 1557 m, 1506 m, 1470 m, 1443 s, 1338 m, 1206 m, 1100 br, 1014 m, 933 m, 888 m, 803 m, 772 m, 703 m, 622 m, 544 m, 507 m, 463 m.

*7.4.10 Synthesis of [Fe(**L4.3**)$_3$](ClO$_4$)$_2$·CH$_2$Cl$_2$ – **4.11***

A suspension of **L4.3** (130 mg, 0.50 mmol) in 3 mL dichloromethane was added portion-wise to an 0.5 mL acetonitrile solution of $Fe(ClO_4)_2·6H_2O$ (60 mg, 0.17mmol). The resulting dark red solution was heated at reflux for 1 hour and allowed to slowly cool to room temperature. The solution was diluted to 10 mL with dichloromethane and layered with 5 mL of diethyl ether and

left to stand covered overnight to yield red crystalline plate crystals. Yield 60 mg (0.060 mmol, 35%); Found (%): C, 35.82; H, 2.61; N, 12.52; $C_{30}H_{24}N_9O_8Cl_2FeBr_3$ requires (%): C, 35.85; H, 2.41; N, 12.54; *m/z* (ESMS) 402.4510 $[FeL_3^{2+}]$ calculated for $[C_{30}H_{24}N_9Br_3Fe]^{2+}$ 401.4522; υ_{max} (KBr) cm^{-1} 3419 br, 3316 m, 3223 m, 1606 m, 1556 m, 1482 m, 1468 m, 1436 s, 1339 w, 1207 m, 1183 w, 1093 br s, 1005 m, 932 m, 886 m, 781 m, 618 s, 541 m.

*7.4.11 Synthesis of [Fe(**L4.4**)$_3$](BF$_4$)$_2$ – **4.12***

$Fe(BF_4)_2 \cdot 6H_2O$ (20 mg, 0.05 mmol) dissolved in 0.5 mL acetonitrile was added to a 3 mL dichloromethane suspension of **L4.4** (40 mg, 0.19 mmol). The resulting suspension was heated gently at reflux for 1 hour after which time the reactants had fully dissolved and a red solution had formed. The reaction solution was left to cool to room temperature and filtered to remove any unreacted starting materials. The filtrate was carefully layered with approximately 2 mL of diethyl ether and sealed and left to stand. Orange plate crystals suitable for single crystal X-ray diffraction formed after approximately one week. Yield 36 mg (0.04 mmol, 85%); Microanalysis shows highly variable solvent content; m.p. > 250 °C; *m/z* (HR-ESMS) complex fragments; υ_{max} (KBr) cm^{-1} 3292 br, 1658 m, 1590 m, 1437 m, 1276 m, 1008 br s, 893 m, 846 m, 702 m, 591 m.

*7.4.12 Synthesis of [Fe(**L4.5**)$_3$](BF$_4$)$_2$·CH$_3$CN – **4.13***

L4.5 (65 mg, 0.35 mmol) and $Fe(BF_4)_2.6H_2O$ (40 mg, 0.11 mmol) were mixed in 1 mL acetonitrile with gentle heating for 15 minutes. The resulting bright orange solution was filtered and 1 mL dichloromethane was added to the filtrate. The filtrate was then layered with approximately 5 mL diethyl ether and left to stand in the freezer for over a week. After this time yellow block crystals suitable for X-ray crystallography formed. Yield 41 mg (0.05 mmol, 45%); Found (%): C, 48.4; H, 4.25; N, 15.4; $C_{33}H_{33}B_2N_9F_8Fe \cdot 2H_2O$ requires (%): C, 48.3; H, 4.54; N, 15.4 ; m.p. 198-202 °C; ν_{max} (KBr) cm^{-1} 3147 br, 2257 m, 1624 s, 1507 s, 1449 s, 1296 s, 1231 m, 1082 br s, 892 s, 824 s, 618 s, 550s.

7.5 Synthesis of Chapter Five Compounds

*7.5.1 Synthesis of 4-nitro-(pyridine-2-ylmethylene) aniline – **L5.1***

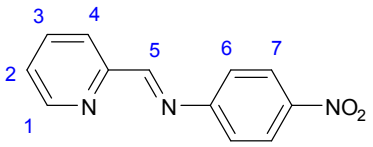

p-Nitro aniline (630 mg, 4.6 mmol), pyridine-2-carboxaldehyde (490 mg, 4.6 mmol) were dissolved in 20 mL ethanol. The reaction mixture was heated at reflux for 3 hours and the resulting yellow solution was cooled to room temperature. The excess solvent was removed *via* rotary evaporation to give an orange residue. The residue was then dissolved in 10 mL of dichloromethane and was dried over anhydrous $MgSO_4$ and the excess solvent removed again *via* rotary evaporation to give an orange waxy solid. Attempts to purify the ligand were unsuccessful with various recrystallisation attempts resulting in fragmentation of the product. As such the ligand was used in its crude form for complexation. M.P. 143-145 °C; υ_{max} (KBr) cm^{-1} 1595 m, 1552 m, 1525 m, 1307 m, 1181 m, 1132 m, 1123 m, 1001 m, 906 m, 840 m, 828 m, 775 m, 751 m, 723 m, 694 m.

*7.5.2 Synthesis of 4-(pyridine-2-ylmethyleneamino)benzonitrile – **L5.2***

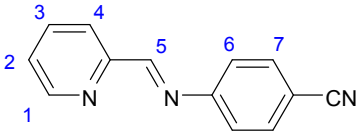

p-Aminobenzonitrile (310 mg, 2.6 mmol) and pyridine-2-carboxaldehyde (280 mg, 2.6 mmol) were dissolved in 20 mL methanol. The reaction mixture was heated at reflux for 3 hours and the resulting yellow solution was cooled to room temperature. The excess solvent was removed *via* rotary evaporation to give a yellow residue. The residue was then dissolved in 10 mL of dichloromethane and was dried over anhydrous $MgSO_4$ and the excess solvent removed again *via* rotary evaporation to give the product as a yellow oil. Attempts to purify the ligand were unsuccessful, as observed with **L5.1**, and the ligand was used in its crude form for complexation. *m/z* (ESMS) 208.0868 [M + H^+] calculated for $C_{11}H_{10}N_3$ 208.0869; υ_{max} (KBr) cm^{-1} 3317 m, 2216 m, 1593 s, 1518 m, 1436 m, 1422 m, 1320 m, 1093 m, 1051 m, 1015 m, 991 s828 m, 780 m, 753 m, 625 m, 613 m, 535 m.

7.5.3 *Synthesis of (1H-imidazol-2-yl)methylene)-4-nitroaniline – **L5.3***

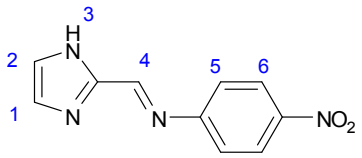

p-Nitroaniline (720 mg, 5.2 mmol) was dissolved in 20 mL ethanol with gentle heating. A separate suspension of imidazole-2-carboxaldehyde (510 mg, 5.3 mmol) was prepared in 20 mL ethanol. The imidazole suspension was added portion wise to the aniline solution and the resulting mixture was refluxed for 5 hours and subsequently cooled to room temperature and the excess solvent was removed *via* rotary evaporation to give the yellow product. Attempts to purify the compound were unsuccessful and the ligand was used in its crude form for complexation. m.p. decomposes at 160 °C; *m/z* (ESMS) 217.0720 [M + H^+] calculated for $C_{10}H_9N_4O_2$ 217.0725; υ_{max} (KBr) cm^{-1} 3259 br, 2922 m, 1923 m, 1600 m, 1488 m, 1352 m, 1268 s, 1235 m, 1197 m, 1101 m, 551 m.

7.5.4 *Synthesis of 4-(1H-imidazol-2-yl)methyleneamino)benzonitrile – **L5.4***

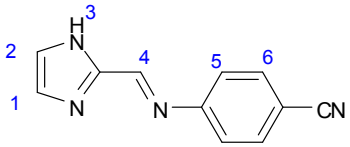

p-Aminobenzonitrile (590 mg, 5.0 mmol) was dissolved in 20 mL methanol. Imidazole-2-carboxaldehyde (480 mg, 5.0 mmol) was added portion wise with constant stirring. The reaction mixture was heated at reflux for 5 hours to give a pale yellow solution. The solution was concentrated to give the crude product as a white powder. Attempts to purify the compound were unsuccessful and the ligand was used in its crude form for complexation. m.p. decomposes at 168 °C; *m/z* (ESMS) 197.0822 [M + H^+] calculated for $C_{11}H_9N_4$ 197.0822; υ_{max} (KBr) cm^{-1} 3251 br, 2922 m, 2222 m, 1610 m, 1532 m, 1485 m, 1450 m, 1327 m, 1273 m, 1235 m, 1179 m, 1103 s, 829 m, 755 m, 546 m.

7.5.5 *Synthesis of [Fe(**L5.1**)$_2$(CH$_3$CN)$_2$](BF$_4$)$_2$ – **5.5***

L5.1 (50 mg, 0.22 mmol) was suspended in 5 mL acetonitrile. To this solution $Fe(BF_4)_2 \cdot 6H_2O$ (45 mg, 0.12 mmol) was added resulting in the formation of a raspberry red solution. The reaction mixture was carefully layered with approximately 3 mL diethyl ether and left to stand for a few days. After this time the product formed as black block crystals. Yield 62 mg (0.41 mmol, 74%); Found: C, 42.8; H, 2.9; N, 13.5; $C_{26}H_{21}B_2N_7F_8Fe$ requires: C, 43.0; H, 3.00; N, 13.7; m.p. 186 – 190 °C; UV-Vis (ε) 543 nm (2430 L mol^{-1} cm^{-1}) υ_{max} (KBr) cm^{-1} 3504 br, 1624 m, 1588 m, 1486 m, 1447 w, 1346 s, 1312 w, 1198 w, 1166 w, 1026 br s, 1006 br s, 912 m, 855 m, 779 m, 743 m, 701 m, 689 m, 546 m, 522 m, 455 m.

*7.5.6 Synthesis of [Fe(**L5.2**)$_2$(CH$_3$CN)$_2$](BF$_4$)$_2$·2CH$_3$CN – **5.6***

L5.2 (20 mg, 0.10 mmol) and $Fe(BF_4)_2 \cdot 6H_2O$ (20 mg, 0.05 mmol) were mixed in 1 mL acetonitrile. The resulting purple solution was carefully layered with 2 mL diethyl ether and left to stand in the freezer for two days. After this time dark purple block crystals suitable for single crystal X-ray diffraction formed. Yield: 10 mg (0.01 mmol, 20%); m.p. 208-212 °C; Microanalysis showed highly variable solvent content; ν_{max} (KBr) cm^{-1} 3518 br, 2232 s, 1600 s, 1499 m, 1444 m, 1204 m, 1065 br s, 852 m, 786 m, 568 m, 523 s, 502 m, 463 m.

*7.5.7 Synthesis of [Fe(**L5.3**)$_2$(CH$_3$CN)$_2$](ClO$_4$)$_2$·CH$_3$CN – **5.7***

L5.3 (30 mg, 0.14 mmol) was suspended in 10 mL acetonitrile. To this suspension was added $Fe(ClO_4)_2 \cdot 6H_2O$ (15 mg, 0.05 mmol). The resulting red solution was heated at reflux for 1 hour and left to cool to room temperature. The reaction solution was filtered. The filtrate was separated equally into two vials (5 mL per vial) and 2.5 mL of diethyl ether was carefully layered. Red block crystals suitable for single crystal X-ray diffraction formed after a few days. Yield: 12 mg (0.02 mmol, 36%); Microanalysis showed highly variable solvent content; υ_{max} (KBr) cm^{-1} 1609 m, 1583 m, 1507 m, 1465 w, 1435 m, 1392 w, 1345 m, 1305 w, 1248 w, 1210 w, 1171 w, 1061 br s, 930 m, 891 m, 859 m, 833 m, 770 m, 750 m, 691 m, 543 m, 487 s.

*7.5.8 Synthesis of [Fe(**L5.4**)$_2$(CH$_3$CN)$_2$](ClO$_4$)$_2$·CH$_3$CN – **5.8***

$Fe(ClO_4)_2 \cdot 6H_2O$ (85 mg, 0.24 mmol) was added to a suspension of **5.4** (140 mg, 0.73 mmol) in 12 mL acetonitrile. The reaction mixture immediately turned bright red and was gently heated to ensure completely dissolution of the reactants. The reaction mixture was left to cool to room temperature and the solution was reduced to half its initial volume *via* rotary evaporation. Diethyl ether was added in 1mL aliquots until the solution became turbid and a red oil formed. The oil was dissolved in 5 mL acetonitrile and layered with 5mL diethyl ether and left to stand at 4 °C. Crystals suitable for single crystal X-ray diffraction formed after one week. Yield 63 mg (0.10 mmol; 42%); microanalysis showed highly variable solvent content; υ_{max} (KBr) cm^{-1} 3159 br, 2930 s, 2284 m, 2233 m, 1591 m, 1499 m, 1438 m, 1215 m, 1103 br s, 920 m, 625 m, 567 m.

APPENDIX I

Crystallographic Refinement Data

Table A-I.1 *Crystallographic Data for* ***2.4 – 120 K*** *and* ***2.5 – 120 K***

Compound reference	**2.4 – 120 K**	**2.5 - 120 K**
Chemical formula	$C_{84}H_{66}Fe_2N_{18}$•2($CHCl_3$)• 4(BF_4)•5(H_2O)•3(C_2H_3N)	[$C_{72}H_{66}Fe_2N_{24}$](BF_4)$_4$• 2.5(CH_3CN)
Formula Mass	2228.39	1829.02
Crystal system	Monoclinic	Orthorhombic
a/Å	27.8765(10)	18.3905(4)
b/Å	28.1735(6)	22.6878(9)
c/Å	14.1356(4)	19.0917(6)
α/°	90.00	90.00
β/°	114.958(4)	90.00
γ/°	90.00	90.00
Unit cell volume/Å^3	10065.1(5)	7965.8(4)
Temperature/K	120.01	119.99(10)
Space group	*C*2/*c*	*Pccn*
No. of formula units per unit cell, *Z*	4	4
No. of reflections measured	18611	31739
No. of independent reflections	9051	7175
R_{int}	0.0351	0.0379
Final R_1 values ($I > 2\sigma(I)$)	0.0792	0.0763
Final $wR(F^2)$ values ($I > 2\sigma(I)$)	0.2271	0.2210
Final R_1 values (all data)	0.0948	0.1117
Final $wR(F^2)$ values (all data)	0.2434	0.2528

Table A-I.2 *Crystallographic Data for* ***2.6 – 120 K*** *and* ***2.6 – 240 K***

Compound reference	**2.6-120 K**	**2.6 - 240 K**
Chemical formula	$C_{72}H_{66}Fe_2N_{24}$•3($CHCl_3$)•4(BF_4)• 1.5(C_2H_3N)•H_2O	$C_{72}H_{66}Fe_2N_{24}$•2($CHCl_3$)• 4(BF_4)•C_2H_3N•OH_2
Formula Mass	2161.11	2002.33
Crystal system	Triclinic	Triclinic
a/Å	13.9106(5)	14.1516(9)
b/Å	15.9337(6)	16.1395(8)
c/Å	24.8612(9)	24.9544(11)
α/°	73.547(3)	73.358(4)
β/°	75.732(3)	76.332(5)
γ/°	73.498(3)	73.466(5)
Unit cell volume/Å^3	4983.8(3)	5160.2(5)
Temperature/K	120.01	240.01(10)
Space group	$P\bar{1}$	$P\bar{1}$
No. of formula units per unit cell, *Z*	2	2
No. of reflections measured	33653	37010
No. of independent reflections	17150	20320
R_{int}	0.0601	0.0740
Final R_1 values ($I > 2\sigma(I)$)	0.1173	0.1477
Final $wR(F^2)$ values ($I > 2\sigma(I)$)	0.3217	0.3684
Final R_1 values (all data)	0.1418	0.2079
Final $wR(F^2)$ values (all data)	0.3514	0.4205

Table A-I.3 *Crystallographic Data for* ***3.2·H_2O – 150 K*** *and* ***4.7 – 120 K***

Compound reference	**3.2·H_2O – 150 K**	**4.7-120 K**
Chemical formula	$C_{66}H_{60}Cl_4Fe_2N_{18}O_{20.5}$	$C_{33}H_{33}FeN_9O_3$•2(BF_4)
Formula Mass	1686.82	833.15
Crystal system	Monoclinic	Triclinic
a/Å	14.82(4)	10.6462(7)
b/Å	27.22(8)	12.0783(7)
c/Å	18.98(6)	15.0902(8)
α/°	90	84.209(5)
β/°	107.88(4)	85.779(5)
γ/°	90	69.963(6)
Unit cell volume/Å^3	7284(36)	1812.09(19)
Temperature/K	150(2)	120.01(10)
Space group	$P2_1/c$	$P\bar{1}$
No. of formula units per unit cell, *Z*	4	2
No. of reflections measured	37303	13475
No. of independent reflections	7330	7107
R_{int}	0.5358	0.0270
Final R_1 values ($I > 2\sigma(I)$)	0.1242	0.0440
Final $wR(F^2)$ values ($I > 2\sigma(I)$)	0.2600	0.1160
Final R_1 values (all data)	0.3104	0.0469
Final $wR(F^2)$ values (all data)	0.3435	0.1189

Table A-I.4 *Crystallographic Data for* ***4.7 – 220 K*** *and* ***4.8 – 120 K***

Compound reference	**4.7 – 220 K**	**4.8 – 120 K**
Chemical formula	$C_{33}H_{33}FeN_9O_3$•2(BF_4)	$C_{33}H_{33}FeN_9O_3$•2(ClO_4)•C_2H_3N
Formula Mass	833.15	899.49
Crystal system	Triclinic	Monoclinic
a/Å	10.7453(4)	15.1780(4)
b/Å	12.1999(5)	22.4061(5)
c/Å	15.2439(3)	12.0957(4)
α/°	84.049(3)	90.00
β/°	86.608(2)	109.643(3)
γ/°	70.308(4)	90.00
Unit cell volume/Å^3	1870.70(11)	3874.1(2)
Temperature/K	220.01(10)	120.01(10)
Space group	$P\bar{1}$	$P2_1/c$
No. of formula units per unit cell, *Z*	2	4
No. of reflections measured	12664	14557
No. of independent reflections	7329	6662
R_{int}	0.0215	0.0386
Final R_1 values ($I > 2\sigma(I)$)	0.0362	0.0523
Final $wR(F^2)$ values ($I > 2\sigma(I)$)	0.0995	0.1277
Final R_1 values (all data)	0.0398	0.0652
Final $wR(F^2)$ values (all data)	0.1017	0.1371

Table A-I.5 *Crystallographic Data for* ***4.9 – 120 K*** *and* ***4.9 – 220 K***

Compound reference	**4.9 – 120 K**	**4.9 – 220 K**
Chemical formula	$C_{33}H_{33}FeN_9$•2(BF_4)• 0.5(H_2O)•C_2H_3N	$C_{33}H_{33}FeN_9$•2(BF_4)• 0.5(H_2O)•C_2H_3N
Formula Mass	835.22	835.21
Crystal system	Triclinic	Triclinic
a/Å	10.5295(7)	10.6625(10)
b/Å	12.3300(8)	12.4407(7)
c/Å	15.2713(8)	15.5379(12)
α/°	89.304(5)	88.978(5)
β/°	79.523(5)	80.696(7)
γ/°	74.926(6)	75.583(6)
Unit cell volume/Å^3	1881.2(2)	1969.4(3)
Temperature/K	120.01(10)	220.01(10)
Space group	$P\bar{1}$	$P\bar{1}$
No. of formula units per unit cell, *Z*	2	2
No. of reflections measured	12757	14534
No. of independent reflections	7344	7679
R_{int}	0.0295	0.0199
Final R_1 values ($I > 2\sigma(I)$)	0.0650	0.0554
Final $wR(F^2)$ values ($I > 2\sigma(I)$)	0.1738	0.1616
Final R_1 values (all data)	0.0904	0.0672
Final $wR(F^2)$ values (all data)	0.1950	0.1710

Table A-I.6 *Crystallographic Data for* ***4.10 – 120 K*** *and* ***4.10 – 220 K***

Compound reference	**4.10 – 120 K**	**4.10 – 220 K**
Chemical formula	$C_{33}H_{33}FeN_9$•2(ClO_4)•0.5(H_2O)• C_2H_3N	$C_{33}H_{33}FeN_9$•2(ClO_4)•0.5(OH_2)• C_2H_3N
Formula Mass	860.50	860.49
Crystal system	Triclinic	Triclinic
a/Å	10.6980(4)	10.8735(3)
b/Å	12.3476(5)	12.4139(6)
c/Å	15.1074(7)	15.4818(7)
α/°	88.661(3)	88.173(4)
β/°	79.589(3)	80.124(3)
γ/°	75.939(3)	75.269(4)
Unit cell volume/Å^3	1903.51(13)	1990.99(15)
Temperature/K	120.01(10)	220.01(10)
Space group	$P\bar{1}$	$P\bar{1}$
No. of formula units per unit cell, *Z*	2	2
No. of reflections measured	12516	18651
No. of independent reflections	6837	7856
R_{int}	0.0304	0.0304
Final R_1 values ($I > 2\sigma(I)$)	0.0419	0.0495
Final $wR(F^2)$ values ($I > 2\sigma(I)$)	0.1056	0.1488
Final R_1 values (all data)	0.0520	0.0671
Final $wR(F^2)$ values (all data)	0.1124	0.1555

Table A-I.7 *Crystallographic Data for* ***4.11 – 120 K*** *and* ***4.12 – 120 K***

Compound reference	**4.11 - 120 K**	**4.12 – 120 K**
Chemical formula	$C_{30}H_{24}Br_3FeN_9$•2(ClO_4)•CH_2Cl_2	$C_{36}H_{33}FeN_9O_3$•2(BF_4)
Formula Mass	1089.99	869.18
Crystal system	Triclinic	Triclinic
a/Å	11.9317(4)	12.7391(9)
b/Å	11.9504(4)	13.0880(8)
c/Å	15.7160(6)	14.4069(7)
α/°	73.340(3)	88.094(5)
β/°	72.007(3)	66.500(6)
γ/°	75.384(3)	61.926(7)
Unit cell volume/Å^3	2008.61(13)	1907.9(2)
Temperature/K	120.01(10)	120.01(10)
Space group	$P\bar{1}$	$P\bar{1}$
No. of formula units per unit cell, *Z*	2	2
No. of reflections measured	13245	18899
No. of independent reflections	6569	7482
R_{int}	0.0234	0.0375
Final R_1 values ($I > 2\sigma(I)$)	0.0394	0.0591
Final $wR(F^2)$ values ($I > 2\sigma(I)$)	0.1031	0.1722
Final R_1 values (all data)	0.0440	0.0712
Final $wR(F^2)$ values (all data)	0.1075	0.1790

Table A-I.8 *Crystallographic Data for* ***4.13 – 120 K*** *and* ***L4.2***

Compound reference	**4.13 - 120 K**	**L4.2**
Chemical formula	$C_{33}H_{33}FeN_9$•2(BF_4)•C_2H_3N	$C_{11}H_{11}N_3$
Formula Mass	826.21	185.23
Crystal system	Triclinic	Monoclinic
a/Å	10.5514(5)	7.01564(12)
b/Å	12.4912(4)	13.9141(2)
c/Å	15.0853(7)	9.80620(13)
α/°	93.498(3)	90.00
β/°	98.508(4)	93.7002(14)
γ/°	99.868(4)	90.00
Unit cell volume/Å^3	1929.63(15)	955.25(3)
Temperature/K	120.01(10)	120.01(10)
Space group	$P\bar{1}$	$P2_1/c$
No. of formula units per unit cell, *Z*	2	4
No. of reflections measured	13359	10156
No. of independent reflections	7558	1649
R_{int}	0.0248	0.0191
Final R_1 values ($I > 2\sigma(I)$)	0.0382	0.0324
Final $wR(F^2)$ values ($I > 2\sigma(I)$)	0.0986	0.0856
Final R_1 values (all data)	0.0424	0.0348
Final $wR(F^2)$ values (all data)	0.1025	0.0880

Table A-I.9 *Crystallographic Data for* ***L4.3*** *and* ***5.5 – 293 K***

Compound reference	**L4.3**	**5.5 – 293 K**
Chemical formula	$C_{10}H_8BrN_3$	$C_{28}H_{24}FeN_8O_4$•2(BF_4)
Formula Mass	250.10	766.02
Crystal system	Orthorhombic	Monoclinic
a/Å	9.7092(4)	22.4485(17)
b/Å	15.5149(6)	10.0696(7)
c/Å	25.8573(9)	14.9835(15)
α/°	90.00	90.00
β/°	90.00	106.877(7)
γ/°	90.00	90.00
Unit cell volume/Å^3	3895.1(3)	3241.1(5)
Temperature/K	113.9	293(2)
Space group	*Pbca*	*C*2/*c*
No. of formula units per unit cell, *Z*	16	4
No. of reflections measured	69358	29439
No. of independent reflections	3453	2860
R_{int}	0.0707	0.0349
Final R_1 values ($I > 2\sigma(I)$)	0.0230	0.0478
Final $wR(F^2)$ values ($I > 2\sigma(I)$)	0.0515	0.1172
Final R_1 values (all data)	0.0324	0.0496
Final $wR(F^2)$ values (all data)	0.0550	0.1187

Table A-I.10 *Crystallographic Data for* ***5.6 – 120 K***, ***5.7 – 120 K*** *and* ***5.8 – 120 K***

Compound reference	**5.6 – 120 K**	**5.7 - 113 K**	**5.8 - 113K**
Chemical formula	$C_{30}H_{24}FeN_8$•2(BF_4)• 2(C_2H_3N)	$C_{24}H_{22}FeN_{10}O_4$• 2(ClO_4)•(C_2H_3N)	$C_{26}H_{22}FeN_{10}$• 2(ClO_4)•C_2H_3N
Formula Mass	808.15	810.32	770.34
Crystal system	Monoclinic	Monoclinic	Monoclinic
a/Å	22.9175(5)	17.5722(6)	17.1935(6)
b/Å	10.37229(18)	16.6454(6)	16.6395(6)
c/Å	16.7019(3)	14.4975(6)	14.2373(5)
α/°	90.00	90.00	90.00
β/°	106.798(2)	124.392(3)	121.248(2)
γ/°	90.00	90.00	90.00
Unit cell volume/Å^3	3800.76(13)	3499.2(2)	3482.3(2)
Temperature/K	120.01(10)	113(2)	113(2)
Space group	*C*2/*c*	*C*2/*c*	*C*2/*c*
No. of formula units per unit cell, *Z*	4	4	4
No. of reflections measured	11923	33787	45867
No. of independent reflections	3774	3833	5219
R_{int}	0.0243	0.0442	0.0505
Final R_1 values ($I > 2\sigma(I)$)	0.0343	0.0582	0.0426
Final $wR(F^2)$ values ($I > 2\sigma(I)$)	0.0916	0.1388	0.1109
Final R_1 values (all data)	0.0361	0.0632	0.0585
Final $wR(F^2)$ values (all data)	0.0934	0.1420	0.1202

APPENDIX II

Selected Bond Lengths and Angles

A-II·1 Selected Coordination Bond Lengths and Angles – Chapter Two

Bond Lengths (Å)		**Bond Angles (°)**			
2.4 – 120 K					
Fe1-N1	1.982(4)	N1-Fe1-N2	80.9(2)	N2-Fe1-N8	97.1(2)
Fe1-N2	1.974(4)	N1-Fe1-N6	91.5(2)	N5-Fe1-N6	81.0(2)
Fe1-N5	1.971(4)	N1-Fe1-N7	94.2(2)	N5-Fe1-N7	91.4(2)
Fe1-N6	1.994(3)	N1-Fe1-N8	91.4(2)	N5-Fe1-N8	96.5(2)
Fe1-N7	1.971(4)	N2-Fe1-N5	93.6(2)	N6-Fe1-N7	94.2(2)
Fe1-N8	1.991(3)	N2-Fe1-N6	87.9(2)	N7-Fe1-N8	81.0(2)
2.5 – 120 K					
Fe1-N1	1.946(5)	N1-Fe1-N3	80.3(2)	N3-Fe1-N11	98.8(2)
Fe1-N3	2.005(4)	N1-Fe1-N8	93.1(2)	N6-Fe1-N8	80.6(2)
Fe1-N6	2.004(4)	N1-Fe1-N9	92.6(2)	N6-Fe1-N9	92.7(2)
Fe1-N8	1.961(4)	N1-Fe1-N11	88.6(2)	N6-Fe1-N11	98.3(2)
Fe1-N9	1.955(4)	N3-Fe1-N6	94.3(2)	N8-Fe1-N9	92.5(2)
Fe1-N11	2.016(4)	N3-Fe1-N8	88.2(2)	N9-Fe1-N11	80.6(2)
2.6 – 120 K					
Fe1-N1	1.990(4)	N1-Fe1-N3	80.4(2)	N6-Fe2-N7	78.6(2)
Fe1-N3	2.040(4)	N1-Fe1-N9	93.8(2)	N6-Fe2-N14	97.6(2)
Fe1-N9	1.964(6)	N1-Fe1-N17	92.2(2)	N6-Fe2-N22	92.1(2)
Fe1-N11	2.033(4)	N1-Fe1-N19	86.4(2)	N6-Fe2-N23	86.1(2)
Fe1-N17	1.986(5)	N3-Fe1-N9	93.8(2)	N7-Fe2-N14	95.9(2)
Fe1-N19	2.016(6)	N3-Fe1-N11	96.5(2)	N7-Fe2-N16	95.9(2)
Fe2-N6	2.113(6)	N3-Fe1-N19	93.4(2)	N7-Fe2-N23	90.2(2)
Fe2-N7	2.046(5)	N9-Fe1-N11	80.5(2)	N14-Fe2-N16	79.0(2)
Fe2-N14	2.105(5)	N9-Fe1-N17	92.8(2)	N14-Fe2-N22	96.2(2)
Fe2-N16	2.043(8)	N11-Fe1-N17	91.4(2)	N16-Fe2-N22	94.0(2)
Fe2-N22	2.120(4)	N11-Fe1-N19	99.7(2)	N16-Fe2-N23	97.8(2)
Fe2-N23	2.067(6)	N17-Fe1-N19	79.9(2)	N22-Fe2-N23	78.1(2)

A-II.1 Selected Coordination Bond Lengths and Angles – Chapter Two Continued

Bond Lengths (Å)		**Bond Angles (°)**			
2.6 – 240 K					
Fe1-N1	2.15(1)	N1-Fe1-N3	77.0(3)	N6-Fe2-N7	77.1(3)
Fe1-N3	2.235(9)	N1-Fe1-N9	101.0(4)	N6-Fe2-N14	101.1(3)
Fe1-N9	2.18(1)	N1-Fe1-N11	94.5(4)	N6-Fe2-N15	94.5(4)
Fe1-N11	2.248(9)	N1-Fe1-N17	98.7(4)	N6-Fe2-N22	93.8(3)
Fe1-N17	2.169(9)	N3-Fe1-N11	95.6(3)	N7-Fe2-N15	97.1(4)
Fe1-N19	2.23(1)	N3-Fe1-N17	98.0(3)	N7-Fe2-N22	96.2(3)
Fe2-N6	2.211(7)	N3-Fe1-N19	97.2(3)	N7-Fe2-N23	96.8(4)
Fe2-N7	2.14(1)	N9-Fe1-N11	76.4(4)	N14-Fe2-N15	76.0(4)
Fe2-N14	2.23(1)	N9-Fe1-N17	90.2(4)	N14-Fe2-N22	90.9(3)
Fe2-N15	2.13(1)	N9-Fe1-N19	85.5(3)	N14-Fe2-N23	86.1(3)
Fe2-N22	2.254(8)	N11-Fe1-N19	91.1(3)	N15-Fe2-N23	95.8(4)
Fe2-N23	2.150(7)	N17-Fe1-N19	76.9(4)	N22-Fe2-N23	77.2(3)

A-II.2 Selected Coordination Bond Lengths and Angles – Chapter Three

Bond Lengths (Å)		**Bond Angles (°)**			
Fe1-N4	2.29(2)	N4-Fe1-N6	76.8(6)	N1-Fe2-N3	80.2(7)
Fe1-N6	2.13(2)	N4-Fe1-N10	99.5(6)	N1-Fe2-N7	92.7(7)
Fe1-N10	2.26(2)	N4-Fe1-N12	95.6(6)	N1-Fe2-N9	92.3(7)
Fe1-N12	2.12(2)	N4-Fe1-N16	98.4(6)	N1-Fe2-N13	88.9(7)
Fe1-N16	2.17(2)	N6-Fe1-N12	90.3(6)	N3-Fe2-N9	97.6(7)
Fe1-N18	2.13(2)	N6-Fe1-N16	95.3(6)	N3-Fe2-N13	90.6(7)
Fe2-N1	1.94(2)	N6-Fe1-N18	88.1(6)	N3-Fe2-N15	90.7(7)
Fe2-N3	1.97(2)	N10-Fe1-N12	76.5(6)	N7-Fe2-N9	79.7(7)
Fe2-N7	1.95(2)	N10-Fe1-N16	98.6(6)	N7-Fe2-N13	92.1(7)
Fe2-N9	1.98(2)	N10-Fe1-N18	96.2(6)	N7-Fe2-N15	96.8(7)
Fe2-N13	1.93(2)	N12-Fe1-N18	89.1(6)	N9-Fe2-N15	99.2(6)
Fe2-N15	1.98(2)	N16-Fe1-N18	78.1(6)	N13-Fe2-N15	80.9(6)

A-II.3 Selected Coordination Bond Lengths and Angles – Chapter Four

Bond Lengths (Å)		**Bond Angles (°)**			
4.7 – 120 K					
Fe1-N1	2.024(2)	N1-Fe1-N3	79.60(8)	N3-Fe1-N7	90.32(7)
Fe1-N3	2.085(2)	N1-Fe1-N4	93.73(8)	N4-Fe1-N6	78.60(7)
Fe1-N4	2.026(2)	N1-Fe1-N7	95.40(8)	N4-Fe1-N9	95.44(7)
Fe1-N6	2.103(1)	N1-Fe1-N9	100.72(8)	N6-Fe1-N7	92.46(7)
Fe1-N7	2.040(2)	N3-Fe1-N4	94.82(7)	N6-Fe1-N9	83.35(7)
Fe1-N9	2.110(2)	N3-Fe1-N6	97.71(7)	N7-Fe1-N9	79.38(7)
4.7 – 220 K					
Fe1-N1	2.141(1)	N1-Fe1-N3	77.42(6)	N3-Fe1-N7	90.22(6)
Fe1-N3	2.229(2)	N1-Fe1-N4	94.39(7)	N4-Fe1-N6	75.87(6)
Fe1-N4	2.135(2)	N1-Fe1-N7	98.92(6)	N4-Fe1-N9	95.43(6)
Fe1-N6	2.258(1)	N1-Fe1-N9	106.19(6)	N6-Fe1-N7	91.27(6)
Fe1-N7	2.135(2)	N3-Fe1-N4	96.55(6)	N6-Fe1-N9	81.13(6)
Fe1-N9	2.243(2)	N3-Fe1-N6	97.41(6)	N7-Fe1-N9	77.11(6)
4.8 – 120 K					
Fe1-N1	2.120(3)	N1-Fe1-N3	77.0(1)	N3-Fe1-N9	94.5(1)
Fe1-N3	2.245(3)	N1-Fe1-N4	97.0(1)	N4-Fe1-N6	77.0(1)
Fe1-N4	2.174(3)	N1-Fe1-N6	89.9(1)	N4-Fe1-N7	89.2(1)
Fe1-N6	2.266(3)	N1-Fe1-N9	98.8(1)	N6-Fe1-N7	95.8(1)
Fe1-N7	2.136(2)	N3-Fe1-N4	95.5(1)	N6-Fe1-N9	96.5(1)
Fe1-N9	2.323(3)	N3-Fe1-N7	98.2(1)	N7-Fe1-N9	75.5(1)
4.9 – 120 K					
Fe1-N1	2.28(1)	N3-Fe1-N4	94.9(1)	N4-Fe1-N11	97.3(3)
Fe1-N3	2.096(8)	N3-Fe1-N6	98.2(1)	N6-Fe1-N7	93.7(1)
Fe1-N4	2.015(5)	N3-Fe1-N7	89.5(1)	N6-Fe1-N9	84.2(1)
Fe1-N6	2.099(3)	N3-Fe1-N11	79.2(3)	N7-Fe1-N9	79.2(1)
Fe1-N7	2.023(4)	N4-Fe1-N6	79.1(1)	N7-Fe1-N11	90.1(3)
Fe1-N9	2.104(4)	N4-Fe1-N9	96.6(2)	N9-Fe1-N11	99.1(3)
Fe1-N11	1.906(8)				

A-II.3 Selected Coordination Bond Lengths and Angles – Chapter Four Continued

Bond Lengths (Å)		**Bond Angles (°)**			
4.9 – 220 K					
Fe1-N1	2.131(3)	N1-Fe1-N3	76.5(1)	N3-Fe1-N9	82.4(1)
Fe1-N3	2.239(2)	N1-Fe1-N4	92.9(1)	N4-Fe1-N6	77.1(1)
Fe1-N4	2.131(3)	N1-Fe1-N6	96.5(1)	N4-Fe1-N9	104.9(1)
Fe1-N6	2.237(2)	N1-Fe1-N9	98.5(1)	N4-Fe1-N7	96.4(1)
Fe1-N7	2.120(3)	N3-Fe1-N6	98.47(9)	N6-Fe1-N7	87.9(1)
Fe1-N9	2.231(2)	N3-Fe1-N7	94.5(1)	N7-Fe1-N9	76.8(1)
4.10 -120 K					
Fe1-N1	1.968(2)	N1-Fe1-N3	80.59(9)	N3-Fe1-N9	85.03(9)
Fe1-N3	2.017(2)	N1-Fe1-N4	92.73(9)	N4-Fe1-N6	80.56(9)
Fe1-N4	1.954(2)	N1-Fe1-N6	92.76(9)	N4-Fe1-N7	91.84(9)
Fe1-N6	2.011(2)	N1-Fe1-N9	96.36(9)	N4-Fe1-N9	96.70(9)
Fe1-N7	1.964(2)	N3-Fe1-N6	98.74(9)	N6-Fe1-N7	90.58(9)
Fe1-N9	2.031(2)	N3-Fe1-N7	94.88(9)	N7-Fe1-N9	80.49(9)
4.10 – 220 K					
Fe1-N1	2.109(3)	N1-Fe1-N3	76.8(1)	N3-Fe1-N9	82.5(1)
Fe1-N3	2.226(3)	N1-Fe1-N4	93.4(1)	N4-Fe1-N6	77.4(1)
Fe1-N4	2.120(3)	N1-Fe1-N6	96.4(1)	N4-Fe1-N7	95.9(1)
Fe1-N6	2.219(3)	N1-Fe1-N9	98.1(1)	N4-Fe1-N9	104.2(1)
Fe1-N7	2.109(3)	N3-Fe1-N6	98.5(1)	N6-Fe1-N7	88.3(1)
Fe1-N9	2.223(3)	N3-Fe1-N7	94.2(1)	N7-Fe1-N9	76.9(1)
4.11 – 120 K					
Fe1-N1	2.131(3)	N1-Fe1-N3	76.5(1)	N3-Fe1-N7	93.0(1)
Fe1-N3	2.322(3)	N1-Fe1-N6	99.0(1)	N4-Fe1-N6	76.7(1)
Fe1-N4	2.095(3)	N1-Fe1-N7	90.7(1)	N4-Fe1-N7	94.5(1)
Fe1-N6	2.276(4)	N1-Fe1-N9	91.5(1)	N4-Fe1-N9	96.3(1)
Fe1-N7	2.164(4)	N3-Fe1-N4	96.4(1)	N6-Fe1-N9	95.9(1)
Fe1-N9	2.226(3)	N3-Fe1-N6	95.5(1)	N7-Fe1-N9	77.2(1)
4.12 – 120 K					
Fe1-N1	2.114(4)	N1-Fe1-N3	75.7(1)	N3-Fe1-N9	78.7(1)
Fe1-N3	2.259(3)	N1-Fe1-N4	91.0(1)	N4-Fe1-N6	76.7(1)
Fe1-N4	2.143(3)	N1-Fe1-N6	97.6(1)	N4-Fe1-N7	97.0(1)
Fe1-N6	2.231(3)	N1-Fe1-N9	96.6(1)	N4-Fe1-N9	107.2(1)
Fe1-N7	2.143(4)	N3-Fe1-N6	100.8(1)	N6-Fe1-N7	89.0(1)
Fe1-N9	2.278(2)	N3-Fe1-N7	96.6(1)	N7-Fe1-N9	76.4(1)

A-II.3 Selected Coordination Bond Lengths and Angles – Chapter Four Continued

4.13 – 120 K					
Fe1-N1	2.147(2)	N1-Fe1-N3	76.00(6)	N3-Fe1-N7	103.09(6)
Fe1-N3	2.234(2)	N1-Fe1-N6	92.79(6)	N4-Fe1-N6	76.67(6)
Fe1-N4	2.145(2)	N1-Fe1-N7	96.61(6)	N4-Fe1-N7	94.24(6)
Fe1-N6	2.238(1)	N1-Fe1-N9	90.12(6)	N4-Fe1-N9	96.10(6)
Fe1-N7	2.142(1)	N3-Fe1-N4	97.74(6)	N6-Fe1-N9	98.98(6)
Fe1-N9	2.218(2)	N3-Fe1-N6	82.87(6)	N7-Fe1-N9	77.24(6)

A-II.4 Selected Coordination Bond Lengths and Angles – Chapter Five

Bond Length (Å)		**Bond Angle (°)**				**Symmetry**
5.5 – 293 K						
Fe1-N1	1.993(2)	N1-Fe1-N2	80.07(9)	N1-Fe1-N4^{1}	94.69(9)	(1) –x+1, y, -z+1/2
Fe1-N2	1.991(2)	N1-Fe1-N2^{1}	92.59(9)	N2-Fe1-N2^{1}	87.79(9)	
Fe1-N4	1.945(2)	N1-Fe1-N4	92.52(9)	N2-Fe1-N4	91.71(8)	
				N4-Fe1-N4^{1}	89.21(9)	
5.6 – 120 K						
Fe1-N1	1.973(1)	N1-Fe1-N2	81.06(6)	N1-Fe1-N4^{1}	95.98(6)	(1) –x+1, y, -z+3/2
Fe1-N2	1.961(1)	N1-Fe1-N2^{1}	92.92(6)	N2-Fe1-N2^{1}	88.59(6)	
Fe1-N4	1.938(1)	N1-Fe1-N4	90.19(6)	N2-Fe1-N4	93.24(6)	
				N4-Fe1-N4^{1}	85.08(6)	
5.7 – 113 K						
Fe1-N1	2.113(3)	N1-Fe1-N3	94.6(1)	N1-Fe1-N5^{1}	97.5(1)	(1) –x+2, y, -z+3/2
Fe1-N3	2.287(3)	N1-Fe1-N3^{1}	75.6(1)	N3-Fe1-N3^{1}	82.6(1)	
Fe1-N5	2.132(3)	N1-Fe1-N5	91.5(1)	N3-Fe1-N5	94.5(1)	
				N5-Fe1-N5^{-1}	91.2(1)	
5.8 – 113 K						
Fe1-N1	2.111(2)	N1-Fe1-N3	91.22(6)	N1-Fe1-N6^{1}	99.84(7)	(1) –x+1,y,-z+1/2
Fe1-N3	2.289(2)	N1-Fe1-N3^{1}	75.55(6)	N3-Fe1-N3^{1}	80.13(6)	
Fe1-N6	2.129(2)	N1-Fe1-N6	92.20(7)	N3-Fe1-N6	95.77(7)	
				N6-Fe1-N6^{-1}	90.84(7)	

APPENDIX III

Hydrogen Bonding Parameters

Table A-III *Hydrogen Bonding Parameters*

D-H···A	d (D-H) Å	d (D-H···A) Å	d (D···A) Å	< (D-H···A) °	Symmetry Code
2.5 -120 K					
N2-H2···F7[1]	0.89(2)	2.10(4)	2.792(7)	134(5)	(1) x+1/2, -y-1, -z-1/2
N2-H2···N13[2]	0.89(2)	2.40(5)	2.972(11)	122(4)	(2) x, -y-1/2, z +1/2
N7-H7···F3	0.89(2)	1.98(5)	2.756(7)	145(7)	(3) –x-1, -y-1, -z-1
N10-H10···F6	0.86(2)	2.08(4)	2.783(8)	138(6)	(4) –x-3/2, y, z+1/2
Hydrogen bonding parameters for **2.6 – 120 K** and **2.6 – 240 K** not included due to low crystal quality					
4.7 – 120 K					
N2-H2···F7[1]	0.888(18)	2.06(2)	2.906(3)	159(3)	(1) –x+2, -y, -z
N2-H2···F8[1]	0.888(18)	2.34(3)	3.064(3)	139(3)	(2) x-1, y, z
N5-H5···F5[2]	0.878(18)	2.07(2)	2.855(3)	149(3)	
N8-H8···F1	0.882(18)	1.99(2)	2.828(3)	157(3)	
4.7 – 220 K					
N2-H2···F2[1]	0.877(17)	2.36(2)	3.039(3)	134(2)	(1) –x, -y+1, -z+1
N2-H2···F3[1]	0.877(17)	2.045(19)	2.884(3)	160(3)	(2) –x+1, -y+1, -z
N5-H5···F1	0.858(18)	2.09(2)	2.877(3)	152(3)	
N8-H8···F8[2]	0.866(17)	1.998(18)	2.829(3)	160(3)	
4.8 – 120 K					
N2-H2···N10[1]	0.87(2)	1.96(2)	2.828(6)	170(7)	(1) x, -y+1/2, z+1/2
N5-H5···O7[2]	0.90(2)	1.97(2)	2.864(6)	172(7)	(2) x, -y+3/2, z+1/2
N8-H8···O9[3]	0.87(2)	2.12(4)	2.910(5)	149(7)	(3) x-1, y, z
4.9 – 120 K					
N2-H2···F1[1]	0.88(2)	2.35(3)	3.031(4)	135(7)	(1) –x, -y+1, -z+1
N2-H2···F3[1]	0.88(2)	2.21(4)	3.019(4)	153(8)	(2) –x+1, -y+1, -z
N5-H5···F2	0.89(2)	1.89(3)	2.757(5)	167(8)	(3) x-1, y, z-1
N8-H8···F7[2]	0.87(2)	2.21(5)	2.976(8)	147(8)	
N8-H8···O1[3]	0.87(2)	2.04(5)	2.819(10)	149(8)	
4.9 – 220 K					
N2-H2···F3[1]	0.87(2)	1.94(6)	2.762(4)	156(13)	(1) –x, -y +1, -z +1
N5-H5···F2[2]	0.87(2)	2.28(8)	3.039(4)	146(12)	(2) 1+x, y-1, z-1
N5-H5···F4[2]	0.87(2)	2.15(7)	2.957(4)	154(13)	(3) –x+1, -y+1, -z+1
N8-H8···F10[3]	0.88(2)	2.25(7)	3.051(10)	152(13)	

Table A-III Continued: *Hydrogen Bonding Parameters*

D-H···A	d (D-H) Å	d (D-H···A) Å	d (D···A) Å	< (D-H···A) °	Symmetry Code
4.10 – 120 K					
N2-H2···O4[1]	0.866(18)	2.02(2)	2.832(2)	157(3)	(1) –x+1, -y+1, -z+1
N5-H5···O1[2]	0.868(18)	2.66(2)	3.451(3)	152(3)	(2) –x-1, y, z
N5-H5···O3[2]	0.868(18)	2.27(3)	2.997(3)	142(3)	(3) –x+1, -y+1, -z
N8-H8···O6[3]	0.851(19)	2.50(4)	2.903(8)	110(3)	(4) –x, -y+1, -z
N8-H8···O11[3]	0.851(19)	2.30(3)	3.019(5)	142(3)	
N8-H8···O13[4]	0.851(19)	2.03(2)	2.850(7)	161(3)	
4.10 – 220 K					
N2-H2···O4[1]	0.874(19)	2.00(2)	2.842(5)	162(4)	(1) x-1, y, z
N5-H5···O1[2]	0.870(19)	2.21(2)	3.063(5)	165(4)	(2) –x+2, -y, -z
N5-H5···O3[2]	0.870(19)	2.45(4)	3.128(5)	135(4)	(3) –x+1, -y+1, -z+1
N8-H8···O6[3]	0.86(2)	2.31(4)	3.058(10)	146(5)	
N8-H8···O13[3]	0.86(2)	2.05(3)	2.868(9)	160(5)	
4.11 – 120 K					
N2-H2···O3[1]	0.868(19)	1.95(2)	2.801(5)	167(5)	(1) x+1, y, z+1
N5-H5···O5[2]	0.864(19)	2.13(4)	2.828(4)	138(4)	(2) x+1, y, z
N5-H5···O5[3]	0.864(19)	2.46(4)	3.088(5)	167(5)	(3) –x+1, -y+1, -z+1
N8-H8···O8[4]	0.877(19)	2.09(2)	2.952(4)	167(4)	(4) x+1, y+1, z
4.12 – 120 K					
N2-H2···F4[1]	0.866(19)	2.36(4)	2.958(4)	126(4)	(1) –x+1, -y+1, -z+2
N2-H2···F4[2]	0.866(19)	2.15(3)	2.892(4)	143(4)	(2) x, y-1, z
N5-H5···O1[3]	0.869(19)	2.32(4)	2.962(5)	131(4)	(3) x-1, y+1, z
N8-H8···F7[4]	0.890(19)	2.13(3)	2.912(5)	146(4)	(4) –x+2, -y, -z+1
4.13 – 120 K					
N2-H2···F3[1]	0.873(17)	1.878(18)	2.750(2)	176(3)	(1) –x+1, -y+1, -z+1
N5-H5···N10[2]	0.881(17)	2.090(18)	2.947(3)	164(3)	(2) x, y+1, z
N8-H8···F2[3]	0.865(17)	2.09(2)	2.807(2)	139(2)	(3) –x+1, -y+2, -z+1

Table A-III Continued *Hydrogen Bonding Parameters*

D-H···A	d (D-H) Å	d (D-H···A) Å	d (D···A) Å	< (D-H···A) °	Symmetry Code
L4.2					
N1-H1···N2[1]	0.925(15)	1.924(15)	2.8463(13)	174.0(19)	(1) x, y+1/2, -z+1/2
L4.3					
N2-H2···N1[1]	0.869(16)	2.031(17)	2.889(3)	169(2)	(1) x+1/2, -y+1/2, -z+2
N5-H5···N4[2]	0.848(16)	1.957(18)	2.791(3)	168(2)	(2) x+1/2, y, -z+3/2
5.7 – 113 K					
N2-H2···O5[1]	0.87(2)	1.97(3)	2.824(4)	167(8)	(1) –x+2, y, -z+3/2
5.8 – 113 K					
N2-H2···O1	0.850(16)	1.962(17)	2.812(2)	180(2)	

APPENDIX IV

Experimental Supplementary Information

A-IV.1 Chapter Two Supplementary Information

*A-IV.1.1 Derivation of Equation **2.4.7***

A spin crossover process in solution can be expressed as the equilibrium between the high- and low-spin species, H and L, respectively

$$\boldsymbol{L \rightleftharpoons H}$$

Therefore the total concentration of the complex in solution

$$\boldsymbol{c = [H] + [L]}$$

The equilibrium constant for the crossover can be expressed in terms of either the concentration of the high-spin [H] or low-spin [L] states.

$$\boldsymbol{K = \frac{[H]}{[L]} = \frac{c - [L]}{[L]}}$$

$$\boldsymbol{K^{-1} = \frac{[L]}{[H]} = \frac{c - [H]}{[H]}}$$

During the UV-Visible spectroscopic measurements the concentrations of the high-spin and low-spin species are unknown, however, the total concentration of the solution is known. As such the concentration of the low-spin and high-spin states may be expressed in terms of the total concentration (c) and the equilibrium constant (K)

$$\boldsymbol{[L] = \frac{c}{K + 1}}$$

$$\boldsymbol{[H] = \frac{c}{K^{-1} + 1}}$$

The absorbance of the low-spin and high-spin states is proportional to the concentration of the low-spin and high-spin states through Beer's Law, where ε_L and ε_H denote the molar extinction coefficient of the low-spin and high-spin states respectively, and *l* is the path length (1 cm).

$$\boldsymbol{A_L = \varepsilon_L[L]l}$$

$$\boldsymbol{A_H = \varepsilon_H[H]l}$$

The absorbance at λ_{max} (540 nm) was monitored during the experiment can be expressed in terms of the molar extinction coefficients of the low-spin and high-spin species.

$$\boldsymbol{A_T = A_L + A_H = \left(\frac{\varepsilon_L}{K+1} + \frac{\varepsilon_H}{K^{-1}+1}\right) cl}$$

In order to obtain the thermodynamic parameters for the enthalpy (ΔH) and the entropy (ΔS), the equilibrium constant (K) may be expressed in terms of ΔG.

$$\boldsymbol{\Delta G = -RT \ln K}$$

$$\boldsymbol{\Delta G = \Delta H - T\Delta S}$$

$$\boldsymbol{K = exp\left(\frac{-\Delta G}{RT}\right) = exp\left(\frac{\Delta S}{R} - \frac{\Delta H}{RT}\right) = \left(\frac{exp(\Delta S/R)}{exp\,(\Delta H/RT)}\right)}$$

The reciprocal of the equilibrium constant (K^{-1}) can also be expressed in this form

$$\boldsymbol{K^{-1} = \left(\frac{exp(\Delta H/RT)}{exp(\Delta S/R)}\right)}$$

Therefore

$$\boldsymbol{K + 1 = \frac{exp(\Delta S/R) + exp(\Delta H/RT)}{exp(\Delta H/RT)}}$$

$$\boldsymbol{K^{-1} + 1 = \frac{exp(\Delta S/R) + exp(\Delta H/RT)}{exp(\Delta S/R)}}$$

Using these parameters it is possible to discuss the measured absorbance at 540 nm (λ_{max}) in terms of ΔS and ΔH.

$$\frac{\boldsymbol{A_T}}{\boldsymbol{cl}} = \frac{\boldsymbol{\varepsilon_L\, exp(\Delta H/RT) + \varepsilon_H exp(\Delta S/R)}}{\boldsymbol{exp(\Delta S/R) + exp(\Delta H/RT)}}$$

At the $T_{1/2}$ the concentrations of the low-spin and high-spin states must be equal and as such at that temperature K = 1 and ΔG = 0; therefore

$$\boldsymbol{T_{1/2}} = \frac{\boldsymbol{\Delta H}}{\boldsymbol{\Delta S}}$$

The final equation may be written in terms of ΔS and $T_{1/2}$ such that

$$\frac{\boldsymbol{A}}{\boldsymbol{cl}} = \frac{\boldsymbol{\varepsilon_L[exp(\Delta S/R)]^{T1/2/T} + \varepsilon_H\, exp(\Delta S/R)}}{\boldsymbol{[exp(\Delta S/R)]^{T1/2/T} + exp(\Delta S/R)}}$$

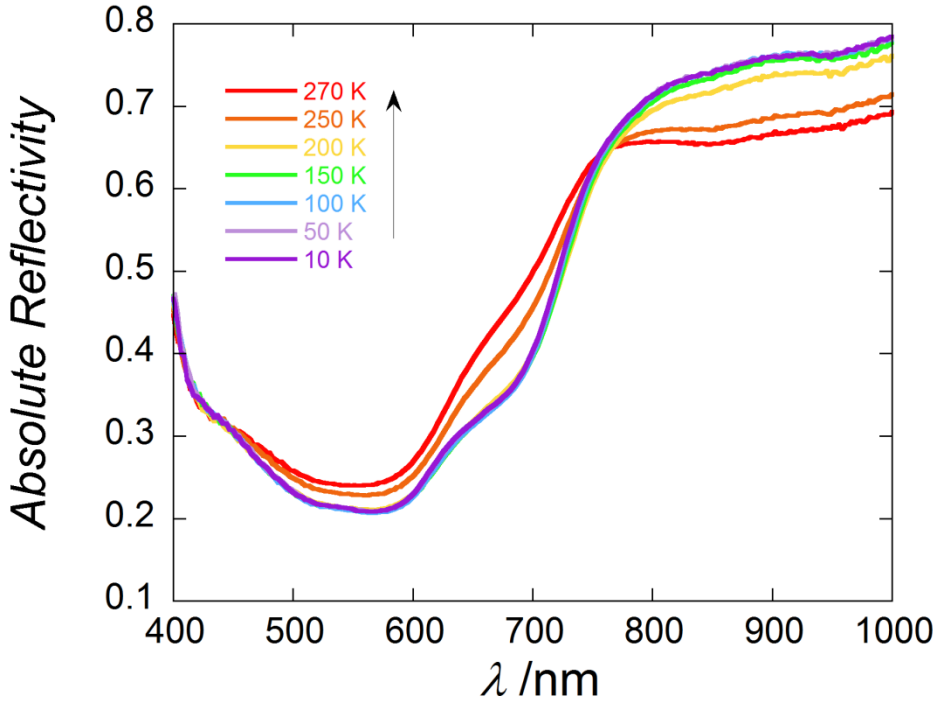

***Fig A-IV.1.2a** Selected surface reflectivity measurements of **2.5** collected with a white light spectroscopic source (0.4 mW cm^{-2}) as a function of temperature during heating mode between 270 – 10 K.*

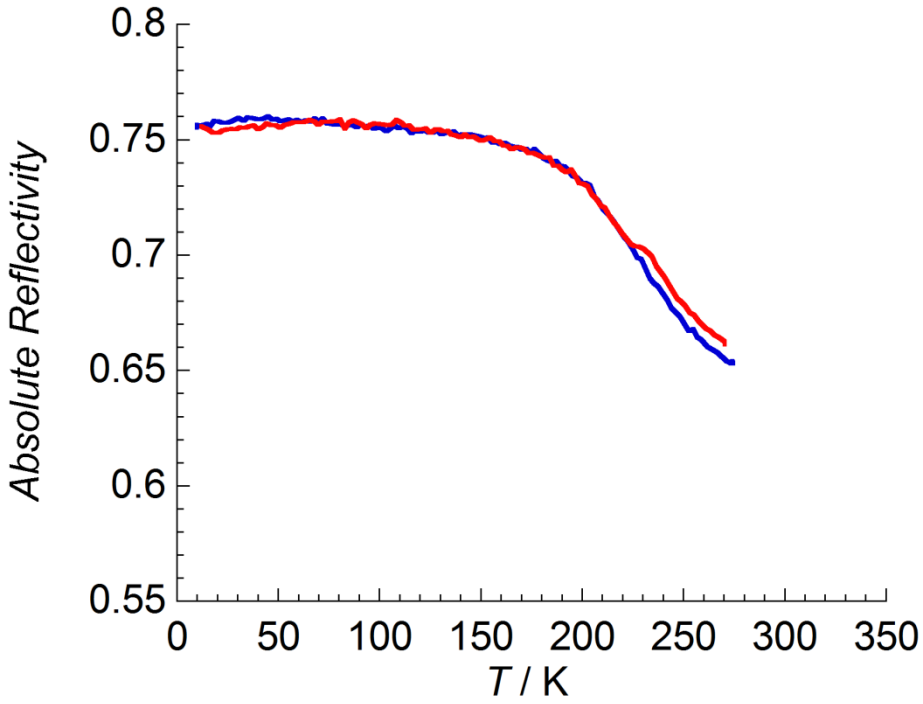

***Fig A-IV.1.2b** Thermal evolution of the reflectivity signal of **2.5** recorded at λ = 900 nm ± 5 nm during cooling mode, 270 – 10 K (**blue trace**) and heating mode 10 – 270 K (**red trace**).*

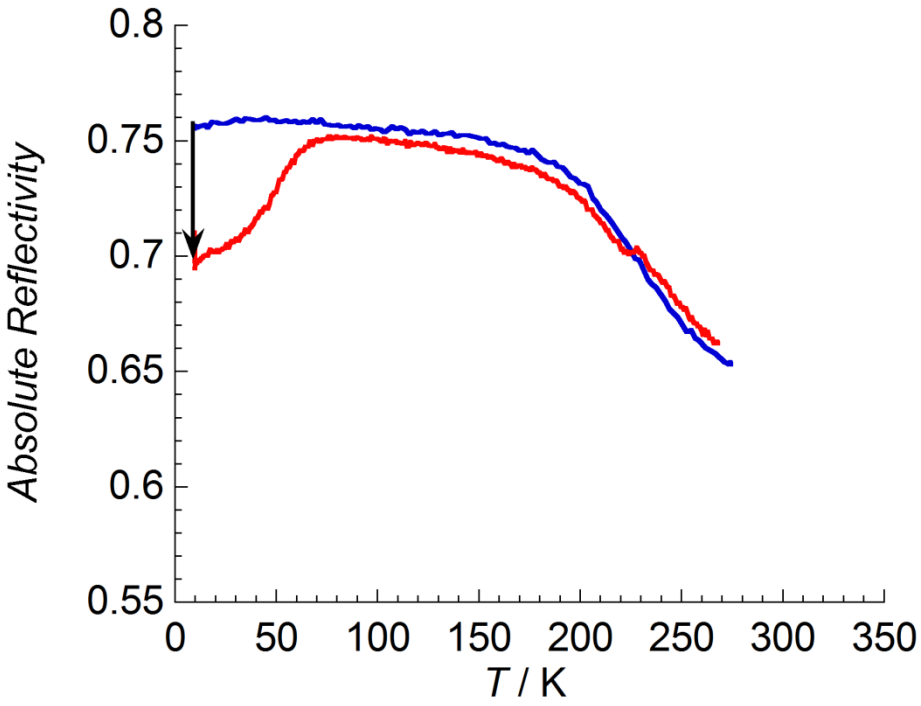

Fig A-IV.1.2c *Thermal evolution of the reflectivity signal of* ***2.5*** *recorded at λ = 900 nm ± 5 nm during cooling mode, 270 – 10 K (**blue trace**) and after white light irradiation (10 K, 0.4 mW cm^{-2}, 80 minutes) in heating mode 10 – 270 K (**red trace**).*

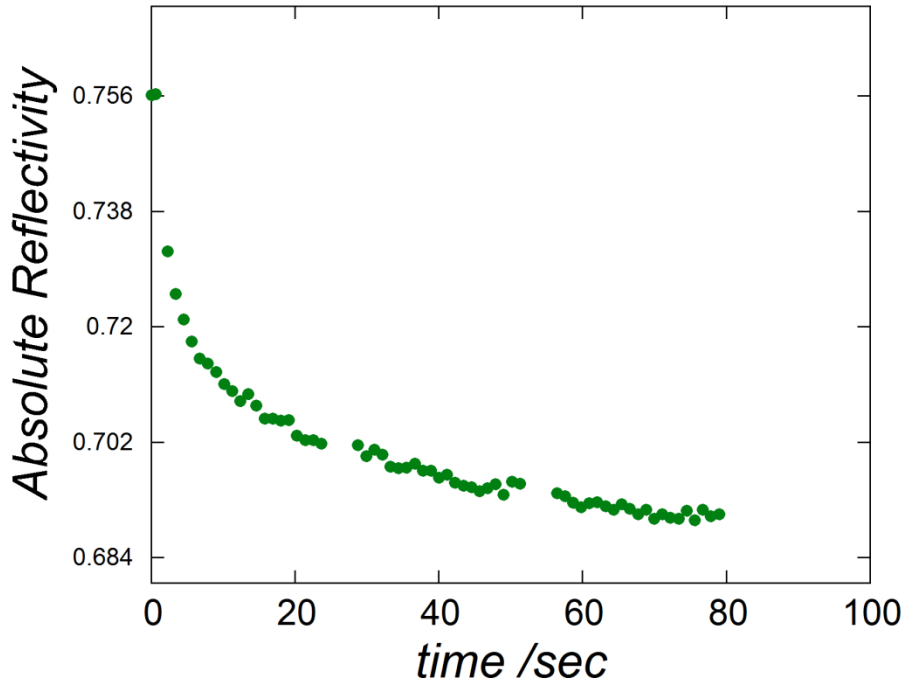

Fig A-IV.1.2d *The time dependence of the absolute reflectivity signal of* ***2.5*** *recorded at λ = 900 ± 5 nm during green light irradiation at 10 K (0.8 mW cm^{-2}, 530 nm).*

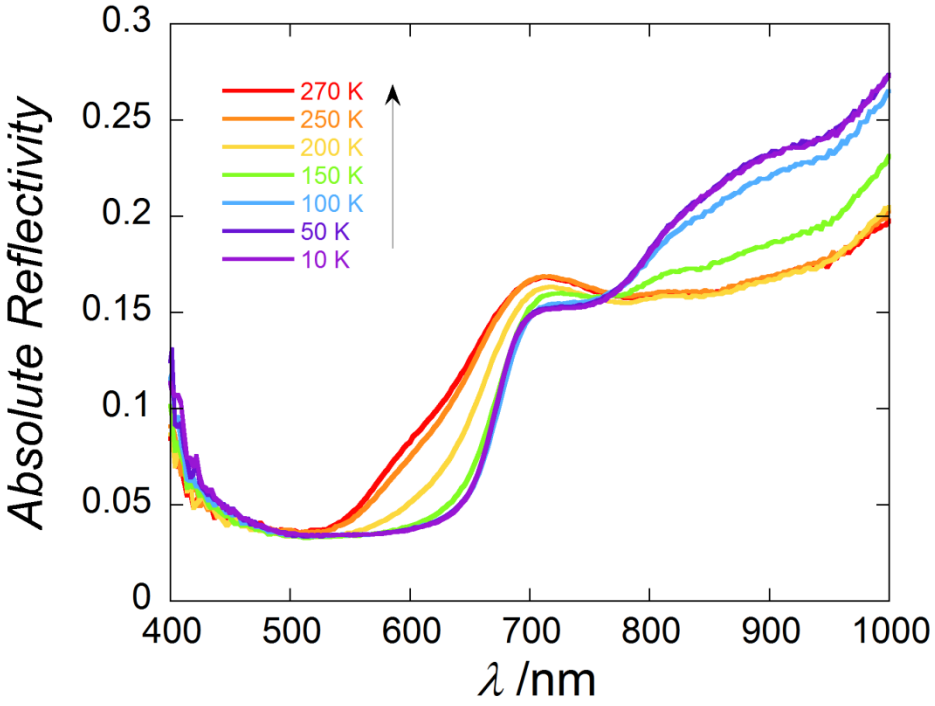

***Fig A-IV.1.3a** Selected surface reflectivity measurements of **2.6** collected with a white light spectroscopic source (0.4 mW cm^{-2}) as a function of temperature during heating mode, 10 – 270 K.*

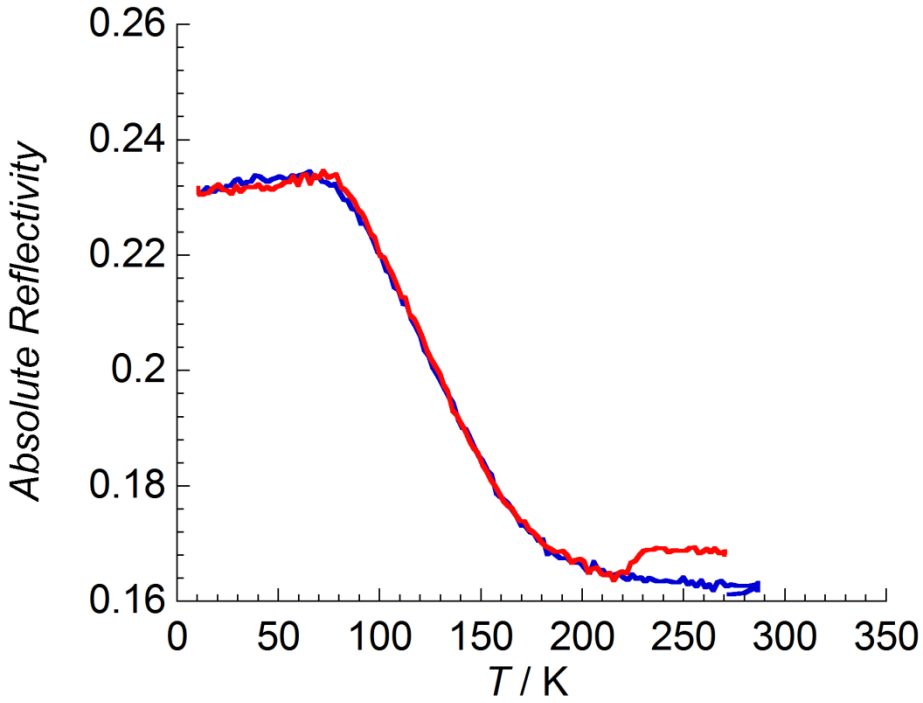

***Fig A-IV.1.3b** Thermal evolution of the reflectivity signal of **2.6** recorded at λ = 900 nm ± 5 nm during cooling mode, 270 – 10 K (**blue trace**) and heating mode 10 – 270 K (**red trace**).*

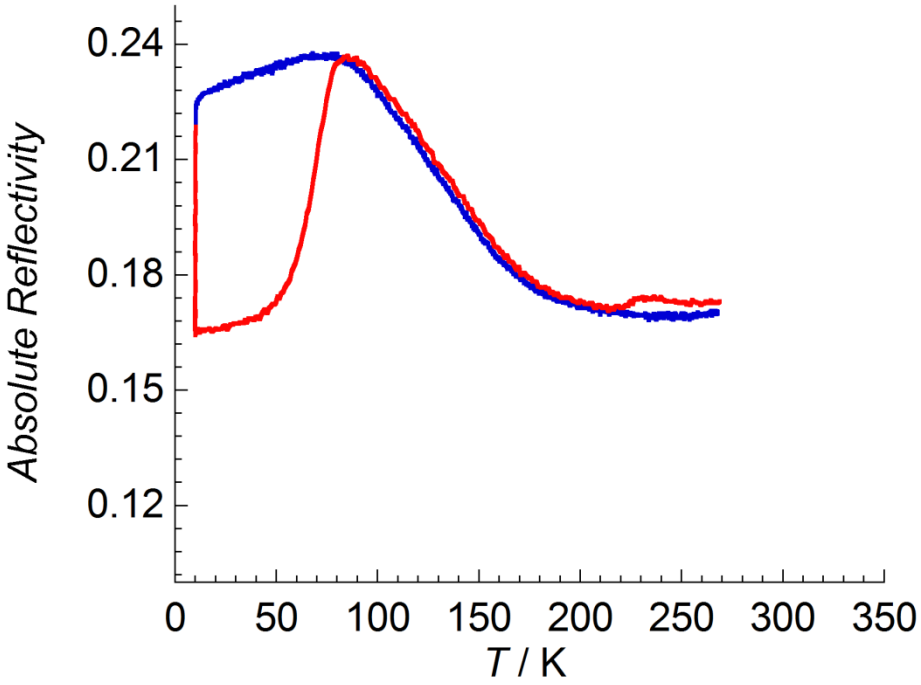

Fig A-IV.2.3c *Thermal evolution of the reflectivity signal of* ***2.6*** *recorded at λ = 900 nm ± 5 nm during cooling mode, 270 – 10 K (**blue trace**) and after white light irradiation at 10 K (0.4 mW cm^{-1}, 4 hours) during heating mode 10 – 270 K (**red trace**).*

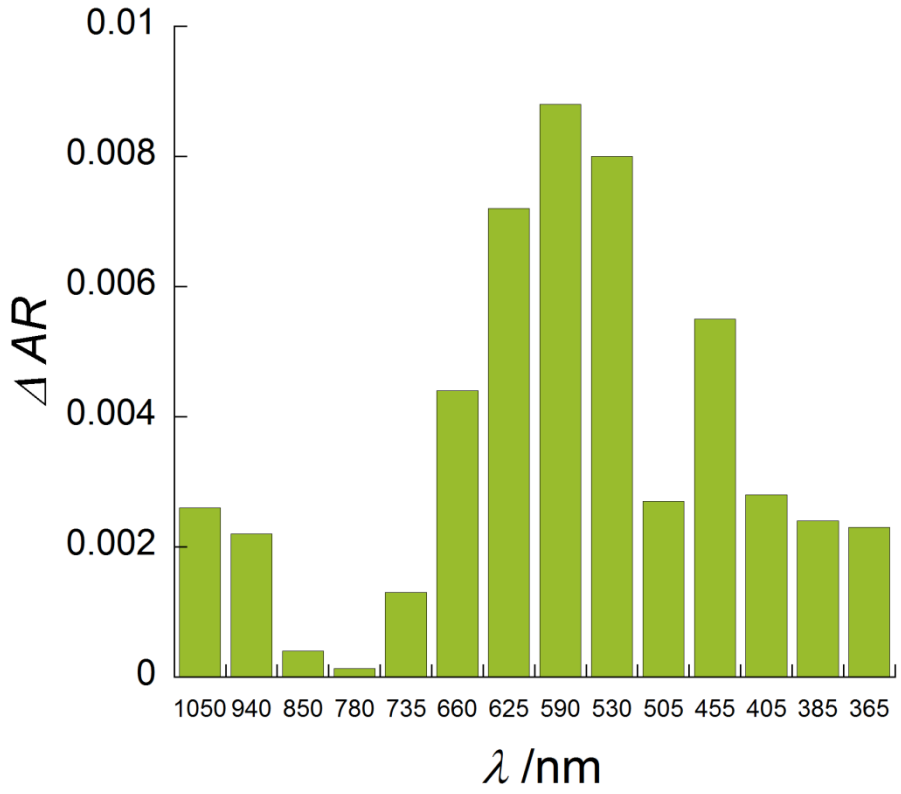

Fig A-IV.1.3d *Relative change in the absolute reflectivity (R_{900}) of* ***2.6*** *under different LED light conditions. Green light of 530 nm selected for subsequent experiments.*

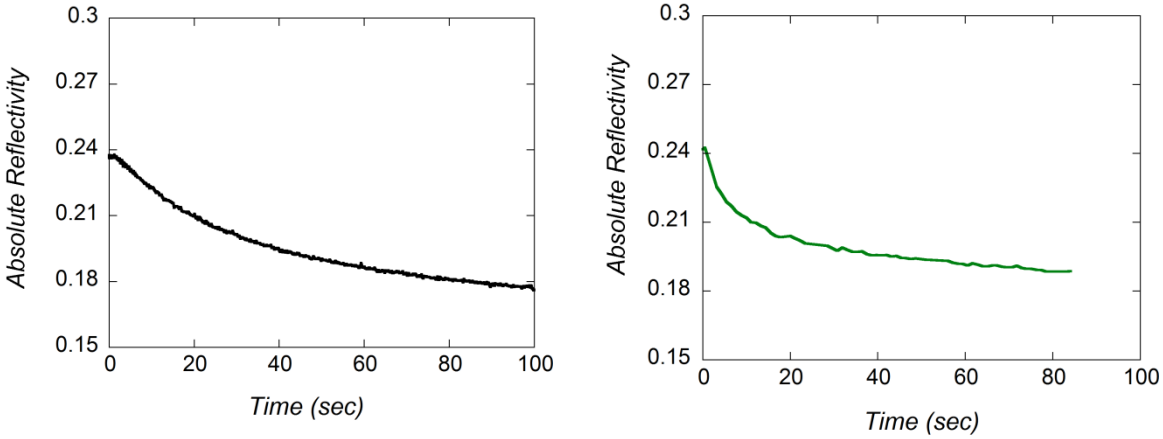

Fig A-IV.1.3e *The time dependence of the absolute reflectivity spectra (R_{900}) of* ***2.6*** *during white light irradiation (10 K, 0.4 mW cm^{-2} –* ***left****) and during green light irradiation (530 nm, 0.8 mW cm^{-2} –* ***right****).*

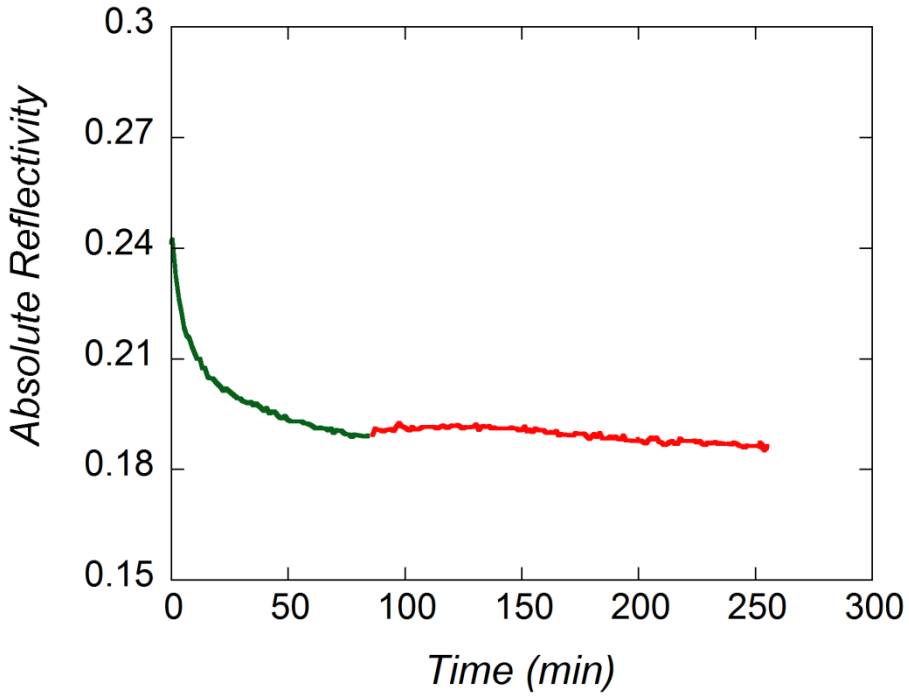

Fig A-IV.1.3f *Reverse-LIESST experiment showing the time dependence on the absolute reflectivity (R_{900}) after green light excitation (****green trace****) and following irradiation with 850 nm light.*

A-IV.2 Chapter Four Supplementary Information

*A-IV.2.1 Structural Analysis of **L4.2** by Single Crystal X-ray Diffraction*

Colourless crystals of **L4.2** suitable for structural analysis *via* X-ray diffraction were formed from the slow evaporation of a methanolic solution of the ligand. The crystallographic data for **L4.2** were solved and refined in the monoclinic space group $P2_1/c$ and shows, as anticipated, the imidazole head group joined to the *p*-toluidine moiety through an imine bond (C6 – N7). The imine bond was confirmed to show double bond character with a bond length of 1.276(1) Å which is consistent with a carbon-nitrogen double bond.[288] The head group is twisted relative to the plane of the phenyl ring through a torsion angle about C6-N7-C8-C9 of 37.3(2)°.

The imidazole N-H acts as a hydrogen bond donor and forms a 1D hydrogen bonding chain through N1-H1···N4 of neighbouring molecules with a donor-acceptor distance of 2.8463(13) Å. The molecular structure, atomic labelling scheme and hydrogen bonding network of **L4.2** are shown in **Fig A-IV.2.1**

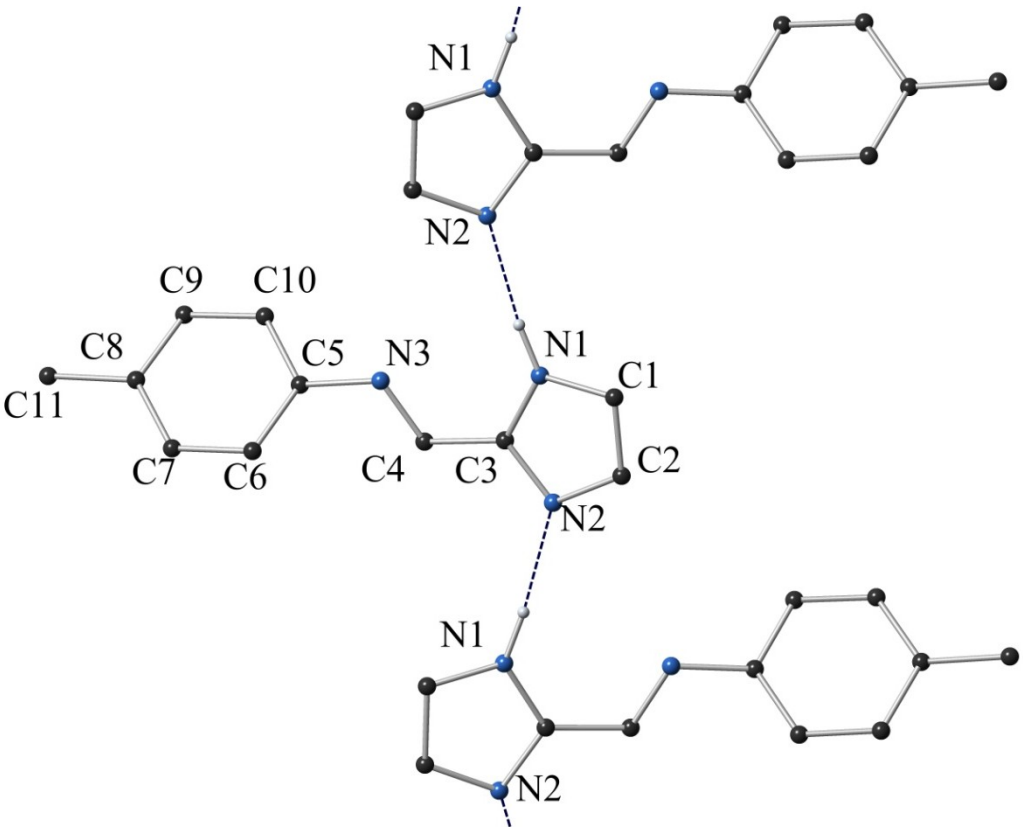

***Fig A-IV.2.1** Molecular structure, atom labelling scheme and 1D hydrogen bonding network of **L4.2**. Hydrogen atoms not involved in hydrogen bonding have been omitted for clarity.*

The crystallographic data for **L4.3** were solved and refined in the orthorhombic space group P*bca* with an R-factor of 2.30%. The structure and atom labelling scheme are shown below in figure **A-IV.2.2**. Interestingly, in this example two crystallography distinct molecules of **L4.3** lying anti-parallel to one another are found in the asymmetric unit. Both of these molecules are consistent with the product as expected with both molecules show the imidazole head group joined to the *p*-bromo aniline moiety through an imine bond. The bond lengths of 1.276(3)Å and 1.278(3)Å for N6-C14 and N3-C4 respectively are consistent with the formation of a C-N double bond.

Once again there is a twisting of the ligand between the imidazole and phenyl ring planes as seen in other ligands in this family. The torsion angle as measured through the *cis* arrangement of bonds including the imine and phenyl ring torsion angles of 34.9(3)° and 22.6(3)° observed in molecules **1** and **2** respectively. The other significant difference between the two molecules within the asymmetric unit is that the imidazole head groups lie in opposite conformations from one another. In molecule 1 the head group lies with the protonated nitrogen in an anti configuration to the imine bond. This places the coordinating imidazole nitrogen in the syn position. In molecule 2 the opposite occurs where the protonated imidazole nitrogen lies in the syn position. These heteroatom hydrogens were placed using a combination of residual electron density near N_2 and N_5 which was not observed near N_1 and N_4 and by investigating the bond lengths to adjacent atoms. N2-C3 shows are bond length of 1.355(3) Å which is significantly longer than the 1.331(3) Å bond length for N1-C3. Likewise N5-C13 shows a bond length of 1.350(3) Å which is longer than the corresponding bond length between N4-C13 at a distance of 1.332(3) Å leading to the assignment of the hydrogen at N1 and N4.

Once again due to the hydrogen bond donating nature of the imidazole head group the molecules within the crystal pack in sheets with the imidazole head groups lining up to form 1D hydrogen bonding polymers between N2-H2A···N1 and N5-H5···N4. Details of the hydrogen bonding distances are provided in the tables within **A-III** and a diagram showing the nature of the hydrogen bonding is provided in figure **A-IV.2.2**.

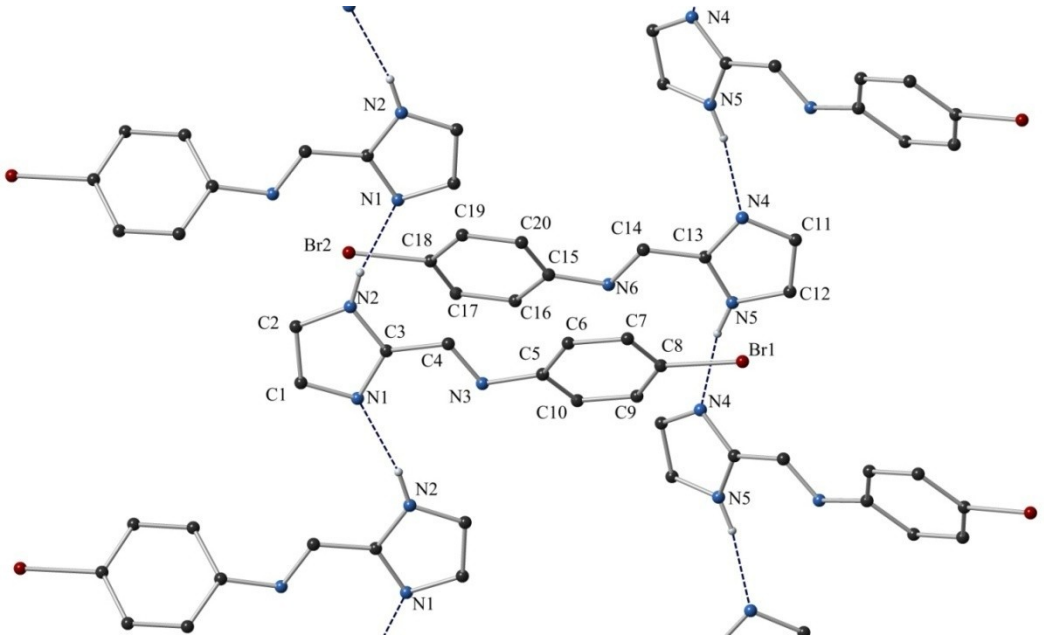

Fig A-IV.2.2 *Molecular structure, atom labelling scheme and 1D hydrogen bonding network of* ***L4.3****. Hydrogen atoms not involved in hydrogen bonding have been omitted for clarity.*

A-IV.2.3 Ideal Solution Model Data Fit for ***4.7***

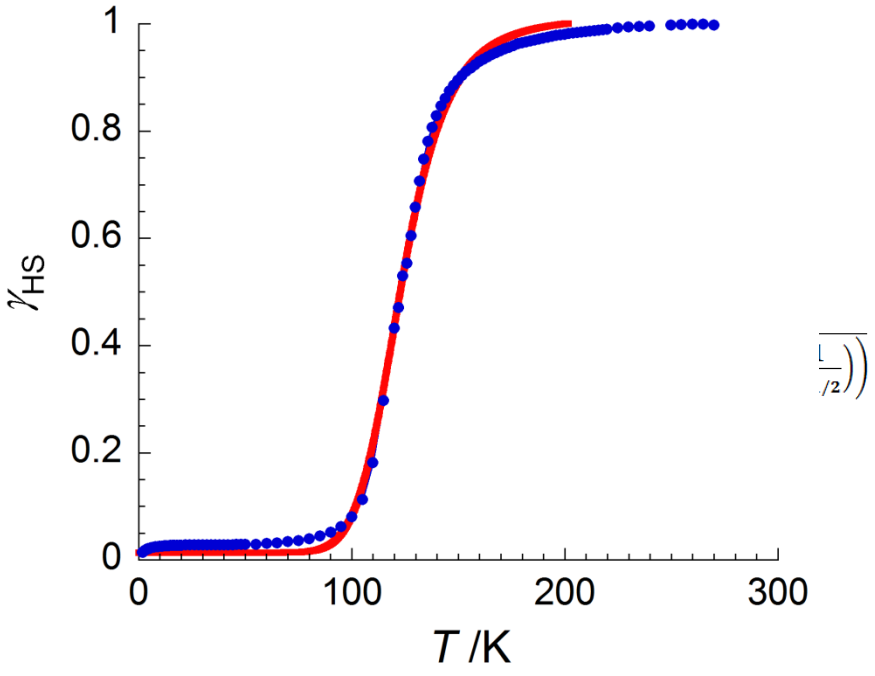

Fig A-IV.2.3 *The γ_{HS} ($\gamma_{HS} = \chi T/\chi T_{HS}$) vs. T plot (**blue circles**) and the data fit to the ideal solution model (**red line**, **inset equation**). The best fit was obtained with ΔH =11.5 kJ mol^{-1}, ΔS = 96 J K^{-1} mol^{-1} and $T_{1/2}$ = 123 K.*

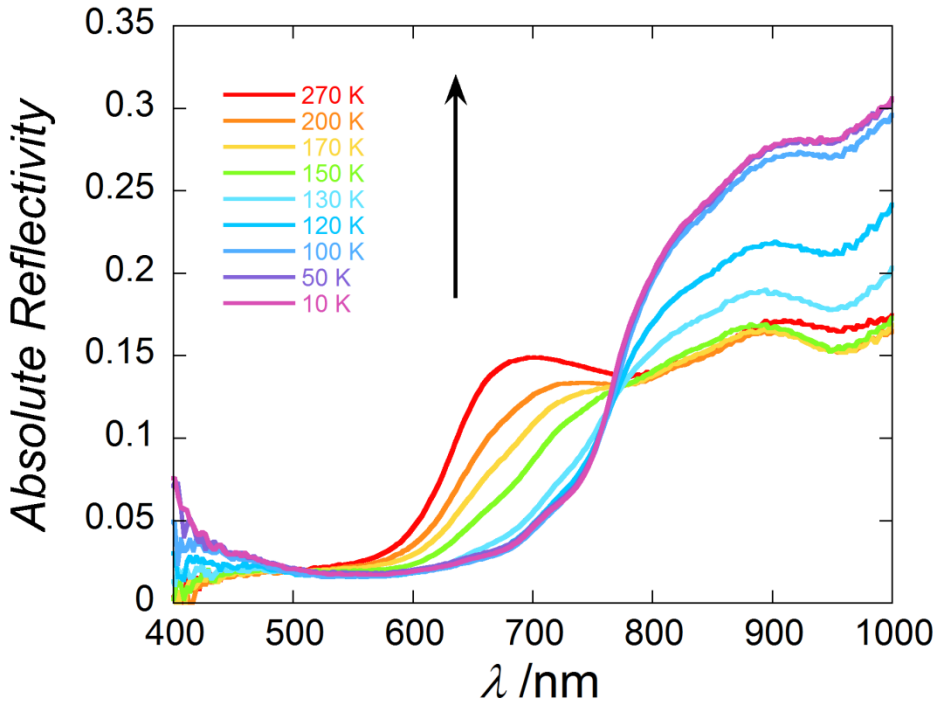

***Fig A-IV.2.4a** Selected surface reflectivity measurements of **4.7** collected with a white light spectroscopic source (0.4 mW cm^{-2}) as a function of temperature during heating mode, 10 – 270 K.*

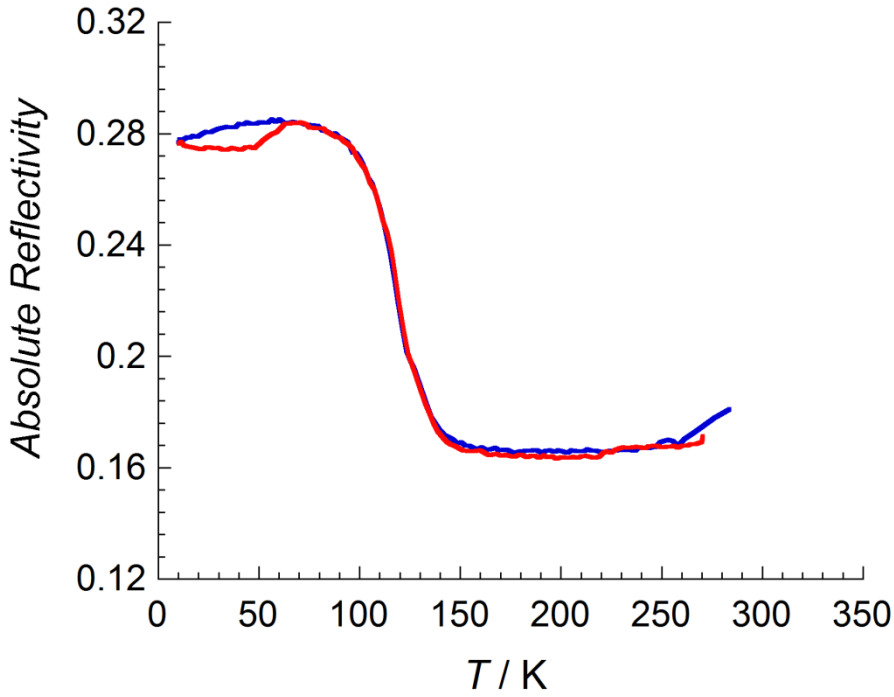

***Fig A-IV.2.4b** Thermal evolution of the reflectivity signal of **4.7** recorded at λ = 900 nm ± 5 nm during cooling mode, 270 – 10 K (**blue trace**) and heating mode 10 – 270 K (**red trace**).*

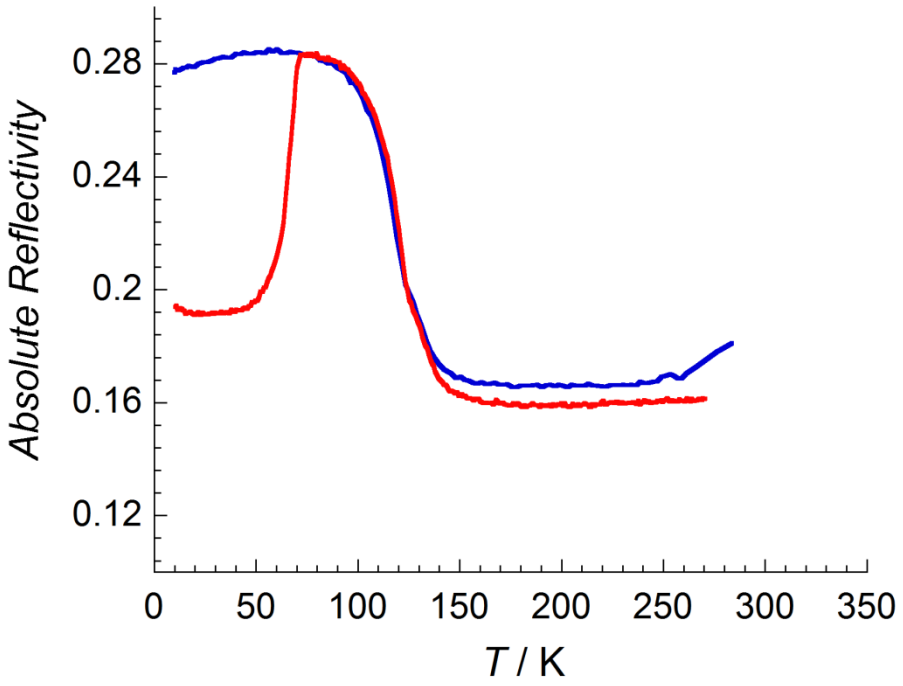

Fig A-IV.2.4c *Thermal evolution of the reflectivity signal of* ***4.7*** *recorded at λ = 900 nm ± 5 nm during cooling mode, 270 – 10 K (****blue trace****) and after white light irradiation at 10 K (0.4 mW cm^{-1}, 3 hours) during heating mode 10 – 270 K (****red trace****).*

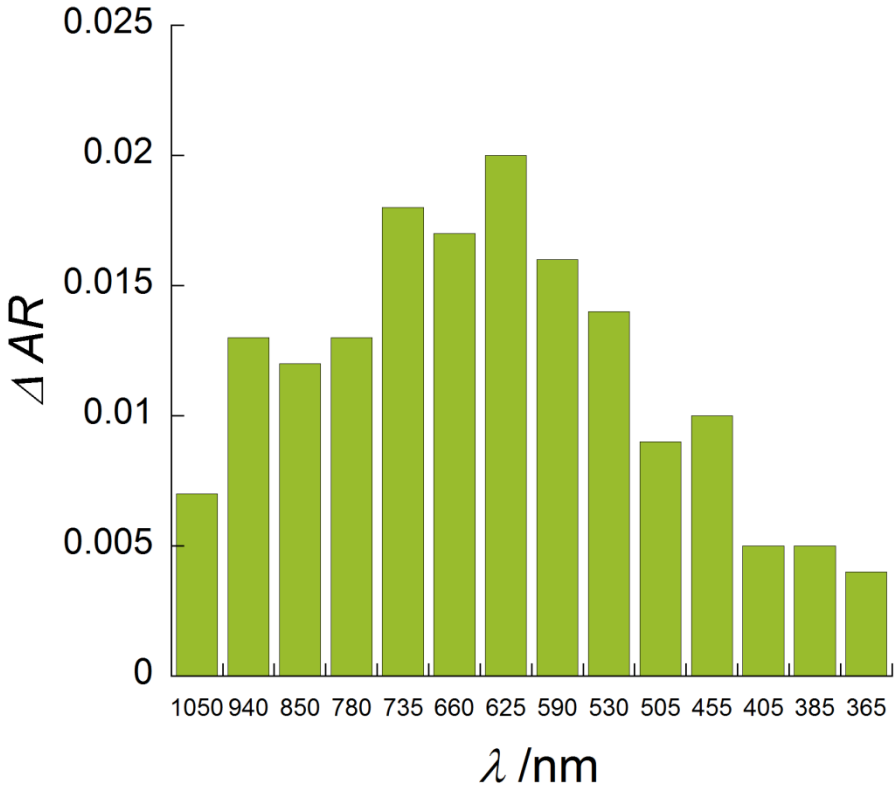

Fig A-IV.2.4d *Relative change in the absolute reflectivity (R_{900}) of* ***4.7*** *under different LED light conditions. Red light of 625 nm selected for subsequent experiments.*

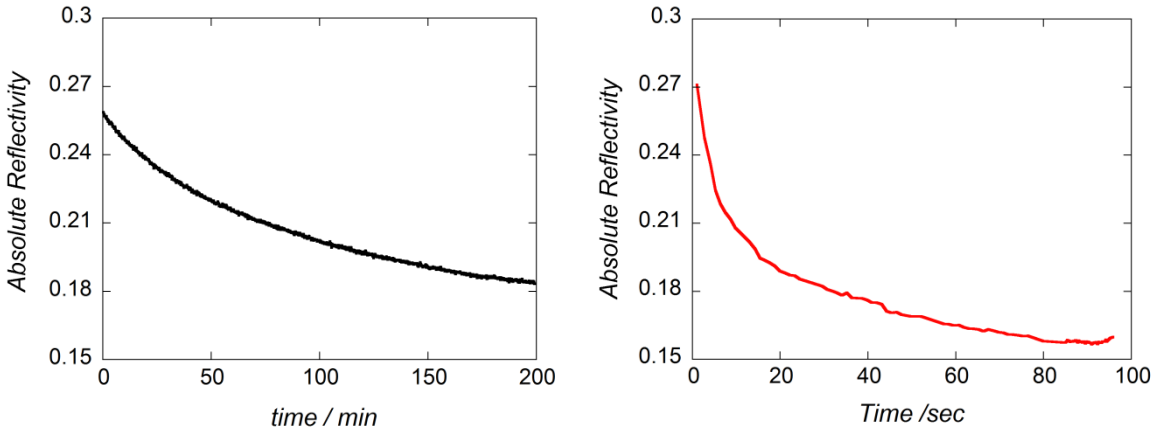

Fig A-IV.2.4e *The time dependence of the absolute reflectivity spectra (R_{900}) of* ***4.7*** *during white light irradiation (10 K, 0.4 mW cm^{-2} –* ***left****) and during red light irradiation (625 nm, 0.8 mW cm^{-2} –* ***right****).*

A-IV.2.5 Surface Reflectivity Measurements – Complex ***4.10-Dried***

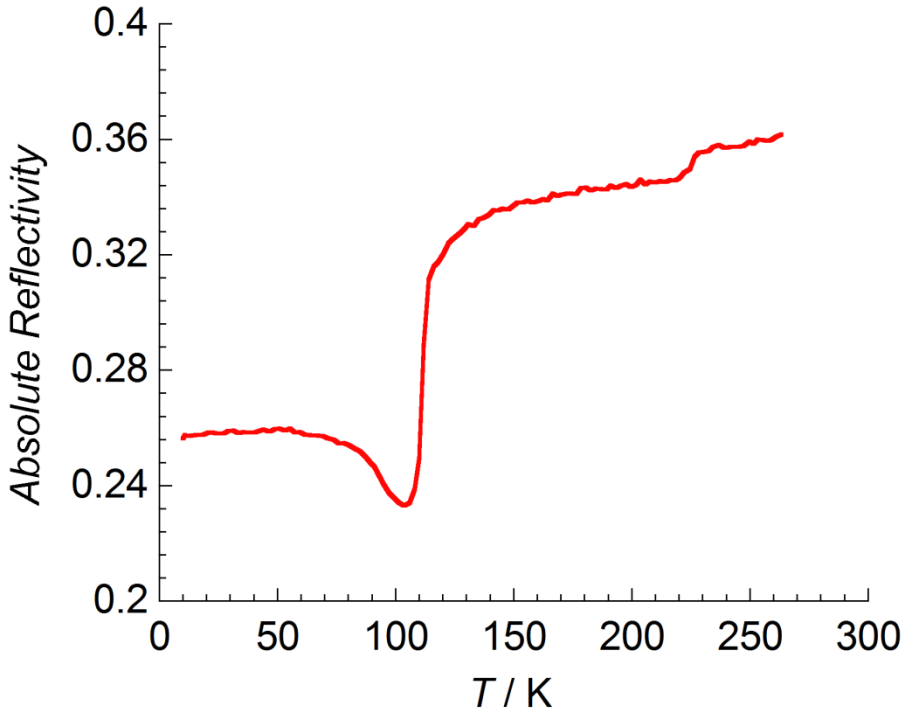

Fig A-IV.2.5a*Thermal evolution of the reflectivity signal of* ***4.10-Dried*** *recorded at λ = 700 nm ± 5 nm during heating mode 10 – 270 K (****red trace****).*

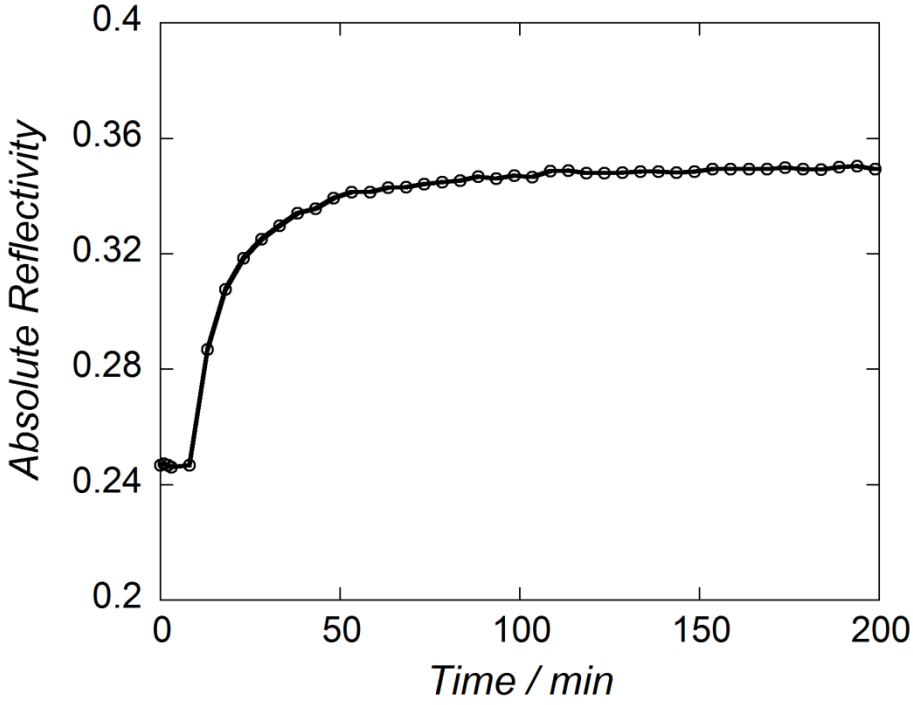

Fig A-IV.2.5b *The time dependence of the absolute reflectivity spectra (R_{700}) of* ***4.10-Dried*** *during white light irradiation (10 K, 0.4 mW cm^{-2})*

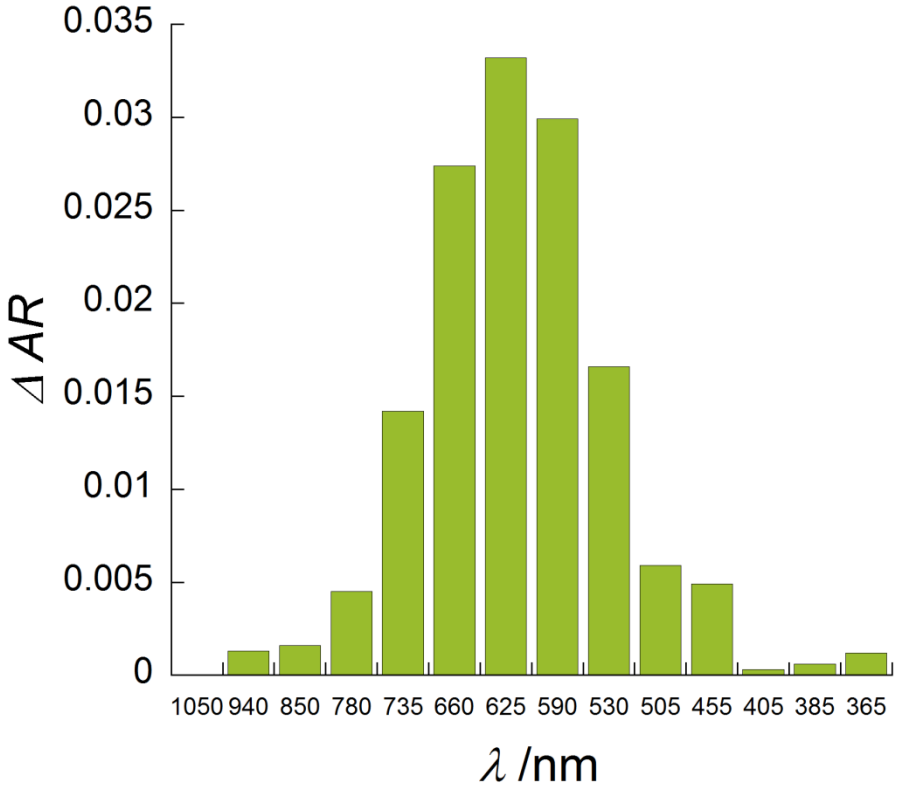

Fig A-IV.2.5c *Relative change in the absolute reflectivity (R_{700}) of* ***4.10-Dried*** *under different LED light conditions. Red light of 625 nm selected for subsequent measurements.*

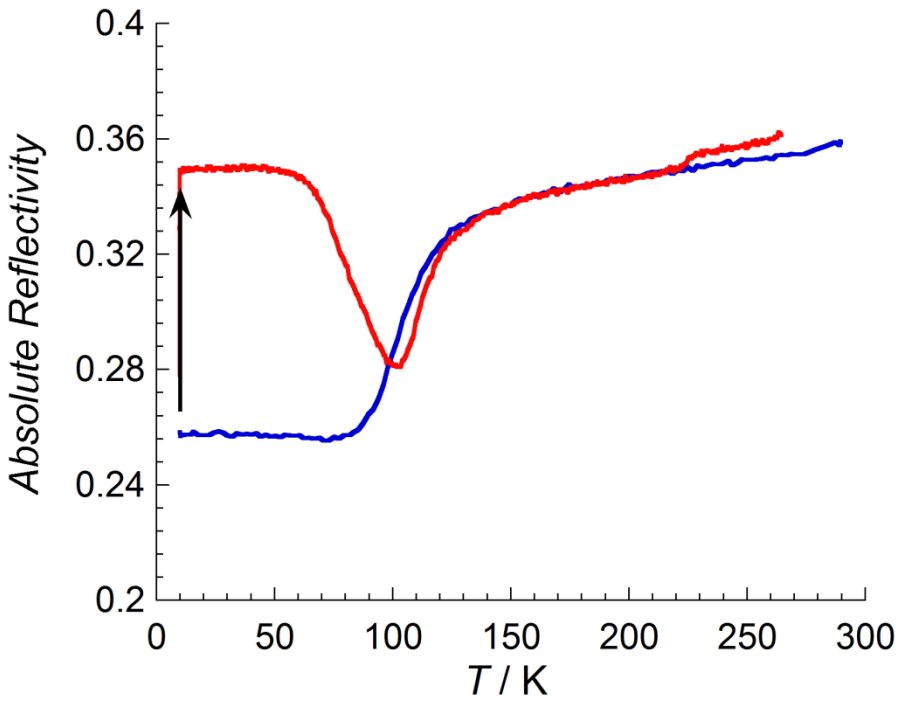

Fig A-IV.2.5d *Thermal evolution of the reflectivity signal of* ***4.10-Dried*** *recorded at λ = 700 nm ± 5 nm during cooling mode (**blue trace**) and after red light irradiation at 10 K (0.8 mW cm^{-2}, 2 hours) in heating mode (**red trace**). Scan rate for both heating and cooling mode 4 K min^{-1}.*

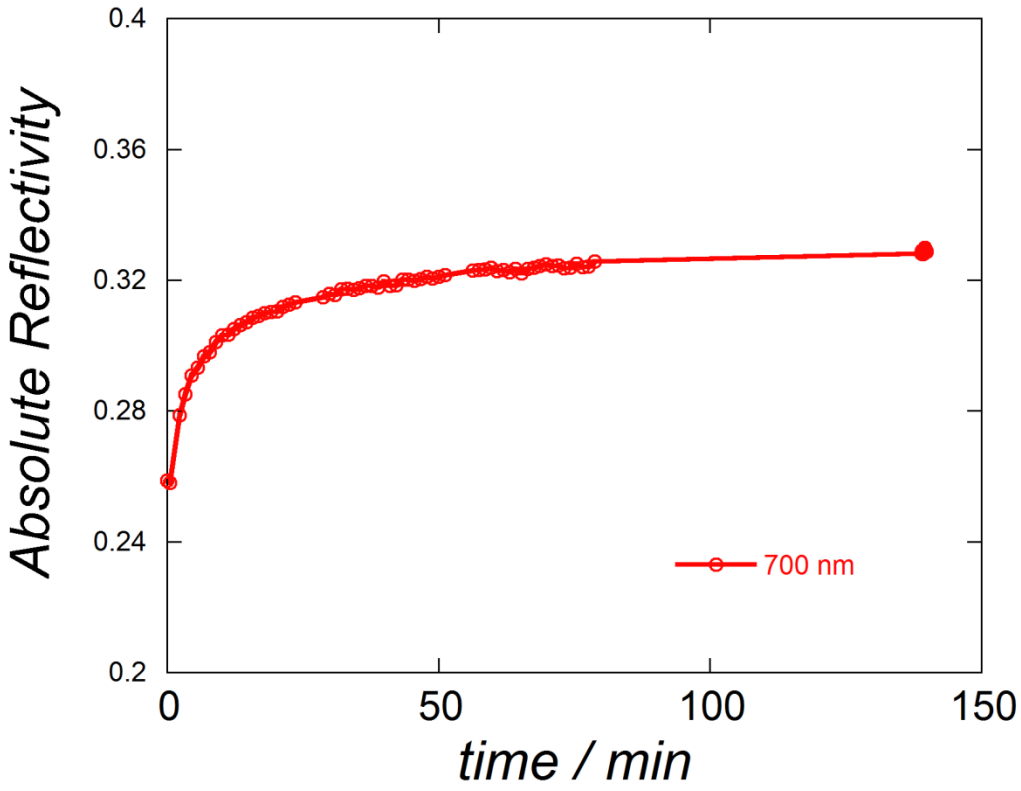

Fig A-IV.2.5e *The time dependence of the absolute reflectivity spectra (R_{700}) of* ***4.10-Dried*** *during red light irradiation (10 K, 0.8 mW cm^{-2}).*

REFERENCES

(1) Gutlich, P.; Garcia, Y.; Goodwin, H. A. *Chem. Soc. Rev.* **2000**, *29*, 419-427.
(2) Halcrow, M. A. *Chem. Soc. Rev.* **2011**, *40*, 4119-4142.
(3) Pederson, C. J. *J. Am. Chem. Soc.* **1967**, *89*, 7017-7036.
(4) Dietrich, B.; Lehn, J. M.; Sauvage, J. P. *Tetrahedron Lett.* **1969**, *34*, 2889-2892.
(5) Dietrich, B.; Lehn, J. M.; Sauvage, J. P. *Tetrahedron Lett.* **1969**, *34*, 2885-2888.
(6) Cram, D. J.; Cram, J. M. *Science* **1974**, *183*, 803-809.
(7) Cram, D. J.; Cram, J. M. *Container Molecules and their Guests*; The Royal Society of Chemistry, Cambridge, 1994.
(8) "The Nobel Prize in Chemistry 1987" Nobelprize.org; http://nobelprize.org/nobel_prizes/chemistry/laureates/1987/; accessed 17/09/2013
(9) Wolf, K. L.; Frahm, F.; Harms, H. *Z. Physik. Chem.* **1937**, *B36*, 237-287.
(10) Image Credit: http://en.wikipedia.org/wiki/Cryptand; accessed 17/09/2013
(11) Image Credit: http://en.wikipedia.org/wiki/File:K(18-C-6).png; accessed 17/09/2013
(12) Image Credit: http://commons.wikimedia.org/wiki/File:Spherand_colour.png; accessed 17/09/2013
(13) Fischer, E. *Ber. Disch. Chem. Ges.* **1894**, *27*, 2985-2993.
(14) Watson, J. D.; Crick, F. H. C. *Nature* **1953**, *171*, 737-8.
(15) Watson, J. D. *The Double Helix*; Penguin: London, 1999.
16) Steed, J. W.; Atwood, J. L. Eds.; *Supramolecular Chemistry*; John Wiley & Sons, Ltd.: West Sussex, 2000.
(17) Atwood, J. L.; Lehn, J. M. Eds.; *Comprehensive Supramolecular Chemistry*; 1 ed.; Pergamon: New York, 1996; Vol. 9.
(18) Sauvage, J. P. Ed.; *Transition Metals in Supramolecular Chemistry*; John Wiley and Sons: Oxford, 1999; Vol. 5.
(19) Lehn, J. M.; *Supramolecular Chemistry: Concepts and Perspectives*; Wiley-VCH, 1995.
(20) Gale, P. A., Steed, J. W., Eds.; *Supramolecular Chemistry: From Molecules to Nanomaterials;* John Wiley & Sons, Inc.: West Sussex, 2012.
(21) Lehn, J. M. *Angew. Chem. Int. Ed.* **1990**, *29*, 1304-1319.
(22) Corey, E. J. *Pure Appl. Chem.* **1967**, *14*, 19-38.
(23) Desiraju, G. *Angew. Chem. Int. Ed.* **1995**, *34*, 2311-2327.
(24) Pauling, L. *J. Am. Chem. Soc.* **1931**, *53*, 1367.
(25) Arunan, E.; Desiraju, G.; Klein, R. A.; Sadlej, J.; Scheiner, S.; Alkorta, I.; Clary, D. C.; Crabtree, R. H.; Dannenberg, J. J.; Hobza, P.; Kjaergaard, H. G.; Legon, A. C.; Mennucci, B.; Nesbitt, D. J. *Pure Appl. Chem.* **2011**, *83*, 1637-1641.
(26) Calhorda, M. J. *Chem. Commun.* **2000**, 801-809.
(27) Steiner, T. *Chem. Commun.* **1997**, 727-734.
(28) Beer, P. D.; Gale, P. A. *Angew. Chem. Int. Ed.* **2001**, *40*, 486-516.

(29) Steed, J. W.; Atwood, J. L. Eds.; *Supramolecular Chemistry*; 2nd Ed.; John Wiley & Sons Ltd.: Chichester, England, 2009.

(30) Desiraju, G. R. *Nature* **2001**, *412*, 397-400.

(31) Jeffrey, G. A. *An Introduction to Hydrogen Bonding*; Oxford University Press: New York, 1997.

(32) Seto, C. T.; Whitesides, G. M. *J. Am. Chem. Soc.* **1990**, *112*, 6409-6411.

(33) Zerkowski, J. A.; Seto, C. T.; Whitesides, G. M. *J. Am. Chem. Soc.* **1992**, 5473-5475.

(34) Kazuo, M.; Hironobu, K.; Koichiso, Y.; Junichi, N. *Jpn. Kokai Tokkyo Koho* **1979**, *79*, 588.

(35) Gamez, P.; Reedijk, J. *Eur. J. Inorg. Chem.* **2006**, *2006*, 29-42.

(36) Hunter, C. A.; Sanders, J. K. M. *J. Am. Chem. Soc.* **1990**, *112*, 5525-5534.

(37) Hunter, C. A. *Chem. Soc. Rev.* **1994**, *23*, 101-109.

(38) Janiak, C. *J. Chem. Soc. Dalton Trans.* **2000**, 3885-3896.

(39) Hunter, C. A. *J. Mol. Biol.* **1993**, *230*, 1025-1054.

(40) Wakelin, L. P. G. *Med. Res. Rev.* **1986**, *6*, 275-340.

(41) Burley, S. K.; Petsko, G. A. *Science* **1985**, *229*, 23-28.

(42) Burley, S. K.; Petsko, G. A. *Adv. Protein Chem.* **1988**, *39*, 125-189.

(43) Sygula, A.; Fronczek, F. R.; Sygula, R.; Rabideau, P. W.; Olmstead, M. M. *J. Am. Chem. Soc.* **2007**, *129*, 3842-3843.

(44) Yoshizawa, M.; Klosterman, J. K.; Fujita, M. *Angew. Chem. Int. Ed.* **2009**, *48*, 3418-3438.

(45) Klosterman, J. K.; Yamauchi, Y.; Fujita, M. *Chem. Soc. Rev.* **2009**, *38*, 1714-1725.

(46) Yoshizawa, M.; Fujita, M. *Bull. Chem. Soc. Jpn.* **2010**, *83*, 609-618.

(47) Yoshizawa, M.; Nakagawa, J.; Kumazawa, K.; Nagao, M.; Kawano, M.; Ozeki, T.; Fujita, M. *Angew. Chem. Int. Ed.* **2005**, *44*, 1810-1813.

(48) Yoshizawa, M.; Nagao, M.; Kumazawa, K.; Fujita, M. *J. Organomet. Chem.* **2005**, *690*, 5383-5388.

(49) Hawes, C. S., *1,2-Diazoles: Versatile Tectons for Metallosupramolecular Assemblies*; **2012**, University of Canterbury

(50) Pyykko, P. *Chem. Rev.* **1997**, *97*, 597-636.

(51) Horvath, U. E. I.; McKenzie, J. M.; Cronje, S.; Raubenheimer, H. G.; Barbour, L. J. *Chem. Commun.* **2009**, 6598-6600.

(52) Chu, Q.; Swenson, D. C.; MacGillivray, L. R. *Angew. Chem. Int. Ed.* **2005**, *44*, 3569-3572.

(53) Barreiro, E.; Casas, J. S.; Couce, M. D.; Laguna, A.; Lopez-de-Luzuriaga, J. M.; Monge, M.; Sanchez, A.; Sordo, J.; Vazquez Lopez, E. M. *Dalton Trans.* **2013**, *42*, 5916-5923.

(54) Duriska, M. B.; Batten, S. R.; Price, D. J. *Aust. J. Chem.* **2006**, *59*, 26-29.

(55) Hassel, O. *Science* **1970**, *170*, 497-502.

(56) Metrangolo, P.; Neukirch, H.; Pilati, T.; Resnati, G. *Acc. Chem. Res.* **2005**, *38*, 386-395.

(57) Metrangolo, P.; Meyer, F.; Pilati, T.; Resnati, G.; Terraneo, G. *Angew. Chem. Int. Ed.* **2008**, *47*, 6114-6127.

(58) Corradi, E.; Meille, S. V.; Messina, M. T.; Metrangolo, P.; Resnati, G. *Angew. Chem. Int. Ed.* **2000**, *39*, 1782-1786.

(59) Bent, H. A. *Chem. Rev.* **1968**, *68*, 587-648.

(60) Legon, A. C. *Angew. Chem. Int. Ed.* **1999**, *38*, 2686-2714.

(61) Rissanen, K. *Cryst. Eng. Comm.* **2008**, *10*, 1107-1113.

(62) Mele, A.; Metrangolo, P.; Neukirch, H.; Pilati, T.; Resnati, G. *J. Am. Chem. Soc.* **2005**, *127*, 14972-14973.

(63) Parisini, E.; Metrangolo, P.; Pilati, T.; Resnati, G.; Terraneo, G. *Chem. Soc. Rev.* **2011**, *40*, 2267-2278.

(64) Fourmigue, M.; Batail, P. *Chem. Rev.* **2004**, *104*, 5379-5418.

(65) Cariati, E.; Forni, A.; Biella, S.; Metrangolo, P.; Meyer, F.; Resnati, G.; Righetto, S.; Tordin, E.; Ugo, R. *Chem. Commun.* **2007**, 2590-2592.

(66) Bruce, D. W.; Metrangolo, P.; Meyer, F.; Pilati, T.; Prasang, C.; Resnati, G.; Terraneo, G.; Wainwright, S. G.; Whitwood, A. C. *Chem. Eur. J.* **2010**, *16*, 9511-9524.

(67) Shepodd, T. J.; Petti, M. A.; Dougherty, D. A. *J. Am. Chem. Soc.* **1988**, *110*, 1983-1985.

(68) Dougherty, D. A.; Ma, J. C. *Chem. Rev.* **1997**, *97*, 1303-1324.

(69) Dougherty, D. A.; Stauffer, D. A. *Science* **1990**, *250*, 1558-1560.

(70) Chifotides, H. T.; Dunbar, K. R. *Acc. Chem. Res.*, *46*, 894-906.

(71) Schottel, B. L.; Chifotides, H. T.; Dunbar, K. R. *Chem. Soc. Rev.* **2008**, *37*, 68-83.

(72) Mareda, J.; Matle, S. *Chem. Eur. J.* **2009**, *15*, 28-37.

(73) Dawson, R. E.; Hennig, A.; Welmann, D. P.; Emery, D.; Ravlkumar, V.; Montenegro, J.; Takeuchi, T.; Gabutti, S.; Mayor, M.; Mareda, J.; Schalley, C. A.; Matle, S. *Nat. Chem.* **2010**, *2*, 533-538.

(74) Rowan, S. J.; Cantrill, S. J.; Cousins, G. R. L.; Sanders, J. K. M.; Stoddart, J. F. *Angew. Chem. Int. Ed.* **2002**, *41*, 898-952.

(75) Lehn, J. M. *Angew. Chem. Int. Ed.* **1990**, *29*, 1304-1319.

(76) Fiedler, D.; Leung, D. H.; Bergman, R. G.; Raymond, K. N. *Acc. Chem. Res.* **2005**, *38*, 349-358.

(77) Sanders, J. K. M. *Chem. Eur. J.* **1998**, *4*, 1378-1383.

(78) Breit, B. *Angew. Chem. Int. Ed.* **2005**, *44*, 6816-6825.

(79) Gianneschi, N. C.; Bertin, P. A.; Nguyen, S. T.; Mirkin, C. A.; Zakharov, L. N.; Rheingold, A. L. *J. Am. Chem. Soc.* **2003**, *125*, 10508-10509.

(80) Fabbrizzi, L.; Poggi, A. *Chem. Soc. Rev.* **1995**, *24*, 197-202.

(81) Stang, P. J.; Olenyuk, B. *Acc. Chem. Res.* **1997**, *30*, 502-518.

(82) Fujita, M.; Yazaki, J.; Ogura, K. *J. Am. Chem. Soc.* **1990**, *112*, 5645-5647.

(83) Fujita, M.; Sasaki, O.; Mitsuhashi, T.; Fujita, T.; Yazaki, J.; Yamaguchi, K.; Ogura, K. *Chem. Commun.* **1996**, 1535-1536.

(84) Anelli, P. L.; Ashton, P. R.; Ballardini, R.; Balzani, V.; Delgado, M.; Gandolfi, M. T.; Goodnow, T. T.; Kaifer, A. E.; Philp, D.; Pietraszkiewicz, M.; Prodi, L.; Reddington, M. V.; Slawin, A. M. Z.; Spencer, N.; Stoddart, J. F.; Vicent, C.; Williams, D. J. *J. Am. Chem. Soc.* **1992**, *114*, 193-218.

(85) Forgan, R. S.; Sauvage, J. P.; Stoddart, J. F. *Chem. Rev.* **2011**, *111*, 5434-5464.

(86) Eddaoudi, M.; Kim, J.; Rosi, N.; Vodak, D.; Wachter, J.; O'Keeffe, M.; Yaghi, O. M. *Science* **2002**, *295*, 469-472.

(87) Yaghi, O. M.; Li, G. M.; Li, H. L. *Nature* **1995**, *378*, 703-706.

(88) Kitagawa, S.; Kitaura, R.; Noro, S. *Angew. Chem. Int. Ed.* **2004**, *43*, 2334-2375.

(89) Varshey, D. B.; Sander, J. R. G.; Friscic, T.; MacGillivray, L. R. In *Supramolecular Chemistry: From Molecules to Nanomaterials*; Steed, J. W., Gale, P. A., Eds.; John Wiley & Sons: Online, 2012.

(90) Chakrabarty, R.; Mukherjee, P. S.; Stang, P. J. *Chem. Rev.* **2011**, *111*, 6810-6918.

(91) Mathias, J. P.; Stoddart, J. F. *Chem. Soc. Rev.* **1992**, *21*, 215-225.

(92) Robson, R.; Hoskins, B. F. *J. Am. Chem. Soc.* **1990**, *112*, 1546-1554.

(93) Saalfrank, R. W.; Maid, H.; Scheurer, A. *Angew. Chem. Int. Ed.* **2008**, *47*, 8794-8824.

(94) Fujita, M.; Kwon, Y. J.; Washizu, S.; Ogura, K. *J. Am. Chem. Soc.* **1994**, *116*, 1151-1152.

(95) Stang, P. J.; Cao, D. H.; Saito, S.; Arif, A. M. *J. Am. Chem. Soc.* **1995**, *117*, 6273-6283.

(96) Stang, P. J. *Chem. Eur. J.* **1998**, *4*, 19-27.

(97) Kuehl, C. J.; Huang, S. D.; Stang, P. J. *J. Am. Chem. Soc.* **2001**, *123*, 9634-9641.

(98) Thanasekaran, P.; Liao, R.-T.; Liu, Y.-H.; Rajendran, T.; Rajagopal, S.; Lu, K.-L. *Coord. Chem. Rev.* **2005**, *249*, 1085-1110.

(99) Schalley, C. A.; Muller, T.; Linnartz, P.; Witt, M.; Schafer, M.; Lutzen, A. *Chem. Eur. J.* **2002**, *8*, 4843-4849.

(100) Mukherjee, P. S.; Das, N.; Kryschenko, Y. K.; Arif, A. M.; Stang, P. J. *J. Am. Chem. Soc.* **2004**, *126*, 2464-2473.

(101) Stang, P. J.; Persky, N. E.; Manna, J. *J. Am. Chem. Soc.* **1997**, *119*, 4777-4778.

(102) Ruben, M.; Rojo, J.; Romero-Salguero, F. J.; Lehn, J. M. *Angew. Chem. Int. Ed.* **2004**, *43*, 3644-3662.

(103) Manna, J.; Whiteford, J. A.; Stang, P. J.; Muddiman, D. C.; Smith, R. D. *J. Am. Chem. Soc.* **1996**, *118*, 8731-8732.

(104) Lehn, J.-M.; Rigault, A.; Siegel, J.; Harrowfield, J.; Chevrier, B.; Moras, D. *Proc. Natl. Acad. Sci. USA* **1987**, *84*, 2565-2569.

(105) Albrecht, M. *Chem. Rev.* **2001**, *101*, 3457-3497.

(106) Kramer, R.; Lehn, J. M.; Marquis-Rigault, A. *Proc. Natl. Acad. Sci. USA* **1993**, *90*, 5394-5398.

(107) Piguet, C.; Bernardinelli, G.; Hopfgartner, G. *Chem. Rev.* **1997**, *97*, 2005-2062.

(108) Hannon, M. J.; Childs, L. J. *Supramol. Chem.* **2004**, *16*, 7-22.

(109) Pascu, G. I.; Hotze, A. C. G.; Sanchez-Cano, C.; Kariuki, B. M.; Hannon, M. J. *Angew. Chem. Int. Ed.* **2007**, *46*, 4374-4378.

(110) Amendola, V.; Fabbrizzi, L.; Pallavicini, P.; Sartirana, E.; Taglietti, A. *Inorg. Chem.* **2003**, *42*, 1632-1636.

(111) Amendola, V.; Fabbrizzi, L.; Foti, F.; Licchelli, M.; Mangano, C.; Pallavicini, P.; Poggi, A.; Sacchi, D.; Taglietti, A. *Coord. Chem. Rev.* **2006**, *250*, 273-299.

(112) Saraogi, I.; Hamilton, A. D. *Chem. Soc. Rev.* **2009**, *38*, 1726-1743.

(113) Juwarker, H.; Suk, J.-M.; Jeong, K.-S. *Chem. Soc. Rev.* **2009**, *38*, 3316-3325.

(114) Constable, E. C.; Drew, M. G. B.; Forsyth, G.; Ward, M. D. *J. Chem. Soc., Chem. Commun.* **1988**, 1450-1451.

(115) Constable, E. C.; Walker, J. V.; Tocher, D. A.; Daniels, M. A. M. *J. Chem. Soc., Chem. Commun.* **1992**, 768-771.

(116) Constable, E. C.; Edwards, A. J.; Martinez-Manez, R.; Raithby, P. R. *J. Chem. Soc. Dalton Trans.* **1995**, 3253-3261.

(117) Hasenknopf, B.; Lehn, J. M.; Kneisel, B. O.; Baum, G.; Fenske, D. *Angew. Chem. Int. Ed.* **1996**, *35*, 1838-1840.

(118) Hasenknopf, B.; Lehn, J. M.; Boumediene, N.; Dupont-Servais, A.; Van Dorsselaer, A.; Kneisel, B. O.; Fenske, D. *J. Am. Chem. Soc.* **1997**, *119*, 10956-10962.

(119) Image Credit: http://en.wikipedia.org/wiki/File:Supramolecular_Chemistry_Lehn.jpg; accessed 17/09/2013

(120) Pelleteret, D.; Clerac, R.; Mathoniere, C.; Harte, E.; Schmitt, W.; Kruger, P. E. *Chem. Commun.* **2009**, 221-223.

(121) Ayme, J.-F.; Beves, J. E.; Campbell, C. J.; Leigh, D. A. *Chem. Soc. Rev.* **2013**, *42*, 1700-1712.

(122) Dietrich-Buchecker, C. O.; Sauvage, J. P. *Angew. Chem. Int. Ed.* **1989**, *28*, 135-252.

(123) Dietrich-Buchecker, C. O.; Guilhem, J.; Pascard, C.; Sauvage, J. P. *Angew. Chem. Int. Ed.* **1990**, *29*, 1154-1156.

(124) Adams, H.; Ashworth, E.; Breault, G.; Guo, J.; Hunter, C. A.; Mayers, P. C. *Nature* **2001**, *411*, 763-764.

(125) Guo, J.; Mayers, P. C.; Breault, G.; Hunter, C. A. *Nat. Chem.* **2010**, *2*, 218-222.

(126) Li, F.; Clegg, J. K.; Lindoy, L. F.; Macquart, R. B.; Meehan, G. V. *Nat. Commun.* **2011**, *2*, 205-208.

(127) Ayme, J.-F.; Beves, J. E.; Leigh, D. A.; McBurney, R. T.; Rissanen, K.; Schultz, D. *Nature Chem.* **2012**, *4*, 15-20.

(128) Chichak, K. S.; Cantrill, S. J.; Pease, A. R.; Chiu, S.-H.; Cave, G. W. V.; Atwood, J. L.; Stoddart, J. F. *Science* **2004**, *304*, 1308-1312.

(129) Wasserman, E. *J. Am. Chem. Soc.* **1960**, *82*, 4433-4434.

(130) Hubin, T. J.; Busch, D. H. *Coord. Chem. Rev.* **2000**, *200*, 5-52.

(131) Hunter, C. A. *J. Am. Chem. Soc.* **1992**, *114*, 5303-5311.

(132) Vickers, M. S.; Beer, P. D. *Chem. Soc. Rev.* **2007**, *36*, 211-225.

(133) Balzani, V.; Gomez-Lopez, M.; Stoddart, J. F. *Acc. Chem. Res.* **1998**, *31*, 405-414.

(134) Cardenas, D. J.; Livoreil, A.; Sauvage, J. P. *J. Am. Chem. Soc.* **1996**, *118*, 11980-11987.

(135) Bissell, R. A.; Cordova, E.; Kaifer, A. E.; Stoddart, J. F. *Nature* **1994**, *369*, 133-137.

(136) Ashton, P. R.; Ballardini, R.; Balzani, V.; Baxter, I.; Credi, A.; Fyfe, M. C. T.; Gandolfi, M. T.; Gomez-Lopez, M.; Martinez, M. V.; Piersanti, A.; Spencer, N.; Stoddart, J. F.; Venturi, M.; White, A. J. P.; Williams, D. J. *J. Am. Chem. Soc.* **1998**, *120*, 11932-11942.

(137) Brouwer, A. M.; Frochot, C.; Gatti, F. G.; Leigh, D. A.; Mottier, L.; Paolucci, F.; Roffia, S.; Wurpel, G. W. H. *Science* **2001**, *291*, 2124-2128.

(138) Stoddart, J. F. *Chem. Soc. Rev.* **2009**, *38*, 1802-1820.

(139) Badjic, J. D.; Balzani, V.; Credi, A.; Silvi, S.; Stoddart, J. F. *Science* **2004**, *303*, 1845-1849.

(140) Kay, E. R.; Leigh, D. A.; Zerbetto, F. *Angew. Chem. Int. Ed.* **2006**, *46*, 72-191.

(141) Ali, H. D. P.; Kruger, P. E.; Gunnlaugsson, T. *New. J. Chem.* **2008**, *32*, 1153-1161.

(142) Mal, P.; Breiner, B.; Rissanen, K.; Nitschke, J. R. *Science* **2009**, *324*, 1697-1699.

(143) Kang, J.; Rebek, J. *Nature* **1997**, *385*, 50-52.

(144) Yoshizawa, M.; Tamura, M.; Fujita, M. *Science* **2006**, *312*, 251-254.

(145) Chen, J.; Rebek Jr., J. *Org. Lett.* **2002**, *4*, 327-329.

(146) Yoshizawa, M.; Takeyama, Y.; Kusukawa, T.; Fujita, M. *Angew. Chem. Int. Ed.* **2002**, *41*, 1347-1349.

(147) Takaoka, K.; Kawano, M.; Ozeki, T.; Fujita, M. *Chem. Commun.* **2006**, 1625-1627.

(148) Sundaresan, A. K.; Ramamurthy, V. *Org. Lett.* **2007**, *9*, 3575-3578.

(149) Kaanumalle, L. S.; Gibb, C. L. D.; Gibb, B. C.; Ramamurthy, V. *Org. Biomol. Chem.* **2007**, *5*, 236-238.

(150) Gibb, C. L. D.; Sundaresan, A. K.; Ramamurthy, V.; Gibb, B. C. *J. Am. Chem. Soc.* **2008**, *130*, 4069-4080.

(151) Furusawa, T.; Kawano, M.; Fujita, M. *Angew. Chem. Int. Ed.* **2007**, *46*, 5717-5719.

(152) Furutani, Y.; Kandori, H.; Kawano, M.; Nakabayashi, K.; Yoshizawa, M.; Fujita, M. *J. Am. Chem. Soc.* **2009**, *131*, 4764-4768.

(153) Brown, C. J.; Bergman, R. G.; Raymond, K. N. *J. Am. Chem. Soc.* **2009**, *131*, 17530-17531.

(154) Leung, D. H.; Fiedler, D.; Bergman, R. G.; Raymond, K. N. *Angew. Chem. Int. Ed.* **2004**, *43*, 963-966.

(155) Janiak, C. *Dalton Trans.* **2003**, 2781-2804.

(156) Ferey, G. *Chem. Soc. Rev.* **2008**, *37*, 191-214.

(157) Rosi, N. L.; Eckert, J.; Eddaoudi, M.; Vodak, D.; Kim, J.; O'Keeffe, M.; Yaghi, O. M. *Science* **2003**, *300*, 1127-1129.

(158) Batten, S. R.; Robson, R. *Angew. Chem. Int. Ed.* **1998**, *37*, 1460-1494.

(159) Czaja, A. U.; Trukhan, N.; Ulrich, M. *Chem. Soc. Rev.* **2009**, *38*, 1284-1293.

(160) Kuppler, R. J.; Timmons, D. J.; Fang, Q.-R.; Li, J.-R.; Makal, T. A.; Young, M. D.; Yuan, D.; Zhao, D.; Zhuang, W.; Zhou, H.-C. *Coord. Chem. Rev.* **2009**, *253*, 3042-3066.

(161) Ma, S.; Zhou, H.-C. *Chem. Commun.* **2010**, *46*, 44-53.

(162) Gutlich, P.; Hauser, A.; Spiering, H. *Angew. Chem. Int. Ed.* **1994**, *33*, 2024-2054.

(163) Real, J. A.; Gaspar, A. B.; Munoz, M. C. *Dalton Trans.* **2005**, 2062-2079.

(164) Gutlich, P.; Goodwin, H. A. In *Spin Crossover in Transition Metal Compounds 1*; Gutlich, P., Goodwin, H. A., Eds.; Springer: Berlin, 2004; Vol. 233; pp 1-49.

(165) Weber, B. In *Spin Crossover Materials: Properties and Applications*; 1st ed.; Halcrow, M. A., Ed.; John Wiley & Sons, Ltd, 2013.

(166) Image Credit: http:///www.quimica.urv.es/w3qf/magnetisme/sco.html; accessed 15/11/2013

(167) Ganguli, P.; Gutlich, P.; Muller, E. W. *Inorg. Chem.* **1982**, *21*, 3429-3433.

(168) Weber, B.; Bauer, W.; Obel, J. *Angew. Chem. Int. Ed.* **2008**, *47*, 10098-10101.

(169) Wei, R.-J.; Huo, Q.; Tao, J.; Huang, R.-B.; Zheng, L.-S. *Angew. Chem. Int. Ed.* **2011**, *50*, 8940-8943.

(170) Sato, T.; Nishi, K.; Iijima, S.; Kojima, M.; Matsumoto, N. *Inorg. Chem.* **2009**, *48*, 7211-7229.

(171) Halder, G. J.; Chapman, K. W.; Neville, S. M.; Moubaraki, B.; Murray, K. S.; Letard, J. F.; Kepert, C. J. *J. Am. Chem. Soc.* **2008**, *130*, 17552-17562.

(172) Real, J. A.; Bolvin, H.; Bousseksou, A.; Dworkin, A.; Kahn, O.; Varret, F.; Zarembowitch *J. Am. Chem. Soc.* **1992**, *114*, 4650-4658.

(173) Garcia, Y.; Kahn, O.; Rabardel, L.; Chansou, B.; Salmon, L.; Tuchagues, J. P. *Inorg. Chem.* **1999**, *38*, 4663-4670.

(174) Niel, V.; Thompson, A. L.; Goeta, A. E.; Enachescu, C.; Hauser, A.; Galet, A.; Munoz, M. C.; Real, J. A. *Chem. Eur. J.* **2005**, *11*, 2047-2060.

(175) Nishi, K.; Kondo, H.; Fujinami, T.; Matsumoto, N.; Iijima, S.; Halcrow, M. A.; Sunatsuki, Y.; Kojima, M. *Eur. J. Inorg. Chem.* **2013**, 927-233.

(176) Telfer, S. G.; Bocquet, B.; Williams, A. F. *Inorg. Chem.* **2001**, *40*, 4818-4820.

(177) Bonnet, S.; Siegler, M. A.; Costa, J. S.; Molnar, G.; Bousseksou, A.; Spek, A. L.; Gamez, P.; Reedijk, J. *Chem. Commun.* **2008**, 5619-5621.

(178) Matouzenko, G. S.; Letard, J. F.; Lecocq, S.; Bousseksou, A.; Capes, L.; Salmon, L.; Perrin, M.; Kahn, O.; Collet, A. *Eur. J. Inorg. Chem.* **2001**, 2935-2945.

(179) Bonnet, S.; Molnar, G.; Costa, J. S.; Siegler, M. A.; Bousseksou, A.; Spek, A. L.; Fu, W. T.; Gamez, P.; Reedijk, J. *Chem. Mat.* **2009**, *21*, 1123-1136.

(180) Matouzenko, G. S.; Luneau, D.; Molnar, G.; Ould-Moussa, N.; Zein, S.; Borshch, S. A.; Bousseksou, A.; Averseng, F. *Eur. J. Inorg. Chem.* **2006**, 2671-2682.

(181) Klingele, J.; Kaase, D.; Klingele, M. H.; Lach, J.; Demeshko, S. *Dalton Trans.* **2010**, *39*, 1689-1691.

(182) McGarvey, J. J.; Lawthers, I. *J. Chem. Soc., Chem. Commun.* **1982**, 906-907.

(183) Lawthers, I.; McGarvey, J. J. *J. Am. Chem. Soc.* **1984**, *106*, 4280-4282.

(184) Decurtins, S.; Gutlich, P.; Kohler, C. P.; Spiering, H. *Chem. Phys. Lett.* **1984**, *105*, 1-4.

(185) Decurtins, S.; Gutlich, P.; Hasselbach, K. M.; Spiering, H. *Inorg. Chem.* **1985**, *24*, 2174-2178.

(186) Hauser, A. *Chem. Phys. Lett.* **1986**, *124*, 543-548.

(187) Gutlich, P.; Garcia, Y.; Woike, T. *Coord. Chem. Rev.* **2001**, *219*, 839-879.

(188) Hauser, A.; Vef, A.; Adler, P. *J. Chem. Phys.* **1991**, *95*, 8710-8717.

(189) Hauser, A. In *Topp. Curr. Chem. Spin Crossover in Transition Metal Compounds*; Gutlich, P., Goodwin, H. A., Eds.; Springer: Berlin Heidelberg, 2004; Vol. 234; pp 155-198.

(190) Letard, J.-F.; Capes, L.; Chastanet, G.; Moliner, N.; Letard, S.; Real, J. A.; Kahn, O. *Chem. Phys. Lett.* **1999**, *313*, 115-120.

(191) Buchen, T.; Gutlich, P.; Goodwin, H. A. *Inorg. Chem.* **1994**, *33*, 4573-4576.

(192) Wu, C.-C.; Jung, J.; Gantzel, P. K.; Gutlich, P.; Hendrickson, D. N. *Inorg. Chem.* **1997**, *36*, 5339-5347.

(193) Renz, F.; Oshio, H.; Ksenofontov, V.; Waldeck, M.; Spiering, H.; Gutlich, P. *Angew. Chem. Int. Ed.* **2000**, *39*, 3699-3700.

(194) Hayami, S.; Gu, Z.-Z.; Einaga, Y.; Kobayasi, Y.; Ishikawa, Y.; Yamada, Y.; Fujishima, A.; Sato, O. *Inorg. Chem.* **2001**, *40*, 3240-3242.

(195) Buchen, T.; Gutlich, P.; Sugiyarto, K. H.; Goodwin, H. A. *Chem. Eur. J.* **1996**, *2*, 1134-1138.

(196) Letard, J. F.; Guionneau, P.; Nguyen, O.; Costa, J. S.; Marcen, S.; Chastanet, G.; Marchivie, M.; Goux-Capes, L. *Chem. Eur. J.* **2005**, *11*, 4582-4589.

(197) Hauser, A. *Coord. Chem. Rev.* **1991**, *111*, 275-290.

(198) Image Credit: http://www.rugl.nl/research/zenike/news/colloquia/20050407gutlichphilipp; accessed 08/10/2013

(199) Shimamoto, N.; Ohkoshi, S. I.; Sato, O.; Hashimoto, K. *Inorg. Chem.* **2002**, *41*, 678-684.

(200) Thies, S.; Hanno, S.; Schutt, C.; Bornholdt, C.; Nather, C.; Tuczek, F.; Herges, R. *J. Am. Chem. Soc.* **2011**, *133*, 16243-16250.

(201) Orgel, L. E., *Quelques Problemes de Chimie Minerale; 10 eme Conseil de Chimie, Bruxelles,* **1956**, 325.

(202) Goodwin, H. A. In *Topp. Curr. Chem. Spin Crossover in Transition Metal Compounds*; Gutlich, P., Goodwin, H. A., Eds.; Springer: Berlin Heidelberg, 2004; Vol. 1; pp 59-90.

(203) Halcrow, M. A. *Polyhedron* **2007**, *26*, 3523-3576.

(204) *Spin Crossover in Transition Metal Compounds*; Gutlich, P.; Goodwin, H. A., Eds.; Springer: Berlin, 2004; Vol. 234, pp 1-289.

(205) *Special Issue:Spin-Crossover Complexes (Cluster Issue) - Eur. J. Inorg. Chem*; Murray, K. S.; Oshio, H.; Real, J. A., Eds., 2013.

(206) Shklover, V.; Nesper, R.; Zakeeruddin, S. M.; Fraser, D. M.; Gratzel, M. *Inorg. Chim. Acta.* **1996**, *247*, 247-255.

(207) Onggo, D.; Hook, J. M.; Rae, A. D.; Goodwin, H. A. *Inorg. Chim. Acta.* **1990**, *173*, 19-30.

(208) Onggo, D.; Goodwin, H. A. *Aust. J. Chem.* **1991**, *44*, 1539-1551.

(209) Craig, D. C.; Goodwin, H. A.; Onggo, D. *Aust. J. Chem.* **1988**, *41*, 1157-1169.

(210) Dosser, R. J.; Eilbeck, W. J.; Underhill, A. E.; Edwards, P. R.; Johnson, C. E. *J. Chem. Soc. A* **1969**, 810-816.

(211) Halcrow, M. A. *Polyhedron* **2007**, *26*, 3523-3576.

(212) Baker, A. T.; Goodwin, H. A.; Rae, A. D. *Inorg. Chem.* **1987**, *26*, 3513-3519.

(213) Sugiyarto, K. H.; Goodwin, H. A. *Aust. J. Chem.* **1988**, *41*, 1645-1663.

(214) Abushamleh, A. S.; Goodwin, H. A. *Aust. J. Chem.* **1979**, *32*, 513-518.

(215) Burnett, M. G.; McKee, V.; Nelson, S. M. *J. Chem. Soc. Dalton Trans.* **1981**, 1492-1497.

(216) Gaudry, J.-B.; Capes, L.; Langot, P.; Marcen, S.; Kollmannsberger, M.; Lavastre, O.; Freysz, E.; Letard, J. F.; Kahn, O. *Chem. Phys. Lett.* **2000**, *324*, 321-329.

(217) Archer, R. J.; Hawes, C. S.; L., J. G. N.; McKee, V.; Moubaraki, B.; Chilton, N. F.; Murray, K. S.; Kruger, P. E. *Dalton Trans.* **2011**, *40*, 12368-12373.

(218) Thompson, J. R.; Archer, R. J.; Hawes, C. S.; Ferguson, A.; Wattiaux, A.; Mathonière, C.; Clérac, R.; Kruger, P. E. *Dalton Trans.* **2012**, *41*, 12720-12725.

(219) Ferguson, A.; Squire, M. A.; Siretanu, D.; Mitcov, D.; Mathonière, C.; Clérac, R.; Kruger, P. E. *Chem. Comm.* **2013**, *49*, 1597-1599.

(220) Tuna, F.; Lees, M. R.; Clarkson, G. J.; Hannon, M. J. *Chem. Eur. J.* **2004**, *10*, 5737-5750.

(221) Sunatsuki, Y.; Kawamoto, R.; Fujita, K.; Maruyama, H.; Suzuki, T.; Ishida, H.; Kojima, M.; Iijima, S.; Matsumoto, N. *Inorg. Chem.* **2009**, *48*, 8784.

(222) Murray, K. S. *Eur. J. Inorg. Chem.* **2008**, 3101.

(223) Tao, J.; Wei, R.-J.; Huang, R.-B.; Zheng, L.-S. *Chem. Soc. Rev.* **2012**, *41*, 703-737.

(224) Naik, A. D.; Tinant, B.; Muffler, K.; Wolny, J. A.; Schunemann, V.; Garcia, Y. *J. Solid State Chem.* **2009**, *182*, 1365-1376.

(225) Reger, D. L.; Gardinier, J. R.; Elgin, J. D.; Smith, M. D. *Inorg. Chem.* **2006**, *45*, 8862-8875.

(226) Real, J. A.; Gaspar, A. B.; Niel, V.; Munoz, M. C. *Coord. Chem. Rev.* **2003**, *236*, 121-141.

(227) Real, J. A.; Gallois, B.; Granier, T.; Suez-Panama, F.; Zarembowitch, J. *Inorg. Chem.* **1992**, *31*, 4972-4979.

(228) Gallois, B.; Real, J. A.; Hauw, C.; Zarembowitch, J. *Inorg. Chem.* **1990**, *29*, 1152-1158.

(229) Zhong, Z. J.; Tao, J.-Q.; Yu, Z.; Dun, C.-Y.; Liu, Y.-J.; You, X.-Z. *J. Chem. Soc. Dalton Trans.* **1988**, 327-328.

(230) Sylva, R. N.; Goodwin, H. A. *Aust. J. Chem.* **1967**, *20*, 479-496.

(231) Renovitch, G. A.; Baker, W. A. *J. Am. Chem. Soc.* **1967**, *89*, 6377-6378.

(232) Sugiyarto, K. H.; Craig, D. C.; Rae, A. D.; Goodwin, H. A. *Aust. J. Chem.* **1994**, *47*, 869-890.

(233) Kennedy, B. J.; McGrath, A. C.; Murray, K. S.; Skelton, B. W.; White, A. H. *Inorg. Chem.* **1987**, *26*, 483-495.

(234) Yamada, M.; Hagiwara, H.; Torigoe, H.; Matsumoto, N.; Kojima, M.; Dahan, F.; Tuchagues, J. P.; Re, N.; Iijima, S. *Chem. Eur. J.* **2006**, *12*, 4536-4549.

(235) Leita, B. A.; Neville, S. M.; Halder, G. J.; Moubaraki, B.; Kepert, C. J.; Letard, J. F.; Murray, K. S. *Inorg. Chem.* **2007**, *46*, 8784-8795.

(236) Yamada, M.; Hagiwara, H.; Kojima, M.; Dahan, F.; Tuchagues, J. P.; Re, N.; Iijima, S. *Chem. Eur. J.* **2006**, *12*, 4536-4549.

(237) Klug, C. M.; McDaniel, A. M.; Fiedler, D.; Schulte, K. A.; Newell, B. S.; Shores, M. P. *Dalton Trans.* **2012**, *41*, 12577-12585.

(238) Hostettler, M.; Tornroos, K. W.; Chernyshov, D.; Vangdal, B.; Burgi, H.-B. *Angew. Chem. Int. Ed.* **2004**, *43*, 4589-4594.

(239) Real, J. A.; Munoz, C.; Andres, E.; Granier, T.; Gallois, B. *Inorg. Chem.* **1994**, *33*, 3587-3594.

(240) Garcia, Y.; Van Koningsbruggen, P. J.; Lapouyade, R.; Fournes, L.; Rabardel, L.; Kahn, O.; Ksenofontov, V.; Levchenko, G.; Gutlich, P. *Chem. Mater.* **1998**, *10*, 2426-2433.

(241) Li, B.; Wei, R.-J.; Tao, J.; Huang, R.-B.; Zheng, L.-S.; Zheng, Z. *J. Am. Chem. Soc.* **2010**, *132*, 1558-1566.

(242) Wu, C.-C.; Jung, J.; Gantzel, P. K.; Gutlich, P.; Hendrickson, D. N. *Inorg. Chem.* **1997**, *36*, 5339-5347.

(243) Matouzenko, G. S.; Bousseksou, A.; Lecocq, S.; Van Koningsbruggen, P. J.; Perrin, M.; Kahn, O.; Collet, A. *Inorg. Chem.* **1997**, *36*, 5869-5879.

(244) Ni, Z.; Shores, M. P. *J. Am. Chem. Soc.* **2009**, *131*, 32-33.

(245) Ni, Z.; McDaniel, A. M.; Shores, M. P. *Chem. Sci.* **2010**, *1*, 615-621.

(246) Ni, Z.; Shores, M. P. *Inorg. Chem.* **2010**, *49*, 10727-10735.

(247) Ni, Z.; Fiedler, S. R.; Shores, M. P. *Dalton Trans.* **2011**, *40*, 944-950.

(248) Duriska, M. B.; Neville, S. M.; Moubaraki, B.; Cashion, J. D.; Halder, G. J.; Balde, C.; Chapman, K. W.; Letard, J.-F.; Murray, K. S.; Kepert, C. J.; Batten, S. R. *Angew. Chem. Int. Ed.* **2009**, *48*, 2549-2552.

(249) Image Credit: http://monash.edu/science/about/schools/chemistry/honours/2009/batten-stuart/project1.html; accessed 14/10/2013

(250) Kahn, O.; Martinez, C. J. *Science* **1998**, *279*, 44-48.

(251) Kroeber, J.; Audiere, J.-P.; Claude, R.; Codjovi, E.; Kahn, O.; Haasnoot, J. G.; Groliere, F.; Jay, C.; Bousseksou, A. *Chem. Mater.* **1994**, *6*, 1404-1412.

(252) Krober, J.; Codjovi, E.; Kahn, O.; Groliere, F.; Jay, C. *J. Am. Chem. Soc.* **1993**, *115*, 9810-9811.

(253) Roubeau, O. *Chem. Eur. J.* **2012**, *18*, 15230-15244.

(254) Lavrenova, L. G.; Shakirova, O. G. *Eur. J. Inorg. Chem.* **2013**, 670-682.

(255) Aromi, G.; Barrios, L. A.; Roubeau, O.; Gamez, P. *Coord. Chem. Rev.* **2011**, *255*, 485-546.

(256) Van Koningsbruggen, P. J. *Topp. Curr. Chem*. **2004**, 123.

(257) Ferey, G. *Chem. Soc. Rev.* **2008**, *37*, 191-214.

(258) Niel, V.; Martinez-Agudo, J. M.; Munoz, M. C.; Gaspar, A. B.; Real, J. A. *Inorg. Chem.* **2001**, *40*, 3838-3839.

(259) Ohba, M.; Yoneda, K.; Agusti, G.; Munoz, M. C.; Gaspar, A. B.; Real, J. A.; Yamasaki, M.; Ando, H.; Nakao, Y.; Sakaki, S.; Kitagawa, S. *Angew. Chem. Int. Ed.* **2009**, *48*, 4767-4771.

(260) Bousseksou, A.; Molnar, G.; Salmon, L.; Nicolazzi, W. *Chem. Soc. Rev.* **2011**, *40*, 3313-3335.

(261) Forestier, T.; Mornet, S.; Daro, N.; Nishihara, T.; Mouri, S.-I.; Tanaka, K.; Fouche, O.; Freysz, E.; Letard, J. F. *Chem. Commun.* **2008**, 4327-4329.

(262) Letard, J. F. *Top. Curr. Chem.* **2004**, *235*, 221.

(263) Coronado, E.; Galan-Mascaros, J. R.; Monrabal-Capilla, M.; Garcia-Martinez, J.; Pardo-Ibanez, P. *Adv. Mater.* **2007**, *19*, 1359-1361.

(264) Galan-Mascaros, J. R.; Coronado, E.; Forment-Aliaga, A.; Monrabal-Capilla, M.; Pinilla-Cienfuegos, E.; Ceolin, M. *Inorg. Chem.* **2010**, *49*, 5706-5714.

(265) Soyer, H.; Dupart, E.; Gomez-Garcia, C. J.; Mingotaud, C.; Delhaes, P. *Adv. Mater.* **1999**, *11*, 382-384.

(266) Soyer, H.; Dupart, E.; Mingotaud, C.; Gomez-Garcia, C. J.; Delhaes, P. *Colloids Surf. A* **2000**, *171*, 275-282.

(267) Letard, J. F.; Nguyen, O.; Soyer, H.; Mingotaud, C.; Delhaes, P.; Kahn, O. *Inorg. Chem.* **1999**, *38*, 3020-3021.

(268) Bodenthin, Y.; Pietsch, U.; Mohwald, H.; Kurth, D. G. *J. Am. Chem. Soc.* **2005**, *127*, 3110-3114.

(269) Boillot, M.-L.; Pillet, S.; Tissot, A.; Riviere, E.; Claiser, N.; Lecomte, C. *Inorg. Chem.* **2009**, *48*, 4729-4736.

(270) Lee, S.-W.; Lee, J.-W.; Jeong, S.-H.; Park, I.-W.; Kim, Y.-M.; Jin, J.-I. *Synth. Met.* **2004**, *142*, 243-249.

(271) Nakamoto, A.; Ono, Y.; Kojima, N.; Matsumura, D.; Yokoyama, T. *Chem. Lett.* **2003**, *32*, 336-337; Correction 476.

(272) Cobo, S.; Molnar, G.; Real, J. A.; Bousseksou, A. *Angew. Chem. Int. Ed.* **2006**, *45*, 5786-5789.

(273) Hammond, P. T. *Adv. Mater.* **2004**, *16*, 1271-1293.

(274) Agusti, G.; Cobo, S.; Gaspar, A. B.; Molnar, G.; Moussa, N. O.; Szilagyi, P. A.; Palfi, V.; Vieu, C.; Munoz, C.; Real, J. A.; Bousseksou, A. *Chem. Mater.* **2008**, *20*, 6721-6732.

(275) Molnar, G.; Real, J. A.; Carcenac, F.; Daran, E.; Vieu, C.; Bousseksou, A. *Adv. Mater.* **2007**, *19*, 2163-2167.

(276) Decher, G. *Science* **1997**, *277*, 1232-1237.

(277) Bartual-Murgui, C.; Akou, A.; Salmon, L.; Molnar, G.; Thibault, C.; Real, J. A.; Bousseksou, A. *Small* **2011**, *7*, 3385-3391.

(278) Guionneau, P.; Marchivie, M.; Bravic, G.; Letard, J. F.; Chasseau, D. *Top. Curr. Chem.* **2004**, *234*, 97-128.

(279) Ortega-Villar, N.; Thompson, A. L.; Munoz, C. M.; Ugalde-Saldivar, V. M.; Goeta, A. E.; Moreno-Esparza, R.; Real, J. A. *Chem. Eur. J.* **2005**, *11*, 5721-5734.

(280) Hauser, A. *Top. Curr. Chem.* **2004**, *234*, 155-198.

(281) Charbonniere, L. J.; Williams, A. F.; Piguet, C.; Bernardinelli, G.; Rivara-Minten, E. *Chem. Eur. J.* **1998**, *4*, 485-493.

(282) Garcia, Y.; Grunert, C. M.; Reiman, S.; Van Campenhoudt, O.; Gutlich, P. *Eur. J. Inorg. Chem.* **2006**, 3333-3339.

(283) Fujita, K.; Kawamoto, R.; Tsubouchi, R.; Sunatsuki, Y.; Kojima, M.; Iijima, S.; Matsumoto, N. *Chem. Lett.* **2007**, *36*, 1284-1285.

(284) Sunatsuki, Y.; Kawamoto, R.; Fujita, K.; Maruyama, H.; Suzuki, T.; Ishida, H.; Kojima, M.; Iijima, S.; Matsumoto, N. *Coord. Chem. Rev.* **2010**, *254*, 1871-1881.

(285) Schneider, C. J.; Cashion, J. D.; Chilton, N. F.; Etrillard, C.; Fuentealba, M.; Howard, J. A. K.; Letard, J.-F.; Milsmann, C.; Moubaraki, B.; Sparkes, H. A.; Batten, S. R.; Murray, K. S. *Eur. J. Inorg. Chem.* **2013**, 850-864.

(286) Yamada, M.; Ooidemizu, M.; Ikuta, Y.; Osa, S.; Matsumoto, N.; Iijima, S.; Kojima, M.; Dahan, F.; Tuchagues, J. P. *Inorg. Chem.* **2003**, *42*, 8406-8416.

(287) Sunatsuki, Y.; Ikuta, Y.; Matsumoto, N.; Ohta, H.; Kojima, M.; Iijima, S.; Hayami, S.; Maeda, Y.; Kaizaki, S.; Dahan, F.; Tuchagues, J. P. *Angew. Chem. Int. Ed.* **2003**, *42*, 1614-1618.

(288) Allen, F. H.; Kennard, O.; Watson, D. G.; Brammer, L.; Orpen, A. G.; Taylor, R. *J. Chem. Soc., Perkin Trans.* **1987**, *2*, S1-S19.

(289) Barrett, S. A.; Kilner, C. A.; Halcrow, M. A. *Dalton Trans.* **2011**, *40*, 12021-12024.

(290) Turner, J. W.; Schultz, F. A. *Inorg. Chem.* **2001**, *40*, 5296-5298.

(291) Purcell *J. Am. Chem. Soc.* **1979**, *101*, 5147-5152.

(292) Toftlund, H. *Coord. Chem. Rev.* **1989**, *94*, 67-108.

(293) McGarvey, J. J.; Lawthers, I.; Heremans, K.; Toftlund, H. *J. Chem. Soc., Chem. Commun.* **1984**, 1575-1576.

(294) Ohtani, R.; Yoneda, K.; Furukawa, S.; Horike, N.; Kitagawa, S.; Gaspar, A. B.; Munoz, C. M.; Real, J. A.; Ohba, M. *J. Am. Chem. Soc.* **2011**, *133*, 8600-8605.

(295) Scifinder structure search; 25/10/2013

(296) Heider, S.; Petzold, H.; Chastanet, G.; Schlamp, S.; Ruffer, T.; Weber, B.; Letard, J. F. *Dalton Trans.* **2013**, *42*.

(297) Nishi, K.; Arata, S.; Matsumoto, N.; Iijima, S.; Sunatsuki, Y.; Ishida, H.; Kojima, M. *Inorg. Chem.* **2010**, *49*, 1517-1523.

(298) Hibbs, W.; Van Koningsbruggen, P. J.; Arif, A. M.; Shum, W. W.; Miller, J. S. *Inorg. Chem.* **2003**, *42*, 5645-5653.

(299) Matouzenko, G. S.; Luneau, D.; Molnar, G.; Ould-Moussa, N.; Zein, S.; Borshch, S. A.; Bousseksou, A.; Averseng, F. *Eur. J. Inorg. Chem.* **2006**, 2671-2682.

(300) Mikami, M.; Konno, M.; Saito, S. *Chem. Phys. Lett.* **1979**, *63*, 566-569.

(301) Bryliakov, K. P.; Duban, E. A.; Talsi, E. P. *Eur. J. Inorg. Chem.* **2005**, 72-76.

(302) Prat, I.; Company, A.; Corona, T.; Parella, T.; Ribas, X.; Costas, M. *Inorg. Chem.* **2013**, *52*, 9229-9244.

(303) Clayden, J.; Greeves, N.; Warren, S.; Worthers, P. *Organic Chemistry*; Oxford University Press: New York, 2001.

(304) Cozzi, F.; Cinquini, M.; Annuziata, R.; Siegel, J. S. *J. Am. Chem. Soc.* **1993**, *115*, 5330-5331.

(305) Toftlund, H. *Monatsh. Chem.* **2001**, *132*, 1269-1277.

(306) Martinho, P. N.; Rajnak, C.; Ruben, M. In *Spin-Crossover Materials: Properties and Applications*; John Wiley & Sons, 2013; Vol. Ed. Malcom Halcrow.

(307) Cavallini, M. *Phys. Chem. Chem. Phys.* **2012**, *14*, 11867-11876.

(308) Bousseksou, A.; Molnar, G.; Salmon, L.; Nicolazzi, W. *Chemical Society Reviews* **2011**, *40*, 3313-3335.

(309) Matsuda, M.; Tajima, H. *Chem. Lett.* **2007**, *36*, 700-701.

(310) Sheldrick, G. M. *Acta Crystallogr., Sect. A,* **2008***, 64*, 112-122

(311) Sheldrick, G. M., *SHELXL-97, Programs for X-ray Crystal Structure Refinement*, **1997**, University of Gottingen.

(312) Dolomanov, O. V.; Bourhis, L. J.; Gildea, R. J.; Howard, J. A. K.; Puschmann, H. *J. Appl. Cryst.* **2009**, *42*, 339-341.

PUBLICATIONS

Provided as Electronic Supplementary Information